DEVELOPMENT OF WHOLE-BODY TISSUE CLEARING METHODS FACILITATES THE CELLULAR MAPPING OF ORGANISMS

PAN Chenchen

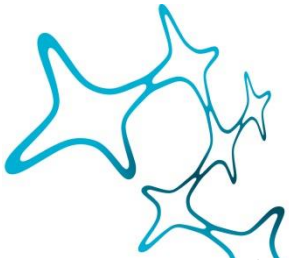

Graduate School of
Systemic Neurosciences

LMU Munich

Dissertation at the
Graduate School of Systemic Neurosciences
Ludwig-Maximilians-Universität München

<March, 2019>

Supervisor
Dr. Ali Ertürk
Institute for Stroke and Dementia Research (ISD)
Klinikum der Universität München

First Reviewer: Dr. Ali Ertürk
Second Reviewer: Prof. Dr. Martin Kerschensteiner

Date of Submission: March 29th, 2019
Date of Defense : July 31st, 2019

Table of Contents

List of abbreviations

HGP	Human Genome Project
PET	Positron emission tomography
MRI	Magnetic resonance imaging
RI	Refractive indices
LSFM	Light-sheet fluorescent microscopy
3DISCO	3D imaging of solvent-cleared organs
uDISCO	Ultimate 3D imaging of solvent-cleared organs
vDISCO	Nanobody(VHH)-boosted 3D imaging of solvent cleared organs
DeepMACT	Deep learning-enabled Metastasis Analysis in Cleared Tissue
iDISCO	Immunolabeling-enabled three-dimensional imaging of solvent-cleared organs
FDISCO	DISCO with superior fluorescence-preserving capability
PEGASOS	Polyethylene glycol (PEG)-associated solvent system
SeeDB	See Deep Brain
CUBIC	Clear, unobstructed brain imaging cocktails and computational analysis
CLARITY	Clear lipid-exchanged acrylamide-hybridized rigid Imaging/Immunostaining/In situ hybridization-compatible tissue hYdrogel
PACT	Passive CLARITY technique
PARS	Perfusion-assisted agent release in situ
ACT-PRESTO	Active clarity technique-pressure related efficient and stable transfer of macromolecules into organs
CNS	Central nervous system
BMSCs	Bone marrow–derived mesenchymal stem cells
BBB	Blood-brain barrier
ALS	Amyotrophic lateral sclerosis
PD	Parkinson’s disease
HD	Huntington’s disease
SCI	Spinal cord injury
ChP	Choroid plexus
SMCs	short vascular connections between skull bone marrow and brain meninges

TCVs	Trans-cortical vessels
EMT	Epithelial-mesenchymal transition
CTCs	Circulating tumor cells
ER	Estrogen receptor
HER-2	Human epidermal growth factor receptor 2
CAs	Carbonic anhydrases
DOX	Doxorubicin
FISH	Fluorescence in situ hybridization
THF	Tetrahydrofuran
DCM	Dichlormethane
DBE	Dibenzylether
DPE	Diphenyl ether
SDS	Sodium dodecyl sulfate
GFP	Green fluorescent protein
RFP	Red fluorescent protein

Abstract

The organism is a complex system composed with different organs and various types of cells. It has become more and more evident that diseases, although originally raised from restrict region, normally lead to a global impact affecting multiple parts of the body. This indicates that the organisms should be regarded as an interconnected system, both physiological and pathological alterations should be studied in an unbiased way. Recent tissue clearing methods start to play an important role in systems biology studies since it enables the screening of the transparent tissue with its entirety. However, because of the light scattering as well as autofluorescence for deep tissue imaging and the limited sample size that can be imaged by a light-sheet microscope, it remains challenging to scan and analyze large samples such as an entire rodent body.

Here, we developed uDISCO and vDISCO whole-body tissue clearing methods which enables the complete scanning of adult rodent bodies with standard light-sheet microscopy. As an organic solvent based tissue clearing method, uDISCO overcomes the fast quenching of fluorescent proteins and preserves the GFP signal over months. Combining with a high pressure transcardial circulating system to deliver the nanobody, vDISCO achieved whole-body immunolabeling and imaging through the intact transparent bone and skin. Applying uDISCO to biological studies, we evaluated the bio-distribution of bone marrow-derived stem cells with intravenous transplantation. By using vDISCO, we studied the global inflammation after acute central nervous system injury and revealed the short connections between skull bone marrow and brain meninges as novel additional immune cells infiltration route. Combining with a deep learning based algorithm, vDISCO enables the automated mapping of cancer metastasis and therapeutic drug distribution through the entire mouse bodies with cellular level resolution.

Taken together, uDISCO and vDISCO whole-body tissue clearing methods provide a powerful platform for unbiased screening and systemic analysis of entire rodent bodies. As practical and efficient techniques, they can be readily used for various biological and biomedical researches.

1. Introduction

The great success of Human Genome Project (HGP) from 1990s has led life science research to a productive ‘genomic era’ to present days (Poliakov et al., 2015). As declared by former President of the Sanger Center, John Sulston, “Think of the human genome as the Book of Life. We are about to read the first chapter, as important an accomplishment as discovering the Earth goes round the sun or that we are descended from apes” (Cooper, 2001; Perbal, 2015).

Regarding the “Book of life”, deciphering individual molecule’s structure/function and resolving the related cellular signaling pathways is like reading each page of the book, which is extremely important, yet insufficient to provide the key information how an organ or organism is assembled and functioning as a complex biological system. To answer this question, in early twenty-first century, the concept of ‘systems biology’ was raised aiming to understand how the individual components and different tissue are structurally connected and dynamically interacted at whole organ or even whole organism level (Kitano, 2002). Although the discoveries in research field of molecular biology and cellular biology were blooming in last two decades, the “organism-level systems biology” is restricted due to the lack of technical approaches despite its importance in life science and biomedical research. Therefore, an advanced methodology which enables the fast screening of an entire organism (e.g. an intact mouse or rat body) at cellular level resolution will provide a powerful platform for systems biology studies and will facilitate various biomedical research fields (Susaki and Ueda, 2016).

Nowadays, the widely used whole rodent body imaging techniques include bioluminescence imaging (Vick et al., 2015; von Neubeck et al., 2018), PET and MRI (Dall'Ara et al., 2016; Schoder and Gonen, 2007). Although scientists can get preliminary metabolism or structure information by using these techniques, the millimeter-level resolution can only provide bulk signals which is impossible to resolve single cells from the whole-body scale. On the other hand, combining tissue sectioning, histological staining and microscopy achieved micrometer-level resolution and became a standard protocol for life science research. However, to section, stain and image the whole-body of an adult mouse will take weeks to months. Although whole-body sectioning method has been used to study T cell distribution by analyzing

representative sections (Odoardi et al., 2012; Reinhardt et al., 2001), it is nearly impossible to achieve the whole-body reconstruction for volumetric analysis. Furthermore, tissue sectioning is not suitable to neuroscience research as it could only provide partial or fragmented information of neuronal projections covering millimeter to centimeter distance (Erturk and Bradke, 2013). Therefore, to systemically study the bio-distribution of specific cell subtypes or drugs and to investigate the neuronal network in health or disease requires a novel methodology which enables the mapping of intact organism at cellular level resolution with its entirety.

As discussed above, ideally the biological samples should be imaged without sectioning. However, because of the different refractive indices (RI) between the lipid based cellular membranes and water-based interstitial fluid or cytoplasm, imaging light is obstructed by light absorption, scattering and aberrations (Tuchin, 2015; Zhu et al., 2013). As a result, the imaging depth of a standard confocal microscopy is limited to 150 μm and 2-photon microscopy to 500–800 μm underneath the tissue surface (Clendenon et al., 2011; Theer and Denk, 2006), which is far from overcoming the intact whole organs, not to mention the entire mouse bodies.

The development of various tissue clearing methods in recent years provides a potential technical pathway to overcome these bottlenecks and holds the promise to image the organism without sectioning. Tissue clearing aims to match the refractive index within the biological samples and thereby achieves the homogeneity of the refractive index (Richardson and Lichtman, 2015). As a result, the samples become optically transparent and the imaging light can illuminate through the biological samples without severe scattering or aberration. Another technical approach is the development of light-sheet fluorescent microscopy (LSFM). Differently from the traditional confocal or 2-photon microscope, light-sheet microscope generates a thin laser to illuminate the specimen at the focal plane and the emission signal from the entire panel will be collected by a vertically integrated objective (Dodt et al., 2007). Combining with various transgenic or immune-fluorescent labeling strategies, tissue clearing enables the fast optical sectioning of the intact biological samples with their entirety.

Although several tissue clearing methods before our approaches (uDISCO and vDISCO) achieved some degree of whole-body clearing, which are PARS and CUBIC, they mainly cleared the whole body of a mouse and dissect the organs of interest for imaging due to the lack of transparency. In my PhD study, I developed uDISCO and vDISCO methods with colleagues which achieved the whole-body tissue clearing and complete imaging at cellular level resolution (Cai et al., 2019; Pan et al., 2016). These two advanced whole-body clearing and imaging methodologies, as the best tools for systems biology studies, will significantly contribute to the a variety of life science and biomedical research fields.

In the introduction section, I will firstly present the overview of tissue clearing field and will focus on the development of u/vDISCO technologies by comparing existing whole-body tissue clearing methods. Secondly, I will present the applications of u/vDISCO methods in diverse biological studies such as stem cell transplantation, global neuroinflammation after CNS injury, cancer metastasis and therapeutic drug bio-distribution, which led to novel biological discoveries in the related fields.

1.1 Optical Tissue clearing

As previously mentioned that imaging light scatters because of the mismatching of RI within biological samples. Biological tissue normally contains 70–80% water with low RI (n = 1.33), ∼10% lipids with high RI (n > 1.45) and ∼10% proteins with high RI (n > 1.44) (Richardson and Lichtman, 2015). Since the proteins are the major functional carriers of cellular events and attract most of the research interests, tissue clearing mainly aims to preserve the protein content and match the RI of protein by using high-RI medium. Depends on different technical approaches to achieve high RI matching, the tissue clearing field can be classified into three categories, 1) water-reagent based clearing, 2) hydrogel based clearing, and 3) organic solvent based clearing.

1.1.1 Water-reagent based clearing

Since sugar based chemicals are highly soluble and are able to increase the RI of water, high concentration sugar solutions are considered as promising high-RI matching medium. SeeDB protocol uses gradient fructose solutions up to 115 wt% to reach the RI around 1.49. It successfully preserved the morphology of samples both

in macro and in micro scale (Ke et al., 2013). However, Since the clearing process depends on the passive diffusion of high concentration viscous sugar solution, it can only clear highly permeabilized tissue such as mouse embryo, neonatal mouse brain (P3) or 1.5 mm thin sections of adult mouse brain.

In addition, urea is also widely used in tissue clearing as it has the strong hyperhydration abilities and can improve the molecular influx (Tainaka et al., 2016). FRUIT combined fructose and urea solutions, which was less viscous and achieved better clearing efficiency than SeeDB. Since no harsh delipidation reagent was used, both SeeDB and FRUIT preserve the cellular membrane and therefore are compatible with DiI labeling (Hou et al., 2015). However, FRUIT is still insufficient to clear and image the intact adult mouse organs.

Alcohol based chemicals which have a high RI are also considered as candidates in tissue clearing field. Scale A2 and ScaleS clearing protocols utilized sorbital and urea as the major components. Combining with detergents such as triton-X 100 and chemicals which can loosen the texture of the tissue (methyl-β-cyclodextrin and N-acetyl-L-hydroxyproline), ScaleS further improved the clearing efficiency (Hama et al., 2015; Hama et al., 2011). In addition, it preserves the ultrastructure of the biological samples, allowing high resolution 2-photon microscopy or even electron microscopy of the cleared samples. Although it achieved proper transparency for an entire brain from a Thy1-YFPH line transgenic mouse, it took 15 months to clear the whole brain which does not match the normal experimental timeline schedule for most of the laboratories.

The first practical whole-organ scale water-reagent based clearing is CUBIC (clear, unobstructed brain imaging cocktails and computational analysis). By using CUBIC reagent1 containing 25% urea, 25% N,N,N',N'-tetrakis(2-hydroxypropyl) ethylenediamine and 15% Triton X-100 and followed by CUBIC-2 which is a mixture of 50 wt% sucrose, 25 wt% urea, 10 wt% 2,20,20'-nitrilotriethanol and 0.1% (v/v) Triton X-100, the whole mouse brain can be cleared within two weeks. The involvement of N,N,N',N'-tetrakis(2-hydroxypropyl) ethylenediamine successfully decolorizes the heme rich tissue by removing the heme chromophore from hemoglobin. As a result, CUBIC achieved sufficient organ transparency for

fluorescent light-sheet microscopy and is compatible with various fluorescent proteins and immunolabeling (Susaki et al., 2014). Furthermore, CUBIC also achieved whole-body clearing with adult mice (Tainaka et al., 2014). The authors used this method to image the cancer metastases in whole mouse bodies from different cancer cell lines expressing fluorescent proteins and to quantify the cancer metastasis in specific organs such as lungs and brains (Kubota et al., 2017). However, the quantifications of metastasis were mainly conducted on individual organs after dissection which limited the advantageous usage of whole-body tissue clearing. On the other hand, the entire clearing process for a dissected organ takes more than ten days which is much longer than the organic solvent-based tissue clearing methods.

1.1.2 Hydrogel based clearing

Hydrogel based clearing aims to generate an extra acrylamide gel within the biological tissue to lock the endogenous proteins in situ. Then the following steps of delipidation by ionic detergent and the high-RI matching by sugar or alcohol based solutions will be conducted to achieve tissue transparency while the proteins of interest will be preserved in the hydrogel crosslink.

The Deisseroth's group developed CLARITY (clear lipid-exchanged acrylamide-hybridized rigid imaging/immunostaining/in situ hybridization-compatible tissue-hydrogel) which combined electrophoretic delipidation (Chung and Deisseroth, 2013; Chung et al., 2013). This method can clear a whole mouse brain within 10 days and achieved high permeability of the tissue which is valuable for whole mount immunohistochemistry analysis. However, the major risk is the integrity of the samples since the harsh treatment and the heat created by electroporation may damage the tissue (Tomer et al., 2014). To overcome this obstacle, PAssive CLARITY technique (PACT) was developed (Yang et al., 2014). It holds the same hydrogel embedding concept with CLARITY but the delipidation is conducted by passive shaking with 8-10% SDS solutions.

Combining with additional treatments or different clearing techniques, other tissue clearing techniques were developed based on hydrogel embedding concept. For instance, complemented with decalcification by EDTA solutions, bone CLARITY was developed for investigating the bone structure and bone marrow cellular content with

their integrity (Greenbaum et al., 2017). Combining with CUBIC, ACT-PRESTO can clear various biological tissues from zebrafish to rodents (Lee et al., 2016). It is worth noting that by active transcardial perfusion of the delipidation solution, PARS (perfusion-assisted agent release in situ) also achieved whole-body clearing of adult mice (Treweek et al., 2015; Yang et al., 2014). Although PARS has been used to evaluate the bio-distribution of virus through the entire mouse body (Deverman et al., 2016), the whole clearing process took more than 3 weeks and the organs were dissected for imaging. This brings the major drawbacks of Hydrogel based clearing, 1) it normally causes tissue swelling which makes the enlarged samples difficult to fit in the imaging system; 2) the hydrogel is quite fragile and not easy to handle.

1.1.3 Organic solvent based clearing

The history of organic solvent based tissue clearing methods can be traced back to early 1900s. Spatleholz used a mixture of organic solvents which reaches the RI of 1.55 to clear large biological samples for anatomical studies (Richardson and Lichtman, 2015). At the beginning of 21st century, organic solvent based clearing was barely used for biological studies because the harsh treatment of dehydration quickly quenched the fluorescent proteins which are widely used for labelling. In 2007, Dodt's group built the first modern light-sheet microscope for imaging cleared samples (Dodt et al., 2007). By using gradient ethanol as dehydration solutions and a mixture of benzyl alcohol/benzyl benzoate as RI matching solution, brain samples from adult Thy1-GFPM line mouse were cleared and the green fluorescent protein (GFP) sparsely labelled neurons were imaged. However, the GFP signal can only stay for a few hours which limits the general application in neuroscience studies.

After screening the organic solvent library, GFP-friendly solvents such as tetrahydrofuran (THF) were selected as dehydration solution and dibenzyl ether (DBE) was chosen as RI matching solution (Becker et al., 2012; Erturk et al., 2011). This termed 3DISCO (3D imaging of solvent-cleared organs), a practical method for whole organ clearing which could render the whole mouse brain transparent within 2 days and preserves the GFP labelled neuronal structures (Erturk et al., 2012). In terms of time consuming, 3DISCO stands as the most efficient clearing methods comparing to water-reagent or hydrogel based clearing methods which usually take more than a week to clear dissected mouse organs. Nevertheless, the quenching of fluorescent

proteins is still the biggest challenge since the half life of GFP is only one to two days after clearing (Erturk et al., 2012). This not only means that the samples need to be imaged immediately after clearing but also implies that the fine structures such as dendritic spines are already not visible after 3DISCO clearing. To overcome this hurdle, Schwarz et al. suggested that 1-propanol and tert -butanol dehydration significantly improved the signal preservation comparing with 3DISCO, as the remaining fluorescence proteins comparing with the signal before clearing was 24.2% and 79.2% respectively (Schwarz et al., 2015).

By using tert -butanol as a mild dehydration solution and by adding diphenyl ether (DPE) which has high RI (1.579) and is inert to further reactions, we developed uDISCO (ultimate DISCO) (Pan et al., 2016). As a robust tissue clearing method, uDISCO is able to clear whole bodies of adult mice within 3-4 days. Benefiting from the signal preservation, we resolved the dendritic spines from cortical neurons with Thy1-GFPM line mice. Among the organic solvent based clearing methods, uDISCO achieved such level of fluorescent protein preservation and subcellular resolution for the first time. For details please see **Research Article 1**.

Method	Clearing capability	Time to clear	Size change	Fluorescence signal	Imaging depth	Chemical permeability
uDISCO	Excellent	One day-days	Strong shrinkage	Preserved	Very deep	—
3DISCO	Excellent	Hours-days	Strong shrinkage	Major loss	Very deep	—
SeeDB	Medium	Days	Slight expansion	Modest loss	Shallow	—
Sca/eS	Medium	Days	Slight expansion	Preserved	Deep	2 mm/4 daysc
Sca/eSQ	Weak	Hours	Strong expansion	Modest loss	Deep	—
CUBIC	Good	Days-weeks	Slight shrinkage	Modest loss	Very deep	3.2 mm/6 daysd
ClearT2	Weak	Hours	Slight shrinkage	Modest loss	Shallow	—
PACT	Excellent	Days	Strong expansion	Modest loss	Very deep	3 mm/7 days

Table 1. Comparison of different tissue clearing methods

The “time to clear” was measured by samples from 2 mm thick brain sections to whole brain. “—,” indicates that the clearing method itself would not improve the antibody penetration. However, the related protocols might still be compatible with immunostaining prior to the clearing process (Wan et al., 2018).

On the other hand, the widely used immunohistochemistry methods provided a promising strategy to further improve the imaging quality by applying bright dye conjugated antibodies. These synthetic dyes are normally stable in organic solvent which dispel the concerns of fluorescence quenching. In order to achieve complete whole mount staining, the permeability of biological samples needs to be increased to improve the penetration of antibodies. To reach this goal, Renier et al. combined graded methanol, dichlormethane (DCM) and H_2O_2 for dehydration/rehydration. After immunostaining, the tissue was then cleared by 3DISCO (Renier et al., 2014). The termed iDISCO/iDISCO+ protocols provide a powerful tool to map the physiology/pathology changes of mouse brains and have been used in various biomedical studies (Liebmann et al., 2016; Renier et al., 2016). Alternatively, by using a mixture of saponin and PBSGT as permeabilization solution, Chedotal's group achieved the homogenous immunolabeling of the human embryos to study the development of the nervous system in health and disease (Belle et al., 2017).

Apart from the conventional antibody, the heavy chain variant antibody, named as nanobody, emerged to be a promising candidate to achieve deep tissue immunolabeling. It is 10 times smaller in size (15 KD) comparing to conventional antibody (150 KD) and therefore holds much higher penetration rate (Muyldermans, 2013). To further increase the permeability of the tissue, we used a mixture of methyl-β-cyclodextrin, trans-1-acetyl-4-hydroxy-l-proline and Triton. Combining decolorization and decalcification with bright Atto dye conjugated nanobodies anti GFP or RFP, we developed vDISCO whole-body immunolabeling method which achieved the homogenous labelling of adult rodent for the first time (Cai et al., 2019). With nanobodies conjugated with Atto dyes (Atto N647 or 594) excited at far red spectrum, the imaging quality of vDISCO increased more than 100 times comparing with imaging the original GFP signal from green/blue spectrum in which the tissue emits severe autofluorecence. This allows the cellular level light-sheet microscopy through intact skin and bone tissue. Applying vDISCO to various lines of transgenic mice, we resolved the first whole-body neuronal connectivity map and discovered novel functional anatomic structure in the intact skull. For details please see **Research Article 2**.

1.2 Applications of u/vDISCO in diverse biological research fields

As a novel technical revolution, whole-body tissue clearing and cellular level imaging bridged the gap for fast and high resolution unbiased screening of the intact organisms. Applying u/vDISCO to various transgenic rodent lines or disease models, we evaluated the bio-distribution of stem cells after systemic transplantation, revealed novel anatomical structures involved in neuroinflammation and developed a deep learning based mapping tool to study the whole-body cancer metastasis and drug distribution at cellular level. In this section, I will summarize the current status of the related research fields.

1.2.1 Bio-distribution of bone marrow–derived mesenchymal stem cells

Bone marrow–derived mesenchymal stem cells (BMSCs) transplantation has long been used as an effective cell therapy strategy to cure a variety of diseases (D'Souza et al., 2015; Parekkadan and Milwid, 2010). Firstly, BMSCs were transplanted after bone marrow ablation to restore the hematopoiesis of cancer patients (Koc et al., 2000). Later on, as a promising restorative therapy, BMSCs transplantation was explored as aid to structural and functional recovery of brain after stroke by enhancing neurogenesis and angiogenesis (Zhang and Chopp, 2009). Furthermore, other chronic or acute neurodegenerative diseases such as amyotrophic lateral sclerosis (ALS) (Vercelli et al., 2008), Parkinson's disease (PD) (McCoy et al., 2008), Huntington's disease (HD) (Lin et al., 2011) and spinal cord injury (SCI) (Gu et al., 2010; Yang et al., 2008) also benefit from BMSCs therapy.

As BMSCs transplantation is usually applied intravenously, visualizing and analyzing the systemic distribution of BMSCs in whole-body becomes extremely important. Various labeling and imaging techniques are available to study the distribution of BMSCs. For instance, traditional fluorescent immunohistochemistry was used to study the BMSCs homing in specific organs (Kawada et al., 2004). Radioactive labeling was applied to evaluate BMSCs whole-body distribution but with limited resolution to detect single stem cells (Barbash et al., 2003). Using these methods, researchers found that the transplanted BMSCs were majorly detected in lungs shortly after transplantation. A potential mechanism is that lung capillary is too narrow for BMSCs and obstructive effects will occur during the lung passage (Leibacher and Henschler, 2016). However, a more time and sensitivity efficient methodology is

required for BMSCs study which enables the cellular detection of sparsely located BMSCs and it will contribute to explore the novel and unexpected homing tissue of BMSCs by unbiased whole-body screening.

Applying uDISCO to the mice intravenously (IV) or intraperitoneally (IP) injected with BMSCs labeled by quantum dots, we found that the majority of BMSCs were accumulated in lungs and livers, which is in line with the previous findings. In addition, we also detected BMSCs in bone marrow and intestine 3 hours after injection. Comparing with IP injection, IV injection provides significantly higher BMSCs delivery efficiency (Pan et al., 2016). Overall, as a valid methodology which enables the unbiased screening of whole mouse bodies with cellular level resolution, uDISCO setup a powerful platform for BMSCs related studies. For details please see **Research Article 1**.

1.2.2 Immune cell infiltration upon acute damage in central nervous system (CNS)

Acute CNS injuries including stroke and brain trauma have become one of the leading cause of death and disability through the whole world (Langlois et al., 2006; Mendis, 2013). Despite the initial neuron death and tissue damage, the subsequent inflammatory response involving local microglia activation and peripheral immune cells infiltration plays an important role in neuronal survival, dead cell debris clearance and tissue regeneration (Gadani et al., 2015; Kyritsis et al., 2014).

As a sophisticated system, the neuronal network is monitored constantly by immune system to react with pathogens and to maintain the microenvironment for neuronal function (Russo and McGavern, 2015). Due to the selectively permeable blood-brain barrier (BBB), peripheral immune cells are inhibited from passing into the health brain freely (Habgood et al., 2007; Muldoon et al., 2013). However, a variety of immune cells are located in the brain meninges and conducting the immune surveillance of the nervous system (Derecki et al., 2010). Furthermore, Kipnis' group recently described lymphatic vessels in the sagittal sinuses which are connected to the cervical lymph nodes functioning as a standard drainage system of the brain, indicating that the CNS is closely connected with global immune system (Da Mesquita et al., 2018; Louveau et al., 2018; Louveau et al., 2015).

When the CNS injuries occur, the mechanical impact as well as the microglia activation responding to alarmin release increases the permeability of BBB and lead to infiltration of peripheral immune cells (Finsen and Owens, 2011). Hours after injury, neutrophils arrive and start to produce anti-microbial products to fight pathogens (Amulic et al., 2012; Trivedi et al., 2006). However, it has been proved that these effects are harmful to neuronal cells. Prohibiting the neutrophils infiltration improved the neuronal survival and functional recovery post injury (Gorio et al., 2007; Semple et al., 2010). In the following hours to days, monocytes, macrophages and lymphocytes are recruited and generally considered as a contributor to the scar formation and angiogenesis which promotes the recovery of CNS (Brancato and Albina, 2011; Koh and DiPietro, 2011).

Apart from the disrupted BBB, the alternative infiltration route of circulating immune cells were recently reviewed (Benakis et al., 2018). Louveau et al. discovered that ablation of lymphatic vessels in the meninges suppressed the activation of T cells upon multiple sclerosis, suggesting that meningeal lymphatic vessels is potentially a recruiting gateway for immune cell infiltration (Louveau et al., 2018). Llovera et al. found that peripheral T leukocytes accumulated in the choroid plexus (ChP) and invaded the peri-infarct cortex after stroke (Llovera et al., 2017). More intriguing, both Nahrendorf's group (Herisson et al., 2018) and we discovered the short vascular connections (SMCs) between skull bone marrow and brain meninges (Cai et al., 2019) which indicates the interaction of bone marrow and CNS. Furthermore, we found that cell number of Lysm+ neutrophils in these connections increased upon stroke, suggesting that SMCs could be a novel alternative infiltration route in addition to meningeal lymphatic vessels and ChP . For details please see **Research Article 2**.

1.2.3 Breast cancer metastasis and antibody-based therapeutic approaches

In 2018, about 8.2 million cancer cases among women were newly diagnosed, from which one fourth of these cases were breast cancer. As the most frequently diagnosed cancer in women, breast cancer led to ~630 thousand cancer deaths last year (Bray et al., 2018). In general, about 90% of cancer-associated deaths was caused by metastatic disease distally from the primary tumors (Lambert et al., 2017). Therefore, breast cancer is more and more treated as a systemic disease (Redig and

McAllister, 2013) and understanding the mechanisms of metastasis as well as the therapeutic approaches blocking the metastasize pathology has great value for breast cancer therapy.

Breast cancer metastasis involves with several steps. Firstly, the cancer cells from the primary tumor conduct epithelial-mesenchymal transition (EMT) and obtain mesenchymal morphology which is more suitable to migrate and metastasize in distant organs (Scully et al., 2012). This proceed can be characterized as reduction of cell-to-cell adhesion mediated by down-regulation of E-cadherin, cytokeratin and up-regulation of N-cadherin, fibronectin and Vimentin (Wu et al., 2016). Then, the cancer cells with mesenchymal morphology will be released into blood or lymphatic vessels (Hunter et al., 2008) and circulated to remote tissue. Although the majority of these circulating tumor cells (CTCs) will be cleared by immune system, the survival cancer cells might invade into the organ parenchyma and form metastasis (Lambert et al., 2017). It is also worth noting the CTCs are regarded as a bio-marker for clinical diagnose since they are rarely found in healthy women (van de Stolpe et al., 2011).

Therapeutic approaches for breast cancer can be categorized into two groups, standard chemotherapy and targeted therapy (Scully et al., 2012). In standard chemotherapy, cytotoxic chemicals are widely used and are notorious for developing drug resistance and severe side effect (Alvarez, 2010). In the targeted therapy, estrogen receptor (ER) has long been considered as a primary target to suppress breast tumor growth by using hormone therapy and ER inhibitors (e.g. tamoxifen) (Nicolini et al., 2006). The emerging immunotherapy involving monoclonal antibodies targeting specific cell surface receptors or enzymes holds great therapeutic potential to improve the survival rates and to reduce the systemic side effect for cancer patients (Nathan and Schmid, 2018). For instance, trastuzumab is an monoclonal antibody targeting the extracellular domain of human epidermal growth factor receptor 2 (HER-2). Binding to HER-2, trastuzumab is able to block the proliferation of the tumor (Baselga et al., 1998). Furthermore, Gondi et al. developed a monoclonal antibody (6A10) blocking the function of carbonic anhydrases (CAs) XII which is producing bicarbonate to maintain pH homeostasis and providing a survival advantage for breast cancer metastasis (Gondi et al., 2013). Intravenous

administration of 6A10 significantly improved the survival rate of the experimental mice and decreased the signal of primary tumor in bioluminescence imaging.

Nevertheless, due to the limited resolution of bioluminescence imaging, Gondi et al. could not extract the information of distant metastasis. Later on, by collaborating with the same group, we combined 6A10 antibody based immunotherapy with doxorubicin (DOX) involved chemotherapy and applied uDISCO tissue clearing to evaluate the therapeutic effect on lung metastasis. With the cellular level resolution and volumetric quantification provided by tissue clearing and light-sheet microscopy, we found that the combined therapy approach nearly eliminated the metastasis in lungs comparing to untreated control or to mice only received DOX (von Neubeck et al., 2018). This result demonstrates that 6A10 antibody makes the breast cancer cells more sensitive to chemotherapy and less prone to metastasis. However, the global metastasis and bio-distribution of therapeutic antibody 6A10 through the entire mouse bodies remains unsolved. Applying vDISCO to cancer mice received 6A10 antibody therapy and by developing a deep learning based algorithm (DeepMACT) which provides automatic identification and quantification of metastasis, we systemically studied the whole-body metastasis and immunotherapeutic antibody targeting efficiency with cellular level resolution for the first time (Pan et al., 2019). The result shows that lung tissue is the primary target for breast cancer metastasis and overall 77% of metastasis are targeted by the 6A10 antibody. For details please see **Research Article 3**.

2. Research Articles

2.1 Research Article 1: Shrinkage-mediated imaging of entire organs and organisms using uDISCO

Tissue clearing techniques are widely used in neuroscience research field as they can provide the intact connectivity information of neuronal network. However, light scattering particularly in hydrogel based and water reagent based clearing methods pose obstacles for deep tissue imaging. In addition, the size or volume of biological samples treated with these two groups of methods usually increases after clearing which further hinders the standard light-sheet microscopy with limited working distance of objectives. On the other hand, while organic solvent based tissue clearing methods have high clearing efficiency and shrink the tissue, they are notorious to rapid reduction of fluorescent protein signals which are widely used for cellular labeling.

We developed 'ultimate DISCO' (uDISCO) clearing to bridge the gap of signal preservation and volumetric reduction in large sample imaging. uDISCO preserves fluorescent proteins over months and renders intact mouse organs transparent while decreasing their size up to 65%. Using uDISCO, we cleared and imaged a whole mouse body from Thy1-GFPM transgenic mouse line and studied the neuronal projections in the intact CNS over 7 cm. Furthermore, uDISCO enables the whole-body clearing of adult rats, which is 4-5 times larger than mouse bodies in volume. We imaged the vasculature of the rat CNS over 13 cm with high resolution light-sheet microscopy. We also used uDISCO to study the bio-distribution of BMSCs after systemic application and found that the majority of BMSCs were accumulated in lungs and livers, while sparse BMSCs were detected in kidney, bone marrow and intestines. Overall, uDISCO provides a powerful platform to study the alterations under health and disease conditions of large organ systems throughout the entire organisms.

Author contribution: developed the uDISCO protocol with Ruiyao Cai; collected and cleared whole-body samples from Thy1-GFPM line, rat, BMSCs transplantation and AAV virus tracing; wrote the manuscript with colleagues (please see section 7 for further details).

Shrinkage-mediated imaging of entire organs and organisms using uDISCO

Chenchen Pan[1,2,6], Ruiyao Cai[1,2,6], Francesca Paola Quacquarelli[1,6], Alireza Ghasemigharagoz[1], Athanasios Lourbopoulos[1], Paweł Matryba[1,5], Nikolaus Plesnila[1–3], Martin Dichgans[1–4], Farida Hellal[1,3] & Ali Ertürk[1–3]

Recent tissue-clearing approaches have become important alternatives to standard histology approaches. However, light scattering in thick tissues and the size restrictions on samples that can be imaged with standard light-sheet microscopy pose limitations for analyzing large samples such as an entire rodent body. We developed 'ultimate DISCO' (uDISCO) clearing to overcome these limitations in volumetric imaging. uDISCO preserves fluorescent proteins over months and renders intact organs and rodent bodies transparent while reducing their size up to 65%. We used uDISCO to image neuronal connections and vasculature from head to toe over 7 cm and to perform unbiased screening of transplanted stem cells within the entire body of adult mice. uDISCO is compatible with diverse labeling methods and archival human tissue, and it can readily be used in various biomedical applications to study organization of large organ systems throughout entire organisms.

Until recently, histological techniques relied on sectioning to observe nonsuperficial cellular structures deep in tissues. However, investigation of complex cells with large projections, such as those in the nervous system, is best performed in intact tissue. While recently developed tissue-clearing methods have overcome obstacles imposed by light scattering[1–10], the difficulties associated with specimen size remain to be addressed. Available clearing methods either increase or do not change the volume of tissues, with the exception of organic-solvent-based methods such as 3D imaging of solvent-cleared organs (3DISCO), which causes a substantial volumetric reduction instead[5,6,11].

When combined with tissue clearing, light-sheet microscopy produces micrometer-resolution image volumes of large specimens within minutes. However, several limitations still exist. Photons traveling through samples (cleared or uncleared) are absorbed or scattered by interaction with the tissue, resulting in attenuation of both excitation and emission light[12,13]. Relatively thick light sheets (thickness ≥ 4 µm) are used to image volumes larger than a few hundred micrometers[14]. These light sheets are generated by cylindrical lenses and have Gaussian profiles; thinnest widths, which provide the best resolution, occur only at the beam waist. Thus, the volume of sample that can be imaged at the highest resolution is limited to the central region of the light sheet. Finally, both small imaging chambers and the short working distance (WD ≤8 mm) of high numerical aperture (NA ≥ 0.9) objectives pose additional challenges. Thus, 3D reconstruction of neuronal connections over 5–8 mm (the approximate size of a mouse brain) has remained a challenging task.

Organic-solvent-based clearing methods, such as 3DISCO, achieve the highest level of transparency and size reduction among all clearing approaches[11,15]. 3DISCO has been used to study immune cells[16], stem cells[17], cancer cells[18], and transdifferentiating lung cells[19]; and it has been combined with deep-tissue antibody labeling and automated activity mapping[20–22]. However, 3DISCO quickly quenches endogenously expressed fluorescent proteins (with a half-life of a few days)[6], which has limited the applicability of 3DISCO. Here, we developed uDISCO, a method that revealed and preserved the signal of endogenous fluorescence over months while retaining the advantageous size reduction. Thus, uDISCO allows subcellular imaging of 2× to 3× larger volumes in a single scan and avoids or reduces artifacts of physical sectioning and mosaic imaging. Using uDISCO, we imaged entire bodies of adult rodents to determine long-distance neuronal and vascular projections and spatial information on stem cell transplants (which have previously been difficult to study) at single-cell resolution.

RESULTS

uDISCO preserves endogenous signal and reduces volume by 65%

We reasoned that 3DISCO-induced shrinkage could be promising for imaging whole rodent bodies. However, 3DISCO resulted in a fast decline of endogenous fluorescence signal during whole-body clearing, where longer treatments with clearing solutions are required (**Supplementary Figs. 1** and **2**). To overcome this, we searched for organic compounds that preserved fluorescence while providing a potent tissue-clearing effect. Our screen

[1]Institute for Stroke and Dementia Research, Klinikum der Universität München, Ludwig Maximilians University of Munich (LMU), Munich, Germany. [2]Graduate School of Systemic Neurosciences (GSN), Munich, Germany. [3]Munich Cluster for Systems Neurology (SyNergy), Munich, Germany. [4]German Center for Neurodegenerative Diseases (DZNE, Munich), Munich, Germany. [5]Current address: Department of Molecular and Cellular Neurobiology, Nencki Institute of Experimental Biology of Polish Academy of Sciences, Warsaw, Poland. [6]These authors contributed equally to this work. Correspondence should be addressed to A.E. (ali.ertuerk@med.uni-muenchen.de).

RECEIVED 1 MARCH; ACCEPTED 26 JULY; PUBLISHED ONLINE 22 AUGUST 2016; DOI:10.1038/NMETH.3964

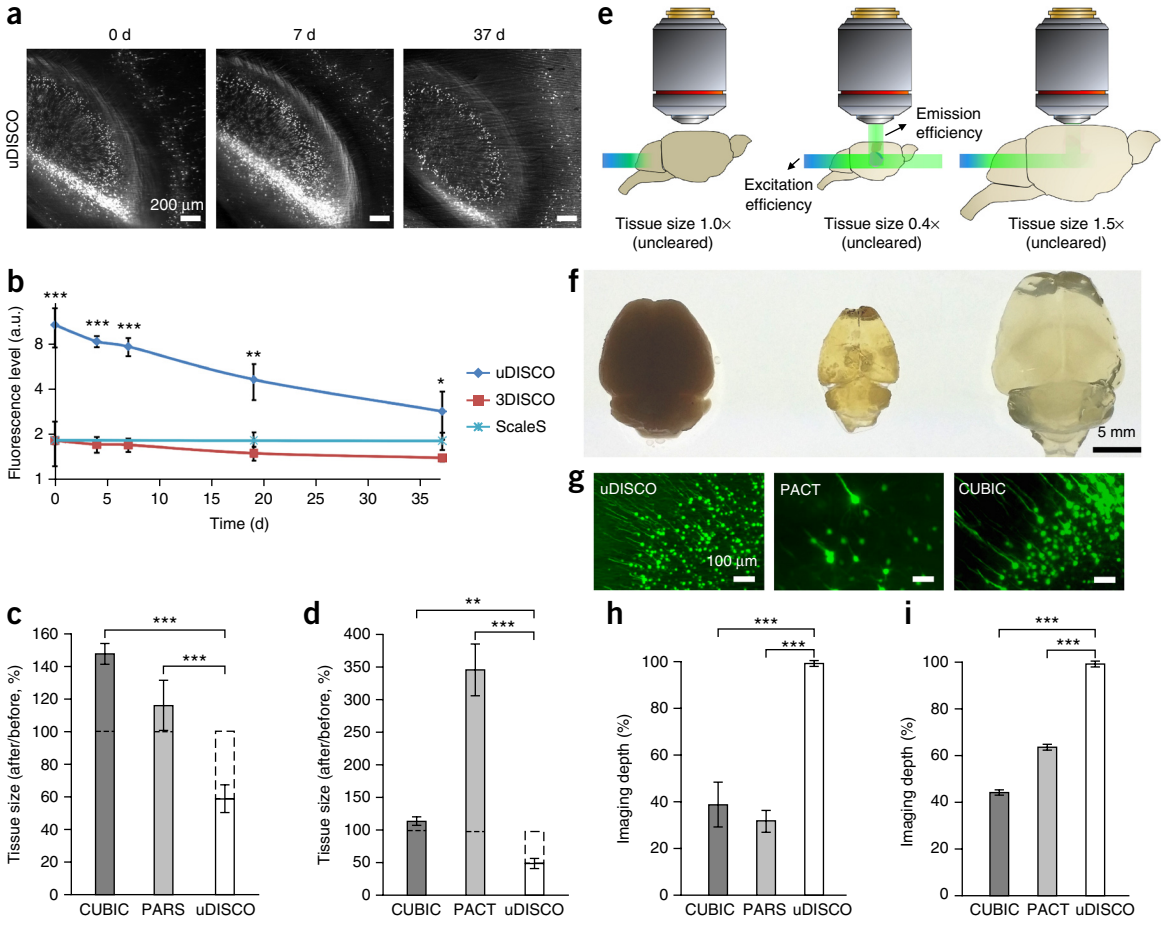

Figure 1 | Development and principles of uDISCO. (**a**) Preservation of GFP (*Thy1*–GFP-M brain) after uDISCO, assessed by light-sheet microscopy. (**b**) Fluorescence-level quantifications in the GFP-M brains after uDISCO, ScaleS, and 3DISCO over time (n = 3, 3, and 4 mice, respectively; a.u., arbitrary unit). (**c**) Volume changes of 4-month-old GFP-M mice after CUBIC, PARS, and uDISCO whole-body clearing (n = 5, 3, and 7 mice, respectively). (**d**) Volume changes of dissected brains from 6-month-old mice after CUBIC, PACT, and uDISCO passive clearing (n = 4, 4, and 3 mice, respectively). (**e**) Illustration of the advantages and disadvantages of tissue shrinkage versus expansion during imaging. (**f**) Mouse brains (GFP-M, 4 months old): uncleared (left), after uDISCO (middle), and after CUBIC (right) whole-body clearing. (**g**) Light-sheet microscopy imaging of cortical neurons in GFP-M brains with shrinkage (uDISCO) and expansion (PACT and CUBIC) after clearing. (**h**) Imaging depth quantifications on brains after CUBIC, PARS, and uDISCO whole-body clearing (n = 4, 4, and 3 mice, respectively). (**i**) Imaging depth quantifications on brains after CUBIC, PACT, and uDISCO passive clearing of dissected brains (n = 4, 3, and 3 mice (6 months old), respectively). All values are mean ± s.d.; statistical significance in **b**–**d**, **h**, and **i** (*, $P < 0.05$; **, $P < 0.01$; and ***, $P < 0.001$) was assessed by one-way ANOVA followed by Dunnett's *post hoc* test.

resulted in a tissue-clearing method (uDISCO) based on diphenyl ether (DPE), an organic solvent with a refractive index of 1.579 (**Supplementary Fig. 3**). uDISCO reveals fluorescence notably better and maintains it several weeks longer within *Thy1*–GFP-M mouse brains (expressing GFP in a sparse neuronal population[23]) compared with 3DISCO and water-based ScaleS protocols (**Fig. 1a**,**b**, **Supplementary Figs. 4**–**6**, and **Supplementary Video 1**). As DPE has a melting point of 26 °C, we mixed it with benzyl alcohol (−15 °C melting point) and benzyl benzoate (18 °C melting point) to obtain a mixture that is liquid at room temperature, which we named BABB-D (**Supplementary Table 1** and **Supplementary Protocol**). Additionally, uDISCO utilizes both the antioxidant α-tocopherol (Vitamin E) to scavenge peroxides and *tert*-butanol[24], a dehydrating reagent that is more stable than tetrahydrofuran (THF) used in 3DISCO. With the resulting protocol, the fine structures of labeled neurons in the lipid-dense brain and spinal cord can be detected over weeks to months.

uDISCO effectively cleared internal organs (**Supplementary Fig. 7**) and hard tissues, including calcified bones (**Supplementary Figs. 8**–**10**; **Supplementary Videos 2** and **3**), without any additional treatment, such as decalcification with EDTA[25]. Bones are heavily mineralized, allowing only minimal exchange of clearing solutions. Therefore, bone clearing requires clearing solutions with similar refractive index (RI) to reduce the clearing duration and light scattering. The RI of bones has been estimated as 1.555–1.564 (refs. 26 and 27), which is very similar to the RI of BABB-D, the final clearing agent in uDISCO.

We measured the size-reduction capability of uDISCO compared with existing whole-body clearing techniques. We found that whole-body clearing by uDISCO reduced the volume of mice (~42%), while both CUBIC (clear, unobstructed brain imaging cocktails and computational analysis) and PARS (perfusion-assisted agent release *in situ*) whole-body clearing methods enlarged it (**Fig. 1c** and **Supplementary Fig. 11**). We also tested the size reduction on dissected organs and found that uDISCO

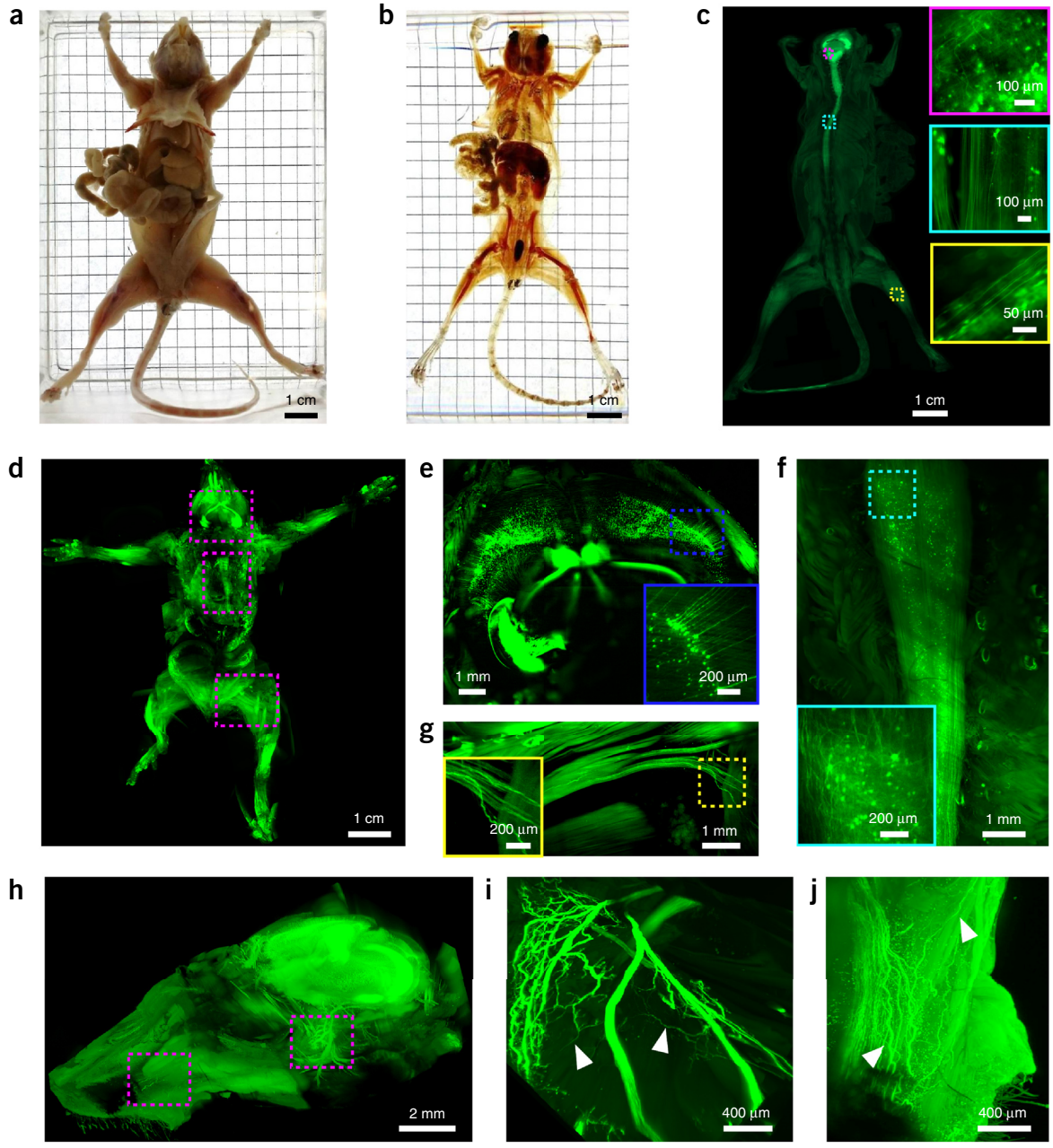

Figure 2 | Whole-body clearing and imaging of adult mouse with uDISCO. (**a**–**c**) Adult GFP-M mouse (3 months old) was transcardially perfused (**a**), cleared with uDISCO (**b**) and imaged by fluorescence stereomicroscope at cellular resolution (**c**). Insets show higher-magnification images of the brain (magenta rectangle), spinal cord (cyan rectangle), and sciatic nerve (yellow rectangle). (**d**) Whole-body light-sheet imaging of intact GFP-M mouse (4 weeks old). (**e**–**g**) High-magnification images of the boxed regions in **d**. Colored rectangles show high-magnification images from the indicated regions in the brain (**e**), spinal cord (**f**), and sciatic nerve (**g**). (**h**) 3D visualization of the intact head from *Thy1*-YFP-H mouse (4 months old) after whole-body uDISCO clearing, indicating the detailed structure of optic nerve (**i**) and nerves at the base of the whiskers (**j**). The arrowheads in **i** and **j** mark some of the individual axons. The composites in **c**, **d**, and **h** were obtained via tile imaging.

reduced the size of adult mouse brains up to 55%, in contrast to CUBIC and PACT (passive CLARITY technique), both of which enlarged mouse brains (**Fig. 1d** and **Supplementary Fig. 11**). This size reduction, together with uDISCO's preservation of fluorescent proteins, resulted in a substantial advantage for imaging larger volumes compared with other tissue-clearing methods (**Fig. 1e**,**f**). Using light-sheet microscopy, we found that the maximum portion of a cleared tissue that can be imaged at once increased 2× to 4× with uDISCO compared with PARS or PACT and CUBIC (**Fig. 1g**–**i**).

To test whether the shrinkage was isotropic, we compared images before and after clearing. We found that brain tissues such as the cortex and hippocampal layers shrank homogenously, ~30% in each dimension at macroscopic scale (**Supplementary Fig. 12**). In addition, the shrinkage of different cell types (neurons, glia, etc.) and vasculature in the same brain region was homogenous in all dimensions (**Supplementary Fig. 13**). Finally, we found that individual cell and vascular morphologies were preserved in brain tissue after uDISCO clearing (**Supplementary Fig. 14**).

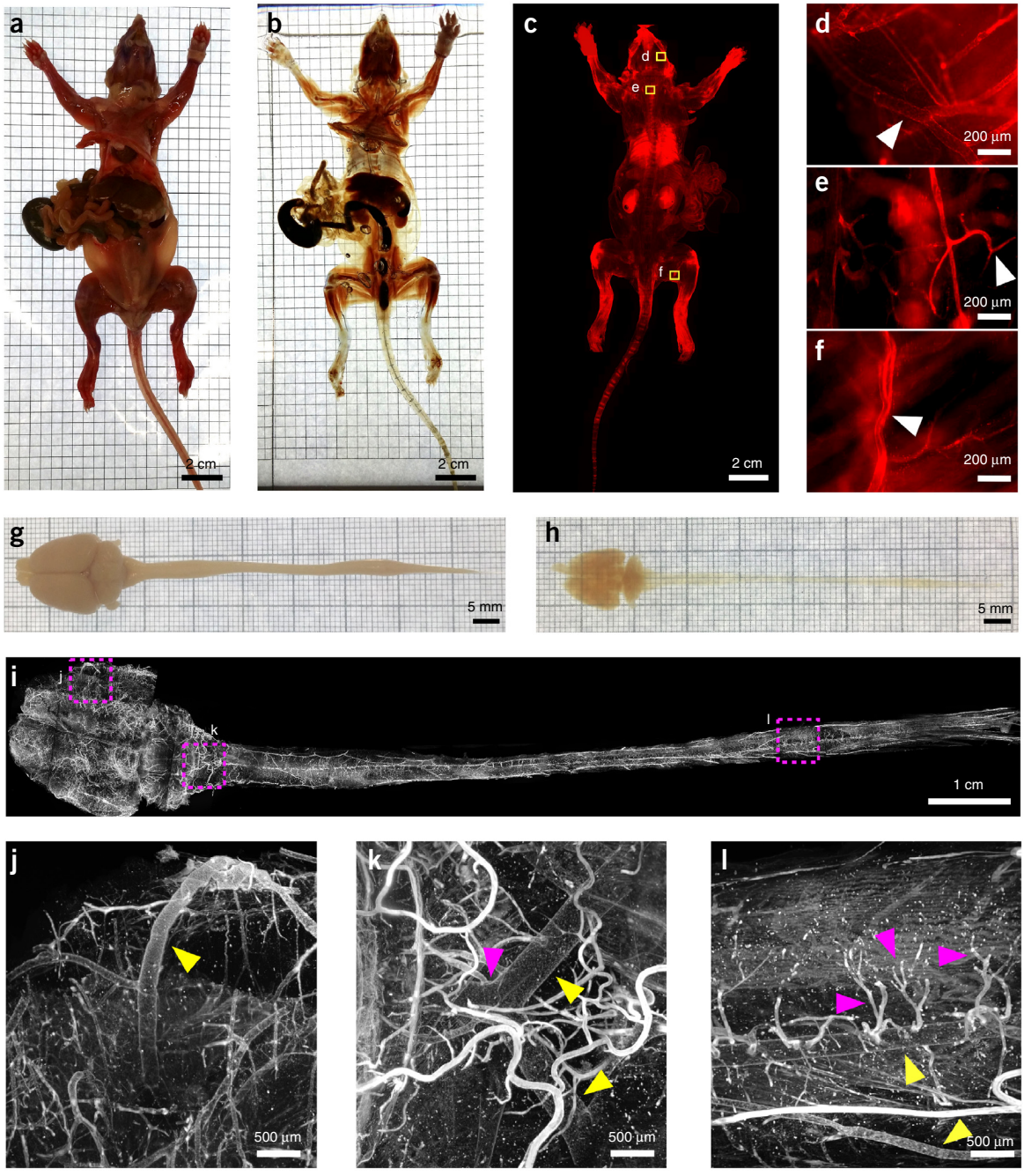

Figure 3 | Whole-body clearing and imaging of rats with uDISCO. (**a**–**c**) A young adult female rat (4 weeks old) was injected with Texas Red Dextran to label the vasculature. The rat was transcardially perfused (**a**), cleared with uDISCO (**b**) 20 min after the dextran injection, and imaged with a fluorescence stereomicroscope (**c**). (**d**–**f**) High-magnification images of the boxed regions in **c**, such as the brain (**d**), spinal cord (**e**), and hindlimb (**f**). (**g**–**i**) Adult rat (10 weeks old) CNS (brain and spinal cord) before (**g**) and after (**h**) uDISCO clearing. (**i**–**l**) 3D visualization of vasculature via light-sheet imaging throughout the entire CNS from the adult rat (**i**). The vasculature in the cortex (**j**) (yellow arrowhead shows the right middle cerebral artery), brainstem (**k**) (yellow arrowheads show the two vertebral arteries, and purple arrowhead shows the basilar artery), and lumbar spinal cord (**l**) (yellow arrowheads show the spinal vessels, and purple arrowheads show their small s ulcal branches) are shown. The composites in **c** and **i** were obtained via tile imaging.

uDISCO enables micrometer-resolution whole-body imaging

We used uDISCO on whole rodent bodies for system-level interrogation. We cleared the whole body of an adult *Thy1*–GFP-M mouse within 3–4 d (**Fig. 2a**,**b**; 3-month-old mouse; the skin was removed before clearing). We first imaged the whole transparent mouse with a standard fluorescence stereomicroscope (**Fig. 2c**; the skull and vertebra were removed for epifluorescence imaging). We readily identified the individual neurons and their extensions throughout the brain, spinal cord, and limbs in the intact mouse (**Fig. 2c**). To accommodate the entire transparent mouse into the imaging chamber of a standard light-sheet microscope, we constructed sample holders to keep the cleared specimens in place within the imaging chamber for automated tile scans without obstructing the excitation light

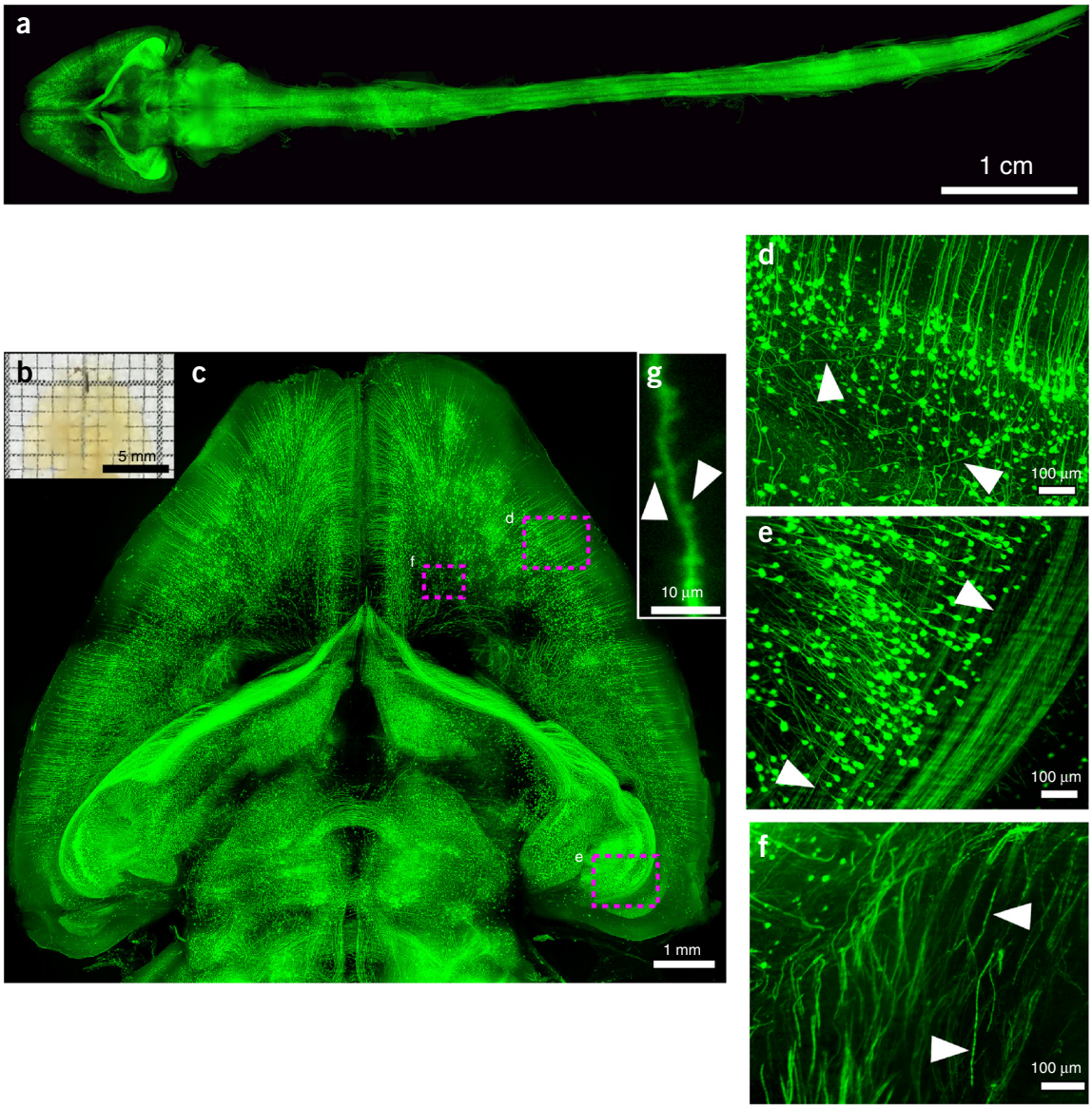

Figure 4 | Projections throughout the entire adult mouse CNS (whole brain and spinal cord). (**a**) The intact CNS from a GFP-M mouse (4 months old) after uDISCO clearing and light-sheet microscopy imaging. (**b**) Image of the brain in **a** showing the transparency after uDISCO. (**c**) Details of neuronal structures in the entire brain in **a**. (**d**–**f**) High-magnification images of boxed regions in **c**, showing the neuronal structures at subcellular resolution in the cortex (**d**), in the hippocampus (**e**), and projecting to the midbrain (**f**). (**g**) After uDISCO, imaging of dendritic spines with light-sheet microscopy. The composites in **a** and **c** were obtained via tile imaging.

(**Supplementary Figs. 15** and **16**). Upon shrinkage, the width of the largest body region (torso) was reduced from 2.24 ± 0.052 cm to 2.0 ± 0.048 cm (mean ± s.e.m., n = 7 mice), allowing us to complete 10-mm depth scans from dorsal and ventral sides of the mouse (**Supplementary Fig. 17**). Subsequently, we imaged the entire transparent mouse using light-sheet microscopy to detect neuronal structures throughout the intact mouse body at ~0.5- to 2-µm lateral and ~4-µm axial resolution (**Fig. 2d**). Subcellular details of neuronal projections in the whole body were visible throughout the animal with light-sheet microscopy (**Fig. 2e**–**g**). In addition, large body regions such as the head, torso, and whole limbs could be studied in detail. For example, when we imaged the entire head from an adult *Thy1*–YFP-H mouse[23], we observed the projections of optic nerves and innervation of whiskers (**Fig. 2h**–**j**).

uDISCO is also applicable to larger rodents. Rats (*Rattus norvegicus*) are valuable experimental models in toxicology and neurological studies because, compared with those of mice, rat physiology and behavior more closely resemble those of humans. uDISCO successfully cleared whole rats (**Fig. 3a**,**b** and **Supplementary Fig. 18**). We could observe the details of Texas Red–dextran-labeled vasculature in the brain, brainstem, and limbs using a standard fluorescence stereomicroscope in the intact 4-week-old rats (**Fig. 3c**–**f**). In addition, uDISCO achieved uniform clearing and over 60% tissue shrinkage of the intact central nervous system (CNS) in adult rats (10 weeks old, n = 4 rats; **Fig. 3g**,**h**). Subsequently, we obtained light-sheet microscopy images of the vasculature in the intact CNS over 13 cm (**Fig. 3i** and **Supplementary Video 4**). We identified vascular structures such as the right middle cerebral artery (**Fig. 3j**); the two vertebral

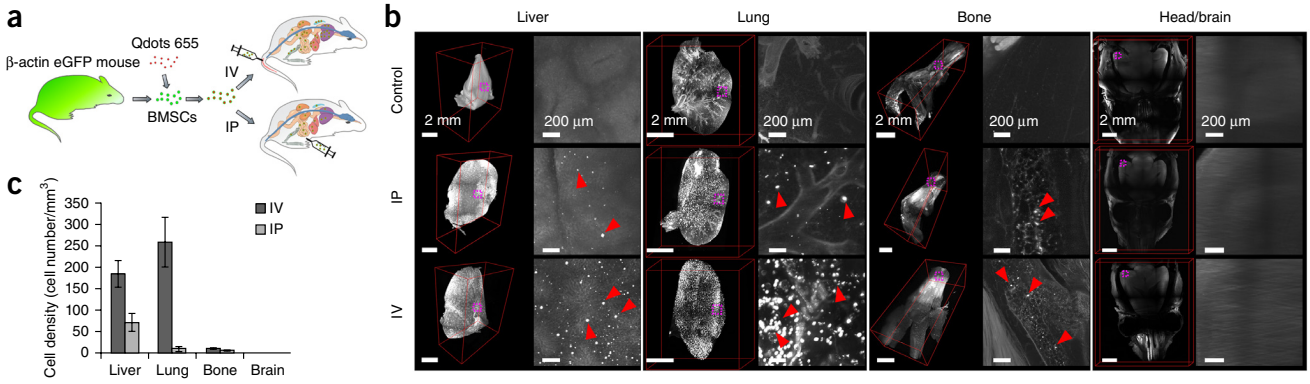

Figure 5 | Distribution of mouse BMSCs after transplantation. (**a**) Illustration of the experimental design. (**b**) Images of liver, lung, limb, and head (brain) from host mice in control, IP, and IV groups assessed by light-sheet imaging. The composites of individual organs were obtained via tile imaging. The background autofluorescence signal outlines the overall morphology of the organs. Some Qdots-positive BMSCs are indicated by red arrowheads. (**c**) Quantification of BMSCs in different organs. Values are mean ± s.e.m.; $n = 3$ mice for each group (control, IP, and IV).

arteries, which merge to form the basilar artery (**Fig. 3k**); and the spinal vessels and their small sulcal branches (**Fig. 3l**).

uDISCO allows tracing of the intact central nervous system

Since we could image the intact CNS of rodents with light-sheet microscopy at subcellular resolution, we used uDISCO to trace neuronal structures from head to toe in the entire CNS (brain and spinal cord) of 3- to 5-month-old *Thy1*–GFP-M adult mice. We could trace individual axons in the intact CNS over several centimeters in these scans (**Fig. 4a**; **Supplementary Videos 5** and **6**). Focusing on the brain, we observed the details of neuronal structures in the cortex, the hippocampus, and fine axonal projections to the midbrain (**Fig. 4b–f** and **Supplementary Video 7**). PACT[1] and CUBIC[8] reported visualization of dendritic spines using confocal or two-photon microscopy. For the first time for an organic-solvent-based clearing method in intact adult mouse brain, uDISCO achieved dendritic-spine resolution using light-sheet microscopy (**Fig. 4g** and **Supplementary Video 8**).

uDISCO allows interrogation of BMSCs in the entire mouse

Bone marrow stem cells (BMSCs) are widely used for neuroprotection, regeneration, immunomodulation, and localized drug delivery studies[28,29]. So far, assessment of their distribution and densities has relied on methods such as histology, bioluminescence, or radiolabeling[30]. These approaches are time consuming and lack the sensitivity to detect sparsely localized cells or unexpected sites of grafting[31]. We used uDISCO whole-body clearing for an unbiased screen of transplanted syngeneic mouse BMSCs in the entire body at single-cell resolution. We collected BMSCs from β-actin EGFP mice as described previously[32] and labeled them with quantum dots (Qdots) (**Supplementary Fig. 19**). Cells easily incorporate Qdots, which do not interfere with cell functionality or migration capacities and therefore Qdots are widely used for cell tracking[33]. Subsequently, we injected the cells either intravenously (IV) or intraperitoneally (IP) into host C57BL/6N mice (**Fig. 5a**). Control animals were injected with vehicle (PBS) only. At 3 h after injection, we euthanized the animals for whole-body clearing. We first imaged whole mouse bodies using a fluorescence stereomicroscope to determine sites of grafted BMSCs (**Supplementary Fig. 20**). Subsequently, we performed high-resolution light-sheet microscopy on body parts and organs that hosted BMSCs. As expected, the majority of BMSCs were trapped in the first-passage, low-flow organs such as the lungs, liver, and spleen after IV injection (**Fig. 5b,c**, **Supplementary Figs. 20–22**, and **Supplementary Video 9**)[31,34]. Moreover, we detected sparsely distributed BSMCs in organs such as kidneys, bone marrow, and intestines (**Fig. 5b,c**; **Supplementary Figs. 21** and **22**). The localizations in bone marrow and intestines are of high interest because they were previously difficult to investigate despite their importance for hematopoietic cell populations or immune reactions[31]. As reported[35], we did not observe any BMSCs in the intact healthy CNS (**Fig. 5b,c**). Overall, our data demonstrate that uDISCO whole-body clearing can be used to study density and distribution of fluorescently labeled transplanted cells throughout the entire host body at single-cell resolution in an unbiased way, combining both high speed and resolution for transplantation studies.

uDISCO is compatible with virus labeling and immunostaining

Most animal models used in the laboratory, as well as human clinical samples, do not express fluorescent proteins. Hence, we sought to test alternative methods to label tissues for uDISCO. To this end, we used adeno-associated virus (AVV) tracing to label neurons in the CNS of mice. We transduced the right motor cortex of mice with AAV2–Syn–EGFP and the left motor cortex with AAV2–Syn–RFP (**Fig. 6a**). 4 weeks after transduction, we performed whole-body uDISCO clearing. Fluorescence expression of the virally delivered proteins was detectable in the brain and throughout the intact spinal cord (**Fig. 6b–f** and **Supplementary Fig. 23**). The pyramidal decussation of descending motor axons was clearly visible (**Fig. 6c**). We detected both bundles of axons as well as individual axons in the brain and spinal cord over several centimeters (**Fig. 6d–f**).

Antibody staining is a valuable approach for labeling molecules of interest without the need for fluorescent tagging. Deep-tissue antibody-labeling methods[20,21] were recently combined with 3DISCO. To test these methods with uDISCO, we cut 1-mm-thick tissue sections of mouse brains and labeled them with antibodies against glial fibrillary acidic protein (GFAP) and ionized calcium binding adaptor molecule 1 (Iba1) as well as with a DNA-specific dye (**Fig. 6g**). After uDISCO, the slices shrank more than 60% in volume. We found that the signals from GFAP (astrocytes), Iba1 (microglia and macrophages), and TO-PRO-3 (DNA dye) were visible

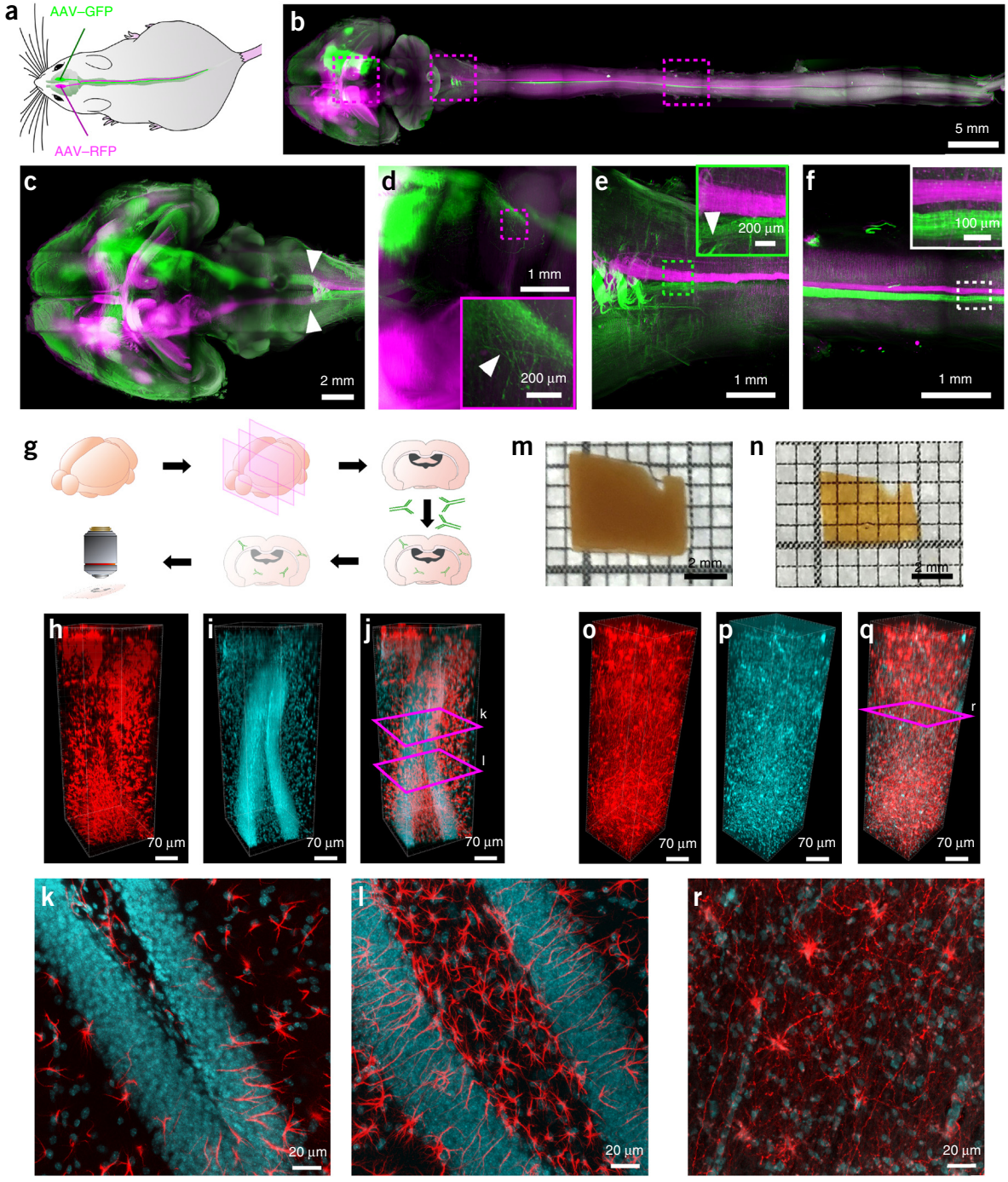

Figure 6 | uDISCO is compatible with AVV neuron tracing and immunolabeling. (**a**) Experimental design for AAV–Syn–RFP and AAV–Syn–GFP injections. (**b**,**c**) Maximum-intensity projections of the entire brain (**b**,**c**) and CNS (**b**) after whole-body uDISCO clearing. Arrowheads in **c** indicate decussation of the descending motor axons. (**d**–**f**) Details of neuronal extensions of boxed regions in (**b**): the thalamus and midbrain (**d**), cervical (**e**), and thoracic (**f**) spinal cord regions. Colored rectangles show the enlarged views from the respective images. (**g**) Immunolabeling workflow. (**h**–**l**) GFAP and TO-PRO-3 labeling of coronal sections. 3D reconstructions show labeling of astrocytes (**h**) and cell nuclei (**i**) stained by GFAP antibody and TO-PRO-3, respectively. (**j**) Merged image of **h** and **i**. (**k**,**l**) Maximum-intensity projections of the *z*-positions marked by purple boxes in **j**; nuclei are shown in cyan and astrocytes in red. (**m**,**n**) 14-month fixed human tissue before (**m**) and after (**n**) uDISCO. (**o**–**r**) GFAP and TO-PRO-3 labeling of 14-month fixed human cortical tissue. Astrocytes (**o**) and nuclei (**p**) are labeled. (**q**) Merged image of **o** and **p**. (**r**) Maximum-intensity projection of the *z*-position marked by the purple box in **q**; nuclei are shown in cyan and astrocytes in red. All values are mean ± s.d. The composites in **b** and **c** were obtained via tile imaging.

throughout the tissue, indicating compatibility of uDISCO with deep-tissue labeling (**Fig. 6h–l** and **Supplementary Fig. 24**).

Human clinical tissue samples are typically stored in 4% formalin over extended periods of time. To determine whether uDISCO could be applied to such specimens, we immunostained 1-mm-thick human samples (archived for either 1 month or 14 months) for GFAP and TO-PRO-3 or Iba1 and TO-PRO-3. We measured shrinkage of 52% and 46% in samples stored for 1 month or 14 months,

respectively (**Fig. 6m**,**n**). uDISCO allowed successful clearing, signal preservation, and imaging of human tissues stored in formalin more than a year (**Fig. 6o–r** and **Supplementary Fig. 25**), although the image quality was better for shorter storage periods (**Supplementary Fig. 25i**). Importantly, the combination of uDISCO and deep-tissue antibody labeling did not require additional antigen retrieval steps. Overall, these results demonstrate that uDISCO is a versatile method that can be used to clear and image different types of tissues with various labeling methods.

DISCUSSION

uDISCO achieved whole-body clearing and imaging because of sample-size reduction and preservation of fluorescent proteins. Another major advantage of organic-solvent-based clearing methods is the easy handling of cleared tissues; specimens become hard because of dehydration, yet are flexible enough for versatile positioning of long samples, such as the entire spinal cord of adult rats. In contrast, concentrated glycerol and sugar solutions used in various clearing methods are difficult to work with because of their high viscosity, the resulting gel-like texture of the cleared tissue, and the air bubbles generated during the refractive-index matching procedures and imaging[11].

Recently, tissue expansion was used to obtain super-resolution images of small volumes (expansion microscopy)[36–38]. Treweek *et al.*[25,39] used a similar concept (expansion (e) PACT) for high-resolution imaging. While expansion provides more resolution, tissue shrinkage, in theory, decreases resolution (30% in one dimension for uDISCO). However, uDISCO resulted in high-quality images (**Supplementary Fig. 26**), allowing the visualization of dendritic spines and individual axons over several centimeters in the intact CNS of adult mice. This high image quality could result from a larger proportion of shrunken samples (compared with nonshrinking samples) fitting into the optimal imaging region of the light sheet. Hence, shrinkage allows imaging of 2× to 3× larger volumes in the same setup without apparent loss of resolution. Importantly, uDISCO did not alter the structural integrity of the brain either at macroscopic (e.g., cortex and hippocampus structures) or microscopic scales (e.g., individual cells). However, isotropic shrinkage remains to be confirmed for other tissues such as muscle or fat. In addition, uDISCO can be combined with microscopy techniques that deliver even higher resolution and/or faster scanning, such as confocal, two-photon, and lattice light-sheet microscopy[40]. We demonstrated that high numerical aperture (NA), long working distance objectives such as Zeiss CLARITY 20× and Olympus 25× are compatible with uDISCO (**Supplementary Fig. 27**).

Acute injuries in the CNS might affect not only the injury site but also uninjured distal parts of the CNS[41,42]. Thus, repair strategies after CNS traumas need to be evaluated throughout the entire CNS. The uDISCO approach enables the assessment of long-range axonal projections and individual cells throughout entire organisms. Hence, this approach can help to reduce (1) the bias of analyzing only selected organs; (2) the time needed to prepare and screen individual organs and body parts of a complete mouse[43]; and (3) by generating whole mouse atlases and databases it can reduce the resources and number of animals needed in experimental research.

Whole-body clearing of diverse tissues, and the compatibility of this method with different imaging techniques, may have broad applications in the biomedical sciences. Whole-body clearing approaches could facilitate the assessment of neurodegeneration in diseases that affect both the central and peripheral nerves such as in amyotrophic lateral sclerosis (ALS), inflammation that may extend from gut to brain, stem cell transplantation studies, or even 3D mapping of the cellular structures in larger brain volumes, possibly even the whole human brain.

METHODS

Methods and any associated references are available in the online version of the paper.

Note: Any Supplementary Information and Source Data files are available in the online version of the paper.

ACKNOWLEDGMENTS

This work was supported by the Vascular Dementia Research Foundation, Synergy Excellence Cluster Munich (SyNergy), ERA-Net Neuron (01EW1501A to A.E. and N.P.), and the European Union's Horizon 2020 research and innovation programme (grant agreement no. 666881, SVDs@target, M.D.). A.L. and N.P. were supported by a Marie Curie Intra European Fellowship grant (FP7-PEOPLE-2013-IEF, project no. 625970). We thank M. Hübener and F. Voss (Max Planck Institute of Neurobiology, Munich) for providing mice; D. Trauner and O. Thorn-Seshold for helpful discussions; A. Weingart for illustrations; and C. Hojer, S. Tappan and T. Misgeld for critical reading of the manuscript. C.P. and R.C. are members of the Graduate School of Systemic Neurosciences (GSN), Ludwig Maximilian University of Munich. Human tissues were provided by the brain bank of the Institute of Anatomy, University of Leipzig.

AUTHOR CONTRIBUTIONS

A.E. designed and led all aspects of the project. C.P., R.C., and F.P.Q. performed most of the experiments. A.G. performed the image rendering and developed algorithms for data analysis. C.P., R.C., F.P.Q., and A.G. analyzed the data. A.L. interpreted data and performed the BMSC cultures, characterization, and transplantations; F.H. performed virus tracing; P.M. assisted first-clearing experiments; N.P. and M.D. supervised A.L. and F.H., respectively. A.E., C.P., R.C., F.P.Q., and A.G. wrote the paper. All authors edited the paper.

COMPETING FINANCIAL INTERESTS

The authors declare no competing financial interests.

1. Yang, B. *et al.* Single-cell phenotyping within transparent intact tissue through whole-body clearing. *Cell* **158**, 945–958 (2014).
2. Hama, H. *et al.* ScaleS: an optical clearing palette for biological imaging. *Nat. Neurosci.* **18**, 1518–1529 (2015).
3. Chung, K. *et al.* Structural and molecular interrogation of intact biological systems. *Nature* **497**, 332–337 (2013).
4. Tainaka, K. *et al.* Whole-body imaging with single-cell resolution by tissue decolorization. *Cell* **159**, 911–924 (2014).
5. Ertürk, A. *et al.* Three-dimensional imaging of the unsectioned adult spinal cord to assess axon regeneration and glial responses after injury. *Nat. Med.* **18**, 166–171 (2011).
6. Ertürk, A. *et al.* Three-dimensional imaging of solvent-cleared organs using 3DISCO. *Nat. Protoc.* **7**, 1983–1995 (2012).
7. Kuwajima, T. *et al.* ClearT: a detergent- and solvent-free clearing method for neuronal and non-neuronal tissue. *Development* **140**, 1364–1368 (2013).
8. Susaki, E.A. *et al.* Whole-brain imaging with single-cell resolution using chemical cocktails and computational analysis. *Cell* **157**, 726–739 (2014).
9. Ke, M.T., Fujimoto, S. & Imai, T. SeeDB: a simple and morphology-preserving optical clearing agent for neuronal circuit reconstruction. *Nat. Neurosci.* **16**, 1154–1161 (2013).
10. Susaki, E.A. *et al.* Advanced CUBIC protocols for whole-brain and whole-body clearing and imaging. *Nat. Protoc.* **10**, 1709–1727 (2015).
11. Richardson, D.S. & Lichtman, J.W. Clarifying tissue clearing. *Cell* **162**, 246–257 (2015).
12. Tuchin, V.V. Tissue optics and photonics: light-tissue interaction. *Journal of Biomedical Photonics & Engineering* **1**, 98–134 (2015).
13. Lichtman, J.W. & Conchello, J.A. Fluorescence microscopy. *Nat. Methods* **2**, 910–919 (2005).

14. Dodt, H.U. *et al.* Ultramicroscopy: three-dimensional visualization of neuronal networks in the whole mouse brain. *Nat. Methods* **4**, 331–336 (2007).
15. Susaki, E.A. & Ueda, H.R. Whole-body and whole-organ clearing and imaging techniques with single-cell resolution: toward organism-level systems biology in mammals. *Cell Chem. Biol.* **23**, 137–157 (2016).
16. Liu, Z. *et al.* Immune homeostasis enforced by co-localized effector and regulatory T cells. *Nature* **528**, 225–230 (2015).
17. Espinosa-Medina, I. *et al.* Neurodevelopment. Parasympathetic ganglia derive from Schwann cell precursors. *Science* **345**, 87–90 (2014).
18. Oshimori, N., Oristian, D. & Fuchs, E. TGF-β promotes heterogeneity and drug resistance in squamous cell carcinoma. *Cell* **160**, 963–976 (2015).
19. Lafkas, D. *et al.* Therapeutic antibodies reveal Notch control of transdifferentiation in the adult lung. *Nature* **528**, 127–131 (2015).
20. Renier, N. *et al.* iDISCO: a simple, rapid method to immunolabel large tissue samples for volume imaging. *Cell* **159**, 896–910 (2014).
21. Belle, M. *et al.* A simple method for 3D analysis of immunolabeled axonal tracts in a transparent nervous system. *Cell Rep.* **9**, 1191–1201 (2014).
22. Renier, N. *et al.* Mapping of brain activity by automated volume analysis of immediate early genes. *Cell* **165**, 1789–1802 (2016).
23. Feng, G. *et al.* Imaging neuronal subsets in transgenic mice expressing multiple spectral variants of GFP. *Neuron* **28**, 41–51 (2000).
24. Schwarz, M.K. *et al.* Fluorescent-protein stabilization and high-resolution imaging of cleared, intact mouse brains. *PLoS One* **10**, e0124650 (2015).
25. Treweek, J.B. *et al.* Whole-body tissue stabilization and selective extractions via tissue-hydrogel hybrids for high-resolution intact circuit mapping and phenotyping. *Nat. Protoc.* **10**, 1860–1896 (2015).
26. Ascenzi, A. & Fabry, C. Technique for dissection and measurement of refractive index of osteones. *J. Biophys. Biochem. Cytol.* **6**, 139–142 (1959).
27. Genina, E.A., Bashkatov, A.N. & Tuchin, V.V. Optical clearing of cranial bone. *Adv. Opt. Technol.* **2008**, 1–8 (2008).
28. De Miguel, M.P. *et al.* Immunosuppressive properties of mesenchymal stem cells: advances and applications. *Curr. Mol. Med.* **12**, 574–591 (2012).
29. D'souza, N. *et al.* Mesenchymal stem/stromal cells as a delivery platform in cell and gene therapies. *BMC Med.* **13**, 186 (2015).
30. Guenoun, J. *et al.* *In vivo* quantitative assessment of cell viability of gadolinium or iron-labeled cells using MRI and bioluminescence imaging. *Contrast Media Mol. Imaging* **8**, 165–174 (2013).
31. Leibacher, J. & Henschler, R. Biodistribution, migration and homing of systemically applied mesenchymal stem/stromal cells. *Stem Cell Res. Ther.* **7**, 7 (2016).
32. Nemeth, K., Mayer, B., Sworder, B.J., Kuznetsov, S.A. & Mezey, E. A practical guide to culturing mouse and human bone marrow stromal cells. *Curr. Protoc. Immunol.* **102**, Unit 22F.12 (2013).
33. Rosen, A.B. *et al.* Finding fluorescent needles in the cardiac haystack: tracking human mesenchymal stem cells labeled with quantum dots for quantitative *in vivo* three-dimensional fluorescence analysis. *Stem Cells* **25**, 2128–2138 (2007).
34. Goldmacher, G.V. *et al.* Tracking transplanted bone marrow stem cells and their effects in the rat MCAO stroke model. *PLoS One* **8**, e60049 (2013).
35. Detante, O. *et al.* Intravenous administration of 99mTc-HMPAO-labeled human mesenchymal stem cells after stroke: *in vivo* imaging and biodistribution. *Cell Transplant.* **18**, 1369–1379 (2009).
36. Chen, F., Tillberg, P.W. & Boyden, E.S. Optical imaging. Expansion microscopy. *Science* **347**, 543–548 (2015).
37. Chozinski, T.J. *et al.* Expansion microscopy with conventional antibodies and fluorescent proteins. *Nat. Methods* **13**, 485–488 (2016).
38. Chen, F. *et al.* Nanoscale imaging of RNA with expansion microscopy. *Nat. Methods* **13**, 679–684 (2016).
39. Treweek, J.B. & Gradinaru, V. Extracting structural and functional features of widely distributed biological circuits with single cell resolution via tissue clearing and delivery vectors. *Curr. Opin. Biotechnol.* **40**, 193–207 (2016).
40. Chen, B.C. *et al.* Lattice light-sheet microscopy: imaging molecules to embryos at high spatiotemporal resolution. *Science* **346**, 1257998 (2014).
41. Bareyre, F.M. *et al.* The injured spinal cord spontaneously forms a new intraspinal circuit in adult rats. *Nat. Neurosci.* **7**, 269–277 (2004).
42. Wahl, A.S. *et al.* Neuronal repair. Asynchronous therapy restores motor control by rewiring of the rat corticospinal tract after stroke. *Science* **344**, 1250–1255 (2014).
43. Reinhardt, R.L., Khoruts, A., Merica, R., Zell, T. & Jenkins, M.K. Visualizing the generation of memory CD4 T cells in the whole body. *Nature* **410**, 101–105 (2001).

ONLINE METHODS

A step-by-step protocol for uDISCO is available as **Supplementary Protocol** (and ref. 44).

Animals. We used the following animals in the study: 1- to 6-months-old, mixed gender 27 (15 male and 12 female) C57BL/6N (Charles Rivers Laboratories), 57 (28 male and 29 female) *Thy1*–GFP mice (line GFP-M), 5 (2 male and 3 female) *Thy1*–YFP mice (line YFP-H)[23], 32 (13 male and 19 female) CX3CR1–GFP mice (B6.129P-Cx3cr1tm1Litt/J, Jackson Laboratory strain code: 005582), 6 (3 male and 3 female) β-actin EGFP mice (C57BL/6-Tg(CAG–EGFP); 131Osb/LeySopJ, Jackson Laboratory strain code: 006567), and four rats (4 female) (CD IGS Rat strain 001). Sample sizes were chosen based on preliminary experiments. Sample sizes are specified in figure legends. The animals used in this study were selected for each experiment based on their genetic background (wild type or fluorescent transgenes), and animals that resulted fluorescent-protein negative by genotyping were excluded from the study. Within each strain, animals were randomly selected; different stages of experiments (clearing, imaging, and data analysis) were carried out by different operators. Animals were housed in our animal facility under a 12/12 h light/dark cycle and were provided food and water ad libitum. Experiments were conducted according to institutional guidelines of the Ludwig Maximilian University of Munich after approval of the Ethical Review Board of the Government of Upper Bavaria (Regierung von Oberbayern, Munich, Germany). All data are reported according to the ARRIVE criteria[45].

Human tissue. Human tissues used for this study were obtained from five donors of 64–89 years old (1 male and 4 females). Human tissue donors gave their informed and written consent to the donation of their bodies for teaching and research purposes regulated by the Saxonian Death and Funeral Act of 1994 (third section, paragraph 18 item 8).

Perfusion and tissue preparation. Animals were deeply anesthetized by intraperitoneal injection with the triple combination of midazolam/medetomidine/fentanyl (MMF) (1 ml per 100 g of body mass for mice) before intracardial perfusion. Subsequently, animals were perfused transcardially (100–125 mm Hg pressure on Leica perfusion one system) with heparinized 0.1 M PBS (10 U/ml of heparin, Ratiopharm) for 5–10 min at room temperature until the blood was washed out and with 4% paraformaldehyde in 0.1 M PBS (pH 7.4; Morphisto, 11762.01000) for 20 min using 100–125 mm Hg pressure. The dissected tissue samples (whole brain, spinal cord, whole brain with the spinal cord, and femurs) were postfixed in 4% paraformaldehyde for 1–2 d at 4 °C. Then, tissues were washed once in PBS for 5 min; meninges were removed; and bent samples, such as spinal cords, were kept straight for the clearing procedure.

For cut bone clearing, femurs dissected from CX3CR1–GFP mice were fixed in cold 4% PFA for 24 h. Afterwards, the bones were washed with PBS and incubated in 30% sucrose PBS solution overnight at 4 °C. For longitudinal dissection, a Leica cryostat (Leica, CM3050S) was used to cut the bones embedded in optimum cutting temperature (O.C.T.) formulation (SAKURA, 4583). The section thickness was set at 30 µm, and the serial sectioning was performed until the entire bone marrow appeared. The remaining intact half bones were collected and washed with PBS to remove OCT and then processed for immunostaining and respective clearing[46].

For whole-body clearing, after the mouse body was well perfused and fixed, the skin was separated from the body while avoiding adhesion of pelage. The skull and vertebra were carefully opened, avoiding any damage such as puncturing and squeezing of the tissue. Whole-body tissue clearing was started immediately.

Immunostaining. The following antibodies and dyes were used in this study: Iba1 (Wako, 019-19741, dilution 1:350), GFAP (Dako, Z033401-2, dilution 1:350), Collagen 4 (SouthernBiotech, 1340-01, dilution 1:650), AlexaFluor 647 conjugated anti-GFP rabbit polyclonal antibody (Life Technology, A31852, dilution 1:500), TO-PRO-3 iodide (642/661) (Life Technologies, T3605, dilution 1:500), AlexaFluor 568 goat anti-rabbit IgG (H+L) (Life Technologies, A-11036, dilution 8 µg/mL), AlexaFluor 647 goat anti-rabbit IgG (H+L) (Life Technologies, A-21245, dilution 8 µg/mL), and Cy3 AffiniPure donkey anti-goat IgG (H+L) (Jackson, 705-165-147, dilution 1:300).

For immunostaining, the tissues (mouse brains or human tissue) were cut into 1 mm slices using a vibratome (Leica, VT1200S). Mouse sections were immunostained using iDISCO[20] or Belle *et al.*[21] protocols. We used the following iDISCO protocol. The sections were initially pretreated: first, they were washed in 0.1 M PBS for 50 min two times, then they were incubated in 50% and 80% methanol (in 0.1 M PBS) for 50 min at each step and then in 100% methanol for 1 h two times. Sections were bleached with ice-cold 5% H_2O_2 (Sigma, D216763) and 20% DMSO (Sigma D8418)/methanol (AppliChem, 141091.1211) at 4 °C overnight. After bleaching, sections were washed in methanol for 45 min three times; then in 20% DMSO/methanol for 45 min two times; then in 80% and 50% methanol for 45 min each step; then in 0.1 M PBS for 45 min two times; and finally in PBS/0.2% Triton X-100 (Sigma, T8787) for 45 min two times. For the immunostaining step, pretreated sections were incubated in PBS–0.2% Triton X-100–20% DMSO–0.3 M glycine (Sigma, G8898) at 37 °C overnight, then blocked in PBS–0.2% Triton X-100–10% DMSO–6% goat serum at 37 °C for 1 d, washed in PBS–0.2% Tween-20 (Sigma, P9416) with 10 mg/ml heparin (PTwH) overnight and then incubated with primary antibody dilutions in PTwH–5% DMSO–3% goat serum at 37 °C with gentle shaking on an oscillator for 6–8 d, refreshing the primary antibodies once after 3–4 d. Sections were then washed for 1 h with PTwH four times and then incubated with secondary antibodies diluted in PTwH–3% goat serum at 37 C° with gentle shaking on an oscillator for 3–4 d, refreshing once after 2 d. Sections were finally washed in PTwH 30 min five times and incubated with TO-PRO-3 iodide (642w/661) (dilution 1:750) in PTwH for 5 h at room temperature with gentle oscillation, washed again for 1 h four times with PTwH, and stored at 4 °C in 0.1 M PBS until clearing.

Human sections were immunostained using a modification of the protocol from Belle *et al.*[21]; briefly, 1 mm thick brain sections were incubated on a rocker (IKA, 2D digital) at room temperature in PBSGT solution, which consists of 0.1 M PBS with 0.2% porcine skin gelatin (Sigma, G2500), 0.5% Triton X-100, and 0.05% sodium azide (Sigma, 71290) for 24 h. Next, PBSGT was exchanged with PBSGT + 1% goat serum containing the primary antibodies and left in incubation at 37 °C with gentle shaking on

doi:10.1038/nmeth.3964

an oscillator (IKA, MS 3 basic) for 8–9 d. The primary antibodies were refreshed once after 4–5 d. Then, samples were washed for 30 min with PBSGT five times at room temperature and incubated with secondary antibodies, diluted in PBSGT + 1% goat serum at 37 °C with gentle shaking on an oscillator for 4–5 d. The secondary antibody was refreshed once after 2 d. Finally, samples were washed for 30 min three times with PBSGT, incubated with TO-PRO-3 in PBSGT for 5 h at room temperature with gentle oscillation, washed again for 1 h four times with PBSGT and stored at 4 °C in 0.1 M PBS until clearing.

For cut bone immunostaining, collected half bones were pretreated with 5 d of PBSGT incubation at room temperature. Then, the tissue was incubated in PBSGT with 1% goat serum and AlexaFluor 647 conjugated anti-GFP antibody (dilution 1:500) at 37 °C for 10 d, refreshing once after 5 d, and finally washed five times with PBSGT for 10 min.

Preparation of uDISCO solutions. Dehydrating solutions were prepared by mixing *tert*-butanol (Sigma, 360538) and distilled water in the following concentrations: 30 vol% *tert*-butanol, 50 vol% *tert*-butanol, 70 vol% *tert*-butanol, 80 vol% *tert*-butanol, 90 vol% *tert*-butanol, 96 vol% *tert*-butanol. Pure (100%) *tert*-butanol has a melting point between 23 °C and 26 °C; therefore. we recommend keeping it above the melting temperature before use. Delipidation solution dichloromethane (DCM) (Sigma, 270997) was used as a pure solution. Three refractive index matching solutions were used: BABB-D4, prepared by mixing BABB (benzyl alcohol + benzyl benzoate 1:2, Sigma, 24122 and W213802) with diphenyl ether (DPE) (Alfa Aesar, A15791) at a ratio of 4:1 and adding 0.4% vol DL-alpha-tocopherol (Vitamin E) (Alfa Aesar, A17039); BABB-D10, prepared by mixing BABB with DPE at a ratio of 10:1 and adding 0.4% vol vitamin E; BABB-D15, prepared by mixing BABB with DPE at a ratio of 15:1 and adding 0.4% vol vitamin E. In passive clearing, BABB-D4 preserved the fluorescence signal better, while BABB-D15 gave better transparency. BABB-D10 was used for whole-body tissue clearing. The ratio of DPE to BABB can be adjusted to achieve either better preservation of fluorescence or more tissue transparency.

uDISCO passive clearing procedure. All incubation steps were performed in a fume hood with gentle rotation or shaking using 5 ml tubes (Eppendorf, 0030 119.401) for whole mouse brain or smaller samples, or steps were performed using glass chambers (Omnilab, 5163279) for bigger samples such as rat tissues or whole brain and spinal cord. The samples were covered with aluminum foil to keep them in dark.

The clearing consisted of serial incubations of the fixed samples in 5–80 ml of 30 vol%, 50 vol%, 70 vol%, 80 vol%, 90 vol%, 96 vol% and 100% *tert*-butanol at 34–35 °C to dehydrate the tissue, followed by immersion in DCM for 45–60 min at room temperature to remove the lipids. Eventually, they were incubated in BABB-D at room temperature for at least 2 h until samples became transparent. The requirement of DCM step and the incubation time of each step in tert-butanol solutions depended on sample size. For instance, small tissues such as mouse spinal cord or 1-mm-thick coronal slices did not need DCM step and required short incubation times (2–4 h) per each *tert*-butanol step compared with thicker or mineralized tissues such as whole brain and intact bones (12 h). Details of each protocol are showed in **Supplementary Table 1**. Samples could be stored in BABB-D at room temperature in dark for weeks.

All other clearing methods, including PACT, CUBIC, 3DISCO, 1-propanol BABB, ScaleS, SeeDB and Murray's clear (**Fig. 1**; **Supplementary Figs. 5**,**6**, and **9**–**11**), the clearing protocols were performed following the original publications[1,2,6,9,10,14,24,25,47].

uDISCO whole-body clearing procedure. We established a transcardial circulatory system comprised of a peristaltic pump (Gilson, Peristaltic Pump MINIPULS 3; **Supplementary Fig. 28**; see also the step-by-step protocol of uDISCO in **Supplementary Protocol**). In principle, two channels from the pump were required for circulation. The first channel pumped the clearing solution through the mouse body, and the second channel collected the solution exiting the mouse body and recirculated it back to the original bottle. Since clearing solutions are corrosive, Viton reference tubing was chosen (Gilson, F1817745) because it is resistant to clearing chemicals. First, the reference tubing was set up following the instructions, and each end of the tubing was connected to a tubing connector (Omnilab, 5434482). Next, the tubing connectors were linked with additional PVC tubing (Omnilab, 5437920). For the outflow tubing of the first channel, which injected the solution into the heart, the head part cut from a 1 ml syringe (Braun, 9166017V) was inserted as the connector of the perfusion needle and fixed with a mouse transcardiac perfusion needle (Leica, 39471024). Meanwhile, the inflow tubing of the second channel, which recirculated solution, was fixed to the glass chamber containing the mouse body. Eventually, the inflow tubing of the first channel was kept below the surface of the solution, and the circulation was started until air bubbles were pushed out from the tubing system.

All clearing steps should be performed in a fume hood. First, the mouse body was put in a glass chamber, and the perfusion needle was set into the heart through the same pinhole made during tissue preparation in the perfusion setup. Next, the chamber was covered with aluminum foil, and the transcardial circulation was started. Each gradient of dehydration solution was circulated at 8–10 ml/min for 10–12 h. As the melting point of *tert*-butanol is 23 to 26 °C (close to room temperature), a heating plate with 35–40 °C was used for the two rounds of 100% *tert*-butanol circulation to prevent the solution from solidification. The final step of tissue clearing could normally be achieved by circulating BABB-D10 with the same injection rate for 6–12 h. The transparency of the mouse body was checked by eye during clearing. Bubbles were carefully prevented from forming, especially in the first channel, at every step. For rat whole-body clearing, a thicker perfusion needle (Leica, 39471022) without rubber head was used, and each step of circulation was prolonged to 24 h with a flowing rate of 15–20 ml/min. A passive incubation step of DCM for 6–8 h with gentle shaking was included before performing BABB-D10 circulation. **Supplementary Table 1** summarizes the incubation times and temperatures of each clearing solution for whole-body clearing.

As a final note, the amount of solutions for circulation depends on the capacity of the clearing chamber. For mice whole-body clearing, if the maximum volume of the glass chamber is 400 ml, 300 ml of volume of solution was used for circulation. For rat whole-body clearing, a 1,000 ml capacity glass chamber with 800 ml working clearing solution would be sufficient.

PARS and CUBIC whole-body clearing methods (**Fig. 1** and **Supplementary Fig. 11**) were performed following the original papers[10,25].

Vasculature labeling with Texas Red Dextran. Texas Red Dextran (70,000 MW, Lysine Fixable, Invitrogen) was diluted in saline with a concentration of 15 mg/ml for mouse (0.1 ml per animal) and 8 mg/ml for rat (1 ml per animal). A pulled tubing (nonsterile polythene tubing, ID 0.86 mm, OD 1.27 mm, Harvard Apparatus) was attached to the syringe needle to achieve sharp ending thinner than femoral vein. For dextran injection, animals were anesthetized (MMF triple combination, 8 ml/kg, i.p.) and placed ventral side up. The right femoral vein was identified and exposed by surgical dissection in the inguinal region. The sharp ending of the tubing was inserted into the venous sinus of femoral vein, and the dextran was injected at a rate of 0.3–0.4 ml/min. After injection, the tubing was retreated and the wound was sealed by surgical suture. Then, the animals were placed in a warm cage for 15–20 min before proceeding with the standard perfusion and tissue preparation procedure. We experienced that skipping heparin in the prewashing step of the perfusion (and using only 0.1 M PBS instead) resulted in better labeling of the vasculature.

Neuronal tracing by AAV virus. AAVs expressed EGFP (AAV2–Syn–EGFP) and RFP (AAV2–Syn–RFP) under the promoter of human Synapsin (Vector Core, University of North Carolina). The final titers were around 2×10^9 GC (Genome Copy) per µl. For the virus injection, 3- to 4-month-old female C57BL/6N mice were anesthetized (MMF triple combination, 8 ml/kg, i.p.) and placed in a stereotaxic frame. To expose the motor cortex targeted for tracing axons into spinal cords, two cranial windows on each side of the skull were created within the area: 1.0 mm and 2.0 mm lateral; 0.5 mm anterior and 1.5 mm posterior to bregma. AAVs were injected into the cortex using a custom-established injector fixed with a pulled glass pipette. First, ten independent injection sites were targeted with the following coordinates: 1.2 mm and 1.8 mm lateral; 1.0 mm deep; 0.3 mm anterior to bregma, 0.1 mm, 0.5 mm, 0.9 mm, and 1.3 mm posterior to bregma. Next, 400 nl virus was injected at a rate of approximately 200 nl/min for every injection site. The glass pipette was kept *in situ* for 1 min before moving to the next site. After finishing all the injections, the cranial windows were covered by absorbable gelatin sponge (GELITA-SPON, GS-110), and the incision was closed by wound clips (CellPoint Scientific, part no. 203-1000). The animal was placed in a warm cage for waking up and then transferred into a regular keeping room. Carprofen (0.2 ml per injection, 1 mg/ml, i.p.) was given 3 times per d for 3 d. The animal survived for 4 weeks post virus injection before performing uDISCO.

Culture and characterization of mouse BMSCs. Mouse BMSCs were collected and cultured from β-actin EGFP mice as described previously[32,48]. Briefly, femur and tibia from 8- to 12-week-old mice (4–5 mice per culture) were removed under sterile conditions, and bone marrow was flushed out using a 20 gauge needle syringe. After mechanical dissociation with repeated flow of the bone marrow through needles of progressively smaller diameter, the cell suspension was filtered through a sterile 40 µm nylon cell strainer mesh. Cells were resuspended in a final density of 20×10^6 cells per ml of medium and were plated in T25 flasks (5 ml per flask) at 37 °C with 5% CO_2. Culture medium was composed of aMEM, 10% lot-selected mesenchymal-stem-cell-qualified fetal bovine serum (FBS), 1% L-glutamine, 1% penicillin–streptomycin, and medium was stored at 4 °C for 1–3 weeks until usage. The medium was changed on day 2 (half of medium) and day 7 (complete change), followed by a complete change of medium every 3–5 d. Cells were passaged for the first time when 70–80% confluent using 0.05% trypsin–EDTA, and they were split at a 1:3 ratio.

Characterization of mix BMSCs was done with flow cytometry (FACS) and differentiation assays on passage 3. For FACS analysis the following primary antibodies were used in two different staining panels: CD11b-eFluor450 (eBiosciences 48-0112, clone M1/70, dilution 1:400), CD45.2-PE (eBiosciences 12-0454, clone 104, dilution 1:400), CD34-eFluor450 (eBiosciences 48-0341, clone RAM34, dilution 1:100), Sca1-APC (eBiosciences 17-5981, clone D7, dilution 1:200), CD29-PE (eBiosciences 12-0291, clone HMb1-1, dilution 1:200), and CD44-APC (eBiosciences 17-0441, clone IM7, dilution 1:200). Briefly, cells were harvested by trypsinization with 0.05% trypsin, washed with ice-cold PBS, centrifuged at 1,500 r.p.m. for 8 min at 4 °C, resuspended at a concentration of $1–5 \times 10^6$ cells/ml, and stained with the primary antibodies for 45 min at 4 °C in the dark. Following washing with ice-cold PBS three times, cells were immediately read at a flow cytometer (BD Biosciences, FACS Verse). Unstained cells and cells stained with the corresponding isotypic controls were used as negative controls for FSC, SSC, and autofluorescence adjustments.

Osteogenic and adipogenic differentiation capacity of BMSCs was tested on cells of passage 3 as previously detailed[47]. Bone mineralization and fat droplets after osteo- and adipo-differentiation were detected using alizarin red and oil red O staining assays, respectively, according to standard protocols. Chondrogenic differentiation capacity of mBMSCs was studied using the StemPro chondrogenesis differentiation kit (Gibco A10071-01) according to manufacturer instructions; proteoglycans produced by chondrocytes were stained with 1% alcian blue solution according to a standard protocol. Characterization of the transplanted EGFP+ mBMSCs is shown in **Supplementary Fig. 19**. Approximately 30% of the transplanted cells were EGFP+, and 60% were loaded with quantum dots.

Labeling of cells with Qdots. The EGFP+ BMSCs were cultured for 30–45 d until reaching passage 4 or 5. 1 d before transplantation, EGFP+ BMSCs were labeled with fluorescent carboxyl quantum dot nanoparticles (Qtracker Qdots, Invitrogen, emission at 655 nm or 800 nm). The nanoparticles were aseptically reconstituted according to manufacturer's instructions (20 µl of component A and 20 µl of B), allowed to sit at room temperature for 5 min, vortexed for 30 s, mixed with full BMSC medium up to a volume of 400 µl, and then added to the flasks (200 µl per 1 T75 flask with confluent BMSCs). Labeling of the EGFP+ BMSCs with Qdots 655 was checked 24 h later with microscopy and FACS analysis before transplantation. The efficiency of the labeling and the presence of any remaining free Qdots was also checked by sequential transferring of the Qdots-containing medium to a new flask with BMSCs, which did not produce any further cell labeling.

Transplantation procedures. Transplantation of the EGFP+ BMSCs, EGFP+/Qdot-labeled BMSCs, or vehicle (PBS) was

doi:10.1038/nmeth.3964

performed via tail vein intravenous (IV) or intraperitoneal (IP) injections. The injections were performed in C57BL/6N mice. All animals were food-starved overnight before the transplantation to clear the intestines for visualization.

For IV transplantation, animals were shortly anesthetized with 2% isoflurane. To achieve maximum vein dilation for successful infusion, the tail was shortly dipped and gently massaged in warm water (35–38 °C, for 10 s) and was then immediately placed for 5 min between a prewarmed (38 °C) heating pad and warm wet gauzes. The suspension of 1×10^6 BMSCs in 300 µl was injected IV at once using a 30-gauge needle attached to a 1 ml syringe. The injection caused a short heart arrest (approximately 10 s) in some animals that recovered either spontaneously or after short thoracic massaging. For IP transplantations, animals were briefly (30–60 s) anesthetized with isoflurane just before the injection and then received IP injection of 1×10^6 BMSCs in 300µl of PBS at once. Following successful injections, animals recovered from anesthesia in a heat chamber (set at 30–31 °C) for approximately 30 min before returning to their home cage. The control animals were injected with PBS. 3 h after injection, we euthanized the animals for uDISCO.

Imaging setup, light-sheet microscopy. We used LaVision BioTec Ultramicroscope II light-sheet microscope (**Supplementary Table 2**). The axial resolution of the Ultramicroscope is 4 µm, and the lateral resolution is 0.5–2 µm, depending on the objective used (details are in **Supplementary Table 2**). We used exposure times of 250 ms to 50 ms, laser power of 1 to 3mW (25% to 70% of the power level at a given wavelength, mostly centered around 470 nm, 545 nm, or 640 nm), distributed across a Gaussian light sheet of variable width and NA; according to the manufacturer specifications, the light sheet has a thickness of 4.5 µm at its waist at 488 nm. A typical width spanning between 0.5 mm and 0.3 mm was chosen to adjust the illumination extent to the field of view of the objective used. The excitation branch of the imaging setup was used as provided, without further calibration. The microscope features a zoom body (Olympus revolving zoom unit U-TV, 1×, 2×, and 4×) equipped with an automated filter box for 25 mm mounted filters. An enhanced fluorescence acquisition branch consists of refractive-index-corrected long working distance objectives (Clear4brain, Munich): Olympus 2×/0.15 NA (WD 10 mm), Olympus 4×/0.28 NA (WD 10 mm) and Olympus 20×/0.45 NA (WD 5 mm). Making use of the entire scanning area, defined by the built-in scanner capabilities, we acquired tile scans to cover the entire specimens.

Imaging setup, laser-scanning confocal microscopy. Cleared specimens such as brain slices or whole organs were incubated in BABB-D solution for a minimum of 2 h. Samples were mounted on histological glasses using transparent silicone gel (OBI, 4799656): a pool on glass was created with the glass as the bottom surface and silicone as walls, then samples were put into the pool filled with BABB-D. Eventually, glass coverslips were used to seal the pool, creating a closed chamber to prevent leakage of BABB-D.

Regions of brain slices were imaged with an inverted laser-scanning confocal microscopy system (Zeiss, LSM 880) using a 25× water-immersion long working distance objective lens (Leica, 0.95 NA, WD = 2.5 mm) mounted on a custom mounting thread. The *z*-step size was 3–5 µm, and whole stacks of the slices were acquired (**Supplementary Table 2**).

Imaging setup, fluorescence stereomicroscopy. Cleared and uncleared specimens such as brain slices, whole bodies, or organs were immersed either in BABB-D or in PBS, respectively, and imaged with Zeiss AxioZoom EMS3/SyCoP3 fluorescence stereomicroscope using a 1× long working distance air objective lens (Plan Z 1×, 0.25 NA, WD = 56 mm; **Supplementary Table 2**).

Image processing. Processing and 3D rendering was executed by HP workstation with 8 core Xeon processor, 196 GB RAM, and Nvidia Quadro k5000 graphics card. We used Imaris, Amira, and Fiji (ImageJ2) for 3D and 2D image visualization. Stitching of tile scans was done via Fiji's stitching plugin[49]. Stitched images were saved in tiff format to enable fast processing using different software. We removed acquisition errors using Fiji's TrakEM2 plugin and Imglib2 (ref. 50) library.

Image processing consists of three main steps: error correction, image quality enhancement, and quantification.

Error correction. (e.g., **Fig. 3j**) Errors in image acquisition and following steps may occur for various reasons, such as physical interference with the microscope during image acquisition or miscalibration of a dynamic plate of the microscope, resulting in unwanted shifting of tiles or drifting effects between different slices of the same image series.

Quality enhancement. (e.g., **Fig. 5b**) We used filtering techniques (such as Gaussian, median, and anisotropic diffusion filtering) in the spatial domain for noise reduction. Morphological filters were used to correct the artifacts based on their shapes. Owing to the big size of data sets, filtering in the frequency domain is not feasible. Image intensity manipulation and equalization employed local (CLAHE in Fiji) and pseudo flat-field correction in Fiji (**Supplementary Video 1**).

Quantification. (e.g., **Fig. 5c**) To quantify the density of Qdot-positive BMSCs, we developed a simple workflow based on Fiji (**Supplementary Figure 29**).

Quantifications. *Normalized fluorescence signal profile plots and total signal intensity.*

Normalized signal profiles demonstrate the quality of the signal over the background, which defines the ability to trace the individual cellular structures in the scans (e.g., axon tracing in **Supplementary Video 6**). We calculated the total signal intensity to compare the remaining fluorescence signal after each clearing method. We presented details of these calculations with example images in **Supplementary Figure 30**.

For normalized signal profile measurement, a straight line was drawn across the specific area, which includes signal and background, and plotted via Fiji's 'plot profile' option. To calculate the mean background intensity, we chose another line adjacent to the profile line with no intersection to any specific signal. Subsequently, the profile plot was normalized by dividing the profile data over the calculated mean background intensity. Normalized profile of each sample was shown in the representative line chart (**Supplementary Figs. 2**,**5**,**6** and **10**).

For total signal intensity quantification, we selected a rectangular area covering the signal (several cellular structures), and measured the integrated density as the representative of the total signal

intensity of selected area. To calculate the mean background, a straight line was drawn across the area. Eventually, the total sum of the signal intensity in the sample area was determined as:

$$\text{Sum of background intensity} = \text{Number of background pixels} + \text{Mean background value}$$

$$\text{Sum signal intensity} = \text{Total sum of intensity of the area} - \text{Sum of background intensity}$$

We calculated the average total signal intensity by dividing the sum of the signal intensity over the pixel number of the rectangular selection (**Supplementary Figs. 2**,**5**,**6**,**9** and **10**).

Signal-to-noise ratio (SNR). A small part of the image was selected, and pixels belonging to a specific signal were separated from the background by thresholding the input image, *f*, and applying the binary image as the mask to the same image.

$$f(n,m) = S(o,p) + X(i,j)$$

$$o \neq i, p \neq j$$

S is the image that contains only the specific signal, and *X* is the background image. SNR was calculated based on Jahr *et al.*[51]

$$\text{SNR} = \text{Mean}(S)/\text{Std}(X)$$

Peak signal-to-noise ratio (PSNR). PSNR was calculated as previously described[52]. In brief, we used a mean square error (MSE) calculation between the sample image and a reference image. We took the average intensity of the background pixels as the reference image without the noise. Then, we calculated the MSE and PSNR as:

$$MSE = \frac{1}{N * M} \sum_{i=0}^{N-1} \sum_{j=0}^{M-1} [X(i,j) - Y(i,j)]^2$$

Y is the reference image with $N \times M$ dimension.

$$PSNR = 20 * \log_{10}\left(\frac{MAX}{\sqrt{MSE}}\right)$$

MAX represents the maximum intensity of the input image *f* in the selected neighborhood.

RMSE calculation. The root mean square (RMS) of the morphology deformation error at single-cell scale was used as a quantification factor for isotropy. RMSE calculation includes three steps: 1) Postclearing and preclearing images of a single cell were registered by similarity transformation in Fiji's TrakEM2 plugin. To achieve perfect overlay, output images from step 1 were registered with nonrigid transformations using Fiji's bUnwrapj plugin[53]. 2) The deformation parameter for preclearing image pixels was masked with a skeletonized preclearing image to remove irrelevant deformation parameters. 3) RMS of the deformation error with respect to the distance from the center of the cell or vessel (constant point) was calculated[37].

Fluorescence level. Fluorescence level quantification was expressed as a signal-to-background ratio and was calculated using Fiji at the following timepoints after clearing: 0, 4, 7, 19, and 37 d (**Fig. 1b**). From each brain scan, a *z*-projection of three consecutive images in Tiff format was made at the same anatomic region for all the samples. The mean value of the background for each *z*-projection was obtained by averaging the background values of 15–20 regions from equally sized areas of the projection without signal. To calculate the mean value of the signal of each *z*-projection, we used the threshold function of the software; the threshold was adjusted to consider the fluorescence signal visible in the projection. After adjusting the threshold, only the sharp signal from specific cellular structures was analyzed per each *z*-projection. To this end, we used Fiji's "analyze particles" to measure the signal intensity only of particles sized between 10 and 150 pixels (visible fluorescent cells), and we calculated the mean value from all the particles. Next, this value was divided by the mean value of the background of the respective projection, obtaining the fluorescence level on the background.

Imaging depth quantification. To assess the imaging depth between different clearing methods (CUBIC, PARS, PACT, and uDISCO), the tile scans of three whole brains per clearing method were taken with a light-sheet microscope with 4 µm *z* step (in **Fig. 1h**,**i**, and **Supplementary Fig. 11**). 3D reconstructions at the same anatomic level (from the surface of the brain to the center of the brain, including the region of the hippocampus) of each sample were shown in the coronal view using Imaris. Next, the images of the 3D reconstructions were analyzed in Fiji. Using the scale bar provided by Imaris, the distance of imaging depth was measured from the surface (where the signal was sharp) to the inner part of the brain until the last identifiable signal over the background coming from cell body or cellular structure (e.g., axons or dendrites) was detected.

Statistical analysis. Data are presented as mean ± s.d. in **Figures 1b–d**,**h**,**i**;**3i**;**6h**,**n** and in **Supplementary Figures 4**,**7b**,**8c**,**11b**,**12e**,**13s**,**25i**,**26**. Data are presented as mean ± s.e.m. in **Figure 5c** and in **Supplementary Figures 2c**,**5h**,**6h**,**9g**,**10h**. The data distribution in each experiment was checked for normality using Shapiro–Wilk test in IBM SPSS statistics software. *P* values were calculated using unpaired *t*-test to compare data between two groups (**Supplementary Figs. 2c**,**4**,**8c**,**25i**). One-way ANOVA was used to compare more than two groups of data (**Fig. 1b–d**,**h**,**i**; and **Supplementary Figs. 5h**,**6h**,**9g**,**10h**,**11b**,**12e**,**13s**); if ANOVA was significant, it was followed by *post hoc* Dunnett's test for multiple comparisons (**Figs. 1b–d**,**h**,**i** and **Supplementary Figs. 5h**,**6h**,**9g**,**10h**,**11b**).

44. Pan, C., Cai, R., Quacquarelli, F.P., Ghasemi, A. & Ertürk, A. Whole organ and organism tissue clearing by uDISCO. *Protocol Exchange* http://dx.doi.org/10.1038/protex.2016.055 (2016).
45. Kilkenny, C., Browne, W.J., Cuthill, I.C., Emerson, M. & Altman, D.G. Improving bioscience research reporting: the ARRIVE guidelines for reporting animal research. *PLoS Biol.* **8**, e1000412 (2010).
46. Acar, M. *et al.* Deep imaging of bone marrow shows non-dividing stem cells are mainly perisinusoidal. *Nature* **526**, 126–130 (2015).
47. Ertürk, A., Lafkas, D. & Chalouni, C. Imaging cleared intact biological systems at a cellular level by 3DISCO. *J. Vis. Exp.* **89**, e51382 (2014).
48. Zacharaki, D. *et al.* Characterization of *in vitro* expanded bone marrow-derived mesenchymal stem cells isolated from experimental autoimmune encephalomyelitis mice. *J. Mol. Neurosci.* **51**, 282–297 (2013).
49. Preibisch, S., Saalfeld, S. & Tomancak, P. Globally optimal stitching of tiled 3D microscopic image acquisitions. *Bioinformatics* **25**, 1463–1465 (2009).
50. Pietzsch, T., Preibisch, S., Tomancák, P. & Saalfeld, S. ImgLib2–generic image processing in Java. *Bioinformatics* **28**, 3009–3011 (2012).
51. Jahr, W., Schmid, B., Schmied, C., Fahrbach, F.O. & Huisken, J. Hyperspectral light sheet microscopy. *Nat. Commun.* **6**, 7990 (2015).
52. Gonzalez, R. *Digital Image Processing* 3rd edn. (India, Pearson Prentice Hall, 2006).
53. Arganda-Carreras, I. *et al.* Consistent and elastic registration of histological sections using vector-spline regularization. in *Computer Vision Approaches to Medical Image Analysis* (eds. Beichel, R.R. & Sonka, M.) 85–95 (Springer, 2006).

doi:10.1038/nmeth.3964

Supplementary Figure 1: Whole-body clearing and imaging of adult mice with 3DISCO

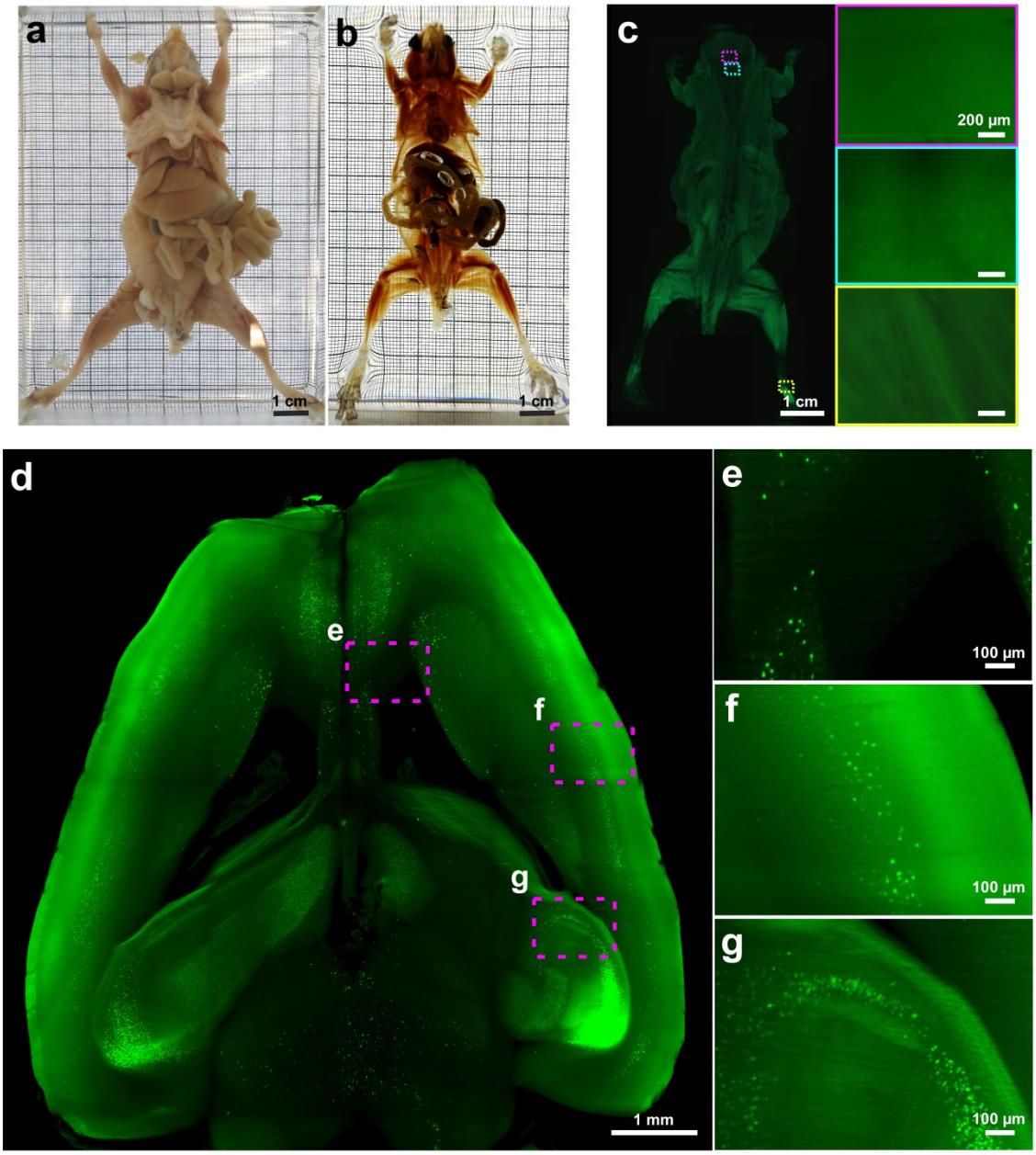

Whole-bodies of adult GFP-M mice (3 months old) were cleared with 3DISCO (same protocol as used in uDISCO). Before (**a**) and after (**b**) 3DISCO whole-body clearing images of a representative mouse body. 3DISCO whole-body clearing provided a comparable optical transparency to uDISCO (see Fig. 2b). (**c-g**) In contrast, preservation of endogenous GFP signal was weak after 3DISCO whole-body clearing. (**c**) Fluorescence stereomicroscope acquisition could not detect any identifiable neuronal structures unlike the uDISCO sample (see Fig. 2c). (**d-g**) Light-sheet microscopy of entire GFP-M mouse brain after 3DISCO whole-body clearing. While a weak GFP signal remained in some cell bodies, neuronal projections were completely undetectable due to diminished signal after 3DISCO whole-body clearing (see Fig. 4c-f).

Supplementary Figure 2: Fluorescence signal quality comparison after whole body uDISCO and 3DISCO clearing

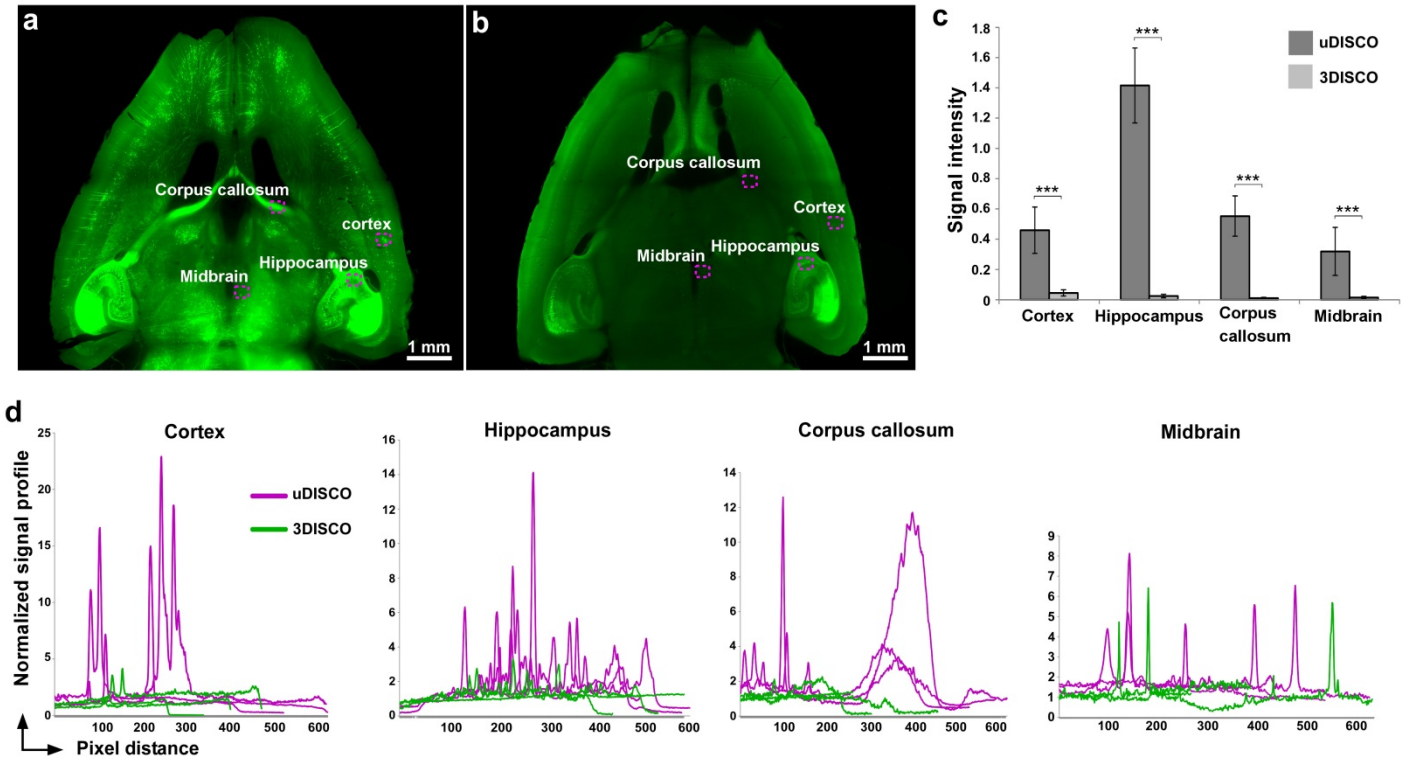

Representative light-sheet microscopy images of GFP-M brains at 2.5 mm depth from the dorsal surface after whole-body uDISCO (**a**) or 3DISCO (**b**) clearing. (**c**) Signal intensity (calculations are explained in Methods and Supplementary Fig. 30) comparison after whole-body uDISCO and 3DISCO clearing. Statistical significance (***$P < 0.001$) was assessed by unpaired *t*-test at each brain region. Values are mean ± s.e.m.; n=3 brains for each group (3 months old GFP-M mice). (**d**) Normalized signal profiles (calculations are explained in Methods and Supplementary Fig. 30) after whole body uDISCO and 3DISCO clearing at different depths (distance from brain surface) to compare the fluorescence signal: cortex (0.5 mm), hippocampus (1.2 mm), corpus callosum (2.5 mm) and midbrain (4.0 mm); n=3 brains for each group plotted (each magenta or green line profile represents one brain).

Supplementary Figure 3: The details of chemicals used in 3DISCO and uDISCO

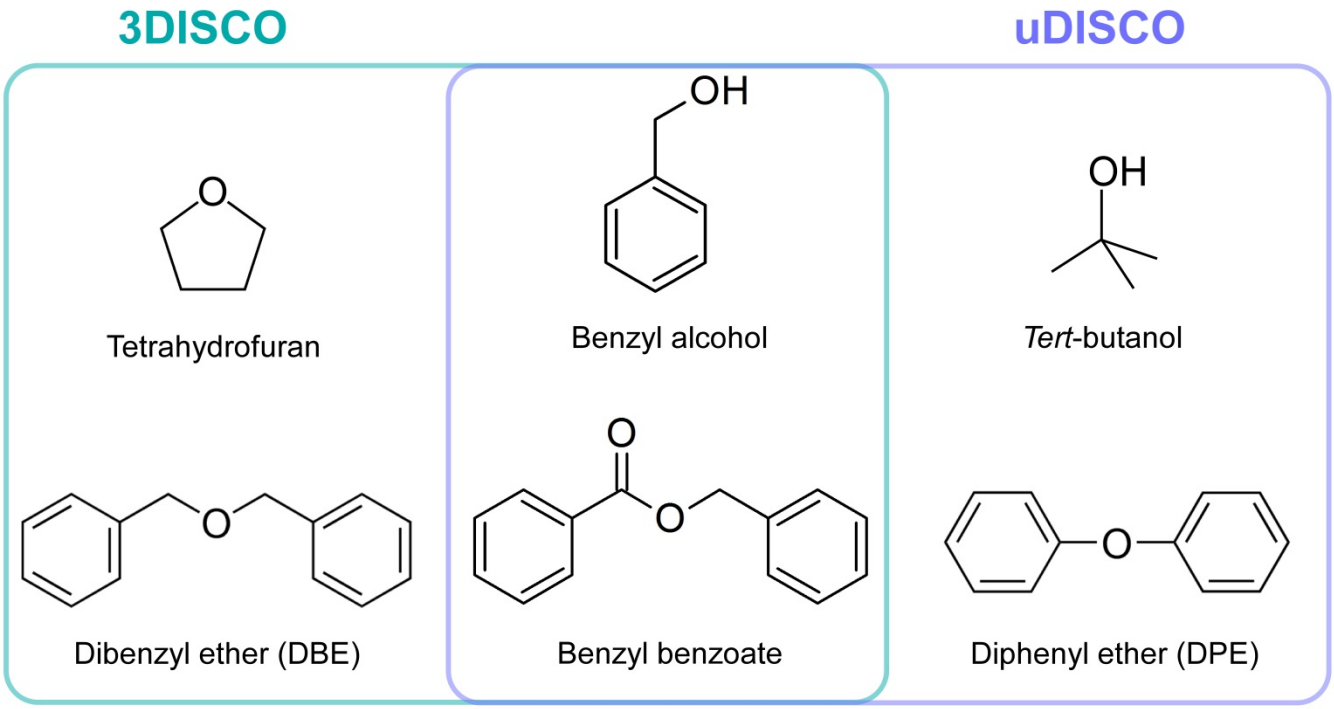

Tetrahydrofuran (THF) used in dehydration step of 3DISCO has an ether functionality, which is prone to oxidation and further reactions. In contrast, *tert*-butanol used in uDISCO is a tertiary alcohol and more stable to oxidation and less reactive. 3DISCO utilizes dibenzyl ether (DBE) or BABB (benzyl alcohol and benzyl benzoate) in refractive index matching step. Both of these chemicals have reactive benzylic C-H and C-O bonds, hence, they can form peroxidase and quench the fluorescence signal. To reduce chemical interactions that could diminish the endogenous fluorescence signal in uDISCO, 1) we performed refractive index matching in the presence of diphenyl ether (DPE): DPE does not have reactive benzylic C-H and C-O bonds, therefore, it is less prone to radical and other oxidative reactions; 2) we used antioxidant vitamin E to scavenge further the peroxides that can destroy the fluorescent proteins.

Supplementary Figure 4: Endogenous fluorescent signal stabilization in uDISCO

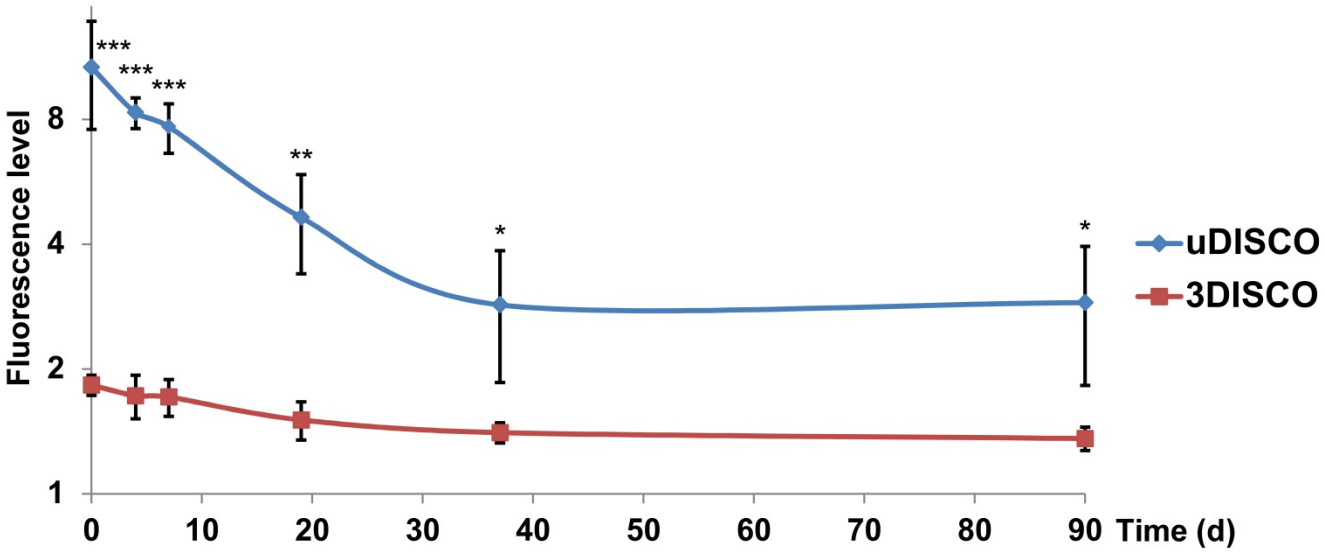

We measured the fluorescence signal of the same uDISCO and 3DISCO samples presented in Fig. 1b, 3 months after the clearing. We observed some decrease in signal level within the first few weeks (most probably due to the further dehydration of tissues in final clearing solutions), which got stabilized after about a month. At all-time points the level of fluorescence after uDISCO was higher compared with the level of fluorescence after 3DISCO. Values are mean ± s.d.; n=3 and 4 mice for uDISCO and 3DISCO, respectively. Statistical significance (*P < 0.05, **P < 0.01, ***P < 0.001) was assessed by unpaired t-test.

Supplementary Figure 5: Fluorescence signal quality comparison after uDISCO, 3DISCO, 1-proponal BABB, PACT, CUBIC, ScaleS and SeeDB clearing in *Thy1*-GFP-M mice

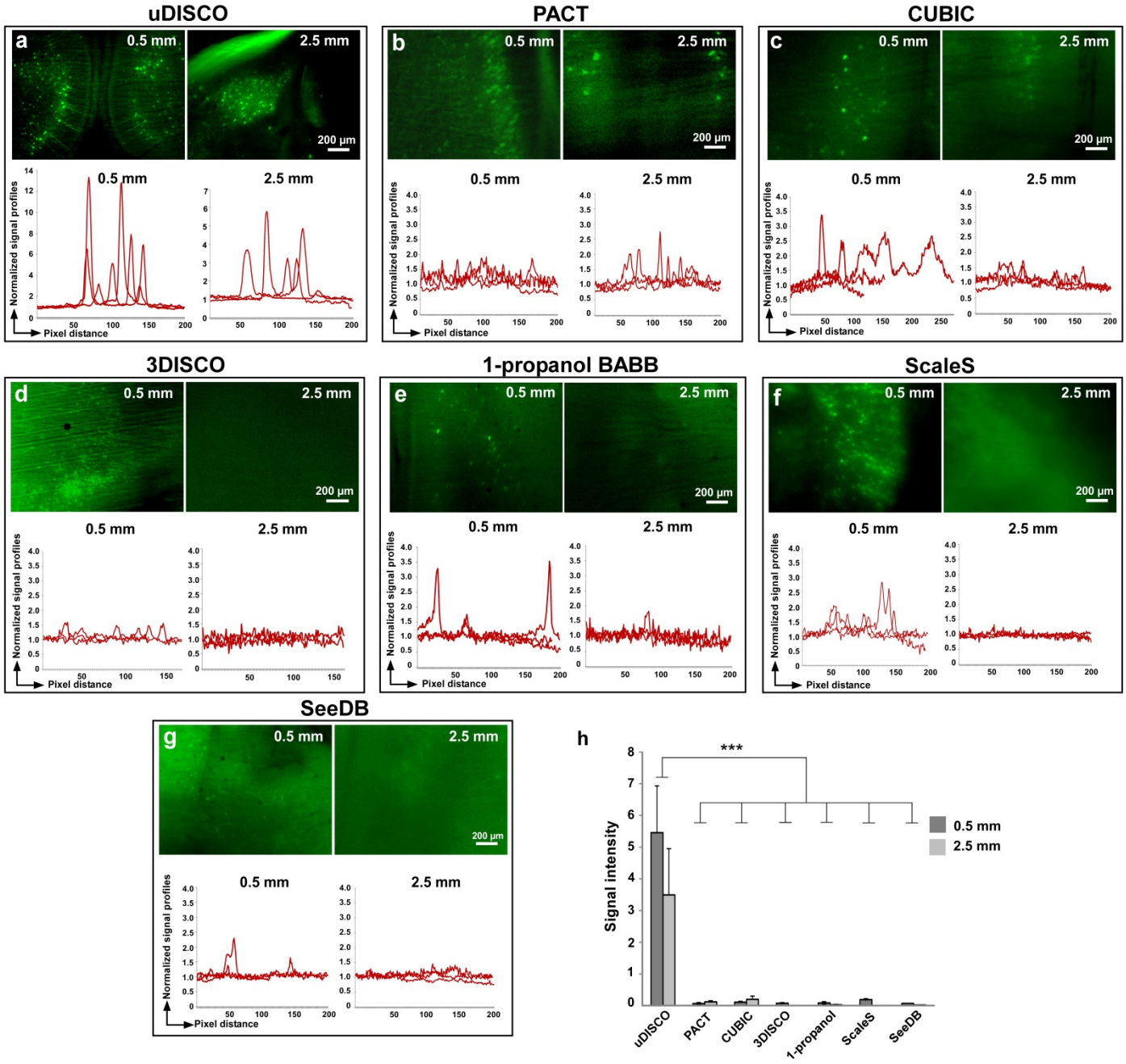

Representative images of normalized signal profiles at 0.5 mm and 2.5 mm depth from the dorsal surface after uDISCO (**a**), PACT (**b**), CUBIC (**c**), 3DISCO (**d**), 1-proponal BABB (**e**), ScaleS (**f**) and SeeDB (**g**) clearing of GFP-M brains. Normalized signal profile for each sample demonstrates the dynamic range of the obtained signal, which is the primary parameter for the tracing of imaged structures (separation of specific signal from the background). (**h**) Quantification of total signal intensity on specific cellular structures (cell bodies) at different depths (0.5 mm and 2.5 mm) of the samples after respective clearing (see the Methods and Supplementary Fig. 30). uDISCO cleared brains resulted in greater signal intensity compared with other methods. Statistical significance (***$P < 0.001$) was assessed by one-way ANOVA followed by Dunnet's post-hoc test. Values are mean ± s.e.m.; n=3 brains for each group (3 months old GFP-M mice).

Supplementary Figure 6: Fluorescence signal quality comparison after uDISCO, 3DISCO, 1-proponal-BABB, PACT, CUBIC, ScaleS and SeeDB clearing in CX3CR1-GFP mice

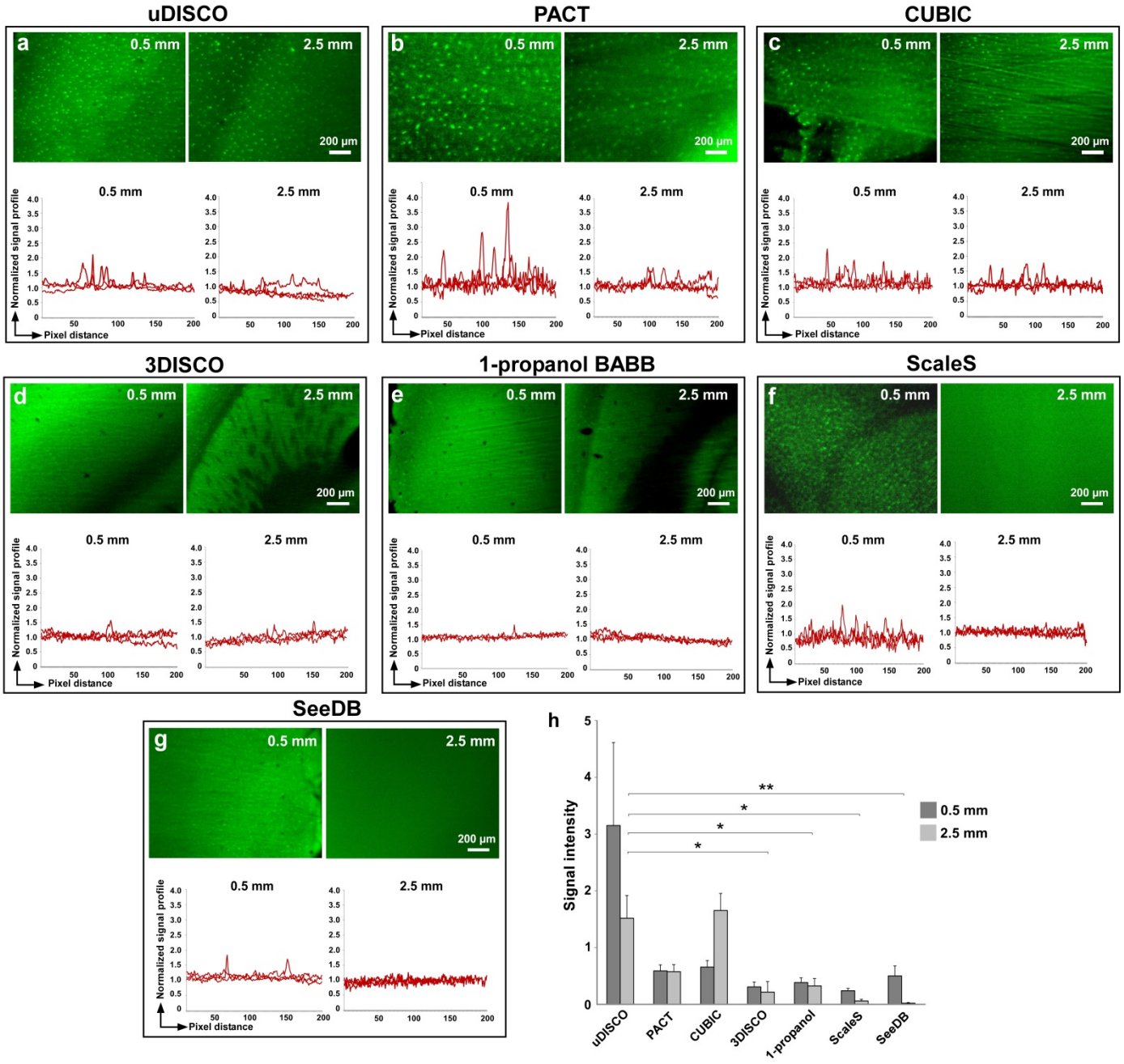

Representative images and normalized signal profiles at 0.5 mm and 2.5 mm depth from the dorsal surface after uDISCO (**a**), PACT (**b**), CUBIC (**c**), 3DISCO (**d**), 1-propanol BABB (**e**), ScaleS (**f**) and SeeDB (**g**) clearing of CX3CR1-GFP brains. In all cases, regions at the same depth and anatomical locations were quantified. Note that tissue shrinkage by uDISCO allowed visualization of larger volumes with the same imaging parameters, while tissue expansion e.g. by PACT allowed visualization of more details as cells appear larger. (**h**) Signal intensity quantifications at different depths of the samples after respective clearing. While uDISCO showed comparable results to PACT and CUBIC clearing, it has outperformed 3DISCO, 1-propanol BABB, Sca*l*eS and SeeDB at deeper brain regions (2.5 mm depth). Statistical significance (*$P < 0.05$, **$P < 0.01$) was assessed by one-way ANOVA followed by Dunnett's post-hoc test. Values are mean ± s.e.m.; n=6 brains for uDISCO group, n=3 brains for each other group (3 months old CX3CR1-GFP mice). See also Supplementary Video 1.

Supplementary Figure 7: Clearing performance of uDISCO for dissected organs and shrinkage quantifications

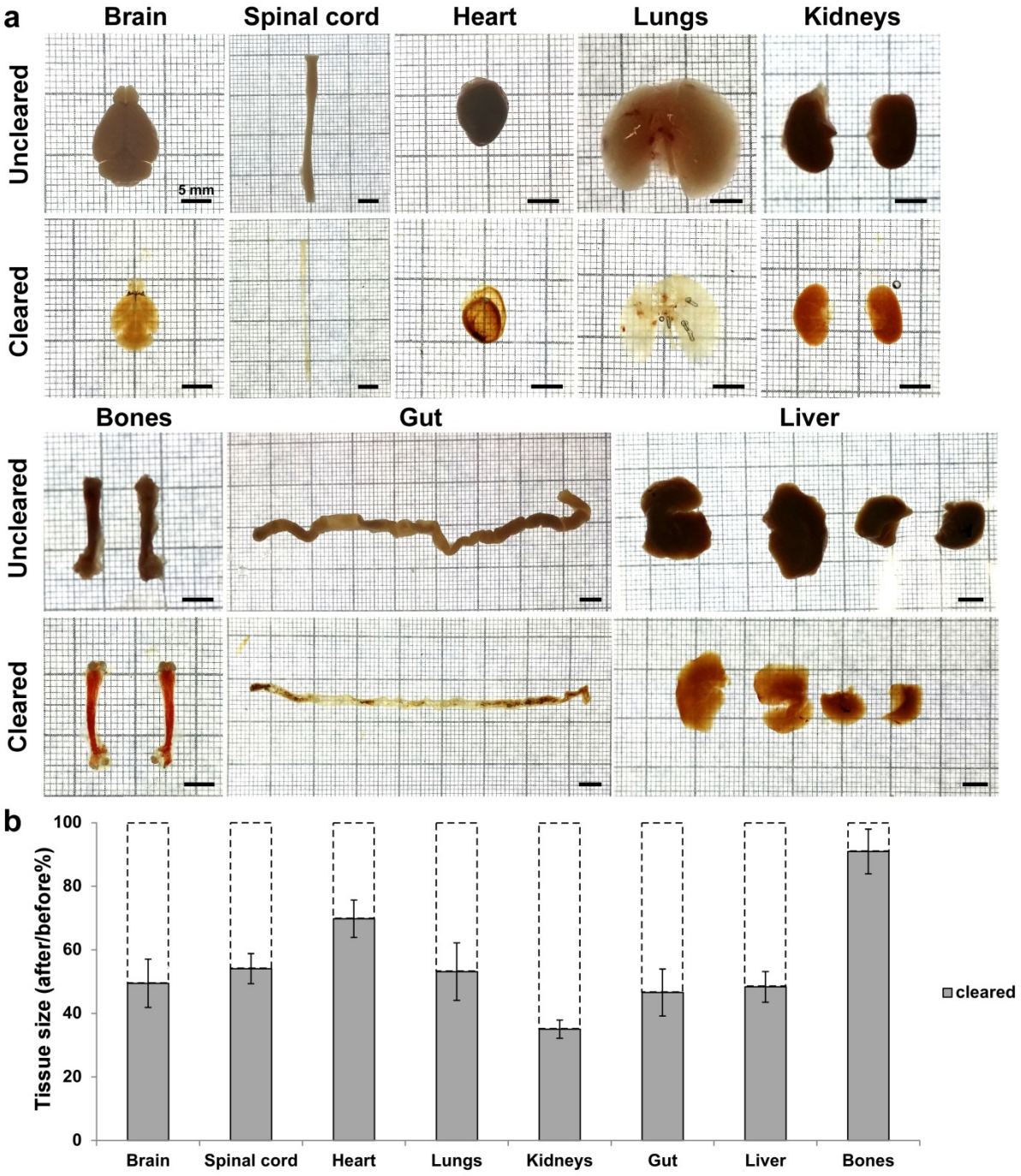

(**a**) Individual organs before and after uDISCO clearing. They became optically transparent after uDISCO clearing. The redness after the clearing is due to the residual blood, which did not impede the imaging of fluorescent structures as shown in Fig. 5 and Supplementary Fig. 22. (**b**) Volume quantifications of individual organs, showing that brain, spinal cord, heart, lungs, kidneys, gut, liver and bones shrank in average 50.54%, 45.92%, 30.22%, 46.85%, 64.94%, 53.44%, 51.76% and 8.08%, respectively. Values are mean ± s.d.; n=4 mice (5 months old) for each organ.

Supplementary Figure 8: uDISCO clearing resulted in similar shrinkage of hard bone and bone marrow

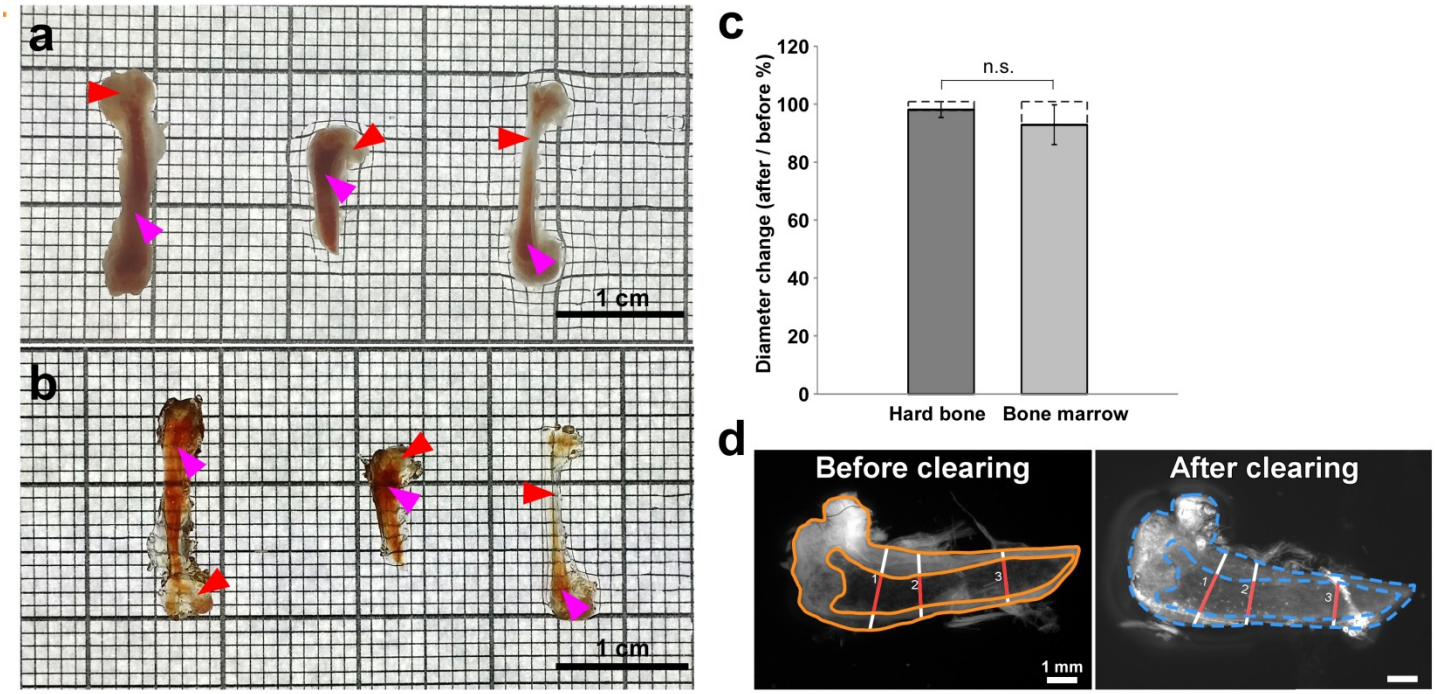

(**a**) Femurs from 6 months old CX3CR1-GFP mice were cut into half for visualization of hard bone (red arrowheads) and bone marrow regions (purple arrowheads). (**b**) Same bones are shown after uDISCO clearing. (**c**) Quantification of diameter change before and after uDISCO clearing: the shrinkage rate was slightly higher for bone marrow regions, even though it did not reach statistical significance (unpaired *t*-test, n.s. = $P > 0.05$). Values are mean ± s.d.; n=3 bones. (**d**) Illustration of how the quantification is performed: 1) the bone images before and after clearing were overlapped with each other, 2) 3 lines were drawn at different positions along the bone, and 3) the diameter change of the same hard bone (white line) and bone marrow (red line) regions were calculated at these three different axes using ImageJ.

Supplementary Figure 9: Different clearing protocols on intact bones: assessment of endogenous GFP signal in CX3CR1-GFP mice

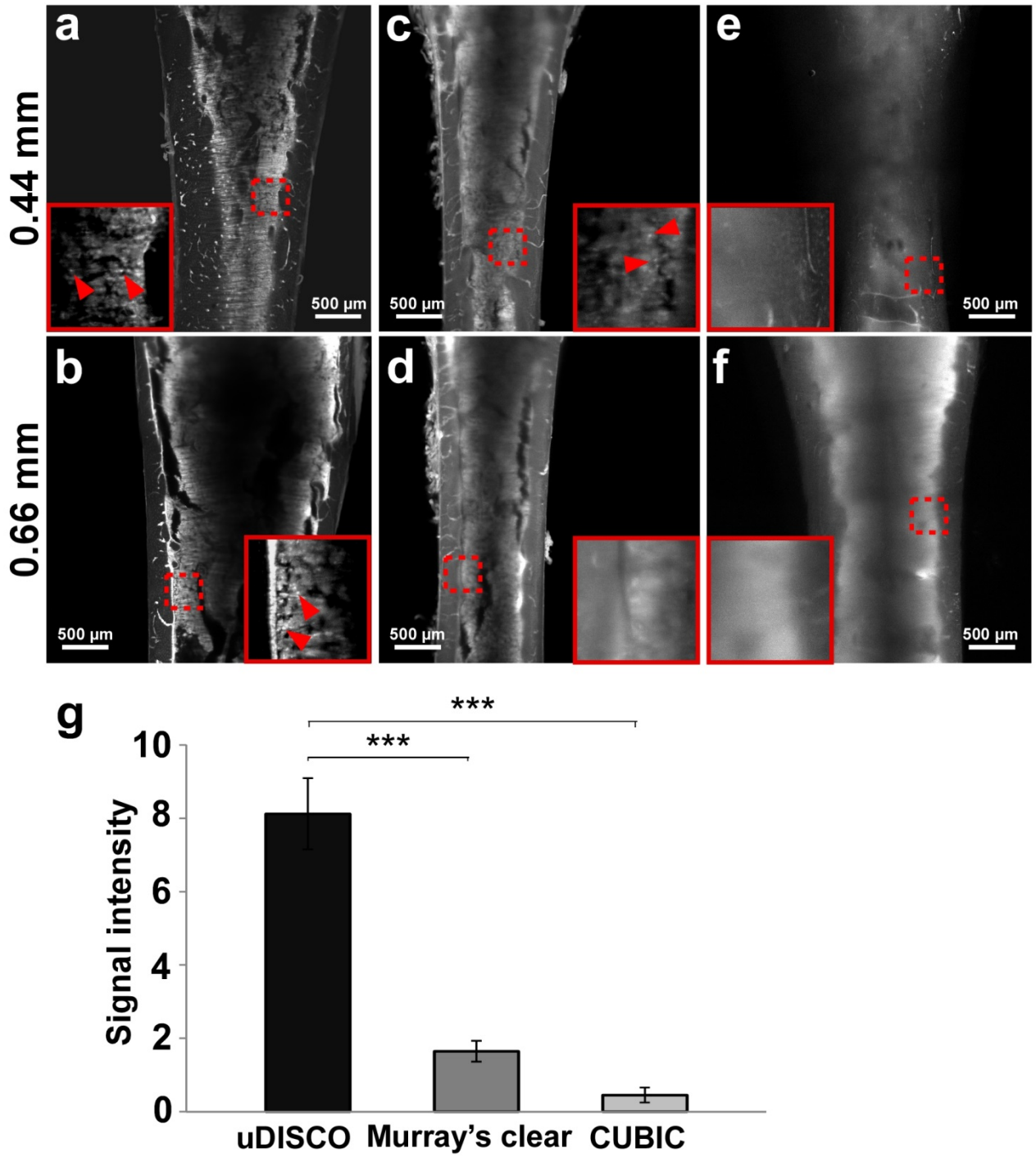

The bones from CX3CR1-GFP transgenic mice were cleared by uDISCO, Murray's clear and CUBIC methods. Maximum intensity projections at 0.4 mm and 0.66 mm depth from the bone surface for uDISCO (**a,b**), Murray's clear (**c,d**), and CUBIC (**e,f**) protocols are shown. (**g**) Quantification of total signal intensity through the bones; statistical significance (***$P < 0.001$) was assessed by one-way ANOVA followed by Dunnett's post-hoc test; values are mean ± s.e.m.; n=8 ROI in uDISCO bones, n=5 ROI in Murray's clear and CUBIC bones (5 months old CX3CR1-GFP mice).

Supplementary Figure 10: Test of IHC with different bone clearing protocols

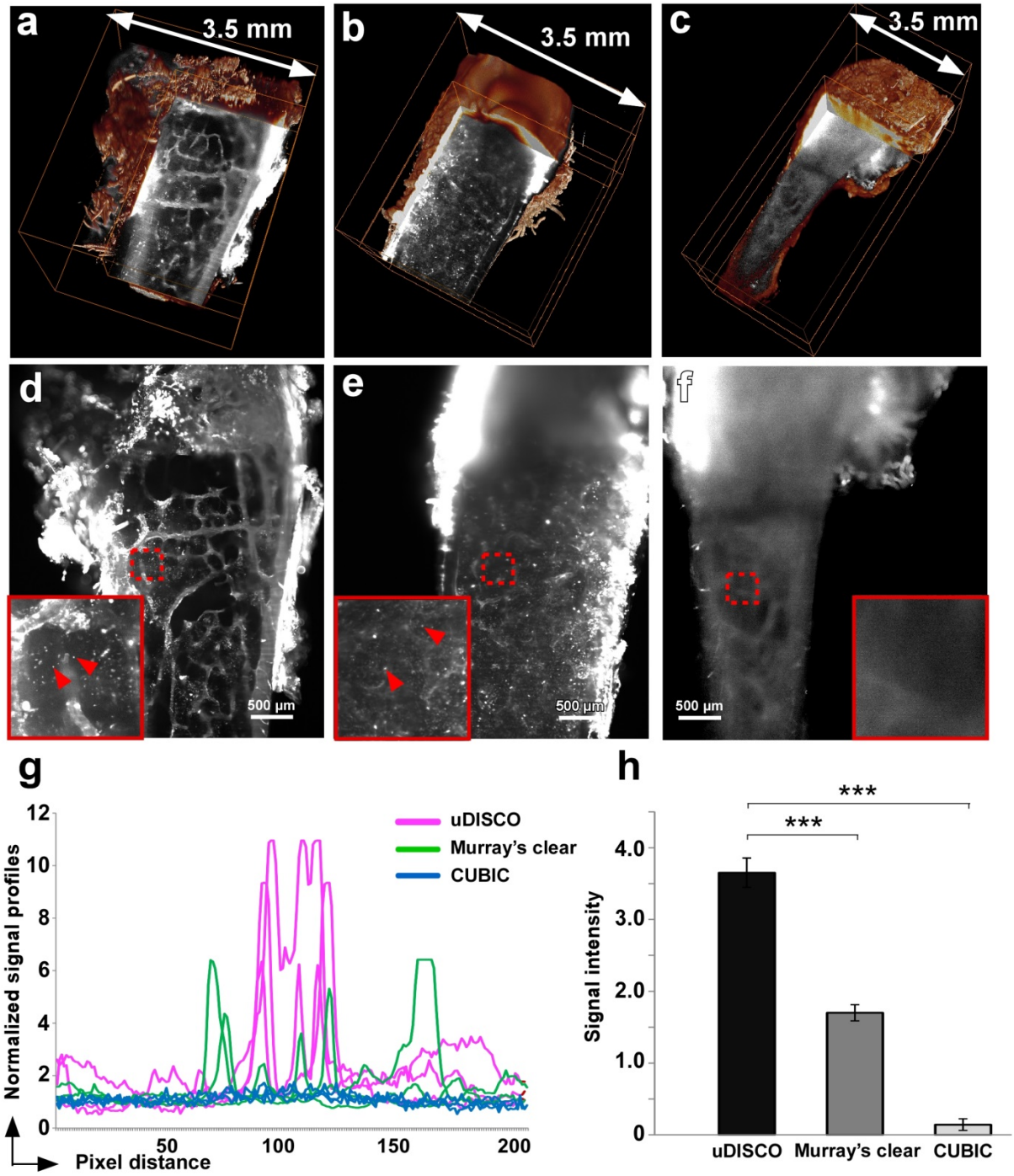

3D reconstruction of CX3CR1-GFP mice bones after (**a**) uDISCO, (**b**) Murray's clear and (**c**) CUBIC clearing. The bones were immunolabeled with AlexaFluor-647 conjugated anti-GFP rabbit polyclonal antibody before clearing. (**d-f**) Projections at 0.66 mm depth (~half-way through the cut bone) showing the signal quality after respective clearing. (**g**) Normalized signal profile plots of AlexaFluor-647 positive cells in uDISCO (magenta line), Murray's clear (green line) and CUBIC (blue line) cleared cut bones. (**h**) Quantification of signal intensity of antibody labeling in the bones after respective clearing. Statistical significance (***P < 0.001) was assessed by one-way ANOVA followed by Dunnett's post-hoc test. Values are mean ± s.e.m.; n=8 ROI in uDISCO and Murray's clear cut bones; n=5 ROI in CUBIC cut bone (5 months old CX3CR1-GFP mice).

Supplementary Figure 11: CUBIC PARS/PACT uDISCO size and imaging comparison

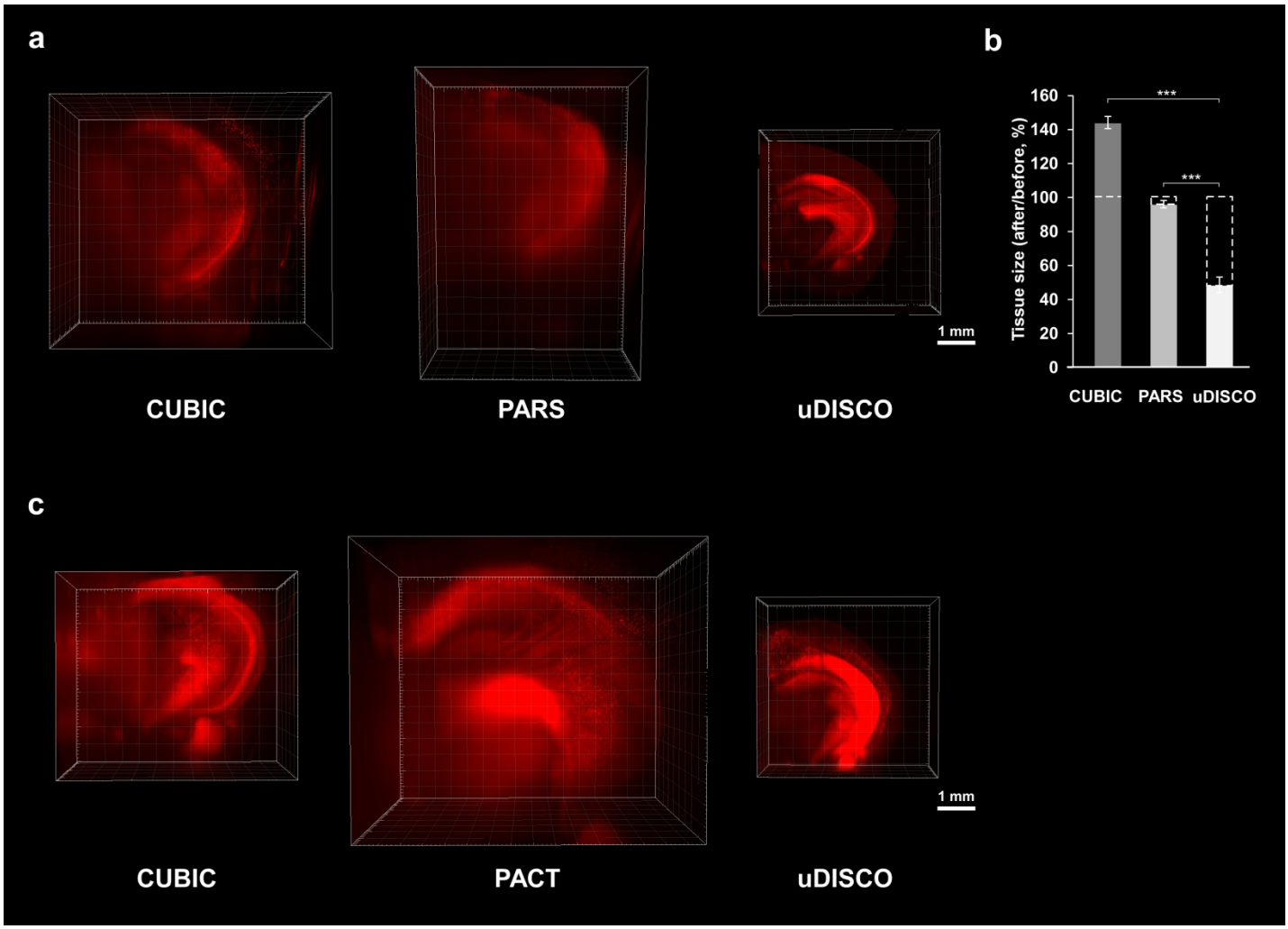

(**a**) 3D reconstruction of brains after CUBIC, PARS and uDISCO whole-body clearing. Imaging depth quantifications on brains in (a) are shown in Fig. 1h. (**b**) Volume changes of brains of 4 months old GFP-M mice after CUBIC, PARS and uDISCO whole-body tissue clearing methods. The final brain volume after uDISCO was significantly lower than after CUBIC and PARS whole-body clearing. Statistical significance (***$P < 0.001$) was assessed by one-way ANOVA followed by Dunnett's post-hoc test. Values are mean ± s.d.; n=4, 3, 3 GFP-M mice for CUBIC, PARS and uDISCO, respectively. (**c**) 3D reconstruction of brains after CUBIC, PACT and uDISCO passive tissue clearing of dissected brains. Imaging depth quantifications on brains in (c) are shown in Fig. 1i. With the same imaging settings at a single scan, more neurons can be imaged with uDISCO (owing to shrinkage) while more detailed structures of individual neurons can be resolved by PACT and CUBIC (owing to expansion) (see also Fig. 1g).

Supplementary Figure 12: Comparison of gross tissue structures before and after uDISCO clearing

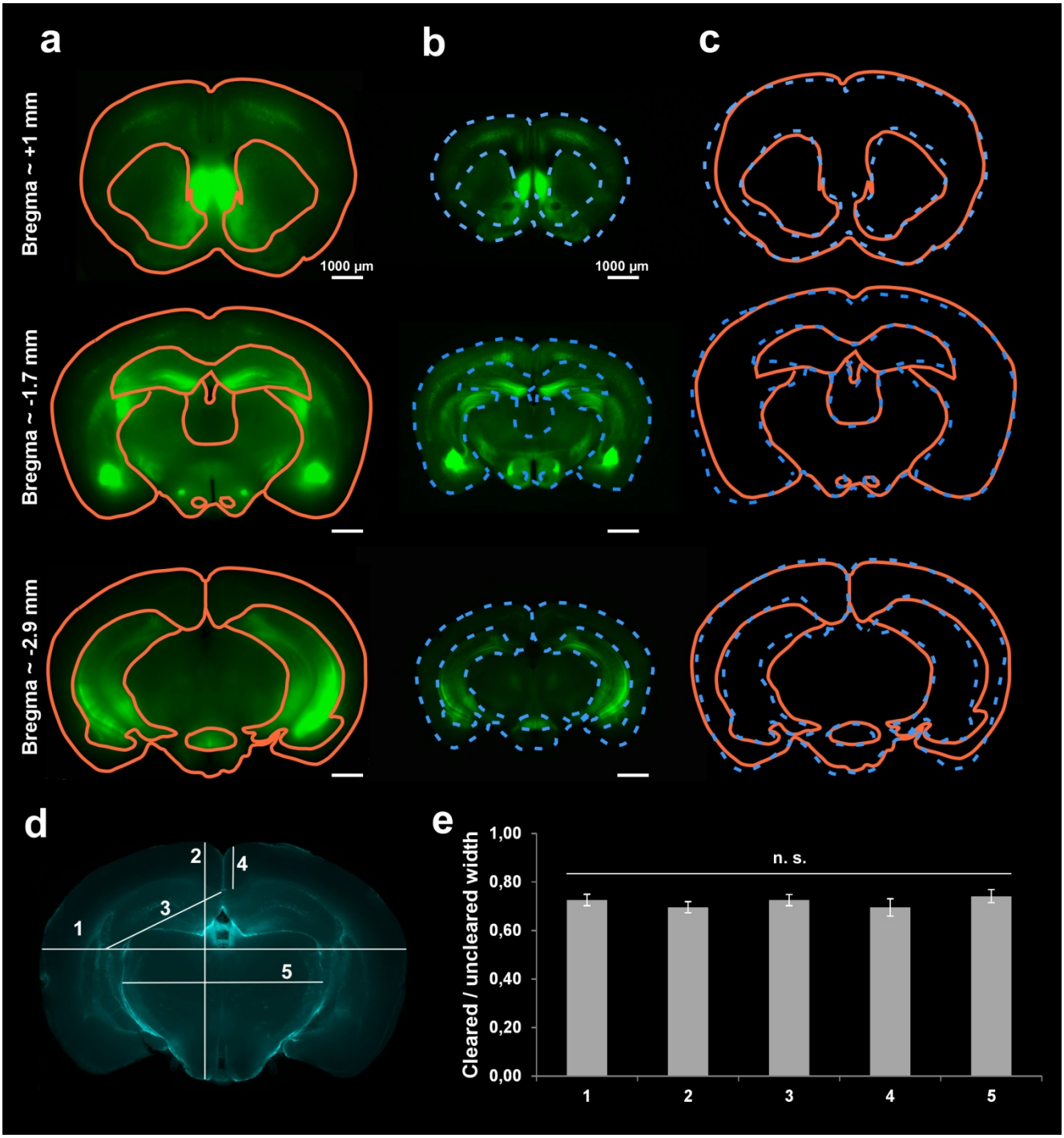

1 mm coronal brains slices from GFP-M mice (5 months old) at different levels were imaged with a fluorescence stereomicroscope before (**a**) and after (**b**) uDISCO clearing. The borders of main structures before and after clearing are highlighted in orange and blue, respectively. (**c**) The overlay of borders by ratio-metric enlargement of shrunken tissue shows a substantial overlap. (**d**) To quantify the proportions of size change on same the slice, we assessed the width of different brain regions (indicated by numbered lines) before and after clearing. (**e**) The quantifications showed that different tissue regions shrank at a similar rate (~30%) in length after clearing (one-way ANOVA, n.s. = $P > 0.05$). Values are mean ± s.d.; n=4, 4, 3, 4, 4 for regions 1, 2, 3, 4, 5, respectively.

Supplementary Figure 13: Microscale changes of different cells and tissues before and after uDISCO clearing

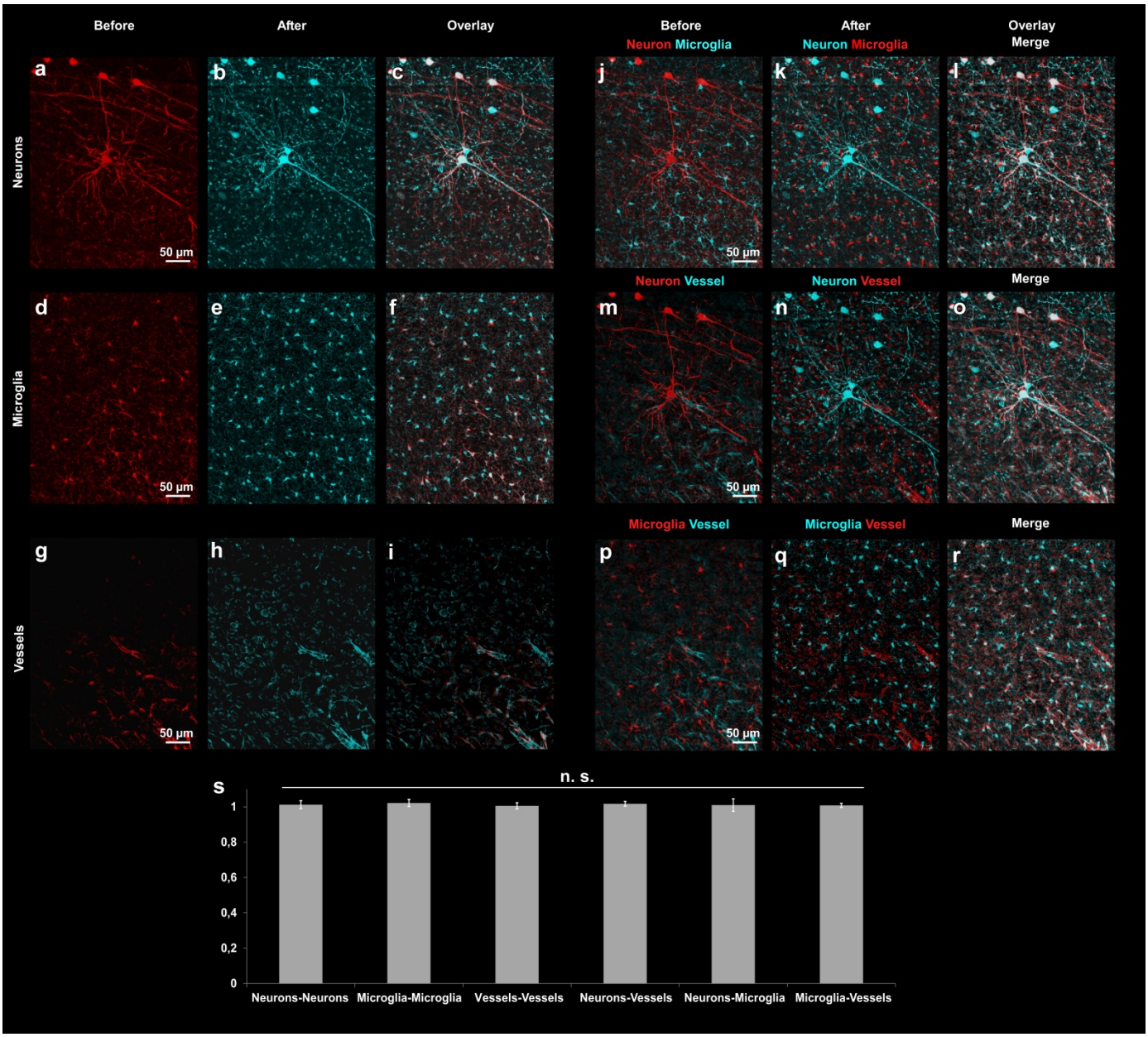

To assess the uniformity of shrinkage on different types of cells and tissues, we measured shrinkage of neurons, microglia and vessels with respect to each other. To this end, we immunolabeled 1 mm thick GFP-M brain slices (from 2 months old mice) with Iba1 (microglia) and Collagen4 (vessels) and acquired confocal images before and after uDISCO clearing. (**a-i**) Single channel views from the same tissue location containing neurons (**a-c**), microglia (**d-f**) and vessels (**g-i**). Overlay channels show a substantial overlap of before and after images. (**j-r**) Double channel views from the same tissue location demonstrating neurons-microglia (**j-l**), neurons-vessels (**m-o**) and microglia-vessels (**p-r**) together. To simplify the interpretation of overlay channels, we used only two colors (red and cyan) and swapped the colors before and after clearing channels, resulting in white color for overlay of tissue components. (**s**) The distances between neurons-neurons, microglia-microglia, vessels-vessels, neurons-microglia, neurons-vessels and microglia-vessels were measured before and after uDISCO and normalized to the rate of gross shrinkage of the slice (n=7 per each tissue structure/cell type from at least 3 different slices). The quantification showed that the relative distances between the structures and cells were not significantly changed after clearing (one-way ANOVA, n.s. = $P > 0.05$). Values are mean ± s.d.

Supplementary Figure 14: Comparison of single cells and vessels before and after uDISCO clearing

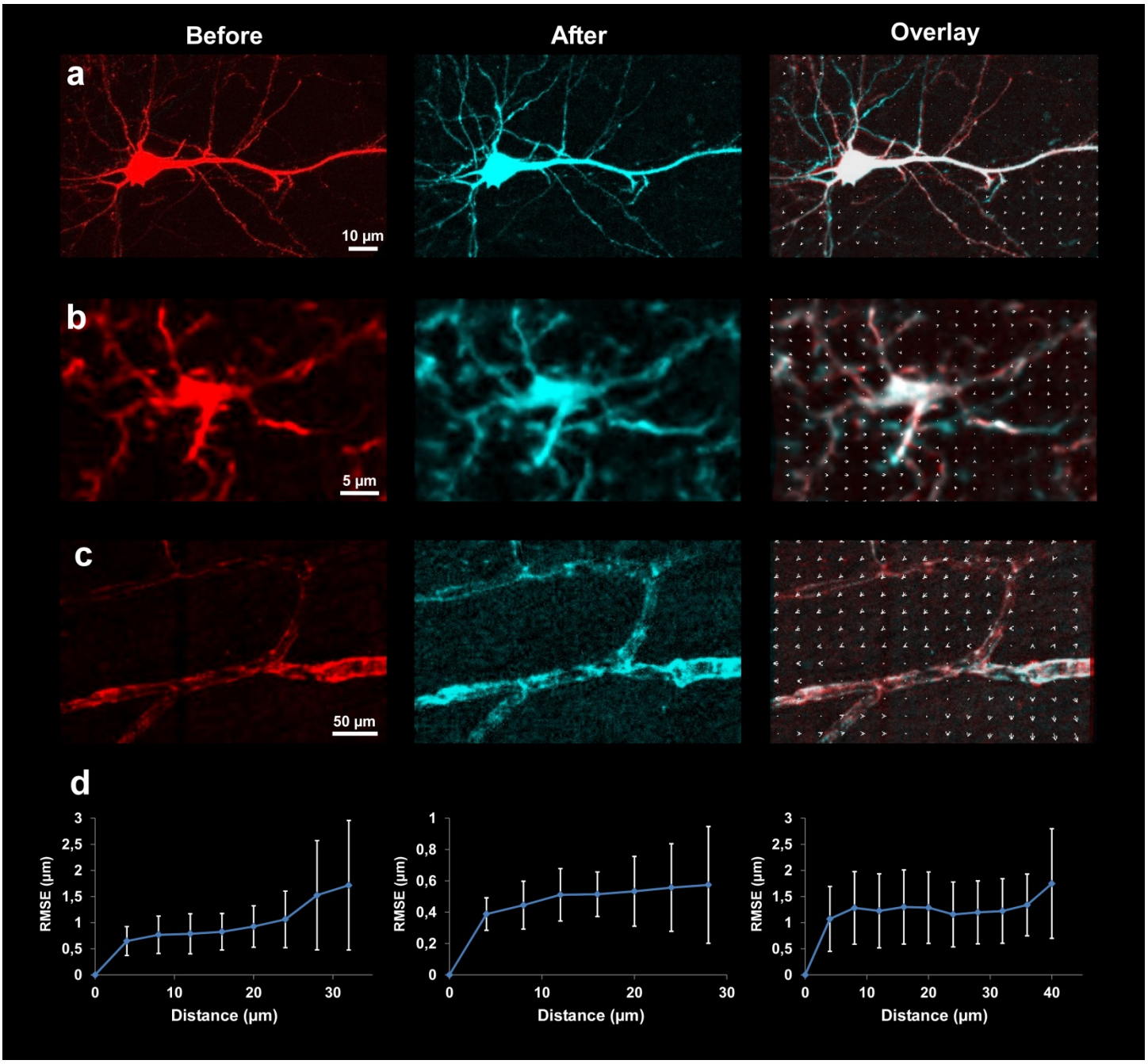

Confocal images of 1 mm coronal brains slices from GFP-M mouse (2 months old) before and after uDISCO clearing, showing individual neurons (**a**), Iba1 stained microglia (**b**), and Collagen4 stained vessels (**c**). The overlay after ratiometric enlargement of shrunken cells and vessels shows a substantial overlap suggesting that individual cell morphology is preserved after uDISCO clearing. Note that more structures are visible after clearing (cyan in "after" and "overlay" images). (**d**) Quantifications of RMSE to evaluate the degree of morphological deformations for neurons (left), microglia (middle) and vessels (right). After defining a center of a cell or a structure as the constant point, displacements of cellular and vascular structures before and after clearing have been plotted with regular intervals from the center point. The degree and direction of regional deformations are shown with arrows in overlay images ($n \geq 6$ cells from at least 3 different slices and $n \geq 3$ vessel structures from at least 3 different slices). Values are mean ± s.e.m.

Supplementary Figure 15: Details of light-sheet microscope and sample holders for whole mouse body imaging

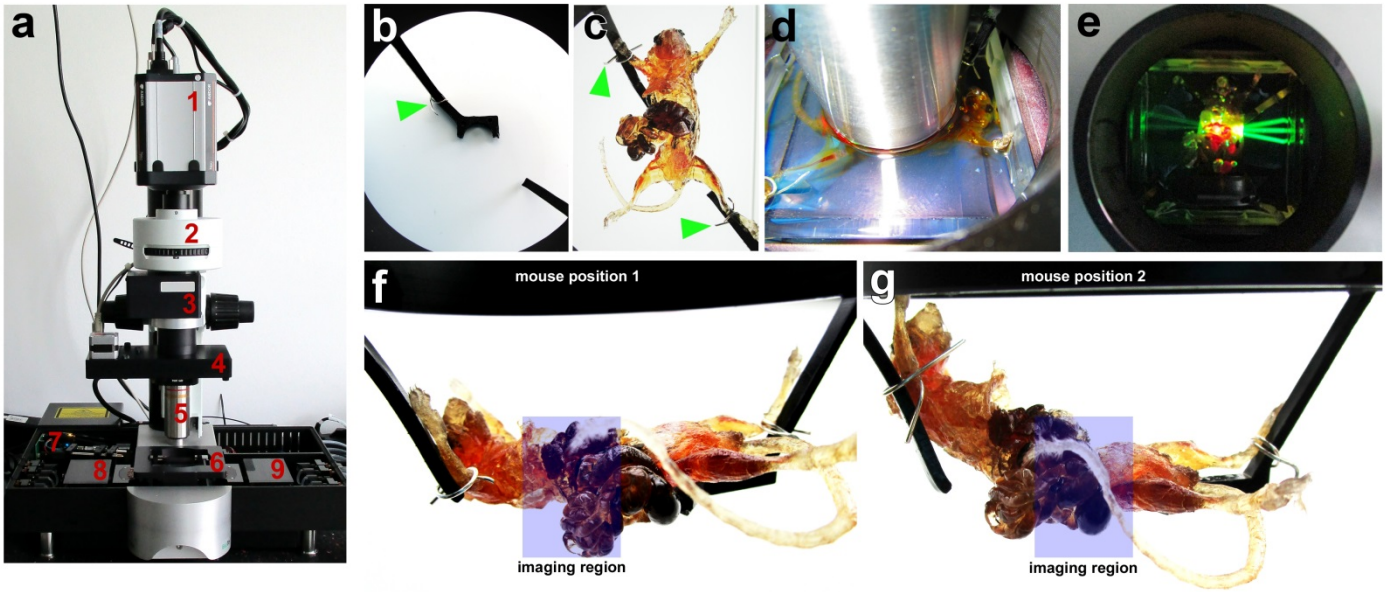

(**a**) LaVision Biotec light-sheet ultramicroscope featuring: (1) Andor Neo 5.5 sCMOS camera; (2) Olympus U-TVCAC revolving zoom unit enabling 1x, 2x, 4x additional magnification with a fourth slot for a shutter plate; (3) LaVision autofocusing unit for automatic focus correction at different wavelengths; (4) filter box with 8 slots for 25 mm mounted filters; (5) BABB corrected Olympus objective; (6) imaging chamber, where LaVision Biotec suspension trays for sample holders are placed; (7) fiber coupled laser outlet for supercontinuum laser (SuperK EXTREME EXW 9 - 450-1000); (8-9) beam profile generation units. (**b**) Half of the central part of the commercial sample holder suspension (LaVision Biotec) is cut to make space, which allows flexible positioning of the mouse body at the center of the imaging beam. Silver plated copper wires are used to secure the mouse (**c**) to the branches of the suspension by its fore- and hind-limb (green arrowheads). (**d**) View of cleared adult mouse body immersed in the imaging chamber. Note that there is a large space left from the sleek immersion objective (Olympus air immersion corrected for RI 1.56), which facilitates the repositioning of the mouse in the chamber. (**e**) Demonstration of laser light sheets crossing the cleared mouse body. After imaging a region (**f**), the mouse is repositioned (**g**) so that next body part is now in the center of imaging area (purple rectangles).

Supplementary Figure 16: Details of customized sample holders for individual brain and other organs

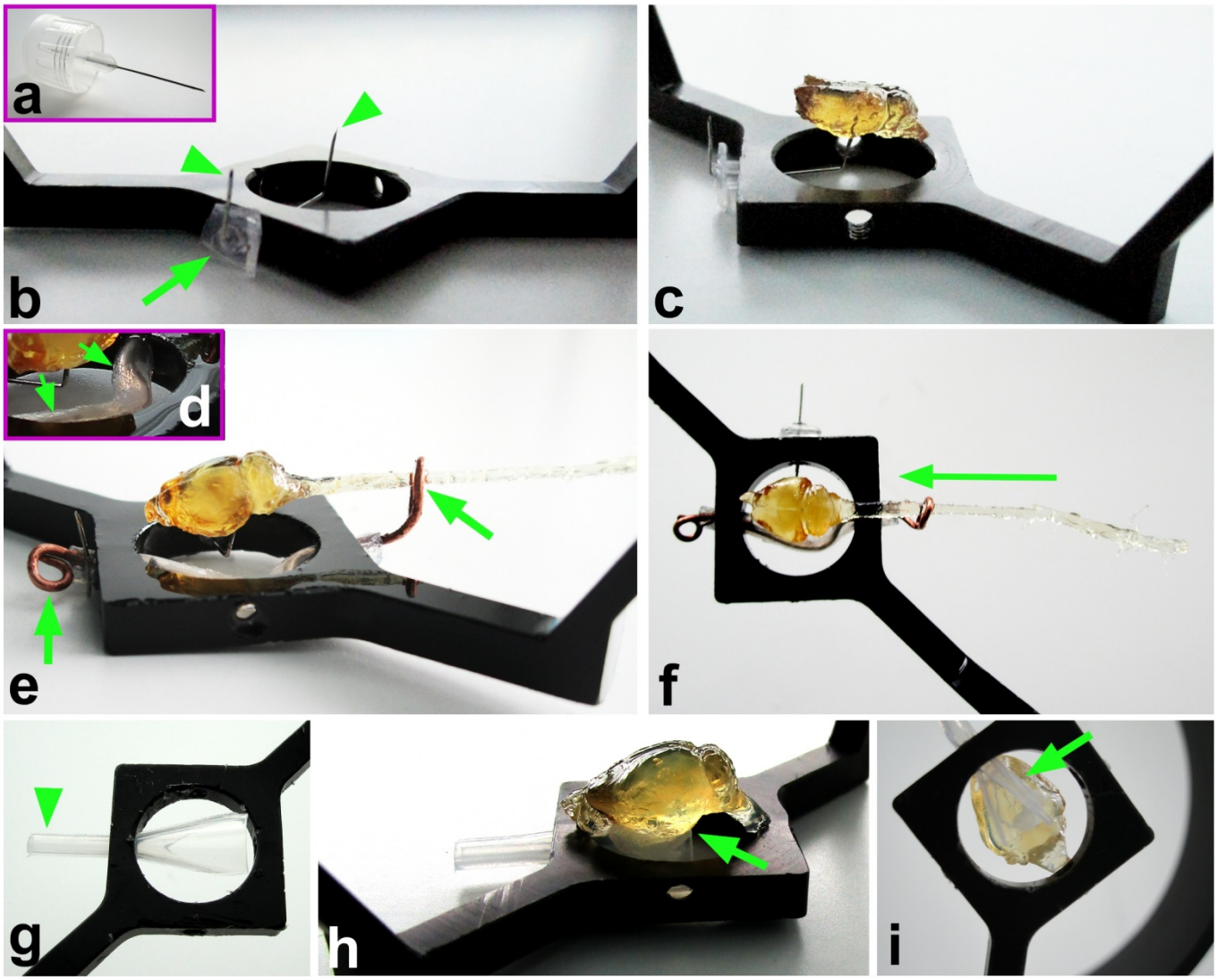

(**a**) To allow maximum flexibility, we used 0.33 mm thick fine needles (BD Micro-Fine Ultra, 325118) in combination with commercially available sample suspension (Lavision Biotec). The plastic cup is trimmed (**b**, arrow) to avoid contact with the bottom of the imaging chamber. The needle is inserted into the hole of sample holder and bent as shown (**b**, arrowheads). (**c**) An example of an uDISCO-cleared brain secured to the fine needle: the resinous consistency of uDISCO cleared brains allows a clean piercing that is not visible in the sample once imaged, owing to the multiple sheets coming from different angles and compensating for cast shadows. (**d-f**) Variation of customized sample holders for long specimens, such as entire CNS (brain and spinal cord together). To this end, in addition to the fine needle holding the brain, we used a cooper wire to stabilize the long spinal cord. The copper wire is prepared as follows: first, we inserted it into a Pasteur pipette tube (**d**, arrowheads) and into the hole of suspension. Finally, we looped the ends as shown (e, arrows). The brain is imaged first while the spinal cord lies in a loop of the wire to keep it at a suitable height. After imaging, the sample is swept along its axis (**f**, arrow), so that a different part of the unsectioned CNS can be imaged, until completion. (**g-i**) Customized sample holders for specimen clarified with water-based clearing methods. If the samples have jelly-like textures, they cannot be held in place with fine needles. Instead, we trimmed a plastic Pasteur pipette as shown (**g**, arrowhead) and glued the specimens on top (**h,i**, arrows). A mounted CUBIC brain is shown from the side (**h**) and bottom (**i**).

Supplementary Figure 17: 10 mm depth z-scan across rodent body parts after uDISCO clearing

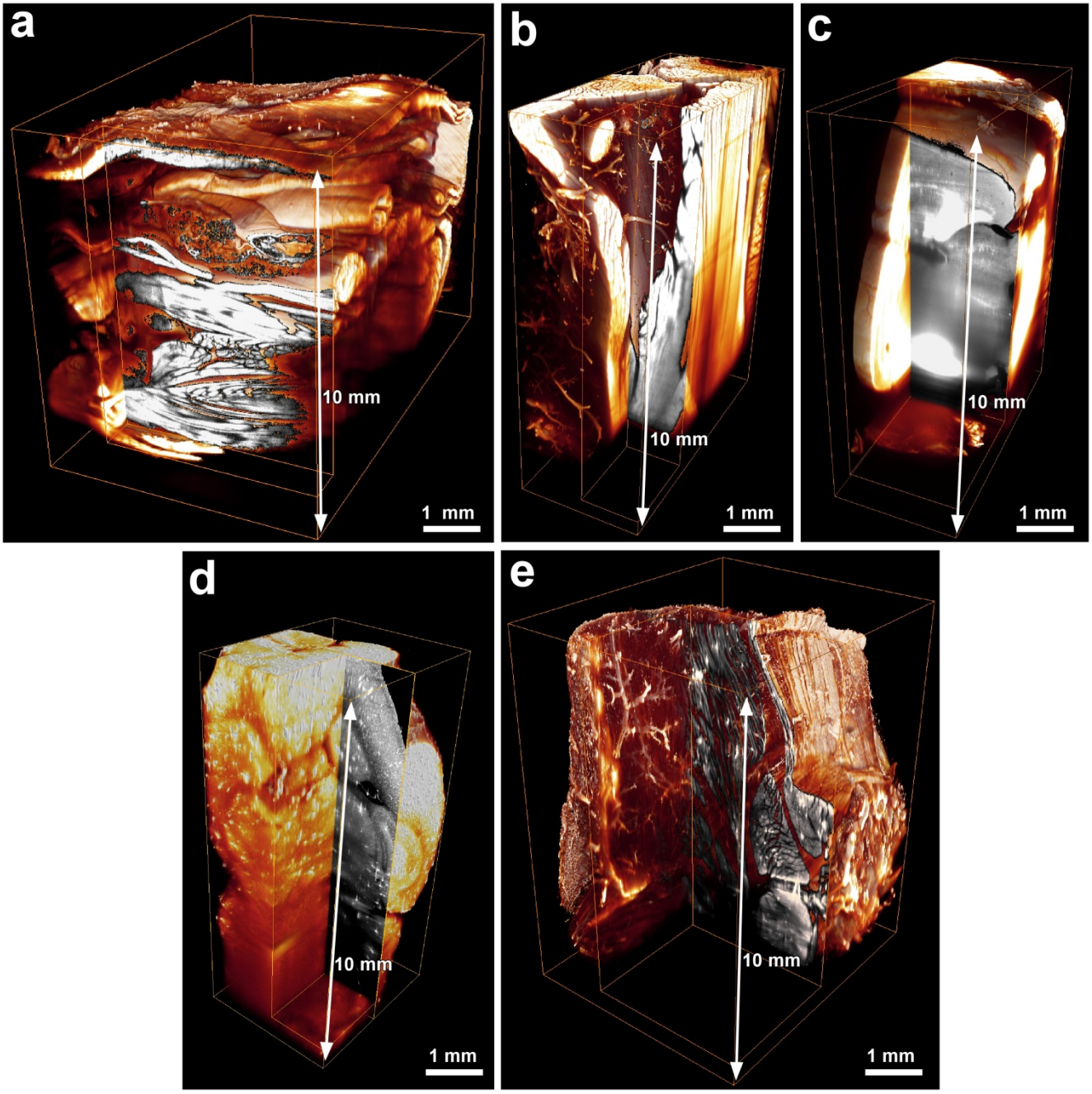

3D Volren surface reconstructions (red-orange) of 10 mm z-scans obtained by light-sheet microscopy. An ortho-slice (black-white) is shown in the corner-cut view (Amira software) to demonstrate the details throughout the scans. (**a-c**) Different body parts of the whole-body light-sheet microscopy scanned mouse in Fig. 2d: the pelvic area (**a**), hindlimb (**b**) and the head (**c**); voxel size: 1.625 x 1.625 x 6 µm. (**d**) A 10 mm z-scan through vasculature labeled (FITC-lectin) mouse brain; voxel size: 1.625 x 1.625 x 4 μm^3. (**e**) 10 mm z-scan through the shoulder of a vasculature labeled (Texas Red) adult rat. Vessels and fine structure are well defined.

Supplementary Figure 18: Rat organs after uDISCO clearing

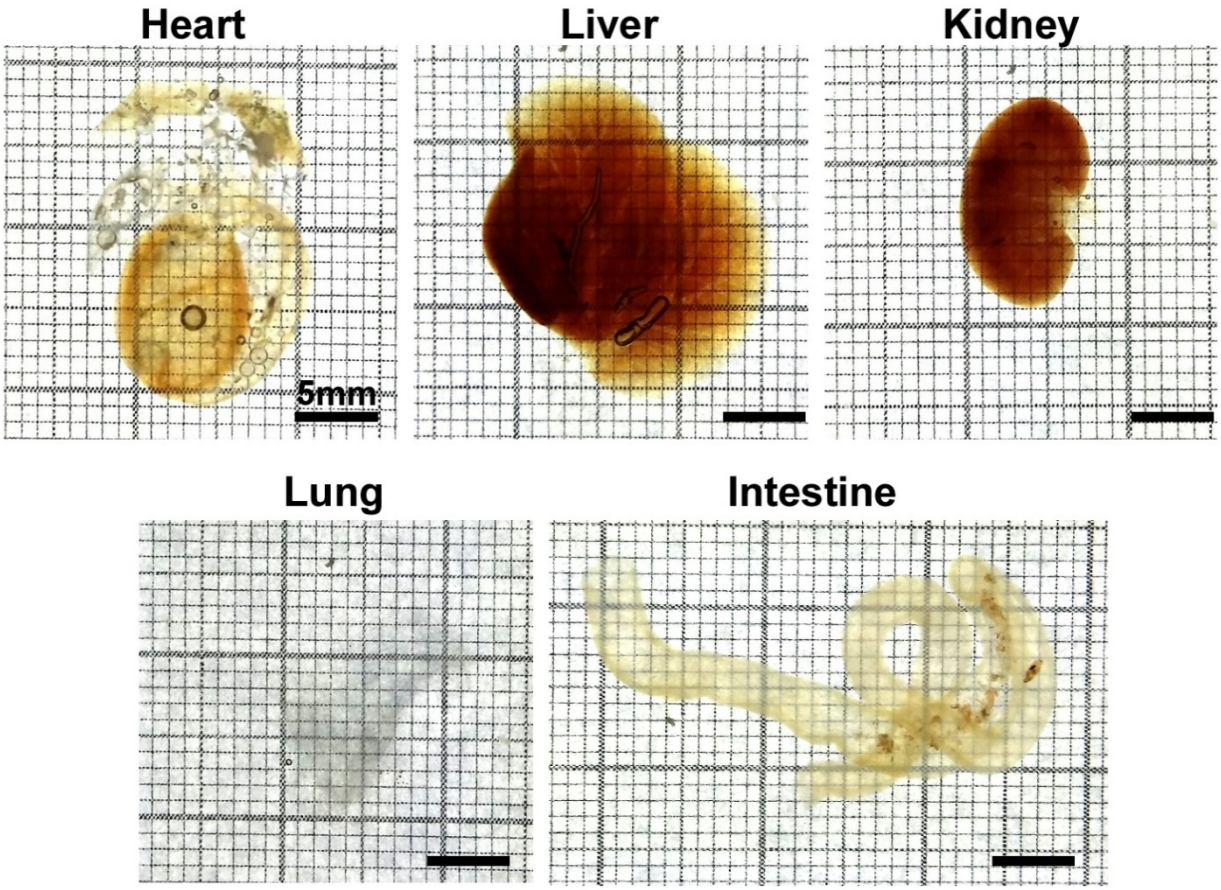

Grid images of individual organs from rat after whole-body uDISCO clearing, showing that the heart, liver, kidney, lung and intestine were rendered optically transparent. The redness after the clearing in liver and kidney images is due to the residual blood.

Supplementary Figure 19: BMSCs characterization

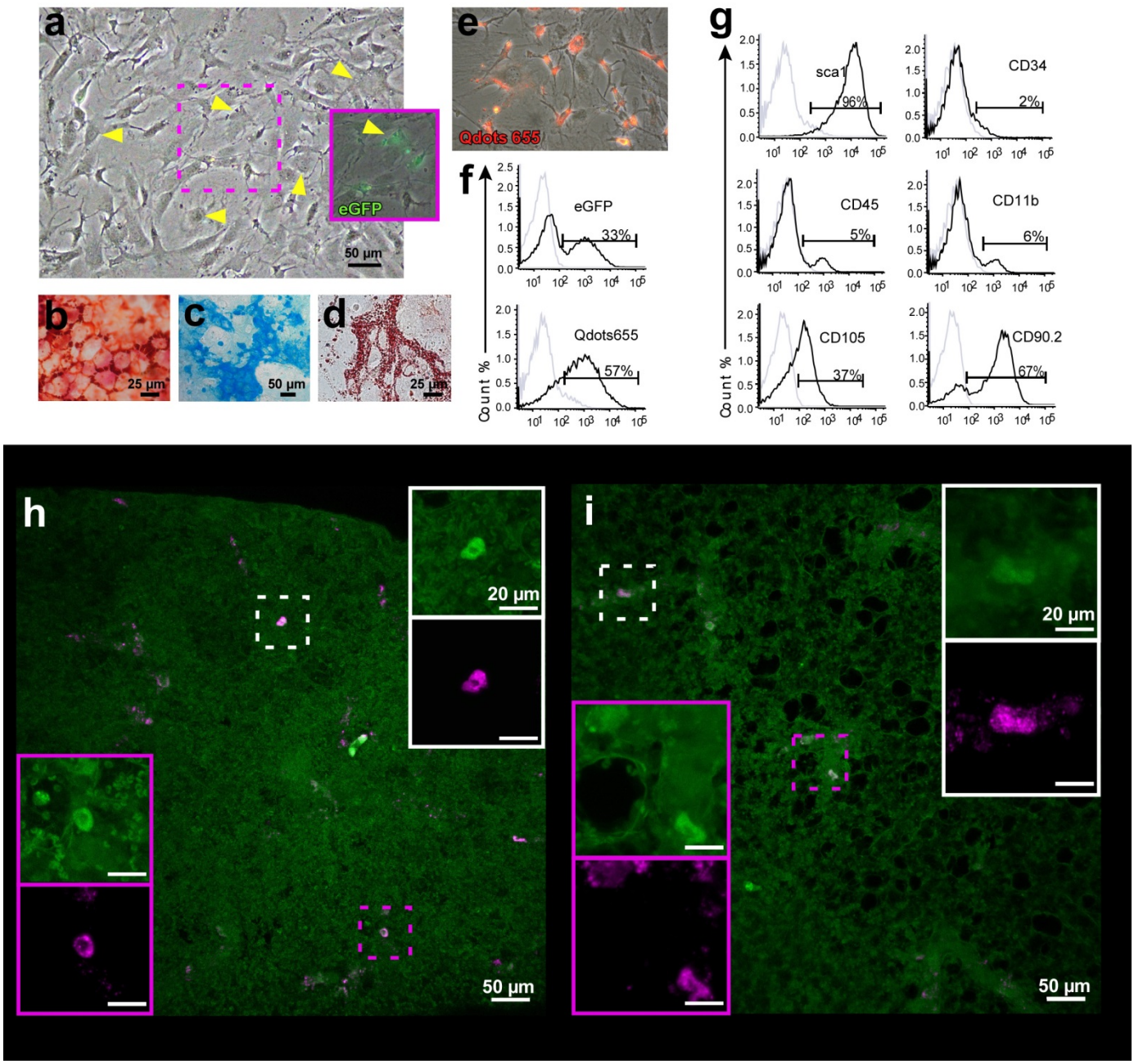

Characterization of β-actin EGFP BMSCs loaded with Qdots. (**a**) Representative picture of BMSCs (passage 4-5) that were harvested for IV transplantation (arrowheads mark some of the BMSCs). The purple insert shows the EGFP+ cells (superimposed image of wide-field and GFP channels). (**b-d**) The osteogenic (**b**), chondrogenic (**c**) and adipogenic (**d**) potential of the BMSCs confirms their mesenchymal origin. (**e**) BMSCs loaded with Qdots, shown as red cytoplasmic aggregates (superimposed image of wide-field and Qdot channels). (**f**) FACS characterization of the EGFP+ and Qdot+ BMSCs before their harvest for transplantation. (**g**) BMSCs were sca1+, CD34-, CD45- and CD11b- while expressing medium levels of CD105 and CD90.2 as characterized by FACS; the population only contained a small fracture of CD11b+ and CD45+ monocytes, as expected. (**h,i**) Colocalization of GFP and Qdot signals in cleared lungs from animals injected with BMSCs, imaged by confocal microscopy. White and magenta rectangles show high-magnification single channel images (EGFP (green), Qdot (magenta)) of dashed marked regions in the same images.

Supplementary Figure 20: Whole-body clearing and imaging of mouse after BMSCs transplantation

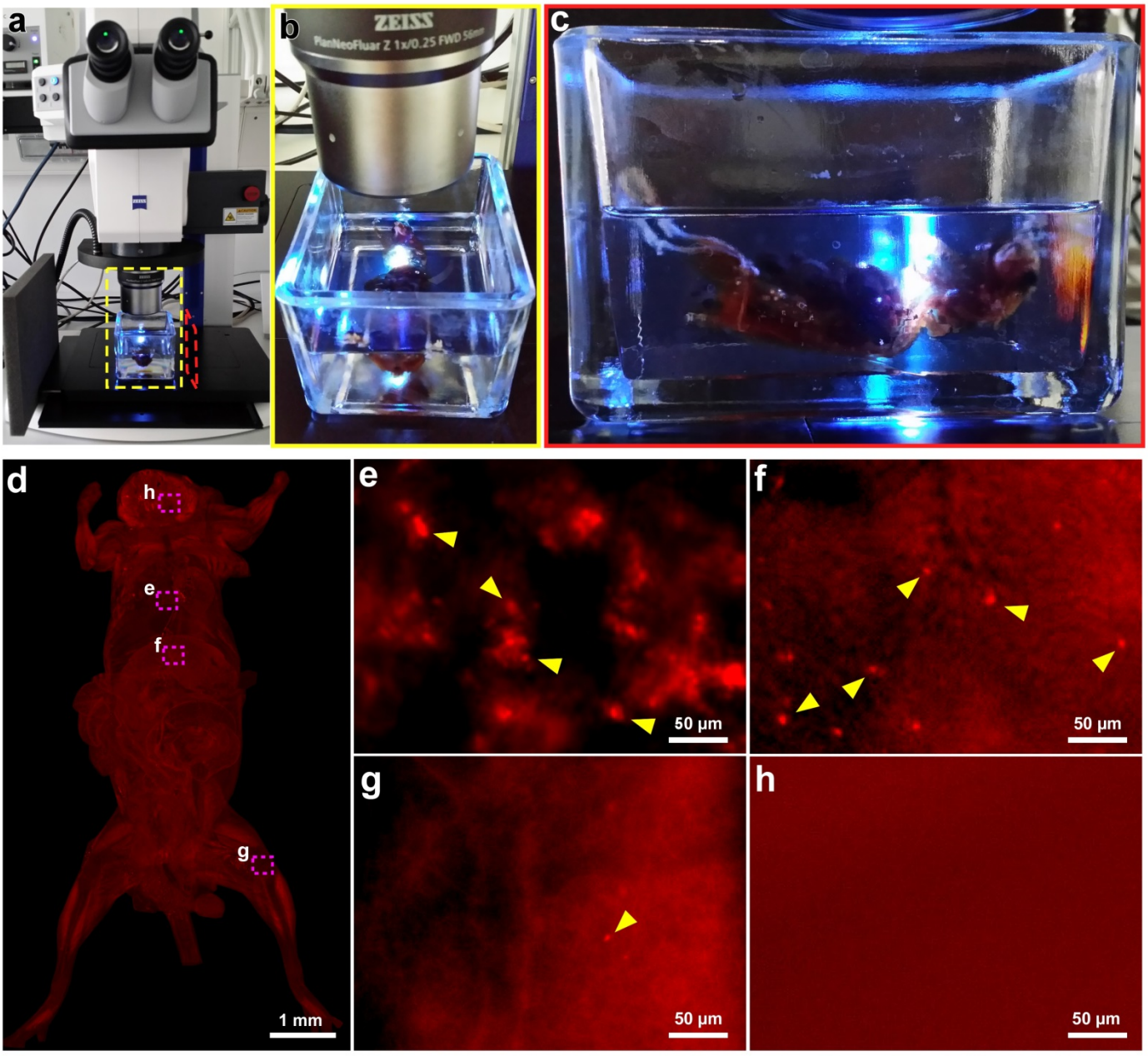

BMSCs were collected and labeled with Qdots, then transplanted into 2 months old C57BL/6N mice through IV injection. The mice were transcardially perfused and cleared with uDISCO. The intact mouse bodies could readily be screened by fluorescent stereomicroscope (**a-c**). (**d**) Whole-body stereomicroscope imaging of intact host mouse body. The individual cells were identifiable throughout the body, e.g. in the lung (**e**), liver (**f**) and bone marrow (**g**). No BMSCs were detected in the brain as expected (**h**).

Supplementary Figure 21: 3D reconstruction of internal organs from intact mouse transplanted with Qdot labeled BMSCs

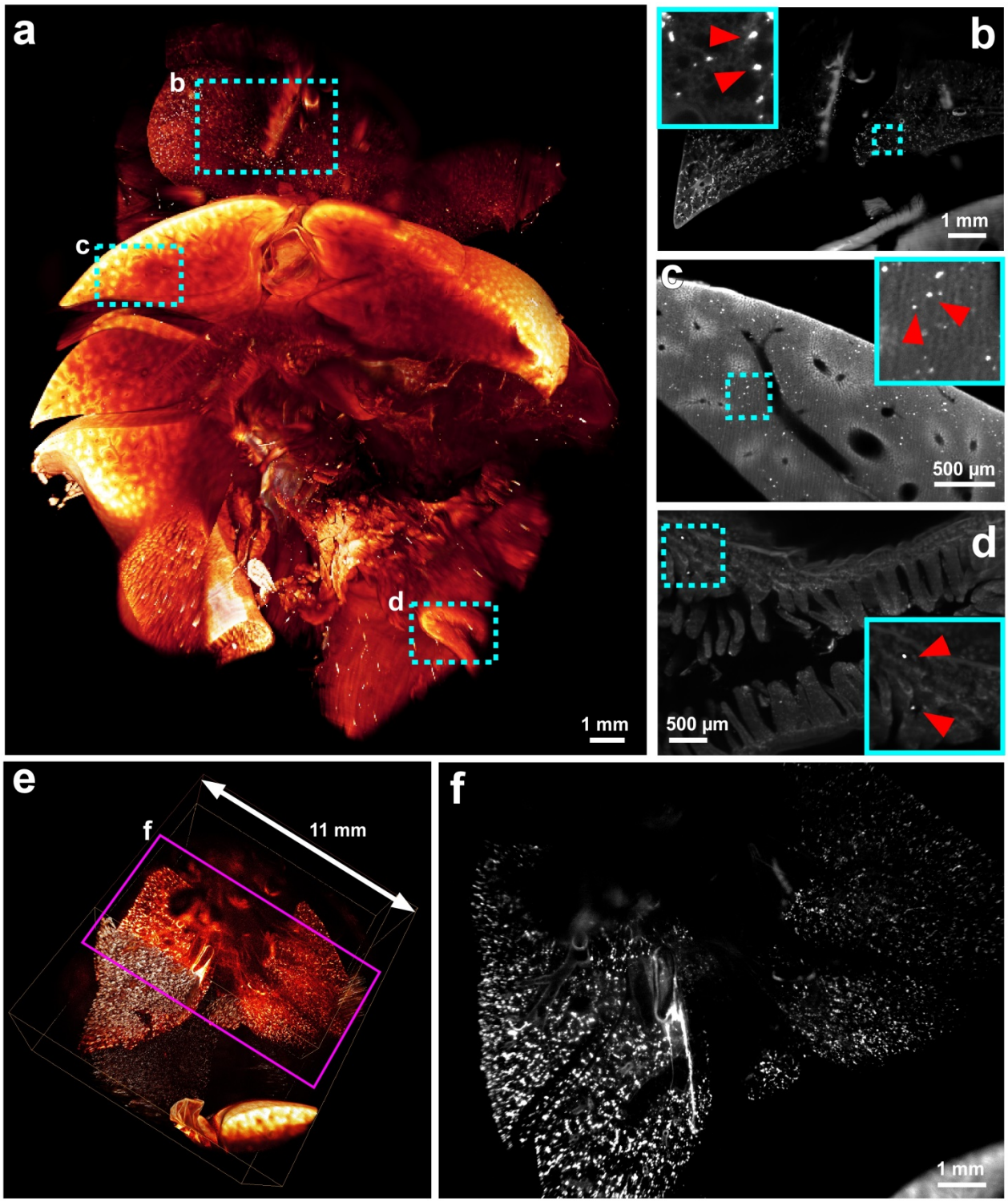

Light-sheet microscopy images from intact mice, which were transplanted with Qdot loaded BMSCs. (**a**) Lungs, liver layers, right kidney and part of the intestine shown in 3D surface rendering view. (**b-d**) The projection images of regions marked in (a): lung (**b**), upper liver layer (**c**) and intestine (**d**). (**e**) 3D surface reconstruction of lungs from another mouse. (**f**) The projection image of region marked in (e).

Supplementary Figure 22: Distribution of mouse BMSCs in kidney, spleen and intestine

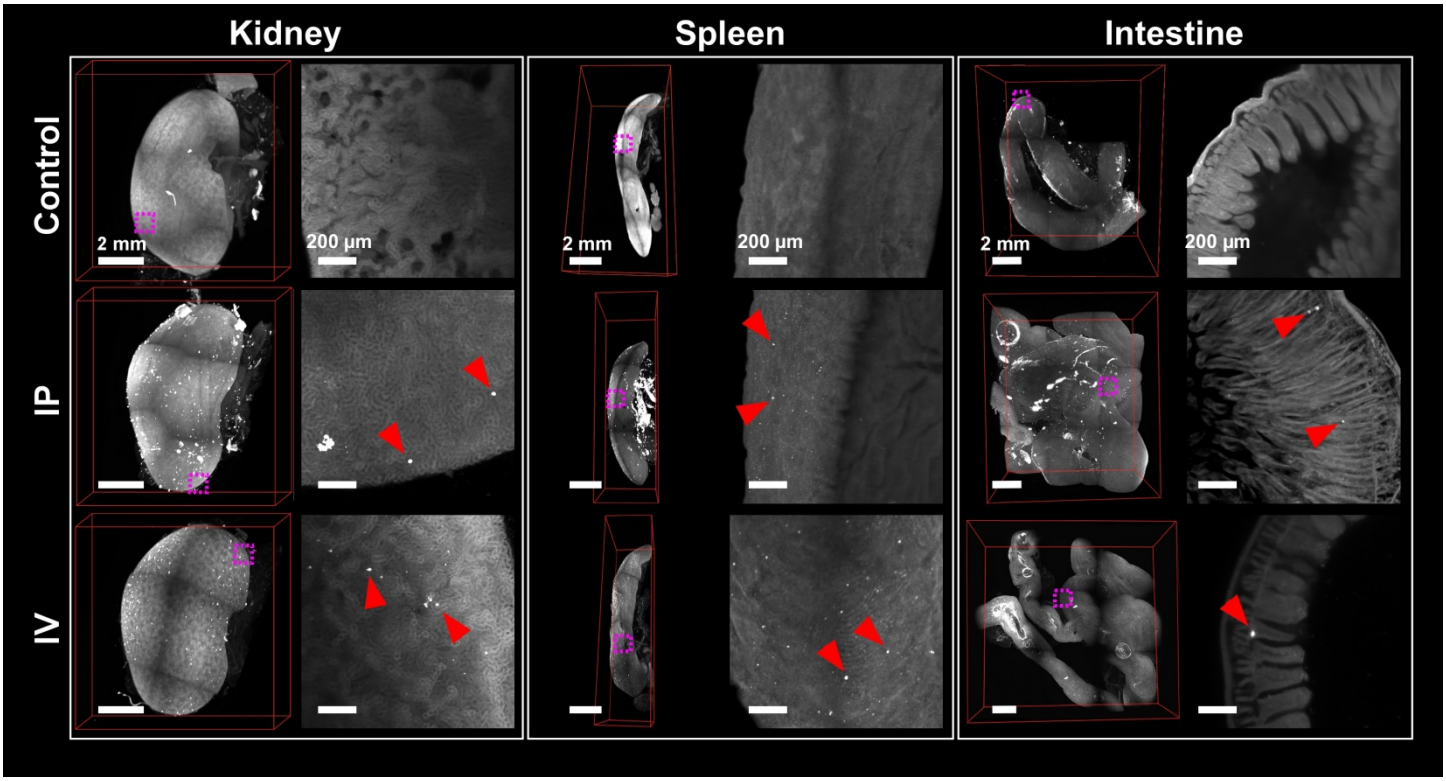

Images of kidney, spleen and intestine from host mice in control, IP and IV groups. We found a sparse distribution of Qdot positive BMSCs throughout the kidney, spleen and intestine in both IP and IV groups

Supplementary Figure 23: AVV tracing of whole adult mouse CNS

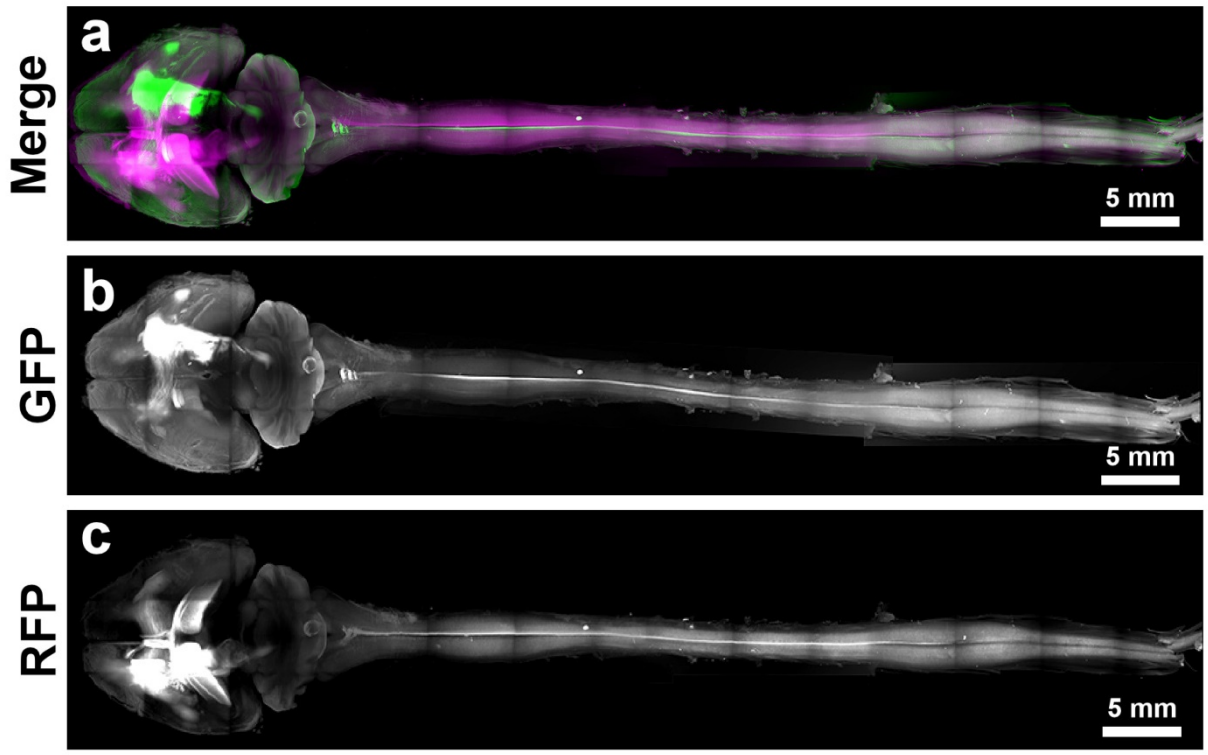

Individual channels of traced adult mouse CNS (**a**) shown in Fig. 6. AAV-syn-GFP signal in the entire CNS is shown in (**b**), AAV-syn-RFP signal in (**c**).

Supplementary Figure 24: Microglia/macrophage IHC on mouse brain

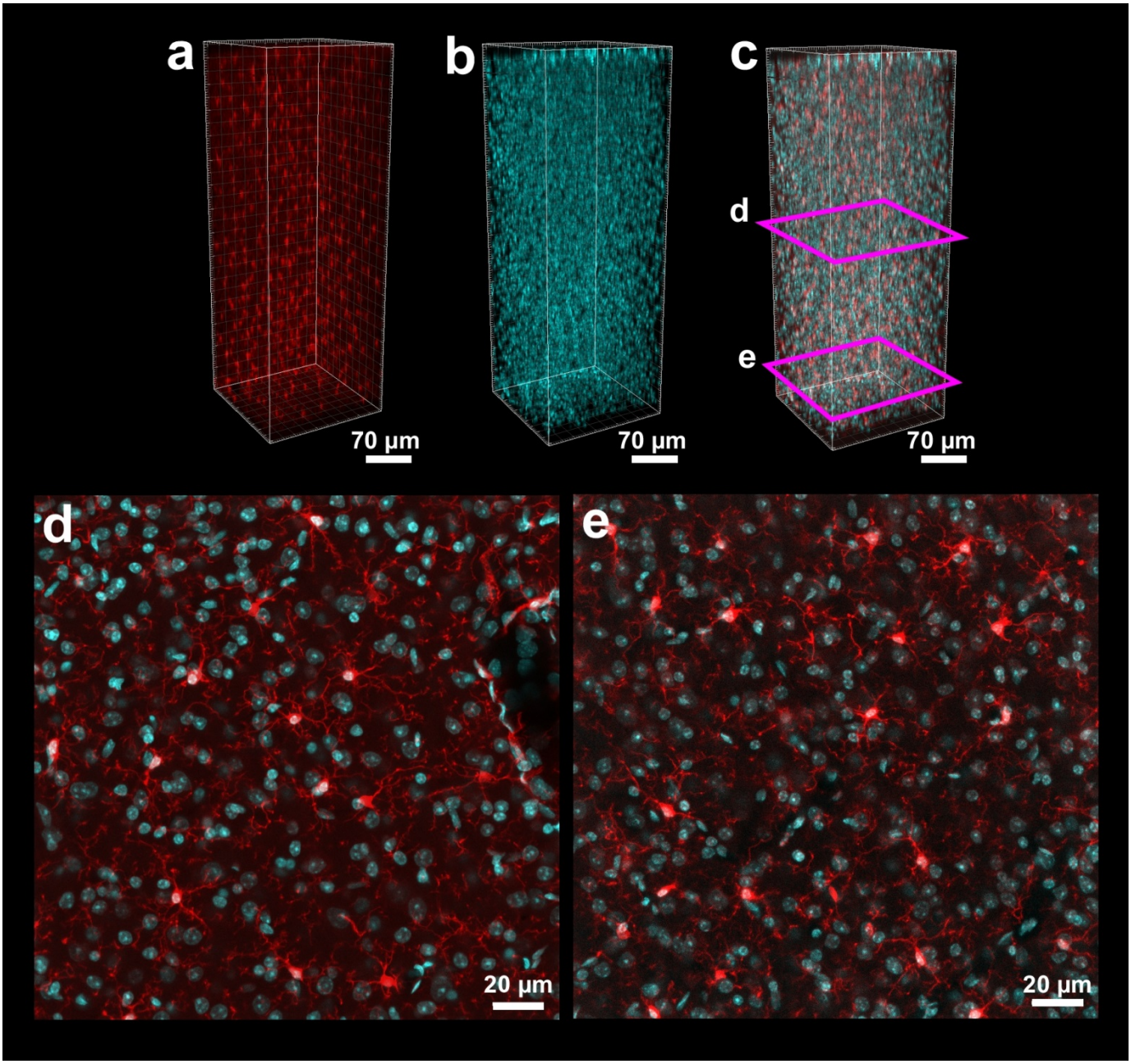

Iba1 and TO-PRO-3 labeling of coronal sections from the cortex of 4 months old mouse brain. (**a-c**) 3D reconstructions showing the homogeneous labeling of microglia and cell nuclei stained with Iba1 antibody (**a**) and TO-PRO-3 (**b**) and their merge (**c**). (**d,e**) Maximum intensity projections of the z-positions marked by purple boxes in (c); microglia are shown in red and TO-PRO-3 staining in cyan.

Supplementary Figure 25: Microglia/macrophage IHC on short and long-term formalin-fixed human clinical tissue slices

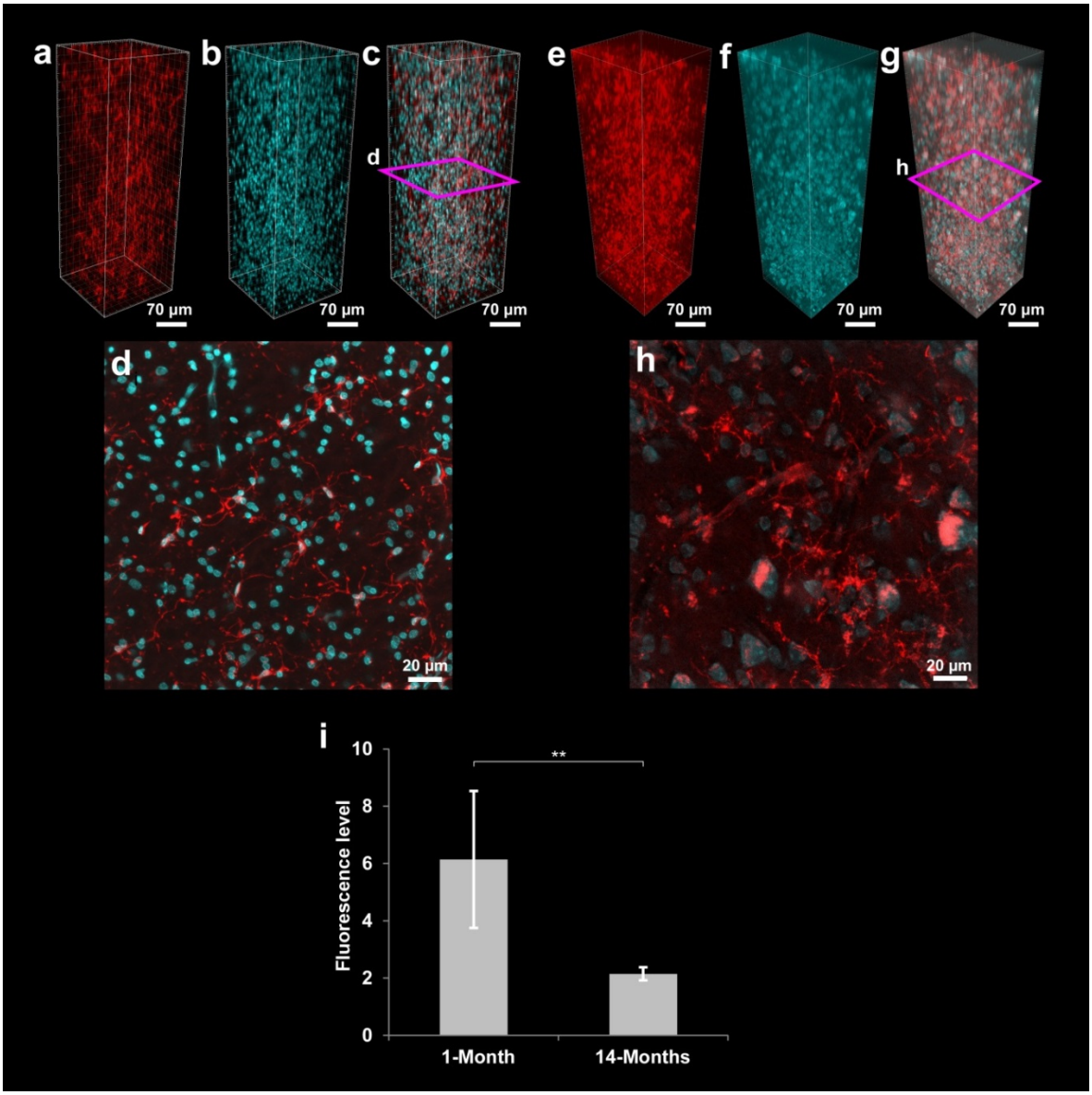

Iba1 and TO-PRO-3 labeling of short-term (1-month) (**a-d**) and long-term (14-months) stored (**e-h**) clinical cortical tissue samples of human brains. 3D reconstructions showing the homogeneous labeling of microglia (Iba1) (**a,e**) and cell nuclei (TO-PRO-3) (**b,f**) and their merge (**c,g**) throughout the 1 mm human tissue samples stored short-term (**a-c**) or long-term (**e-g**). (**d,h**) Maximum intensity projections of the z-position marked by the purple box in (c,g), respectively. Nuclei are shown in cyan, microglia and their processes are in red. All the images were taken by confocal microscopy with 3-4 µm z-steps. (**i**) Fluorescence level quantification. Antibody (microglia) and dye (cell nuclei) labelings were complete and specific on both short-term and long-term stored human clinical tissue samples even though the fluorescence level was significantly lower in long-term stored tissues, mostly owing to the increased background in long-term storage. Note that the 1-month fixed sample was obtained from an individual without any obvious brain pathology reported vs. the 14-months fixed sample from an individual who suffers from obesity. Values are mean ± s.d.; n=6, 4 slices for short-term fixed samples and long-term fixed samples, respectively. Statistical significance (**$P < 0.01$) was assessed by unpaired *t*-test.

Supplementary Figure 26: SNR and PSNR in uDISCO cleared samples

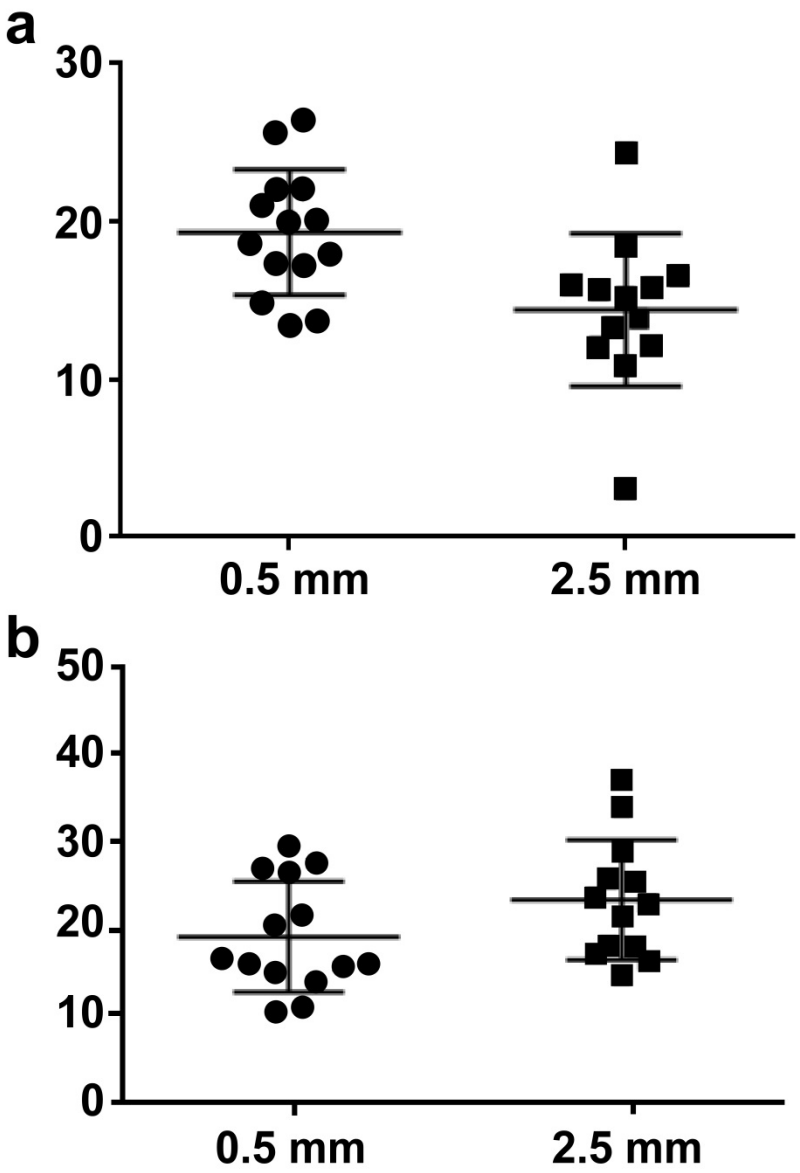

Signal-to-noise ratio (SNR) (**a**) and peak signal-to-noise ratio (PSNR) (**b**) range at different depths for uDISCO clearing as assessed on 3 months old GFP-M mice. Lines represent mean ± s.d.; n=3 brains for each group. The exact formulas and more details are given in the Methods part.

Supplementary Figure 27: Different objectives in BABB-D

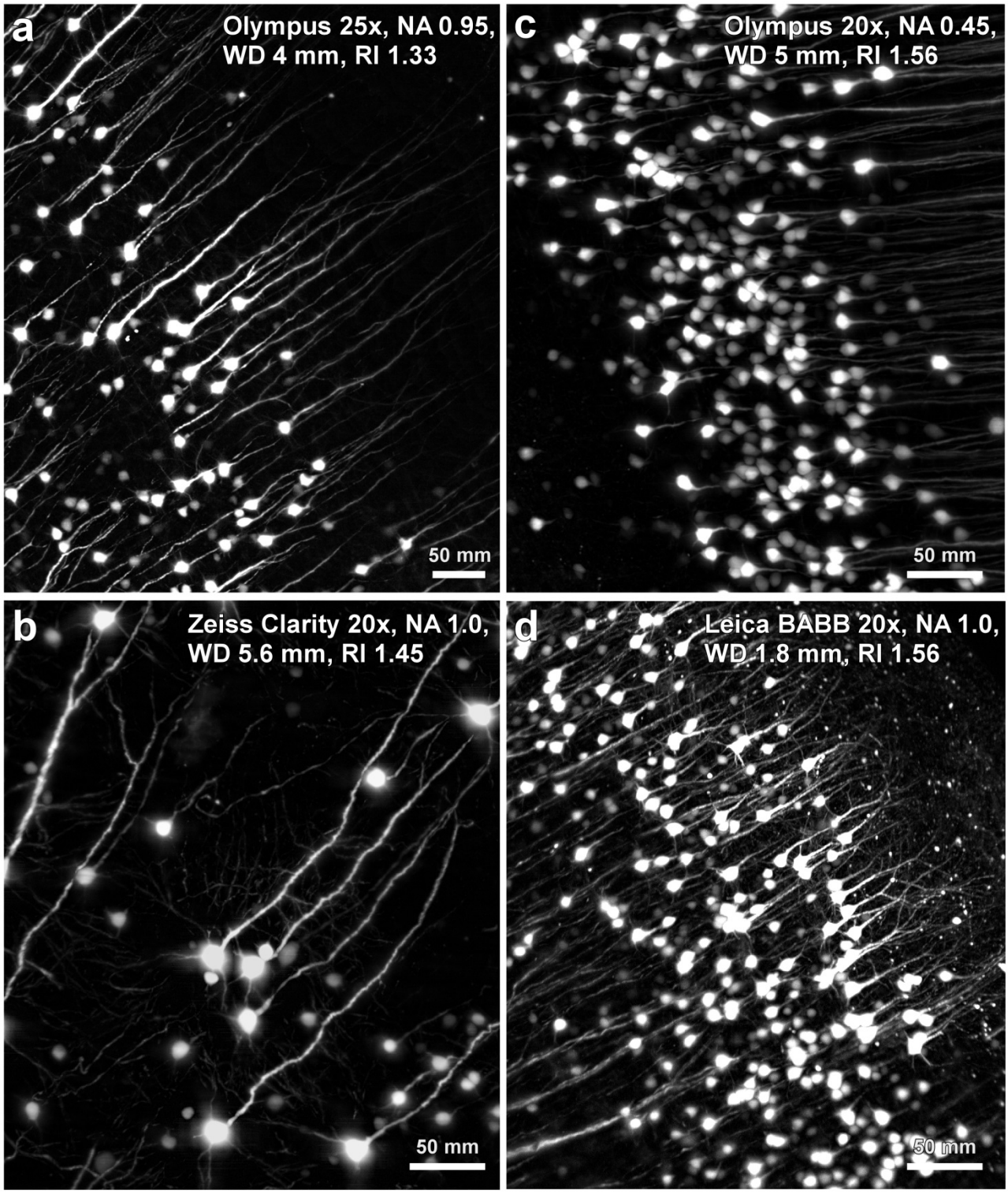

The quality comparison of four commercially available objectives (as indicated in the respective images) in BABB-D (RI 1.56) after uDISCO clearing of GFP-M brains. All images were generated using light-sheet microscopy at 1.5 mm depth from the cortex surface. It is worth mentioning that the water (**a**) and CLARITY (**b**) corrected objectives (therefore not corrected for BABB-D refractive index) generated comparable quality images to BABB corrected objectives (**c,d**). NA = numerical aperture, WD = working distance, RI = refractive index.

Supplementary Figure 28: The transcardiac circulatory system for uDISCO whole body tissue clearing

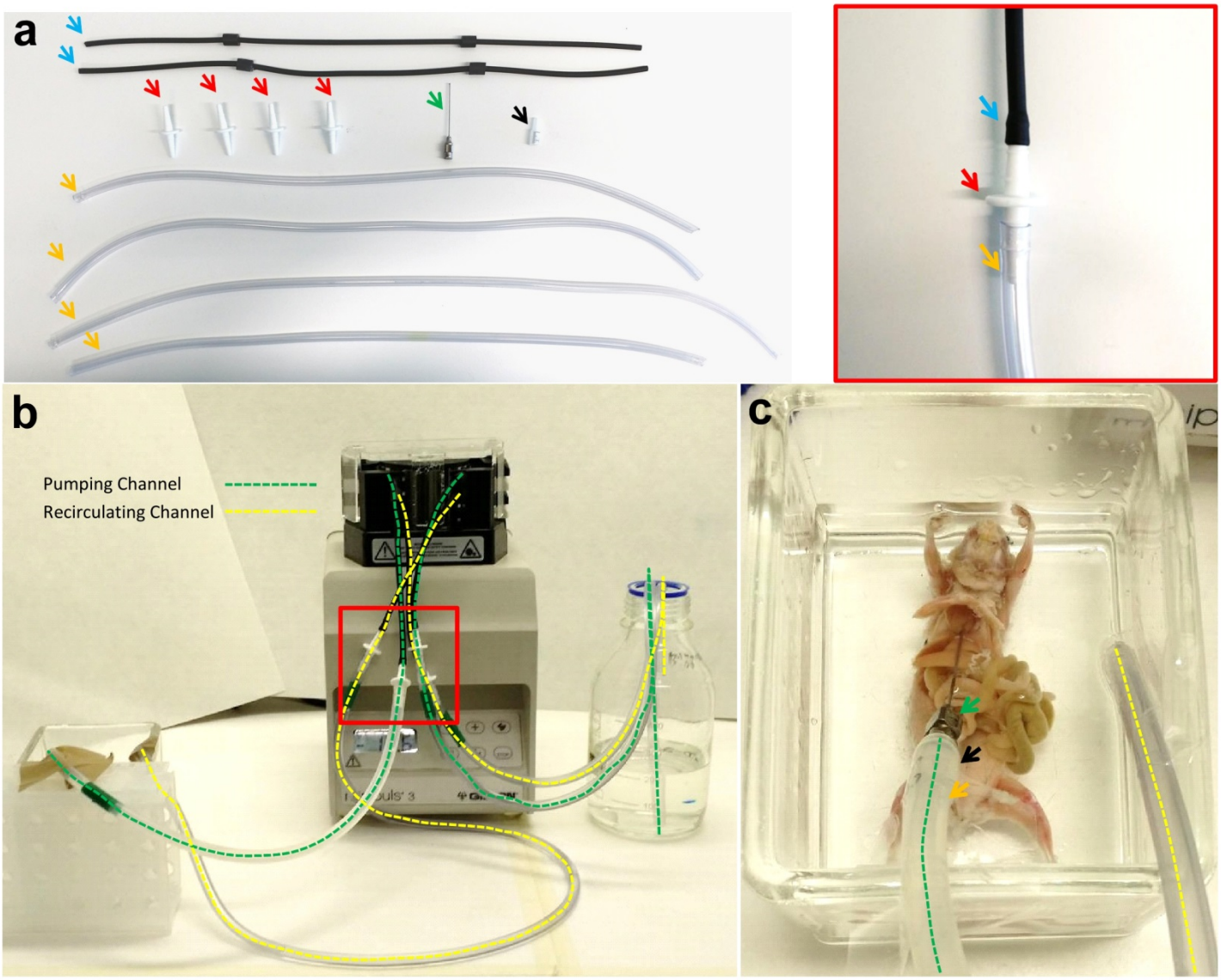

(**a**) Components of the circulation loop: 2x Viton reference tubing (Gilson, F1817745) (blue arrow), 4x tubing connectors (Omnilab, 5434482) (red arrow), 4x PVC tubing for extension (Omnilab, 5437920) (orange arrow), 1x transcardiac perfusion needle (Leica, 39471024) (green arrow), 1x needle connector cut from 1 ml syringe (Braun, 9166017V) (black arrow). The red box shows the connection of each Viton tubing ending indicated in (b). (**b**) A completed setup of the transcardiac circulatory system. Green dash highlights the first channel for pumping the clearing solution through whole mouse body. The yellow dash shows the second channel for collecting and recirculating the solution back to the original bottle. (**c**) Insert the cutting connector (black arrow) into the outflow tubing of the pumping channel (orange arrow) and fix it with a transcardiac perfusion needle (green arrow). After pushing the air bubble out of the tubing system, the animal is placed in the glass clearing chamber and the perfusion needle is inserted into the left ventricle of the heart.

Supplementary Figure 29: Workflow for cell counting

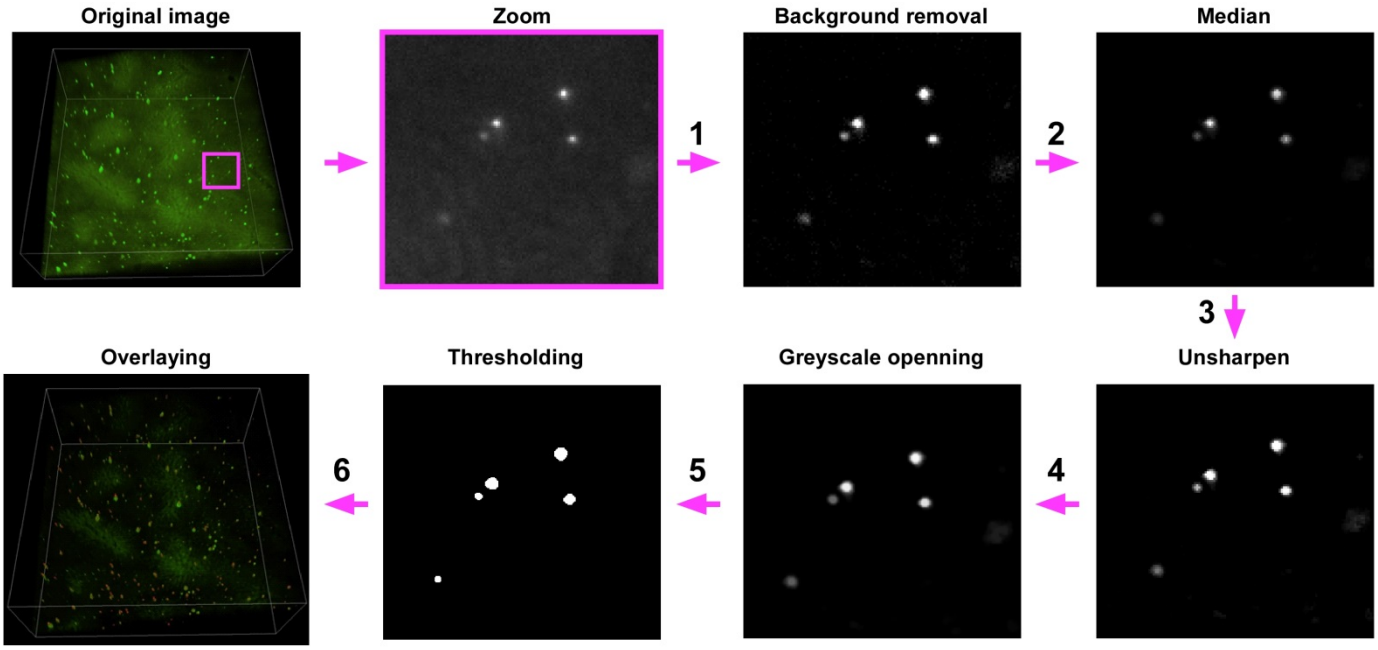

To count the number of bone marrow stem cells (BMSCs), we used publicly available ImageJ and its plugins as detailed below. Here we showed each step of the analysis on a sample image (a single optical section from a liver scan at 1.62 x1.62 x 12 µm voxel size). 1) To improve the background, we used convoluted median background subtraction option in BioVoxxel plugin. This plugin works fast, and removes the background smoothly in our samples because of low artifacts. 2) Median filtering was performed to remove artifacts coming from background subtraction. In this filtering, the radius is equal to the smallest object to be maintained (4 µm in our example). 3) Unsharpen mask was used when the signal-to-background ratio was lower than 2. In this mask, R stands for the average radius of the cells (6 um in our example). 4) To remove all the artifacts smaller than the cells, we used Grayscale opening morphological filter option in MorpholibJ plugin. In this filter, R is the radius of the biggest object to be removed (3 µm in our example) and disk option was used as structuring elements. 5) To decrease complexity of the quantification, we converted processed images to binary images by thresholding. To perform automatic thresholding, we used Otsu Limited function in DeadEasy plugin, which can perform multi-level thresholding. In addition, watershed can be used to separate the connected cells in densely labeled samples (this step was not performed in the example above because of sparse distribution). 6) Finally, detected cells were overlaid with the original data to check accuracy of the cell detection.

Supplementary Figure 30: Methods for normalized signal profile and intensity quantifications

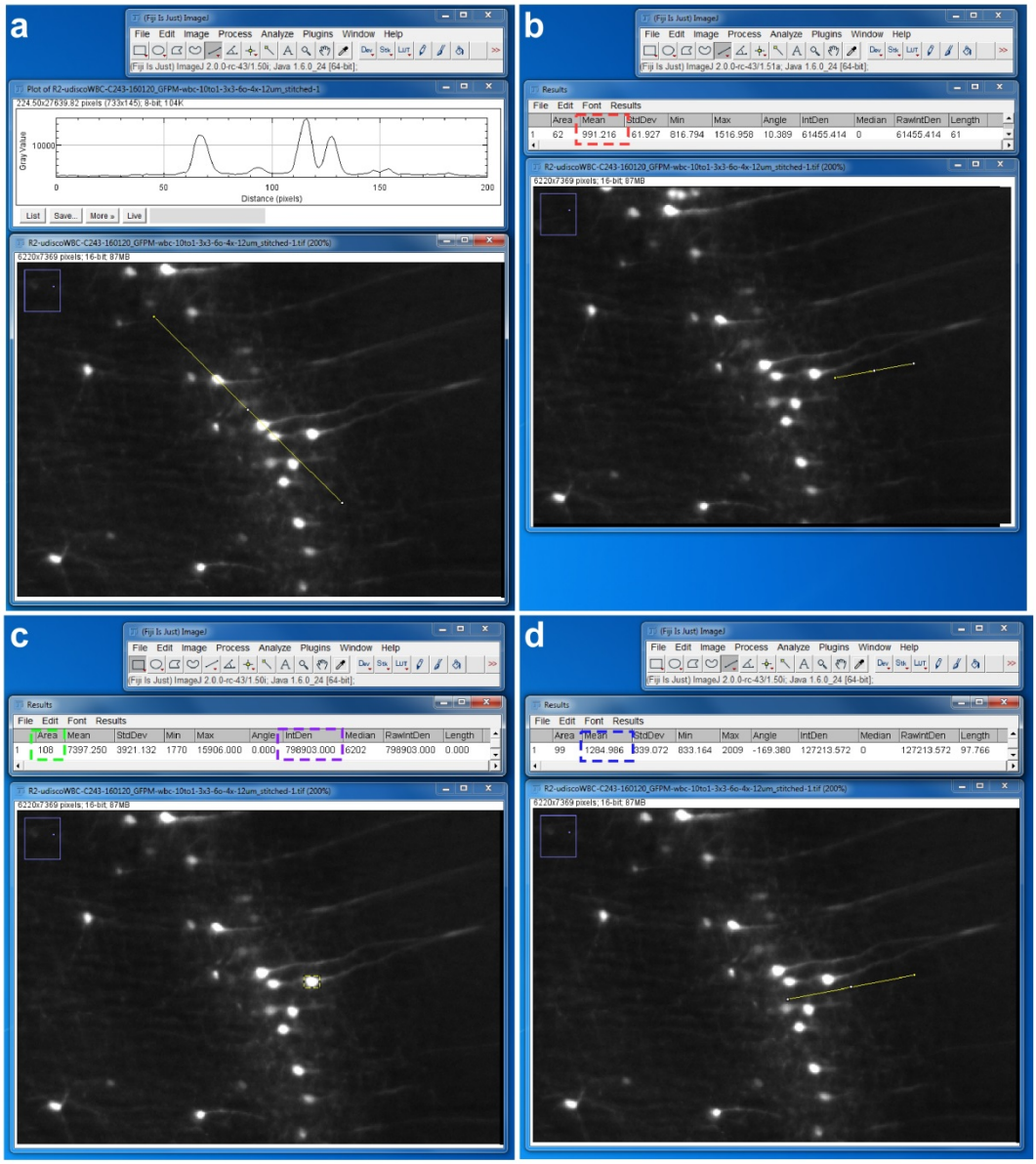

In Fiji (ImageJ2) software, a straight line was drawn across the specific signal spots and the plot profile of the signal was measured (**a**). Another straight line was drawn across the background area close to the specific signal spot to measure the mean value of the background (red box) (**b**). Next, the profile was divided by the selected background value and normalized profile of each sample was shown in the representative line chart (Supplementary Figs. 2, 5, 6, and 10). For signal intensity quantification, a rectangular selection covering the signal spot (a specific cellular structure) was made within the defined region and the integrated density of the signal was recorded (purple box) (**c**). A straight line was drawn across the background area close to the signal spot and the mean gray value of the background was measured (blue box) (**d**). (**e**) Formula for the signal intensity: 1) the total mean value of the background of the rectangular selection was subtracted from the integrated density of the signal to get the total signal density in the rectangular selection, and 2) the average intensity of the signal without background was calculated by dividing the total signal density with the pixel number of the rectangular selection (green box) (Supplementary Figs. 2, 5, 6, 9 and 10).

Supplementary Protocol

Perfusion and tissue preparation

Before intracardial perfusion, anesthetize the animals deeply with a combination of anesthetics, such as midazolam/medetomidine/fentanyl (MMF) (1ml/100g of body mass for mice).

1. Transcardially perfuse the animals (e.g. using Leica perfusion one system at 100-125 mmHg pressure) first with heparinized (10U/ml of Heparin, ratiopharm GmbH, N68542.03) 0.1 M PBS for 5-10 minutes then with 4% paraformaldehyde (PFA, Morphisto, 11762.01000) in 0.1 M PBS for 20 minutes at room temperature.
   TIP: Skipping the Heparin when vasculature is labeled can increase the quality of labeling. For all perfusion steps, the needle should be placed and kept in the left ventricle of the heart and should not cross to the right side of the heart.
2. For whole-body clearing, remove the skin and carefully open the skull and vertebra without damaging the CNS tissue. At this point, the whole body clearing can be performed immediately, or the mouse body can be stored in 0.1M PBS at 4 °C up to 4 weeks. For clearing dissected organ, collect the tissues directly and post-fix them in 4% PFA for 1-2 days at 4°C. Wash the samples once in 0.1M PBS for 5 min before clearing.

Preparation of uDISCO solutions

1. Prepare *tert*-butanol (Sigma, 360538) solutions with distilled water at 30 Vol%, 50 Vol%, 70 Vol%, 80 Vol%, 90 Vol%, 96 Vol% and 100 Vol% for gradient dehydration.
2. Use Dichloromethane (DCM) (Sigma, 270997) as a pure solution, for delipidation step.
3. Prepare refractive index matching solutions by mixing BABB (benzyl alcohol + benzyl benzoate 1:2, Sigma, 24122 and Sigma, W213802, respectively) and diphenyl ether (DPE) (Alfa Aesar, A15791) at following ratio: BABB-D4, BABB:DPE at a ratio 4:1 (Vol/Vol); BABB-D10, BABB:DPE at a ratio 10:1 (Vol/Vol); BABB-D15, BABB:DPE at a ratio 15:1 (Vol/Vol). Add 0.4% Vol vitamin E (Alfa Aesar, A17039) into BABB-D solutions to scavenge the peroxides.

Tert-butanol is flammable, DCM is toxic and BABB-D components can cause skin irritation, therefore they should be handled carefully. Waste should be treated and discarded accordingly.

uDISCO passive clearing procedure for dissected organs

All incubation steps are performed in a fume hood with gentle rotation or shaking using 5 ml tubes (Eppendorf, 0030 119.401) for whole mouse brain or smaller samples, or using 80 ml glass chambers (omnilab, 5163279) for bigger samples such as rat tissues or whole brain + spinal cord. The samples are covered with aluminum foil to keep them in dark.

1. Incubate the fixed samples in 30 Vol%, 50 Vol%, 70 Vol%, 80 Vol%, 90 Vol%, 96 Vol% and 100% *tert*-butanol for 2-12 hours at 34-35°C (**Supplementary Table 1**).
2. Incubate in DCM for 45-60 minutes at room temperature (small tissues such as mouse spinal cord or 1 mm thick coronal slices can skip this step).
3. Incubate in BABB-D for 2-6 hours until the samples become optically transparent.

TIP: The higher amount of DPE in BABB yields better signal preservation (e.g. BABB-D15), while the lower amount of DPE in BABB results in higher transparency (e.g. BABB-D4). We recommend to use BABB-D4 for small tissues e.g. spinal cord or tissue slices, and BABB-D15 for large tissues e.g. for rat brain clearing. For whole-body clearing with perfusion system, use BABB-D10.

4. Samples can be stored in BABB-D at room temperature in the dark for several weeks. **TIP:** It is recommended to image sample as soon as possible to yield the best outcome.

uDISCO whole-body clearing procedure with perfusion system

Establish the transcardial-circulatory system as in **Supplementary Fig. 28**. Here, we used a peristaltic pump (Gilson, Peristaltic Pump MINIPULS 3) with one pumping channel (green dash line) and one recirculating channel (yellow dash line). All steps should be performed in a fume hood.

1. Connect the Viton reference tubing to the peristaltic pump.
   TIP: As the clearing solutions can be corrosive to various tubing material, we recommend usage of Viton tubing (Gilson, F1817745).
2. Insert the tubing connectors (Omnilab, 5434482) (red arrow) at each end of the Viton tubing (blue arrow).
3. Connect the tubing connectors (red arrow) with additional PVC tubing (Omnilab, 5437920) for extension (orange arrow).
   TIP: Transparent PVC tubing, which is compatible with clearing solutions, helps for checking unwanted air bubbles in the tubing system.
4. Cut the head part of the 1 ml syringe (Braun, 9166017V) as a connector (black arrow) and insert it into the outflow tubing of the pumping channel (orange arrow).
5. Connect the transcardiac perfusion needle (Leica, 39471024) (green arrow) for mouse or the thinnest perfusion needle (Leica, 39471022) without rubber head for rat with this connector. Subsequently, fix the inflow tubing of the recirculating channel in the glass chamber containing animal body ready for clearing.
   TIP: Fix the tubing with tapes (any kind). Keep a certain height between the inflow tubing head and bottom of the glass chamber to ensure that the sample is covered by clearing solutions during clearing at all times.
6. Keep the inflow tubing of the pumping channel beneath the surface of the clearing solution and start the circulation until air bubbles are pushed out from the tubing system.
   TIP: Avoid pumping air bubbles by keeping the tubing always immersed into solution while pumping.
7. Set the perfusion needle into the heart of the animal through the same pinhole made during perfusion and circulate the clearing solutions one by one as indicated in **Supplementary Table 1**.
   TIP 1: When starting the circulation, it might be visible that some ripples occur beside the right atrial appendage because the PBS in the sample is pushed into 30 Vol% *tert*-butanol solutions. This would be a good signal that the pumping is working appropriately. If not, try to change the angle of the perfusion needle to reach the best position and fix it with tapes. Because of the shrinkage during dehydration, the needle should stay in the heart without slipping out.
   TIP 2: Stop the pump temporarily when changing the clearing solutions between steps. Collect the last solution back to the bottle by using a serological pipette and fill the glass chamber with the next solution quickly to minimize exposure to air. Because serological pipettes are not stable in BABB-D, use them only in the prior steps. Hold the inflow tubing ending of the pumping channel carefully to avoid any air

bubble and put it beneath the surface of next solution. If there are large air bubbles within the tubing, they can be eliminated by a brief run of the pump in the reverse direction.

TIP 3: As the melting point of *tert*-butanol is between 23 and 26 °C (close to room temperature), use a heating plate at 35-40 °C for 100% *tert*-butanol circulation steps to prevent the solution from solidification.

TIP 4: The amount of solutions for circulation depends on the capacity of the clearing chamber and the size of the animal that is being cleared. For example, for mice, a 400 ml capacity glass chamber with 300 ml working clearing solution and for rats, a 1000 ml capacity glass chamber with 800 ml working clearing solution would be sufficient.

TIP 5: For rat clearing, because PVC tubing is not resistant to DCM, the DCM step can be performed with gentle shaking to increase the efficiency.

TIP 6: The flowing rate was set at 8-10 ml/min for mouse clearing and 15-20 ml/min for rat clearing.

8. At the final step, circulate BABB-D10 until full transparency is achieved (about 6-12 hours for mouse and ~24 hours for rat).

   TIP: It is recommended to image sample as soon as possible to yield the best outcome.

Supplementary Table 1: Notes for clearing steps

steps

Tissue type / reagents temperature	half brain from adult animals	whole organs from adult animals such as brain, brain + intact spinal cord, kidney liver, bones	rat brain + spinal cord	Tissue type / reagents temperature	small tissues such as spinal cord, hippocampus, cerebellum	1 mm slices	whole body with perfusion system (mouse)	whole body with perfusion system (rat)
30% *tert*-but at 35°C	ON	ON	1 day	**30% *tert*-but at RT**	4 hr	2 hr	12 hr	1 day
50% *tert*-but at 35°C	4 hr	10 hr	1 day	**50% *tert*-but at RT**	4 hr	2 hr	12 hr	1 day
70% *tert*-but at 35°C	4 hr	ON	1 day	**70% *tert*-but at RT**	ON	2 hr	12 hr	1 day
80% *tert*-but at 35°C	ON	10 hr	1 day	**80% *tert*-but at RT**	4 hr	2 hr	–	–
90% *tert*-but at 35°C	4 hr	ON	1 day	**90% *tert*-but at RT**	4 hr	2 hr	12 hr	1 day
96% *tert*-but at 35°C	4 hr	10 hr	1 day	**96% *tert*-but at RT**	ON	ON	–	–
100% *tert*-but at 35°C	ON	ON	1 day x 2	**100% *tert*-but at RT**	–	2 hr	12 hr x 2	1 day x 2
DCM at RT	40-50 min	50-70 min	2 hr	**DCM at RT**	–	–	–	6-8 hr
BABB-D4 or BABB-D15	> 2 hr	> 3 hr	> 5 hr	**BABB-D4 or BABB-D15**	> 2 hr	> 1 hr	NA	NA
				BABB-D10			> 6 hr	> 24 hr

tert-but : *tert*-butanol, ON : overnight, hr : hour(s), min : minute(s), RT : room temperature, DCM : dichloromethane, BABB : benzyl alcohol + benzyl benzoate (1:2 in volume), BABB-D4 : BABB + diphenyl ether (4:1 in volume), BABB-D10 : BABB + diphenyl ether (10:1 in volume), BABB-D14 : BABB + diphenyl ether (14:1 in volume), –: skip the step

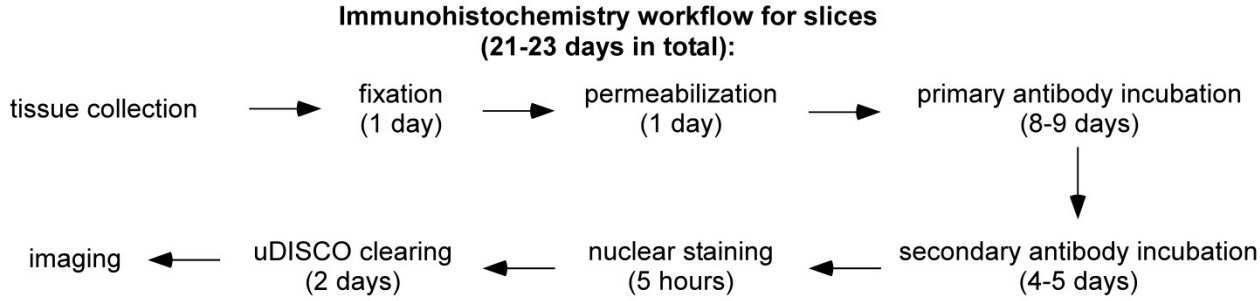

Times for each experiment step can be shortened (e.g to half) or extended (e.g. to double) depending on tissue size to improve antibody penetration or clearing performance. To preserve the signal better in low fluorescence conditions, dehydration can be ceased at 90% or 96% and proceed to the BABB-D step. We found that active (perfusion mediated) whole-body clearing provided superior transparency compared to passive clearing of dissected organs e.g. the brain.

Nature Methods: doi:10.1038/nmeth.3964

Supplementary Table 2: Imaging specifications

FIGURES		SYSTEM	OBJECTIVE SPECIFICATIONS				ACQUISITION PARAMETERS			
			Magnification	NA	RI	WD	Zoom	Image pixel size	z-step	imaging depth
Figures										
1	a	UM II	4X corr.	0.28	1.56	10mm		1.625µmx1.625µm	8µm	1mm
	g	UM II	4X corr.	0.28	1.56	10mm		1.625µmx1.625µm	2µm	2.0-2.2mm
2	c	AxioZoom	Zeiss 1X	0.25	1.0	56mm		6.49µmx6.49µm	n.a.	n.a.
	d	UM II -MVX10	Oly. 2X	0.5	1.33/1.56	6mm	0.63	5.16µmx5.16µm	8µm	3D reconstruction
	e	UM II -MVX10	Oly. 2X	0.5	1.33/1.56	6mm	0.63	5.16µmx5.16µm	8µm	1mm
	f	UM II -MVX10	Oly. 2X	0.5	1.33/1.56	6mm	0.63	5.16µmx5.16µm	8µm	3mm
	g	UM II -MVX10	Oly. 2X	0.5	1.33/1.56	6mm	0.63	5.16µmx5.16µm	8µm	5mm
	h	UM II -MVX10	Oly. 2X	0.5	1.33/1.56	6mm	0.63	5.16µmx5.16µm	10µm	projection of 8mm scan
	i,j	UM II -MVX10	Oly. 2X	0.5	1.33/1.56	6mm	3.2	1.015µmx1.015µm	4µm	projection of 8mm scan
3	c	AxioZoom	Zeiss 1X	0.25	1.0	56mm		6.49µmx6.49µm	n.a.	n.a.
	d,e,f	AxioZoom	Zeiss 1X	0.25	1.0	56mm		1.42µmx1,42µm	n.a.	n.a.
	j,k,l,m	UM II	4X corr.	0.28	1.56	10mm		1.625µmx1.625µm	20µm	projection of 10mm scan
4	a,c	UM II	4X corr.	0.28	1.56	10mm		1.625µmx1.625µm	4µm	entire scan projection
	d	UM II	4X corr.	0.28	1.56	10mm		1.625µmx1.625µm	4µm	1.8mm
	e	UM II	4X corr.	0.28	1.56	10mm		1.625µmx1.625µm	4µm	2.0mm
	f	UM II	4X corr.	0.28	1.56	10mm		1.625µmx1.625µm	4µm	3.0mm
	g	UM II	Zeiss 20x	1.0	1.45	5.6mm	2	0.1625µmx0.1625µm	2µm	500µm
5	b	UM II	4X corr.	0.28	1.56	10mm	0.63	2.56µmx2.56µm	16µm	1.5-3mm
		UM II -MVX10	Oly. 2X	0.5	1.33/1.56	6mm	0.63	5.16µmx5.16µm	16µm	3D reconstruction
6	virus b,c,d,e,f	UM II	4X corr.	0.28	1.56	10mm		1.625µmx1.625µm	12µm	entire scan projection
	mouse l,m	LSM880	Leica 25x	0.95	1.33	2.5mm		0.2µmx0.2µm	3µm	450-480µm, 600-630µm
	human u	LSM880	Leica 25x	0.95	1.33	2.5mm		0.2µmx0.2µm	3µm	270-282µm
Sup. Figures										
S1	c	AxioZoom	Zeiss 1X	0.25	1.0	56mm		6.49µmx6.49µm	n.a.	n.a.
	d,e,f,g	UM II	4X corr.	0.28	1.56	10mm		1.625µmx1.625µm	n.a.	n.a.
S2		UM II	4X corr.	0.28	1.56	10mm		1.625µmx1.625µm	12µm	2.5mm
S5		UM II	2X corr.	0.14	1.56	10mm		3.25µmx3.25µm	8µm	0.5mm, 2.5mm
S6		UM II	2X corr.	0.14	1.56	10mm		3.25µmx3.25µm	8µm	0.5mm, 2.5mm
S8		AxioZoom	Zeiss 1X	0.25	1.0	56mm		5.68µmx5.68µm	n.a.	n.a.
S9	a,c,e	UM II	4X corr.	0.28	1.56	10mm		1.625µmx1.625µm	4µm	0.44mm
	b,d,f	UM II	4X corr.	0.28	1.56	10mm		1.625µmx1.625µm	4µm	0.66mm
S10	a-f	UM II -MVX10	Oly. 2X	0.5	1.33/1.56	6mm	0.63	5.16µmx5.16µm	4µm	0.66mm
S11	a,c	UM II -MVX10	Oly. 2X	0.5	1.33/1.56	6mm	0.63	5.16µmx5.16µm	4µm	3D reconstruction
S12		AxioZoom	Zeiss 1X	0.25	1.0	56mm		5.68µmx5.68µm	n.a.	n.a.
S13		LSM880	Leica 25x	0.95	1.33	2.5mm		0.183µmx0.183µm	3-4µm	0-100µm
S14		LSM880	Leica 25x	0,95	1.33	2.5mm		0.183µmx0.183µm	3-4µm	0-100µm
S17	a	UM II	2X corr.	0.14	1.56	10mm		3.25µmx3.25µm	6µm	10mm
	b,c,d,e	UM II	4X corr.	0.28	1.56	10mm		1.625µmx1.625µm	6µm	10mm
S19	h	LSM880	Leica 25x	0.95	1.33	2.5mm		0.67µmx0.67µm	2µm	18-62µm
	i	LSM880	Leica 25x	0.95	1.33	2.5mm		0.43µmx0.43µm	1µm	6-45µm
	small boxes in figS4h	LSM880	Leica 25x	0.95	1.33	2.5mm		0.16µmx0.16µm	1µm	
	small boxes in figS4i	LSM880	Leica 25x	0.95	1.33	2.5mm		0.10µmx0.10µm	1µm	
S20		AxioZoom	Zeiss 1X	0.25	1.0	56mm		5.68µmx5.68µm	n.a.	n.a.
S21		UM II -MVX10	Oly. 2X	0.5	1.33/1.56	10mm	0.63	5.16µmx5.16µm	8µm	2.35mm
		UM II -MVX10	Oly. 2X	0.5	1.33/1.56	10mm	0.63	5.16µmx5.16µm	8µm	1.4mm
		UM II -MVX10	Oly. 2X	0.5	1.33/1.56	10mm	0.63	5.16µmx5.16µm	8µm	2.9mm
S22		UM II	4X corr.	0.28	1.56	10mm		1.625µmx1.625µm	6µm	1.9mm
S23		UM II	4X corr.	0.28	1.56	10mm		1.625µmx1.625µm	12µm	entire scan projection
S24	d	LSM880	Leica 25x	0.95	1.33	2.5mm		0.2µmx0.2µm	3µm	24-30µm
	e	LSM880	Leica 25x	0.95	1.33	2.5mm		0.2µmx0.2µm	3µm	237-246µm
S25	d	LSM880	Leica 25x	0,95	1,33	2.5mm		0.2µmx0.2µm	3µm	327-387µm
	h	LSM880	Leica 25x	0,95	1,33	2.5mm		0.2µmx0.2µm	4µm	276-292µm
S27	a	UM II	Oly. 25X	0,95	1.31-1.52	4mm		0.26µmx0.26µm	4µm	0.8-1.2mm
	b	UM II	Zeiss 20x	1	1,45	5.6mm		0.325µmx0.325µm	4µm	0.4-0.8mm
	c	UM II	20X corr.	0,45	1,56	5mm		0.325µmx0.325µm	4µm	0.5-1.0mm
	d	UM II	Leica 20X	0,95	1,56	1.8mm		0.325µmx0.325µm	2µm	0.65-1.05mm

Legend of abbreviations

Imaging Systems

UM II	LaVision BioTec - UltraMicroscope II
UM II -MVX	LaVision BioTec - UltramicroscopeM II -MVX10
LSM880	Zeiss confocal LSM880 with Airyscan
AxioZoom	Zeiss AxioZoom EMS3/SyCoP3

NA	Numerical aperture
RI	Refractive Index
WD	Working distance
n.a.	not applicable

Objectives

Oly. 2X	Olympus MVPLAPO2XC
2X corr.	Olympus XLFLUOR2x corrected
4X corr.	Olympus XLFLUOR4x corrected
20X corr.	Olympus LUCPLFLN20x corrected

Oly. 25X Olympus XLPLN25X

Zeiss 1X Zeiss PlanNEOFLUAR Z 1x

Zeiss 20X Zeiss Clr Plan-Neofluar 20x

Leica 20X Leica HCX APO L20×

Leica 25X Leica HCX IRAPO L 25x

2.2 Research Article 2: Panoptic imaging of transparent mice reveals whole-body neuronal projections and skull–meninges connections

Previous tissue clearing methods including uDISCO could not provide the reliable quantification of the signals from fluorescent proteins in deep tissue through intact skull, vertebra and skin because the widely used fluorescent proteins such as EGFP, EYFP and mCherry emit light in the visible spectrum, in which muscles and bone tissue creates severe obstructive autofluorescence. Too overcome this obstacle, a whole-body immunolabeling protocol is needed to stabilized the fluorescence signal by using synthetic fluorophores and to shift the emission signal into far red spectrum with less tissue autofluorescence.

Here, we developed vDISCO, a nanobody-based whole-body immunolabeling technology which enhances the signal of fluorescent proteins by up to two orders of magnitude and allows the reliable imaging and quantification of subcellular details of neuronal structures and immune cells through muscles, bones and skin in intact transparent mice. By using various lines of transgenic mice, we visualized the details of meningeal lymphatic vessels and studied their drainage function. Furthermore, we revealed the short vascular connections between skull marrow and brain meninges functioning as an additional immune cell infiltration route. After stroke, the cell number of Lysm+ neutrophils in these short connections increased significantly comparing with the unlesioned control. Overall, vDISCO significantly enhances the imaging quality of intact cleared sample and enables comprehensive studies of the nervous system and immune system with cellular level resolution at the whole-body scale in an unbiased way.

Author contribution: developed the vDISCO protocol with Ruiyao Cai; cleared and imaged whole-body samples from CX3CR1-GFP line, Prox1-EGFP line, double transgenic line, Lysm-EGFP line, CD68-GFP line and VEGFR3-YFP line; performed experiments for comparing different clearing protocols and perfusion pressure; analyzed the CD68 line after SCI; wrote the manuscript with colleagues (please see section 7 for further details).

nature neuroscience

TECHNICAL REPORT

https://doi.org/10.1038/s41593-018-0301-3

Panoptic imaging of transparent mice reveals whole-body neuronal projections and skull–meninges connections

Ruiyao Cai[1,2,10], Chenchen Pan[1,2,10], Alireza Ghasemigharagoz[1], Mihail Ivilinov Todorov[1,2], Benjamin Förstera[1], Shan Zhao[1], Harsharan S. Bhatia[1], Arnaldo Parra-Damas[1], Leander Mrowka[1], Delphine Theodorou[3,4], Markus Rempfler[5], Anna L. R. Xavier[6], Benjamin T. Kress[6,7], Corinne Benakis[1], Hanno Steinke[8], Sabine Liebscher[3,4,9], Ingo Bechmann[8], Arthur Liesz[1,2,9], Bjoern Menze[5], Martin Kerschensteiner[3,4,9], Maiken Nedergaard[6,7] and Ali Ertürk[1,2,9]*

Analysis of entire transparent rodent bodies after clearing could provide holistic biological information in health and disease, but reliable imaging and quantification of fluorescent protein signals deep inside the tissues has remained a challenge. Here, we developed vDISCO, a pressure-driven, nanobody-based whole-body immunolabeling technology to enhance the signal of fluorescent proteins by up to two orders of magnitude. This allowed us to image and quantify subcellular details through bones, skin and highly autofluorescent tissues of intact transparent mice. For the first time, we visualized whole-body neuronal projections in adult mice. We assessed CNS trauma effects in the whole body and found degeneration of peripheral nerve terminals in the torso. Furthermore, vDISCO revealed short vascular connections between skull marrow and brain meninges, which were filled with immune cells upon stroke. Thus, our new approach enables unbiased comprehensive studies of the interactions between the nervous system and the rest of the body.

Most diseases, even when arising in a specific site, eventually affect the entire organism. Histological techniques developed in the last century have been the standard procedure for charting pathology, yet a more complete understanding of biological mechanisms requires an unbiased exploration of the whole organism, not just pre-defined tissues.

However, mammalian tissues are naturally opaque, hindering high-resolution imaging in any tissue deeper than a few hundred micrometers, a major reason why sectioning is needed for histological examination of target organs[1]. Recent innovations in tissue clearing technology now allow three-dimensional (3D) histological examination of intact organs[2–12]. Tissue clearing is a chemical process aiming to match refractive indices throughout intact tissues, thus rendering them transparent and allowing deep-tissue fluorescent microscope imaging. Most initial applications of tissue clearing relied on the assessment of endogenous fluorescent proteins expressed in the mouse CNS. More recently, deep-tissue immunolabeling methods have enhanced the quality of imaging for whole rodent organs as well as human embryos thanks to the conjugation of bright fluorescent dyes with secondary antibodies[4,13,14]. A few studies have even rendered entire adult mouse bodies transparent after removal of the skin[3,15–18] and allowed head-to-toe light-sheet microscopy imaging of intact adult mice[17,18]. All whole-body clearing and imaging methods to date rely on transgenic expression of fluorescent proteins such as enhanced green fluorescent protein (EGFP), enhanced yellow fluorescent protein (EYFP) and mCherry[17,18]. While these fluorescent proteins emit light in the visible spectrum, skeletal muscles and other bodily tissues possess obstructive autofluorescence in this range[19]. In addition, fluorescent proteins are often less bright compared with many synthetic fluorophores, and their signal intensity is further attenuated during the clearing and imaging procedure. Together, these bottlenecks hinder reliable detection and quantification of subcellular details in centimeters-thick transparent mice and therefore require reliance on imaging of dissected organs for quantifications, compromising the benefits of whole-body transparency.

Here we developed a whole-body immunolabeling method, named vDISCO (nanobody(V_HH)-boosted 3D imaging of solvent-cleared organs), to boost the signal of fluorescent proteins using nanobodies, which consist of the variable domain of heavy chain antibodies (V_HH)[20]. This technology can enhance fluorescent signals more than 100 times and thereby allows head-to-toe light sheet microscopy scanning of transparent mice (panoptic imaging) and quantification of subcellular details. We used this technology to construct the first neuronal projection map of an adult mouse and to reveal far-reaching changes in neuronal projections and inflammatory processes following acute CNS injuries. Panoptic imaging also revealed short vascular connections between the skull marrow

[1]Institute for Stroke and Dementia Research, Klinikum der Universität München, Ludwig-Maximilians University Munich, Munich, Germany. [2]Graduate School of Systemic Neurosciences Munich, Munich, Germany. [3]Institute of Clinical Neuroimmunology, Klinikum der Universität München, Ludwig-Maximilians University Munich, Munich, Germany. [4]Biomedical Center, Ludwig-Maximilians University Munich, Munich, Germany. [5]Department of Computer Science and Institute for Advanced Study, Technical University of Munich, Munich, Germany. [6]Center for Translational Neuromedicine, Faculties of Health and Medical Sciences, University of Copenhagen, Copenhagen, Denmark. [7]Center for Translational Neuromedicine, University of Rochester, New York, NY, USA. [8]Anatomy Institute, University of Leipzig, Leipzig, Germany. [9]Munich Cluster for Systems Neurology (SyNergy), Munich, Germany. [10]These authors contributed equally: Ruiyao Cai, Chenchen Pan. *e-mail: ali.ertuerk@med.uni-muenchen.de

and meninges (both at the brain surface and sagittal sinus), which may serve as immune gateways following stroke.

Results

vDISCO principles and signal enhancement. Quantitative assessments of intact transparent mouse bodies remained a major challenge impeding the study of neurological diseases at the whole-body scale. We reasoned that fluorescent proteins such as EGFP and red fluorescent protein (RFP) are relatively dim compared with bright fluorochromes (for example, Alexa and Atto dyes) after tissue clearing, making them difficult to detect in centimeters-thick mouse bodies, especially through intact thick bones (for example, skull and vertebrae) and skin. Therefore, we set out to enhance the signal of fluorescent proteins via whole-body immunolabeling with brighter and more stable fluorescent dyes to provide a much higher contrast (signal-to-background ratio) in cleared mice. Furthermore, using fluorescent dyes in the far-red spectrum could help to overcome tissue autofluorescence, thus allowing reliable detection of subcellular details in all tissues[4,19] (Supplementary Fig. 1). We reasoned that nanobodies are particularly suited to achieve thorough immunolabeling throughout entire adult mouse bodies because of their small molecular weight (12–15 kDa) compared with that of conventional antibodies (~150 kDa)[3,20]. Indeed, nanobodies were more efficient for labeling large tissues compared with conventional antibodies (Supplementary Figs. 2 and 3).

First, we tested the signal quality of nanobody labeling in dissected mouse brains from *Thy1*-GFP-M mice, in which a subset of neurons express EGFP[21]. Following the nanoboosting, the tissues were cleared using organic solvents[6,7]. We found that nanoboosting enhanced the signal intensity by one to two orders of magnitude compared with direct imaging of fluorescent proteins (Fig. 1a–i). In the nanoboosted samples, fine details of neurons were evident even in the deep brain regions of *Thy1*-GFP-M mice (compare Fig. 1b,c with Fig. 1e,f). We also obtained a similar signal intensity increase in the cerebellum of *Thy1*-GFP-M brains (compare Fig. 1g with Fig. 1h), which is notoriously difficult to clear due to the high lipid content.

A major aim of tissue clearing approaches is to perform automated quantifications in large imaging datasets in an unbiased and timely way. Towards this goal, we used the NeuroGPS-Tree algorithm, a robust, automated neuron-tracing tool that was recently developed for tracing neurons in scans of cortical regions obtained by high-resolution confocal microscopy[22]. We found that virtually all of the neuronal cell bodies and neurites were detected and linked to each other as complete neurons upon vDISCO nanoboosting in light-sheet microscopy scans (Supplementary Figs. 4 and 5). In contrast, in unboosted samples or in standard immunoglobulin G antibody-boosted samples, many fine extensions of neurons were not identified or not connected to somas and neuronal trees (Supplementary Fig. 4). Nanoboosting allowed imaging not only of neuronal details but also of smaller individual cells such as microglia cells and immune cells (Fig. 1j–m and Supplementary Fig. 6). Compared with unboosted samples, we could resolve fine details of microglia cells in intact transparent brains of CX3CR1$^{GFP/+}$ mice using light-sheet microscopy (Fig. 1j–m and Supplementary Video 1). Nanoboosting also enabled automated quantification of CX3CR1 GFP^{+} cells using the ClearMap algorithms[23]: we found approximately 2.3 million microglia cells in the adult mouse brain (Supplementary Fig. 7a). We also automatically quantified microglia in all brain regions annotated by the Allen Brain Atlas. Thereby we found, for example, ~150,000 microglia in the hippocampus and ~50,000 in the thalamus of adult mice (Supplementary Fig. 7b–k). Furthermore, we found no significant decrease in signal intensity over time of the same samples, suggesting that vDISCO nanoboosting stabilizes the fluorescent signal (Fig. 1n,o), allowing long-term preservation and re-imaging of the samples. Thus, owing to the enormous enhancement and stabilization of fluorescent signals using nanobodies, we could use available computational tools to automatically trace neurons and count cell numbers in images acquired by light-sheet microscopy.

vDISCO allows panoptic imaging of intact adult mouse bodies. To apply whole-body clearing technology at the systems level, it is critical to obtain information not only from dissected organs but also from intact transparent bodies. Towards this goal, we aimed at establishing an approach to achieve nanoboosting in the entire mouse body. We reasoned that vDISCO amplification of the fluorescent signals would allow reliable quantification of cells through intact thick bones and highly autofluorescent muscles. To ensure homogeneous delivery of nanobodies into all body regions, we used high-pressure cardiac perfusion with two- to three-fold increased pressure compared with standard perfusion protocols (160–230 mmHg compared with 70–110 mmHg (ref. [24])). We also illustrated the effect of high-pressure delivery compared with standard pressure using methylene blue. This novel high-pressure delivery approach facilitated a consistent distribution of the dye into deep tissues (Supplementary Fig. 8). Assessing the tissue integrity upon high-pressure delivery, we did not observe any structural changes (Supplementary Fig. 9). Furthermore, we used a permeabilization solution containing Triton X-100, methyl-β-cyclodextrin (to extract the cholesterol from membranes) and *trans*-1-acetyl-4-hydroxy-L-proline (to loosen the collagen network)[12]. To further reduce the background signal caused by the residual blood and to decalcify the bones, we treated whole mouse bodies with aminoalcohols[5,15] and EDTA[25] before the whole-body immunolabeling step. Combination of these diverse improvements allowed us to achieve whole-body immunolabeling in adult mice with a high degree of transparency (Fig. 2a and Supplementary Fig. 10) and to obtain quantitative information on single cells in deep brain regions through the intact skull[3,15–18,23] (Supplementary Figs. 11 and 12). Here, we used anti-XFP nanobodies conjugated with bright Atto dyes (called nanoboosters) to boost the fluorescent protein signal in transparent mice. Moreover, we used anti-vimentin nanobodies to label activated glia cells in the brain upon trauma, demonstrating that our approach also works with nanobodies targeting endogenously expressed proteins (Supplementary Fig. 13).

In addition to the specific boosted signal, we also visualized and segmented other major tissues in the transparent body: muscles by their autofluorescence within the blue–green spectrum, and bones and internal organs by propidium iodide (PI) labeling (Fig. 2b,c and Supplementary Fig. 14a–d). Usage of organic solvents, which induce isotropic tissue shrinkage[17], allowed us to perform head-to-toe panoptic imaging of entire mice by light-sheet microscopy.

Being able to image subcellular details of neurons through intact bones and highly autofluorescent muscles in the whole mouse body using vDISCO panoptic imaging, we constructed the first whole-body neuronal projection map of a *Thy1*-GFP-M transgenic mouse (Fig. 2d,e, Supplementary Fig. 14 and Supplementary Video 2). We noticed that in the peripheral nervous system, mainly axons innervating muscles were labeled in this mouse line, which enabled us to investigate the neuromuscular junctions in greater detail. We also observed fluorescent labeling of the internal organs, such as kidneys of *Thy1*-YFP-H mice[21] (Supplementary Fig. 15). Owing to the great increase in signal-to-background ratio by vDISCO, we could readily visualize axonal projections from the spinal cord through intact vertebrae to their terminals into the muscles, even in very remote locations such as toes (Fig. 2f–i and Supplementary Videos 3 and 4). Panoptic imaging of individual neuronal projections through intact bones can now provide more details on neuroanatomy. For example, how axons coming from consecutive roots enter the spinal cord—that is, in an overlapping or non-overlapping manner—has been unclear[26]. Using our technology, we observed that in mice, the

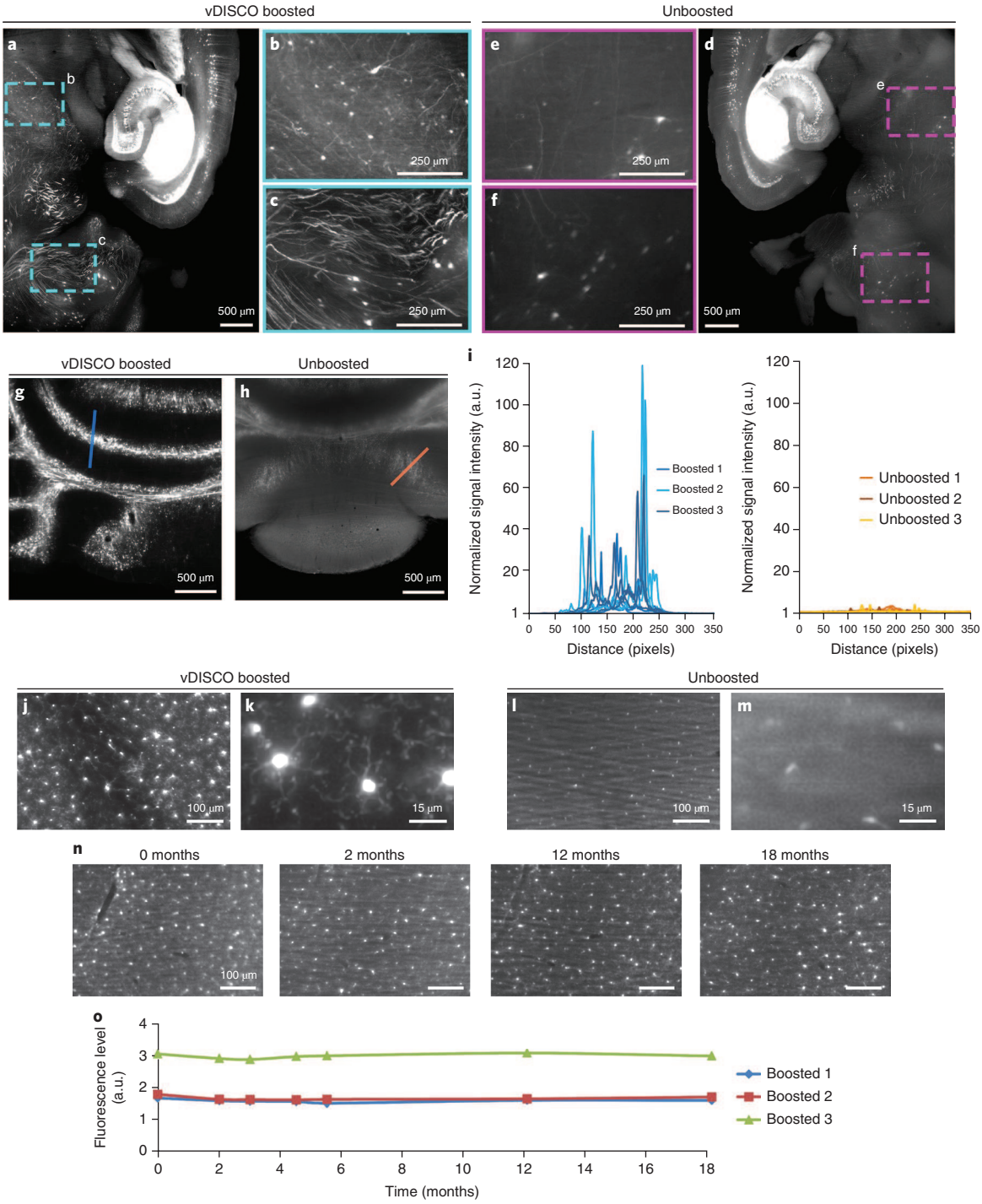

Fig. 1 | Enhancement and permanent preservation of the fluorescence signal with vDISCO. a–**f**, Signal quality comparison between vDISCO-boosted (**a**) and unboosted (**d**) half-brain samples coming from the same 11-month-old *Thy1*-GFP-M mouse. To achieve the best comparison between the two procedures, we divided the mouse brains in two halves for light-sheet microscopy imaging (one hemisphere boosted and imaged in the far-red channel, the other hemisphere unboosted and imaged in the green channel for endogenous EGFP). The boosted hemisphere showed highly distinguishable cellular details (**b**,**c**) such as axonal projections not visible in the unboosted hemisphere (**e**,**f**), especially in the regions with dim GFP labeling in *Thy1*-GFP-M mice, such as mid-brain (**b**,**e**) and cerebellum (**c**,**f**) (representative images, repeated at least on 3 different samples). **g**,**h**, Comparison of signal quality in cerebellum from the boosted (**g**) and unboosted (**h**) samples (repeated with at least 3 mice per group). **i**, Plots of signal intensity profiles from boosted samples (left) versus unboosted samples (right) along the blue and orange lines in **g** and **h**, respectively; $n = 3$ brains for each group (2- to 6-month-old *Thy1*-GFP-M mice). **j**–**m**, Light-sheet microscopy images (×4 and ×25 magnification) of the microglia from CX3CR1$^{GFP/+}$ mice in boosted (**j**,**k**) versus unboosted samples (**l**,**m**) showing the fine details of microglia ramifications obtained with vDISCO boosting (similar results repeated with at least 3 mice per group). **n**, Representative light-sheet microscopy images of 1 of 3 CX3CR1$^{GFP/+}$ mouse brains at 0, 2, 12 and 18 months after boosting, showing the preservation of the fluorescence signal over 18 months. **o**, Fluorescence level quantifications, in arbitrary units (a.u.), in CX3CR1$^{GFP/+}$ brains after boosting at different time points postclearing ($n = 3$ mice, 2–6 months old).

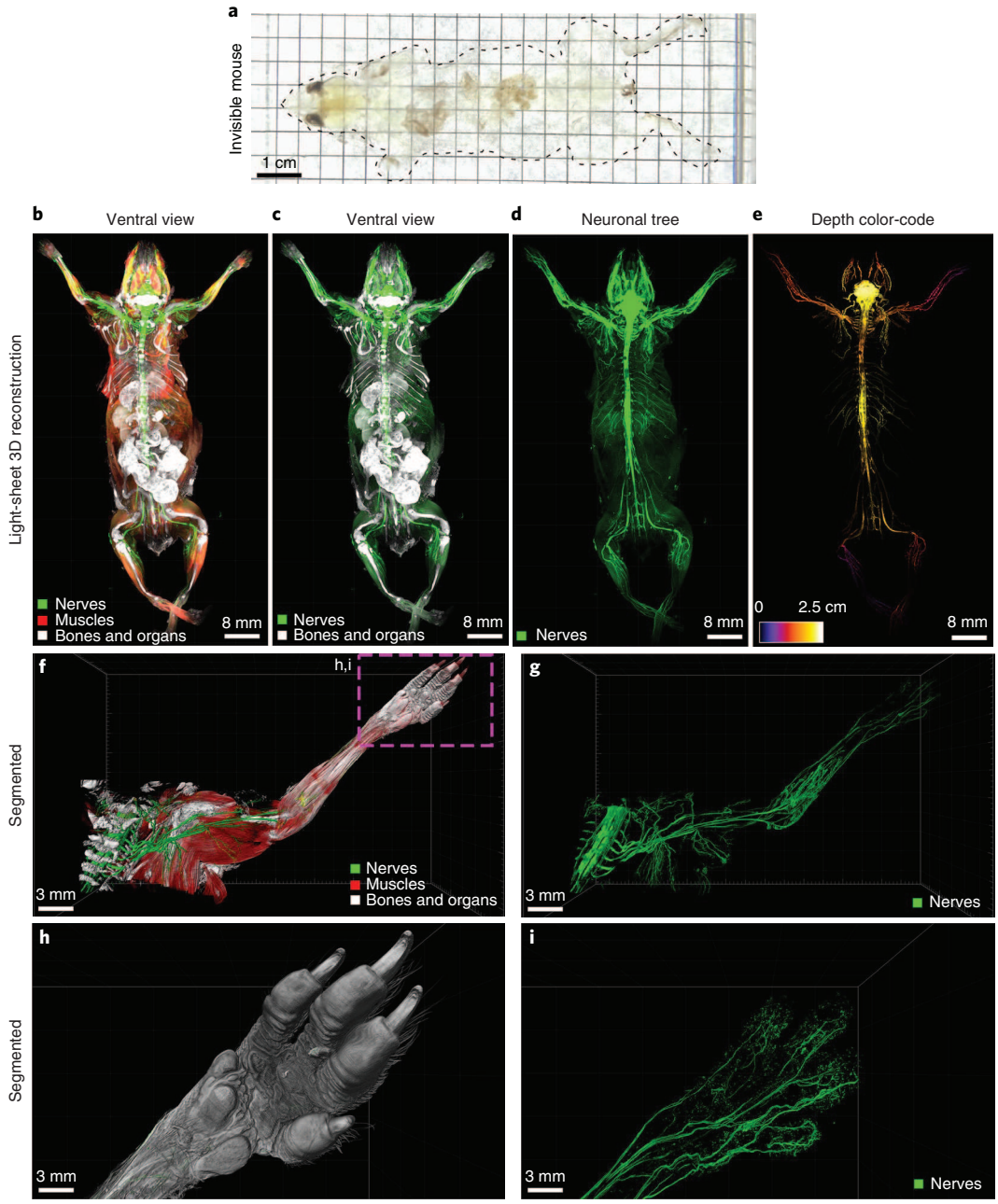

Fig. 2 | vDISCO panoptic imaging uncovers neuronal projections in intact mice. a, An example of a transparent 6-week-old mouse generated by vDISCO (similar results were observed from at least 20 independent mice). **b**–**e**, Three-dimensional reconstruction of complete neuronal projections of a 6-week-old *Thy1*-GFP-M mouse obtained by light-sheet microscopy imaging (similar labeling and imaging results were achieved at least in 5 different mice; whole-body reconstruction was performed on 2 mice). vDISCO boosted GFP$^+$ neuronal structures are shown in green, bones and internal organs are prominent with PI labeling in white, and the muscles visualized by autofluorescence background imaging are in red (**b**–**d**). The depth color-coding shows the neuronal projections at different *z* levels in the 2.5-cm-thick whole mouse body (**e**). **f**,**g**, High-resolution 3D reconstruction views of the left torso and forelimb from the same animal as in **b**–**e**. Details of innervation throughout muscles and bones are evident. **h**,**i**, Surface reconstruction of the paw (**h**) and its nerves (**i**) from the boxed region in **f**. See also Supplementary Videos 2–4.

axonal bundles coming from different roots enter the spinal cord at non-overlapping territories (Supplementary Fig. 16). Thus, the vDISCO approach provides a holistic view of the intact mouse, which should lead to novel discoveries on how interconnected organ systems function in health and what happens during their perturbation in disease.

Clearing of the whole body without removal of the skin. The skin is the largest organ, forming ~15–20% of the body. Among many other components, it consists of nerve endings, glands, immune cells, blood and lymphatic vessels, signifying its diverse biological roles in addition to being a physical barrier against the external environment[27]. However, clearing and imaging whole mice with skin has not been reported. Towards this goal, we adopted the vDISCO protocol to clear and image mice with skin. We observed that vDISCO could efficiently clear whole nude mice without removal of the skin (Fig. 3a,b). In addition, we cleared C57BL/6J (BL6) background mice after shaving the fur. In CX3CR1$^{GFP/+}$ mice, we could readily image

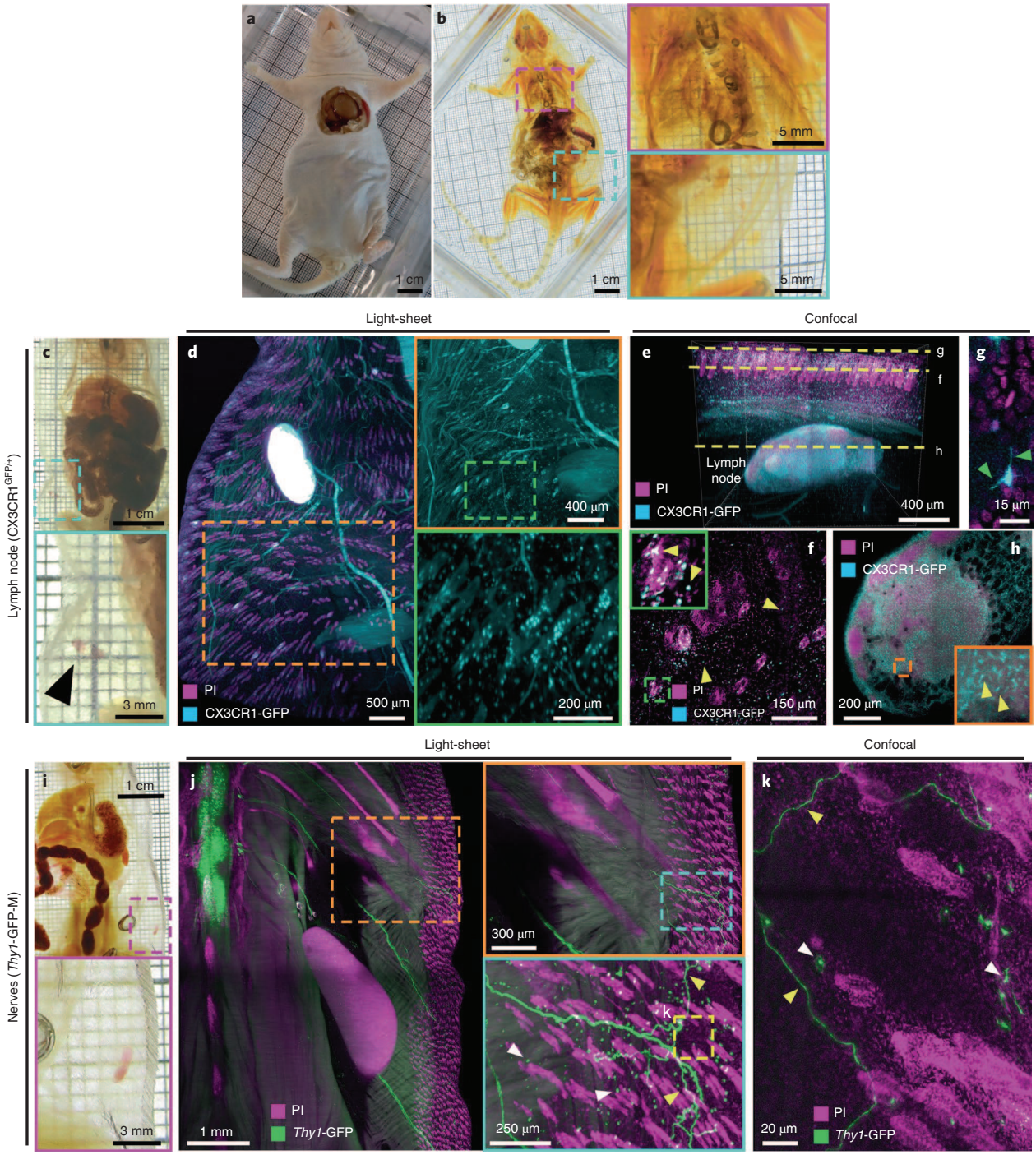

Fig. 3 | vDISCO panoptic imaging on mice with the intact skin. a,**b**, Adult NMRI nu/nu nude mouse, 3–4 months old (**a**), cleared with the vDISCO method (**b**): the insets show close-up views of the cleared lungs (magenta) and skin (cyan) in **b** (similar results were observed from 3 independent NMRI nu/nu mice). **c**–**h**, vDISCO on 6-week-old CX3CR1$^{GFP/+}$ mouse with intact skin. **c**, Cleared body, with the inset (cyan) showing visible inguinal lymph nodes (black arrowhead) through the transparent skin. **d**, Light-sheet images of CX3CR1$^{GFP/+}$ mouse boosted with anti-GFP 647-nanobooster (cyan) and labeled with PI (magenta), showing CX3CR1 GFP$^+$ cells (cyan) densely located in the lymph node and sparsely located in and under the skin, such as around hair follicles (magenta). **e**–**h**, Confocal 1-mm *z*-scan of the skin and lymph node in **d** with visible CX3CR1 GFP$^+$ cells (cyan) and nuclei (magenta). **e**, Three-dimensional rendering of the stack showing the skin and the lymph node beneath. **f**, Two-dimensional image at the level of the skin with individual CX3CR1 GFP$^+$ cells in the tissue and in the hair follicles (yellow arrowheads). **g**, The fine details of the ramifications of the immune cells at the surface of the skin are visible (green arrowheads). **h**, Two-dimensional image of the lymph node with visible immune cells (yellow arrowheads) in the organ. See also Supplementary Video 5. **i**–**k**, vDISCO on 2-month-old *Thy1*-GFP-M mouse with intact skin. **i**, Cleared body, with the inset (magenta) showing a visible inguinal lymph node through the skin. **j**, Light-sheet images of *Thy1*-GFP-M mouse boosted with anti-GFP 647-nanobooster (green) and labeled with PI (magenta), showing *Thy1*-GFP-expressing immune cells (white arrowheads) and neuronal projections coming from the spinal cord and projecting to the rest of the body, including the skin (green); the insets show close-up details of a neuronal projection (green fibers and yellow arrowheads) projecting into the skin. **k**, High-magnification confocal image of the region in **j** (yellow dashed rectangle) showing details of the immune cells (white arrowheads) and neuronal projections (green and yellow arrowheads) into the skin of the animal. All the results from **c** to **k** were similarly observed in 2 independent mice for each mouse line.

immune cells through the intact skin owing to the increase of fluorescent signal by vDISCO (Fig. 3c–h and Supplementary Video 5). In *Thy1*-GFP-M mice, we observed the axonal innervations in the skin in addition to *Thy1* GFP$^+$ immune cells[28] located under the skin (Fig. 3i–k). These results demonstrate that vDISCO allows detailed imaging of intact mice with skin, which may be of great value for studying skin-related pathologies.

Degeneration of peripheral nerve terminals after brain injury. Traumatic brain injury (TBI) is a major cause of death and disability, and currently there is no disease-modifying treatment available to combat especially chronic sequelae. In addition to its acute consequences, TBI often leads to chronic focal and global neurological impairments, such as dementia, epilepsy, progressive motor decline, peripheral neuropathy and dystonia[29,30]. These impairments could be due to degeneration of the corresponding brain regions and/or the dysfunction of nerves outside of the brain. However, so far, the impact of TBI on long-range neuronal projections outside of the brain has not been assessed. For example, while TBI-induced sensory-motor dysfunction has been observed in both animal models and human pathologies[31–34], the underlying mechanisms remain unknown, hampering the development of effective therapeutic approaches. Here, imaging the whole CNS, we found extensive neurodegeneration of the descending motor axons in the brainstem and spinal cord upon TBI over the right somatosensory and motor cortices (Supplementary Fig. 17). However, how TBI alters neuronal projections in the peripheral nervous system remains elusive. We used panoptic imaging to examine neuronal changes throughout the body more than a month after the brain injury (chronic stage) in comparison with control animals. As mainly axons innervating muscles are labelled in *Thy1*-GFP-M mice, we primarily focused on these nerve terminals. Our quantifications conducted in intact cleared mouse bodies demonstrated that the complexity of nerve terminals at the neuromuscular junctions was reduced after TBI, especially in the upper torso, compared with unlesioned control mice (Fig. 4a–d). We observed that nerve endings were reduced in complexity at the contralateral body regions, with fewer axonal ramifications left, implying partial degeneration of these axon terminals (Fig. 4e,f). Interestingly, we also observed changes at the ipsilateral axons, albeit to a smaller degree with respect to the contralateral body region (Fig. 4e). Overall, these data demonstrate that light-sheet microscopy imaging of entire transparent mouse bodies by vDISCO holds great promise for discovering hitherto unknown biological and pathophysiological processes.

Visualizing new routes for immune cell trafficking in the brain and spinal cord. The lymphatic system, which connects various lymphatic organs in the body, is crucial for immune responses. Until recently, the brain was considered to be devoid of any lymphatic vessels. In recent years, brain lymphatic vessels were re-discovered and are considered to play critical roles in brain pathologies[35–38]. As these lymphatic vessels are located between the brain and the skull[39], their connections are largely destroyed when the brain is harvested for standard histology.

We utilized panoptic imaging to overcome this hurdle and imaged details of meningeal vessels in intact transparent mice. We used *Prox1*-EGFP reporter mice, in which lymphatic endothelial cells express EGFP[40]. We readily observed previously described brain lymphatic structures, particularly along the sagittal sinus, pterygopalatine artery and transverse sinus (Fig. 5a–e and Supplementary Fig. 18) in addition to many other body regions (Supplementary Fig. 19 and Supplementary Video 6). Next, we imaged multiple subtypes of immune cells within and outside the meningeal vessels using the CX3CR1$^{GFP/+}$ × CCR2$^{RFP/+}$ mice by multiplexing with two different nanoboosters (anti-GFP conjugated to Atto-647N and anti-RFP conjugated to Atto-594N). The CX3CR1 GFP$^+$ microglia cells in the brain parenchyma (Fig. 5f,g) and CCR2 RFP$^+$ peripheral immune cells in the meningeal vessels were clearly identifiable (Fig. 5g,h and Supplementary Video 7). As expected, we also observed CX3CR1 GFP$^+$ immune cells in meningeal vessels, which likely represent meningeal monocytes and macrophages (Fig. 5h). It remains unclear how the immune cells within meningeal vessels contribute to the pathology of acute brain injuries, as they may be in an advantageous position to invade the brain. To start addressing this query, we used the middle cerebral artery occlusion (MCAO) model of stroke, which was performed in *LysM*-EGFP mice, a transgenic mouse line expressing EGFP in myeloid cells (mainly in neutrophils and monocytes) but not in microglial cells[41]. The mice with MCAO showed an invasion of LysM GFP$^+$ cells into the brain parenchyma, especially in the peri-infarct region, compared with sham-operated controls (Fig. 5i,j). Numbers of LysM GFP$^+$ cells also increased in the meningeal structures after MCAO (Fig. 5i), suggesting that the meninges might play a role as entry and/or exit routes of the brain in addition to the disrupted blood–brain barrier and the choroid plexus[42]. Thus, vDISCO panoptic imaging of transparent mice is a powerful tool to study the anatomy and cellular repertoire of meningeal vessels in health and disease.

Next, we aimed at investigating vascular connections between the skull and the meninges in greater detail. Towards this goal, we injected a cerebrospinal fluid (CSF) tracer (fluorophore-conjugated ovalbumin) into the cisterna magna in *VEGFR3*-YFP mice, another commonly used reporter line for meningeal vessels. We observed that the CSF tracer was quickly transported into the VEGFR3$^+$ meningeal vessels (Fig. 6a–d). Interestingly, we also observed that the tracer-labeled vessels extended into the skull (Fig. 6b,c). We further investigated the details of these new connections using lectin, another vessel tracer binding to endothelial cells. We found that these vascular connections are mostly located between the skull marrow and the outer surface of the meninges (both at the brain and sagittal sinus interfaces; Fig. 6e,f, Supplementary Fig. 20 and Supplementary Videos 8 and 9). We measured that they have an average size of 46.9 ± 5.8 µm in length and 19.2 ± 2.5 µm in width at the brain interface and of 83.7 ± 0.3 µm in length and 28.5 ± 1.8 µm in width at the sagittal sinus interface (mean ± s.e.m., $n = 3$ mice; Supplementary Fig. 20); therefore, we named them as short skull–meninges connections (SMCs). They also occasionally contain cells (Fig. 6e,f and Supplementary Fig. 20). To address whether the SMCs might play a role in neuropathological conditions, we studied the distribution of LysM GFP$^+$ immune cells in these connections after MCAO. The mice with MCAO showed significantly more LysM GFP$^+$ cells in the SMCs compared with sham-operated controls (Fig. 6g–i and Supplementary Video 10), suggesting that they might represent an entry route for myeloid cells from the skull marrow to the meningeal compartments after brain injury. Thus, vDISCO imaging revealed connections between skull and meninges, which might be important for immune cell trafficking, especially during brain pathologies.

Finally, we explored the immune cell trafficking after spinal cord injury using vDISCO panoptic imaging. To this end, we induced a spinal cord injury in *CD68*-EGFP transgenic mice expressing EGFP in monocytes and macrophages[43]. Upon spinal cord injury, we observed an influx of CD68 GFP$^+$ cells at the lesion site as well as a rather widespread increase in CD68 GFP$^+$ cells around the spinal cord (Supplementary Fig. 21 and Supplementary Video 11). Indeed, only 3.5% of these phagocytes were seen in the injured spinal cord, while ~96.5% of the CD68 GFP$^+$ cells were located in the surrounding tissues of the spinal cord including adjacent muscles, spinal cord roots and meningeal vessels, similar to sham mice (Supplementary Fig. 22). Thus, vDISCO is a powerful tool to image and quantify the trafficking of immune cells to and within the injured CNS.

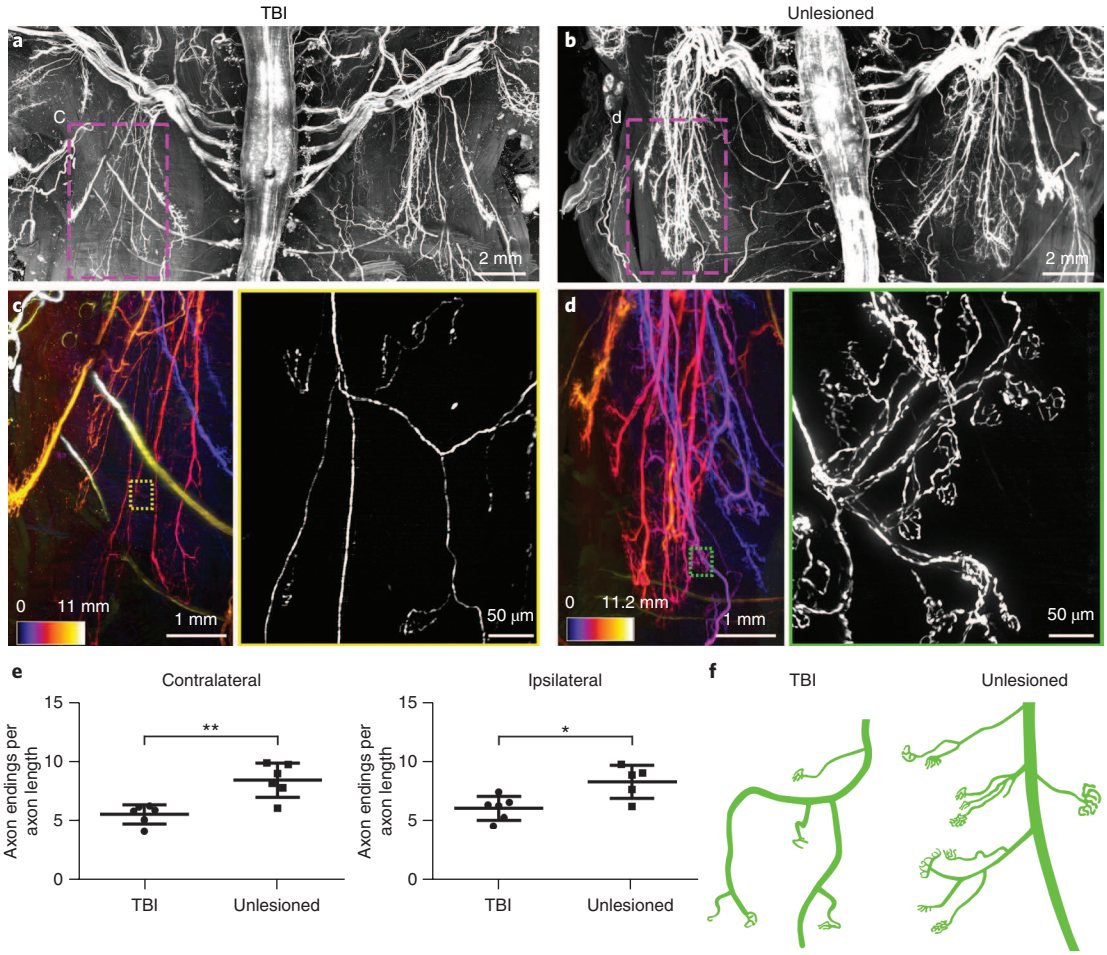

Fig. 4 | TBI-induced peripheral nerve degeneration revealed by vDISCO panoptic imaging. a,**b**, Background-equalized light-sheet microscopy maximum intensity projections of the torso from TBI-induced (**a**) vs. unlesioned control (**b**) *Thy1*-GFP-M mice. **c**,**d**, High-magnification views of marked regions in **a** and **b**, showing the left thoracic peripheral nerve projections in the TBI (**c**) vs. control animal (**d**); the color-code indicates the *z*-depth of anatomical regions as given in the scale bars. The colored rectangles show the high-magnification images of the marked regions in **c** and **d**, respectively, demonstrating fewer intact peripheral nerve endings in TBI mice compared with controls (similar results were observed from 6 independent mice per group). **e**, Quantification of axonal projection complexity expressed as number of peripheral nerve endings over length of axonal ramifications in TBI versus control mice (3–5 months old) at the level of the contralateral side (left) and ipsilateral side (right) (mean ± s.d.; for the contralateral side, $n = 6$ animals per group; for the ipsilateral side, $n = 6$ mice for the TBI group and 5 mice for the unlesioned group, respectively; statistical significance ($^{**}P = 0.003$, $^{*}P = 0.03$) was assessed by two-tailed *t* test). **f**, Representative illustration showing the peripheral nerve ending morphology in TBI versus control mice.

Discussion

Panoptic imaging of transparent adult mouse bodies from head to toe holds the promise of providing an unbiased and highly resolved view of entire organ systems in health and disease. Here, we developed a new whole-body nanobody labeling method in conjunction with whole-body tissue clearing, enabling a reliable visualization and quantification of subcellular details throughout centimeters-thick tissues of intact mouse bodies. This new panoptic imaging technology is straightforward in application and is suitable for systemic analysis of a vast range of biomedical inquires, as demonstrated here in visualization of the neuronal projections in whole mouse bodies, the description of vascular pathways between the skull and meninges, and the visualization of remote neuronal and immune consequences of acute CNS injury models. While we developed vDISCO for panoptic imaging of the whole mouse body, it is readily applicable for individual organs, using a simplified protocol to drastically increase and stabilize the signal contrast, as we show for mouse brains imaged more than a year after boosting and clearing (Supplementary Video 12 and Supplementary Table 1).

The panoptic imaging of nervous and immune systems in intact mouse bodies was achieved owing to the massive enhancement of the signal intensity by one to two orders of magnitude via whole-body immunolabeling employing nanobodies conjugated to bright dyes in the far-red spectrum. Therefore, the strong autofluorescence of tissues in shorter-wavelength spectra, in which traditional fluorescent proteins such as GFP are excited and imaged, is avoided. Here, we primarily used Atto dyes at 647 nm, and additional Atto 594 nm for multiplexing two different cell types. In the future, usage of nanobodies conjugated to dyes that emit in the near-infrared range[44] can further facilitate multiplexed detection of more than two targets. While the number of commercially available nanobodies is still limited, the nanoboosters used in this study can stain a broad selection of 21 different fluorescent proteins including EGFP, YFP, Venus, mCherry, and mRFP. Our method can also be used with nanobodies against endogenous proteins, as we demonstrated using anti-vimentin nanobodies labeling activated glia cells in the brain upon trauma[45,46]. Currently, nanobodies are developed mainly for *in vivo* applications due to their small size (for example, for crossing the blood–brain barrier)[47]; therefore, they are mostly selected for

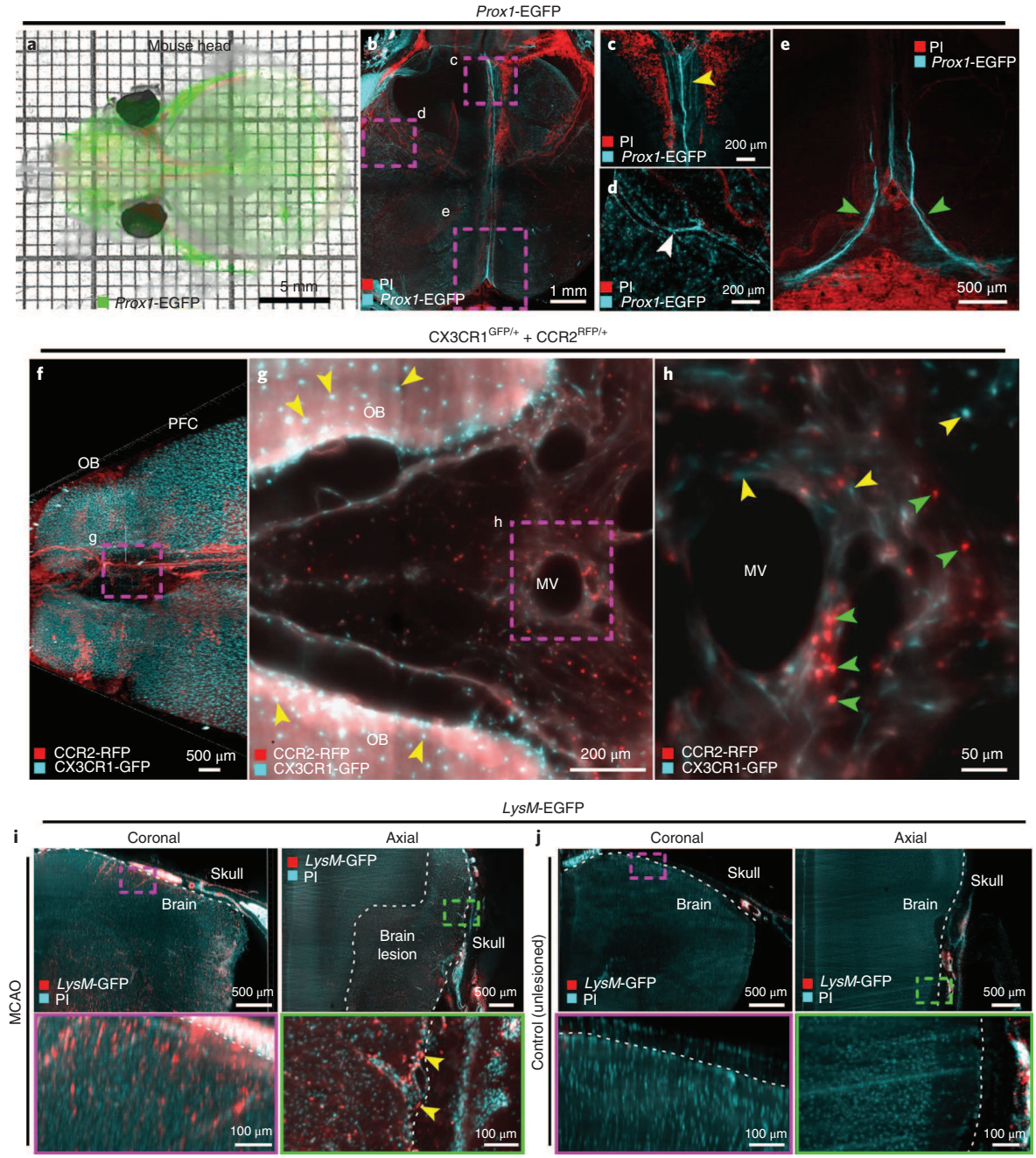

Fig. 5 | Visualizing meningeal vessels through intact skull by vDISCO panoptic imaging. a, A representative 4-week-old transparent *Prox1*-EGFP mouse head from 5 independent animals, showing the labeled vessels underneath the skull. **b**–**e**, The *Prox1*-EGFP mouse head, showing the brain lymphatic vessels along the sagittal sinus, pterygopalatine artery and transverse sinus (yellow, white and green arrowheads in **c**, **d** and **e**, respectively). Bone structures become prominent with PI labeling (red). Single experiment. **f**, Three-dimensional visualization of prefrontal cortex (PFC) and olfactory bulb (OB) in a 2-month-old CX3CR1$^{GFP/+}$ (cyan) and CCR2$^{RFP/+}$ (red) double-transgenic mouse (similar results were observed from 3 independent double-transgenic mice). **g**,**h**, High-magnification image of marked region in **f**, showing CCR2 RFP$^+$ cells (green arrowheads) and CX3CR1 GFP$^+$ cells (yellow arrowheads) in meningeal vessels (MV). See also Supplementary Video 7. **i**,**j**, *LysM*-EGFP transgenic mice (6 months old) with MCAO versus unlesioned control, showing the infiltration of immune cells in MCAO (similar results were observed from 4 independent mice per group). LysM GFP$^+$ cells are shown in red and nucleus labeling by PI in cyan. Immune cells in the meningeal vessels of the injured mice were observed (yellow arrowheads). All images were obtained by light-sheet microscopy.

in vivo epitopes but not for fixed tissues. We believe that our study will encourage the production of diverse nanobodies for deep-tissue immunolabeling.

Here, we used transgenic mice endogenously expressing fluorescent proteins; however, the labeling can also be achieved by rabies virus retrograde tracing, systemic adeno-associated virus injections[48] or transplantation of genetically engineered cells (such as stem cells or adoptive transfer of immune cells). Another key advantage of vDISCO panoptic imaging is that upon staining with Atto dyes through nanoboosting, the signal becomes permanent, permitting long-term imaging sessions and future re-analysis of the same sample if needed. This also enables high-resolution imaging

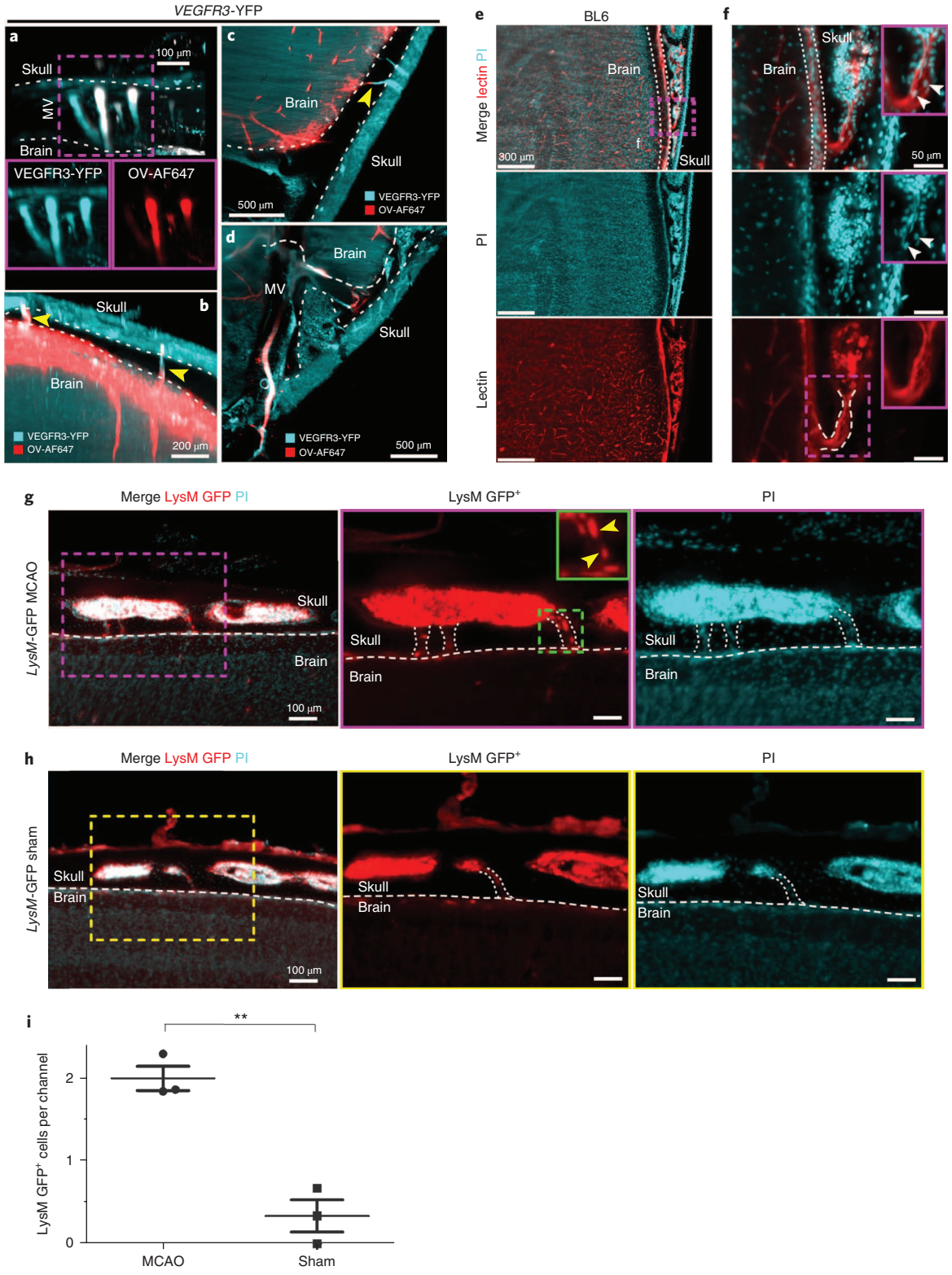

Fig. 6 | Uncovering SMCs through intact skull by vDISCO panoptic imaging. a–d, A 6-month-old *VEGFR3*-YFP mouse head in sagittal (**a**,**b**) and axial (**c**,**d**) views, showing that injected CSF tracer (ovalbumin–Alexa647 (OV-AF647); red) fills not only meningeal vessels but also some short SMCs between skull marrow and brain surface (**b**,**c**; yellow arrowheads). Representative images, single experiment. **e**,**f**, Details of SMCs after whole mouse body PI and lectin labeling of a 3-week-old BL6 mouse processed by vDISCO: the SMCs from skull marrow to brain surface with a funnel-shaped opening are marked with dashed lines in **f**. Cells in the channel are indicated by white arrowheads. Similar results were observed from 5 independent mice. **g**,**h**, *LysM*-EGFP transgenic mice (6 months old) after MCAO (**g**) versus sham control (**h**), showing increased numbers of LysM GFP$^+$ cells (yellow arrowheads) in the SMCs (marked with dashed lines) in MCAO. Similar results were observed from 3 independent mice per group. LysM GFP$^+$ cells are shown in red and nucleus labeling by PI in cyan. See also Supplementary Video 10. **i**, Quantification of LysM GFP$^+$ cells in the SMCs in MCAO versus sham mice (mean ± s.e.m., $n = 3$ animals per group; statistical significance ($^{**}P = 0.003$) was assessed by two-tailed *t* test).

of desired body parts by confocal or two-photon microscopy. Indeed, the samples from this study are available to the scientific community upon request for further studies. We believe making vDISCO-treated samples accessible to other labs for further studies can save time and resources, reduce the number of mice used in experimental research and create more powerful datasets by allowing direct correlation of various inquiries by multiple studies from the same animals.

A current limitation is the absence of light-sheet microscope systems that could image the entire body of a mouse in one session without any displacement and turning of the sample. Construction of such new light-sheet microscopes should further decrease the time needed for data acquisition and simplify data processing for 3D reconstruction. In fact, as shown here, optics and light sources of current commercial light-sheet microscopes are sufficient to image intact mouse bodies at subcellular resolution, although the whole body has to be manually moved in the imaging chamber to achieve the scanning of different body regions. In addition, development of machine learning-based (artificial intelligence) algorithms to automatically identify and quantify cellular changes on the whole-organism scale will be important to further scale up this technology in the future.

Using panoptic imaging, we constructed a neuronal projection map for the *Thy1*-GFP-M transgenic line, showing subcellular details of long-range neuronal connections from the CNS to the distal extremities. Here, we visualized neuronal details in *Thy1*-GFP-M mice, in which only a subset of CNS neurons and peripheral nervous system neurons innervating skeletal muscles are labeled. In the future, panoptic imaging of other transgenic lines labeling a greater and more diverse subset of neurons will allow the exploration of other biological systems such as the autonomic innervation of internal organs.

In recent years, researchers have been providing more evidence on post-TBI changes that seem to form the basis of chronic complications, such as epilepsy, neuropsychiatric disorders, dementia and progressive motor decline[29]. However, the effects of a localized brain lesion on the rest of the body have been poorly understood, mainly due to the technical challenges in studying long-range neuronal projections. Because vDISCO fluorescent signal boosting allows both imaging and quantifications of light-sheet microscopy images of transparent mouse bodies, we identified TBI-induced changes at the peripheral axonal projections innervating the skeletal musculature of the torso. These data are in line with recent work by others and us demonstrating the functional deficits in fine motor movements in mice and the presence of sensory-motor dysfunctions in TBI patients[29,30,33]. Our data provide a possible cellular mechanism for these functional impairments, suggesting that they could arise due to degeneration of long-range axons throughout the spinal cord and peripheral nervous system. This discovery opens alternate avenues for the identification of therapeutic targets. For instance, recent literature showed that microtubule stabilization is a powerful way to block degeneration of axons in spinal cord injury[49]. In this regard, it would be important to assess whether microtubule stabilization would also counteract axon degeneration outside of the brain and circumvent the development of chronic sensory-motor dysfunctions. Here, we also demonstrated that meningeal vessels extending between the cranium and CNS tissue and their cellular content can readily be imaged by vDISCO panoptic imaging in naïve animals and acute CNS injury models. Importantly, we observed short vascular connections between the skull and meninges both at the brain interface (recently seen also by others[50]) and at the sagittal sinus, which were filled with immune cells following ischemic stroke injury. Most of the SMCs seem to be open both at the skull marrow and meningeal ends without being connected to the vascular system of the brain/head (Supplementary Video 9). In the future, it will be important to identify to which meningeal compartment or compartments (subdura, subarachnoid or subpial) the SMCs are connected. In addition, due to the present lack of appropriate reporter mice, it was not possible to distinguish the type of SMCs (blood or lymphatic vessels) with increased LysM$^+$ cells after stroke. In the future, vDISCO imaging of immune cells in a lymphatic vessel reporter mouse line with different fluorescent proteins (for example, *LysM*-EGFP + *Prox1*-RFP double reporter) could reveal more details of this new route for immune cell infiltration. As neuroinflammation is a major determinant of neuronal function and survival following CNS injuries of various etiologies, our technology should accelerate investigation of these novel immune cell infiltration routes in various CNS pathologies.

In conclusion, vDISCO enhancement and stabilization of fluorescent proteins combined with signal acquisition in far-red spectra should facilitate discovery of previously inaccessible biological information. For example, imaging and quantification of neuronal projections, vascular organizations and immune cell populations in the entire mouse body should contribute to a more comprehensive understanding of the initiation, progression and extent of neurological conditions.

Online content

Any methods, additional references, Nature Research reporting summaries, source data, statements of data availability and associated accession codes are available at https://doi.org/10.1038/s41593-018-0301-3.

Received: 1 April 2018; Accepted: 21 November 2018;
Published online: 31 December 2018

References

1. Tuchin, V. V. & Tuchin, V. *Tissue Optics: Light Scattering Methods and Instruments for Medical Diagnosis* (SPIE Press, Bellingham, 2007).
2. Chung, K. et al. Structural and molecular interrogation of intact biological systems. *Nature* **497**, 332–337 (2013).
3. Yang, B. et al. Single-cell phenotyping within transparent intact tissue through whole-body clearing. *Cell* **158**, 945–958 (2014).
4. Renier, N. et al. iDISCO: a simple, rapid method to immunolabel large tissue samples for volume imaging. *Cell* **159**, 896–910 (2014).
5. Susaki, E. A. et al. Whole-brain imaging with single-cell resolution using chemical cocktails and computational analysis. *Cell* **157**, 726–739 (2014).
6. Erturk, A. et al. Three-dimensional imaging of solvent-cleared organs using 3DISCO. *Nat. Protoc.* **7**, 1983–1995 (2012).
7. Erturk, A. et al. Three-dimensional imaging of the unsectioned adult spinal cord to assess axon regeneration and glial responses after injury. *Nat. Med.* **18**, 166–171 (2011).
8. Belle, M. et al. A simple method for 3D analysis of immunolabeled axonal tracts in a transparent nervous system. *Cell Rep.* **9**, 1191–1201 (2014).
9. Costantini, I. et al. A versatile clearing agent for multi-modal brain imaging. *Sci. Rep.* **5**, 9808 (2015).
10. Ke, M. T., Fujimoto, S. & Imai, T. SeeDB: a simple and morphology-preserving optical clearing agent for neuronal circuit reconstruction. *Nat. Neurosci.* **16**, 1154–1161 (2013).
11. Dodt, H. U. et al. Ultramicroscopy: three-dimensional visualization of neuronal networks in the whole mouse brain. *Nat. Methods* **4**, 331–336 (2007).
12. Hama, H. et al. ScaleS: an optical clearing palette for biological imaging. *Nat. Neurosci.* **18**, 1518–1529 (2015).
13. Belle, M. et al. Tridimensional visualization and analysis of early human development. *Cell* **169**, 161–173 (2017).
14. Murray, E. et al. Simple, scalable proteomic imaging for high-dimensional profiling of intact systems. *Cell* **163**, 1500–1514 (2015).
15. Tainaka, K. et al. Whole-body imaging with single-cell resolution by tissue decolorization. *Cell* **159**, 911–924 (2014).
16. Jing, D. et al. Tissue clearing of both hard and soft tissue organs with the PEGASOS method. *Cell Res.* **28**, 803–818 (2018).
17. Pan, C. et al. Shrinkage-mediated imaging of entire organs and organisms using uDISCO. *Nat. Methods* **13**, 859–867 (2016).
18. Kubota, S. I. et al. Whole-body profiling of cancer metastasis with single-cell resolution. *Cell Rep.* **20**, 236–250 (2017).
19. Tuchin, V. V. *Optical Methods for Biomedical Diagnosis* (SPIE Press, Bellingham, WA, USA, 2016).

20. Muyldermans, S. Nanobodies: natural single-domain antibodies. *Annu. Rev. Biochem.* **82**, 775–797 (2013).
21. Feng, G. et al. Imaging neuronal subsets in transgenic mice expressing multiple spectral variants of GFP. *Neuron* **28**, 41–51 (2000).
22. Quan, T. et al. NeuroGPS-Tree: automatic reconstruction of large-scale neuronal populations with dense neurites. *Nat. Methods* **13**, 51–54 (2016).
23. Renier, N. et al. Mapping of brain activity by automated volume analysis of immediate early genes. *Cell* **165**, 1789–1802 (2016).
24. GageG. J., KipkeD. R. & ShainW. Whole animal perfusion fixation for rodents. *J. Vis. Exp.* **65**, e3564 (2012).
25. Greenbaum, A. et al. Bone CLARITY: clearing, imaging, and computational analysis of osteoprogenitors within intact bone marrow. *Sci. Transl. Med.* **9**, eaah6518 (2017).
26. Leijnse, J. N. & D'Herde, K. Revisiting the segmental organization of the human spinal cord. *J. Anat.* **229**, 384–393 (2016).
27. Gimenez-Arnau, A. Standards for the protection of skin barrier function. *Curr. Probl. Dermatol.* **49**, 123–134 (2016).
28. Haeryfar, S. M. & Hoskin, D. W. Thy-1: more than a mouse pan-T cell marker. *J. Immunol.* **173**, 3581–3588 (2004).
29. Smith, D. H., Johnson, V. E. & Stewart, W. Chronic neuropathologies of single and repetitive TBI: substrates of dementia? *Nature Rev. Neurol.* **9**, 211–221 (2013).
30. Frei, K. Posttraumatic dystonia. *J. Neurol. Sci.* **379**, 183–191 (2017).
31. Williams, G., Schache, A. & Morris, M. E. Running abnormalities after traumatic brain injury. *Brain Inj.* **27**, 434–443 (2013).
32. Chen, Y., Constantini, S., Trembovler, V., Weinstock, M. & Shohami, E. An experimental model of closed head injury in mice: pathophysiology, histopathology, and cognitive deficits. *J. Neurotrauma* **13**, 557–568 (1996).
33. Erturk, A. et al. Interfering with the chronic immune response rescues chronic degeneration after traumatic brain injury. *J. Neurosci.* **36**, 9962–9975 (2016).
34. Evans, T. M. et al. The effect of mild traumatic brain injury on peripheral nervous system pathology in wild-type mice and the G93A mutant mouse model of motor neuron disease. *Neuroscience* **298**, 410–423 (2015).
35. Louveau, A. et al. Structural and functional features of central nervous system lymphatic vessels. *Nature* **523**, 337–341 (2015).
36. Nedergaard, M. Neuroscience. Garbage truck of the brain. *Science* **340**, 1529–1530 (2013).
37. Da Mesquita, S. et al. Functional aspects of meningeal lymphatics in ageing and Alzheimer's disease. *Nature* **560**, 185–181 (2018).
38. Andres, K. H., von During, M., Muszynski, K. & Schmidt, R. F. Nerve fibres and their terminals of the dura mater encephali of the rat. *Anat. Embryol.* **175**, 289–301 (1987).
39. Louveau, A. et al. Understanding the functions and relationships of the glymphatic system and meningeal lymphatics. *J. Clin. Investig.* **127**, 3210–3219 (2017).
40. Choi, I. et al. Visualization of lymphatic vessels by *Prox1*-promoter directed GFP reporter in a bacterial artificial chromosome-based transgenic mouse. *Blood* **117**, 362–365 (2011).
41. Faust, N., Varas, F., Kelly, L. M., Heck, S. & Graf, T. Insertion of enhanced green fluorescent protein into the lysozyme gene creates mice with green fluorescent granulocytes and macrophages. *Blood* **96**, 719–726 (2000).
42. Llovera, G. et al. The choroid plexus is a key cerebral invasion route for T cells after stroke. *Acta Neuropathol.* **134**, 851–868 (2017).
43. Iqbal, A. J. et al. Human CD68 promoter GFP transgenic mice allow analysis of monocyte to macrophage differentiation in vivo. *Blood* **124**, e33–e44 (2014).
44. Hong, G., Antaris, A. L. & Dai, H. Near-infrared fluorophores for biomedical imaging. *Nat. Biomed. Eng.* **1**, 0010 (2017).
45. Noristani, H. N. et al. RNA-Seq analysis of microglia reveals time-dependent activation of specific genetic programs following spinal cord injury. *Front. Mol. Neurosci.* **10**, 90 (2017).
46. Villapol, S., Byrnes, K. R. & Symes, A. J. Temporal dynamics of cerebral blood flow, cortical damage, apoptosis, astrocyte-vasculature interaction and astrogliosis in the pericontusional region after traumatic brain injury. *Front. Neurol.* **5**, 82 (2014).
47. Leslie, M. Small but mighty. *Science* **360**, 594–597 (2018).
48. Deverman, B. E. et al. Cre-dependent selection yields AAV variants for widespread gene transfer to the adult brain. *Nat. Biotechnol.* **34**, 204–209 (2016).
49. Hellal, F. et al. Microtubule stabilization reduces scarring and causes axon regeneration after spinal cord injury. *Science* **331**, 928–931 (2011).
50. Herisson, F. et al. Direct vascular channels connect skull bone marrow and the brain surface enabling myeloid cell migration. *Nat. Neurosci.* **21**, 1209–1217 (2018).

Acknowledgements

This work was supported by the Vascular Dementia Research Foundation, Synergy Excellence Cluster Munich (SyNergy; EXC 1010), ERA-Net Neuron (01EW1501A; A.E.), Fritz Thyssen Stiftung (reference 10.17.1.019MN; A.E.), DFG (reference ER 810/2-1; A.E.), National Institutes of Health (A.E. and M.N.), Helmholtz ICEMED Alliance (A.E.), the Novo Nordisk Foundation (M.N.), the Howard Hughes Medical Institute (B.T.K.) and the Lundbeck Foundation (A.L.R.X. and M.N.). We thank A. Weingart for illustrations, F. Hellal for technical advice and critical reading of the manuscript, and F. P. Quacquarelli and G. Locatelli for help during initial optimization. A.E, C.P., R.C., A.L. and M.I.T. are members of the Graduate School of Systemic Neurosciences at the Ludwig Maximilian University of Munich.

Author contributions

A.E. initiated and led all aspects of the project. R.C. and C.P. developed the method and conducted most of the experiments. R.C. A.G., C.P., H.S.B., M.R., and B.M. analyzed data. M.I.T. stitched and analyzed the whole mouse body scans. A.P.D., B.F., S.Z. and L.M. helped to optimize the protocols. I.B., H.S.B., and S.L. helped to investigate skull–meninges connections. D.T. and M.K. contributed spinal cord injury experiments; C.B. and A.L., MCAO experiments; and A.X., B.K. and M.N., cisterna magna injection experiments. A.E., R.C. and C.P. wrote the paper. All the authors edited the manuscript.

Competing interests

A.E. filed a patent on some of the technologies presented in this work.

Additional information

Supplementary information is available for this paper at https://doi.org/10.1038/s41593-018-0301-3.

Reprints and permissions information is available at www.nature.com/reprints.

Correspondence and requests for materials should be addressed to A.E.

Publisher's note: Springer Nature remains neutral with regard to jurisdictional claims in published maps and institutional affiliations.

Methods

Animals. We used the following mixed-gender animals in the study: CX3CR1$^{GFP/+}$ (B6.129P-Cx3cr1tm1Litt/J; Jackson Laboratory strain code 005582)[51], *Thy1*-GFP-M and *Thy1*-YFP-H[21], *Prox1*-EGFP (Tg(Prox1-EGFP)KY221Gsat/Mmucd; Mutant Mouse Resource and Research Centers strain code 031006-UCD), *VEGFR3*-YFP, CX3CR1$^{GFP/+}$×CCR2$^{RFP/+}$ (B6.129(Cg)-Ccr2tm2.1Ifc/J; Jackson Laboratory strain code 017586), *LysM*-EGFP (Lyz2tm1.1^{Graf}, Mouse Genome Informatics strain code 2654931), *CD68*-EGFP (C57BL/6-Tg(CD68-EGFP)1Drg/j; Jackson Laboratory strain code 026827), C57BL/6J, and NMRI nu/nu mice. The animals were housed under a 12/12 h light/dark cycle. The animal experiments were conducted according to institutional guidelines (Klinikum der Universität München/Ludwig Maximilian University of Munich), after approval of the ethical review board of the government of Upper Bavaria (Regierung von Oberbayern, Munich, Germany) and the Animal Experiments Council under the Danish Ministry of Environment and Food (2015-15-0201-00535), and in accordance with the European directive 2010/63/EU for animal research. Ages of the animals are indicated in the figure legends. All data are reported according to the Animal Research: Reporting of In Vivo Experiments (ARRIVE) criteria. Sample sizes were chosen on the basis of prior experience with similar models and are specified in figure legends. Within each strain, animals were randomly selected. Animals that resulted negative for the expression of fluorescent proteins by genotyping were excluded from the study. No statistical methods were used to pre-determine sample sizes, but our sample sizes are similar to those reported in previous publications[17].

TBI. TBI was performed using a controlled cortical impact device (Leica Benchmark Stereotaxic Impactor, 39463923). At 30 min before surgery, we administered carprofen (4 mg per kg body weight) and buprenorphin (0.05 mg per kg) to the animals via subcutaneous injection. Then, anesthesia was induced in animals with 4% isoflurane in a N_2O/O_2 (70%/30%) mixture and afterwards maintained with 1.5% isoflurane in the same mixture for the whole surgery. As soon as the animals did not show any pedal reflex, they were placed in the associated stereotaxic apparatus, and their body temperature was kept at 37 °C using a heating pad for the whole surgery procedure. Next, the scalp of the animals was shaved, aseptically prepared by wiping with Octenisept (Schülke, 22580-A) as disinfectant and the skin of the scalp was incised longitudinally between the occiput and forehead. We identified the target area of the injury, which was the right somatosensory cortex extending to the motor cortex, using the stereotaxic frame (bregma coordinates: 2 mm posterior, 5 mm right lateral). The injury was then triggered via controlled cortical impact machine using the following parameters: impact speed, 6.9 m s^{-1}; impact duration, 400 ms; impact depth, 2 mm. With these parameters, the resulting injury was severe, with cracks in the skull, bleeding and exposed brain tissue. After the impact, the skin was sutured with metallic wound closure clips (VWR, 203-1000), and the animals were kept at 31 °C in a recovery chamber (Mediheat, 34-0516) for at least 30 min until they recovered from the anesthesia. In the following days, animals were subcutaneously injected with carprofen (4 mg per kg) once per day for 4 d and sacrificed at >1 month post-injury by transcardial perfusion according to the 'Perfusion and tissue preparation' section below.

MCAO model. Experimental stroke was induced using the intraluminal filament model of MCAO (fMCAO) for transient, focal brain ischemia. Mice were anesthetized with isoflurane delivered in a mixture of 30% O_2 and 70% N_2O. A heat-blunted nylon suture (6/0) was inserted into the external carotid artery and advanced until it obstructed the middle cerebral artery together with the ligation of the common carotid artery for 30 min. Regional cerebral blood flow (bregma coordinates: 2 mm posterior, 5 mm lateral) was continuously recorded by transcranial laser Doppler flowmetry from the induction of ischemia until 10 min after reperfusion. Following fMCAO, mice were placed in temperature-controlled recovery cages for 2 h to prevent post-surgery hypothermia. For the survival period (3 d), the mice were kept in their home cage with facilitated access to water and food. Sham-operated mice received the same surgical procedure without insertion of the filament. Body temperature was maintained throughout surgery using a feedback-controlled heating pad and kept constant (37.0 ± 0.5 °C). Exclusion criteria were as follows: insufficient MCAO (a reduction in blood flow to 15% of the baseline value) and blood flow recovery >80% within 10 min of reperfusion. Mice were sacrificed at 3 d post-injury by transcardial perfusion according to the 'Perfusion and tissue preparation' section below.

Cisterna magna injection for meningeal vessel labeling. For the cisterna magna injections, mice (*VEGFR3*-YFP; 6 months old) were anesthetized with a mixture of ketamine and xylazine (100 mg per kg and 10 mg per kg, respectively) via intraperitoneal injection. After toe pinch reflexes ceased, mice were fixed in a stereotaxic frame by the zygomatic arch, with the head slightly tilted to form an angle of 120° in relation to the body. The head and neck regions were shaved to expose the neck muscles, which were bluntly dissected to expose the cisterna magna. Cannulas composed of a dental needle (SOPIRA Carpule 30 G 0.3 × 12 mm; Kulzer, AA001) and polyethylene tubing (0.024 in OD (outside diameter) × 0.011 in ID (interior diameter); Scandidact, PE10-CL-500) were used to perform the cisterna magna injections. A cannula filled with CSF tracer (2% ovalbumin 45 kDa conjugated to Alexa Fluor 647 (Thermo Fisher Scientific, O34784), diluted in artificial CSF (126 mM NaCl, 2.5 mM KCl, 1.25 mM NaH_2PO_4, 2 mM Mg_2SO_4, 2 mM $CaCl_2$, 10 mM glucose, 26 mM $NaHCO_3$; pH 7.4 when gassed with 95% O_2 and 5% CO_2)) was inserted into the cisterna magna. With the aid of an injection pump (LEGATO 130 Syringe pump; KD Scientific, 788130), 10 µl of CSF tracer was injected into the cisterna magna at a rate of 1 µl min^{-1}. At the end of the injection, CSF tracer was allowed to circulate in the subarachnoid and paravascular spaces for 1 h. Mice were then transcardially perfused according to the 'Perfusion and tissue preparation' section below.

Spinal cord injury model. Mice were deeply anesthetized by intraperitoneal injection of a combination of midazolam (5 mg per kg), medetomidine (0.5 mg per kg) and fentanyl (0.05 mg per kg). The mid-thoracic spinal cord of anesthetized *CD68*-EGFP mice was surgically exposed by a dorsal laminectomy as previously described[52]. A hemisection of the spinal cord was performed using fine-tip surgical scissors (Fine Science Tools 15000-08 spring scissor, 2.5 mm cutting edge). For sham surgery, the dorsal laminae of mid-thoracic vertebrae were surgically exposed in anesthetized *CD68*-EGFP mice. After spinal cord injury or sham surgery, muscle tissue and skin were sutured with a surgical thread (Ethilon suture 6-0, 667 H) and animals were allowed to recover on a heating pad. After 48 h, mice were transcardially perfused according to the 'Perfusion and tissue preparation' section below.

Perfusion and tissue preparation. Mice were deeply anesthetized using a combination of midazolam, medetomidine and fentanyl (MMF; 1 ml per 100 g body mass for mice; intraperitoneal). As soon as the animals did not show any pedal reflex, they were intracardially perfused with heparinized 0.1 M PBS (10 U ml^{-1} of heparin, Ratiopharm; ~110 mmHg pressure using a Leica Perfusion One system) for 5–10 min at room temperature until the blood was washed out, followed by 4% paraformaldehyde (PFA) in 0.1 M PBS (pH 7.4; Morphisto, 11762.01000) for 10–20 min. Next, optionally, skin and eyes as well as premaxilla and maxilla bones were carefully removed, the palate of the animal was opened (without damaging the tissue beneath), and the feces were gently washed out from the intestine with 0.1 M PBS through small cuts using a syringe. For the animals cleared with skin, the skin was not removed from the bodies, and in case of BL6 background animals, the fur was shaved off using a razor blade (Personna, 604305-001001). Then, the bodies were post-fixed in 4% PFA for 1 d at 4 °C and later washed with 0.1 M PBS for 10 min 3 times at room temperature. Either the whole-body nanoboosting procedure was started immediately or whole mouse bodies were stored in PBS at 4 °C for up to 4 weeks or in PBS containing 0.05% sodium azide (Sigma-Aldrich, 71290) for up to 6 months.

For the collection of dissected tissues such as brains, mice were perfused with PBS and PFA as described above. Subsequently, the organs of interest were dissected out and post-fixed in 4% PFA overnight at 4 °C, washed with 0.1 M PBS for 10 min 3 times at room temperature and kept in PBS plus 0.05% sodium azide for up to 3 weeks.

Clearing of unboosted samples. For the quantification of fluorescence signal after clearing, without boosting, we followed the uDISCO passive clearing protocol as described by Pan et al.[17]. In brief, dissected brains were placed in 5 ml tubes (Eppendorf, 0030 119.401) and covered with 4.5 ml of clearing solution. All incubation steps were performed in a fume hood with gentle shaking or rotation, with the samples covered with aluminum foil to keep them in dark. To clear the samples, we incubated them in a gradient of *tert*-butanol (Sigma-Aldrich, 360538): 30 vol%, 50 vol%, 70 vol%, 80 vol%, 90 vol%, 96 vol% (in distilled water), and 100 vol% twice at 35 °C for 12 h each step followed by immersion in dichloromethane (Sigma-Aldrich, 270997) for 45–60 min at room temperature and finally incubation with the refractive index matching solution BABB-D15, containing 15 parts BABB (benzyl alcohol + benzyl benzoate 1:2; Sigma-Aldrich, 24122 and W213802), 1 part diphenyl ether (Alfa Aesar, A15791) and 0.4 vol% vitamin E (DL-α-tocopherol; Alfa Aesar, A17039), for at least 6 h at room temperature until transparency was achieved.

Nanobodies, antibodies and fluorescent dyes used in this study. The nanobodies, antibodies and fluorescent dyes used in this study are as follows: Atto594-conjugated anti-RFP nanobooster (Chromotek, rba594-100), Atto647N-conjugated anti-GFP nanobooster (Chromotek, gba647n-100), Atto488-conjugated anti-GFP nanobooster (Chromotek, gba488-100), Atto488-conjugated anti-vimentin nanobooster (Vimentin-Label_Atto488; Chromotek, vba488-100), Alexa647-conjugated anti-GFP antibody (Invitrogen, A31852), and PI (Sigma-Aldrich, P4864). For the nanobody and antibody validation information, see the Life Sciences Reporting Summary.

Validation of nanoboosters for vDISCO. Post-fixed brains from fluorescent protein-expressing mice (for example, *Thy1*-GFP-M) were cut into 400 µm slices using a vibratome (Leica, VT1200S). The slices were imaged before staining with a Zeiss AxioZoom EMS3/SyCoP3 fluorescence stereomicroscope to make sure that the samples have fluorescent protein expression. All the following steps were done with gentle shaking. The slices were first incubated for 3 h in a 24 multiwell (Falcon,

353504) at 37 °C with 1 ml of permeabilization solution containing 1.5% goat serum (Gibco, 16210072), 0.5% Triton X-100 (AppliChem, A4975,1000), 0.5 mM of methyl-β-cyclodextrin (Sigma-Aldrich, 332615), 0.2% *trans*-1-acetyl-4-hydroxy-L-proline (Sigma-Aldrich, 441562) and 0.05% sodium azide (Sigma-Aldrich, 71290) in 0.1 M PBS. Subsequently, they were incubated overnight at 37 °C with the same permeabilization solution, and the nanobooster of interest was added with dilution 1:500 considering final volume = 500 µl. The multiwell was covered with aluminium foil to keep the slices in dark and was sealed well with parafilm (Bemis, PM-992) to prevent the solution from drying out. One slice was kept as negative control where there was no adding of nanobooster. After the incubation, slices were washed with the washing solution (1.5% goat serum, 0.5% Triton X-100, 0.05% sodium azide in 0.1 M PBS) at room temperature for 15 min 4 times and then washed with 0.1 M PBS at room temperature for 10 min 3 times. Then the slices were imaged again after staining with the AxioZoom microscope to check whether the staining worked. In the end, slices were moved to 5 ml Eppendorf tubes wrapped with aluminium foil to keep them in dark and cleared with 3DISCO protocol: first they were incubated at room temperature in the following gradient of tetrahydrofuran (THF; Sigma-Aldrich, 186562) in distilled water (45 min for each step): 50 vol% THF, 70 vol% THF, 80 vol% THF, 100 vol% THF and 1 h 100 vol% THF; after dehydration, samples were incubated for 15 min in dichloromethane, and finally in BABB until transparency. Finally, the slices were imaged again with the AxioZoom microscope to make sure that the staining worked even after clearing. For more details of the AxioZoom imaging setup, see the 'Fluorescence stereomicroscopy imaging' section below.

vDISCO whole-body immunostaining, PI labeling and clearing. In order to remove remaining blood and heme after PFA perfusion, and to decalcify the bones, the animals were subjected to perfusion with decolorization solution and decalcification solution before immunostaining. The decolorization solution was made with 25–30 vol% dilution of CUBIC reagent 1[5] in 0.1 M PBS. CUBIC reagent 1 was prepared with 25 wt% urea (Carl Roth, 3941.3), 25 wt% *N,N,N′,N′*-tetrakis (2-hydroxypropyl)ethylenediamine (Sigma-Aldrich, 122262) and 15 wt% Triton X-100 in 0.1 M PBS. The decalcification solution consisted of 10 wt/vol% EDTA (Carl Roth, 1702922685) in 0.1 M PBS, adjusting the pH to 8–9 with sodium hydroxide (Sigma-Aldrich, 71687).

The solutions for the immunolabeling pipeline were pumped inside the body of the animal by transcardial-circulatory perfusion, exploiting the same entry point hole into the heart created during the PBS and PFA perfusion step (see above) and following the procedure described by Pan et al.[17]. In brief, the mouse body was placed in a 300 ml glass chamber (Omnilab, 5163279) filled with 250–300 ml of appropriate solution, which covered the body completely. Next, the transcardial-circulatory system was established involving a peristaltic pump (ISMATEC, REGLO Digital MS-4/8 ISM 834; reference tubing, SC0266), keeping the pressure at 160–230 mmHg (45–60 r.p.m.). One channel from the pump, made by a single reference tube, was set for circulation of the solution through the heart into the vasculature: one ending of the tube was connected to the tip of a syringe (cut from a 1 ml syringe; Braun, 9166017V) which held the perfusion needle (Leica, 39471024), and the other ending was immersed in the solution chamber where the animal was placed. The perfusion needle pumped the appropriate solution into the mouse body, and the other ending collected the solution exiting the mouse body to recirculate the solution, pumping it back into the animal. To fix the needle tip in place and to ensure extensive perfusion, we put a drop of superglue (Pattex, PSK1C) at the level of the hole where the needle was inserted inside the heart. Using the setting explained above, after post-fixation and PBS washing, the mice were first perfused with 0.1 M PBS overnight at room temperature; then, the animals were perfused with 250 ml of decolorization solution for 2 d at room temperature, exchanging with fresh decolorization solution every 6–12 h until the solution turned from yellowish to clear and the spleen became lighter in color (indicating that the blood heme was extracted). Then, they were perfused with 0.1 M PBS, washing for 3 h 3 times, followed by perfusion with 250 ml of decalcification solution for 2 d at room temperature and again perfusion/washing with 0.1 M PBS for 3 h 3 times. After this, the animals were perfused with 250 ml of permeabilization solution containing 1.5% goat serum, 0.5% Triton X-100, 0.5 mM of methyl-β-cyclodextrin, 0.2% *trans*-1-acetyl-4-hydroxy-L-proline and 0.05% sodium azide in 0.1 M PBS for half a day at room temperature. Subsequently, the perfusion proceeded further, through connection of a 0.20 µm syringe filter (Sartorius, 16532) to the ending of the tube not holding the needle to efficiently prevent accumulation of dye aggregates into the sample. At the same time, from this step we used an infrared lamp (Beuer, IL21) directed to the chamber to heat up the solution to 26–28 °C. With this setting, the animals were perfused for 6 d with 250 ml of the same permeabilization solution containing 35 µl of nanobooster, which is 20–35 µg in 250 ml (0.08–0.14 µg ml^{-1}), 1:7,000 in dilution (stock concentration 0.5–1 mg ml^{-1}; the amount of nanobody was adjusted depending on the expected presence of fluorescent protein in the mouse body) and 290 µl of PI (stock concentration 1 mg ml^{-1}). Next, we removed the animals from the chamber, and with fine scissors we removed a tiny piece from the back of the skull (above the cerebellum) at the level of the occipital bone; we then placed the bodies in a 50 ml tube (Falcon, 352070) filled with the same permeabilization solution containing an extra 5 µl of nanobooster and incubated the tubes at 37 °C with gentle shaking for an additional 2–3 d of labeling. After that, the mice were placed back in the perfusion system, and labeling solution was washed out by perfusing with washing solution (1.5% goat serum, 0.5% Triton X-100, 0.05% of sodium azide in 0.1 M PBS) for 3 h 3 times at room temperature and 0.1 M PBS for 3 h 3 times at room temperature.

After the staining, the animals were cleared using a 3DISCO-based passive whole-body clearing protocol optimized for big samples. The mice were incubated at room temperature in dehydration and clearing solutions inside a 300 ml glass chamber, kept with gentle rotation on top of a shaking rocker (IKA, 2D digital) inside a fume hood. For dehydration, mice bodies were incubated in 200 ml of the following gradient of THF in distilled water (12 h for each step): 50 vol% THF, 70 vol% THF, 80 vol% THF, 100 vol% THF and again 100 vol% THF, followed by 3 h in dichloromethane and finally in BABB. During all incubation steps, the glass chamber was sealed with parafilm and covered with aluminum foil. See Supplementary Table 1 and http://www.discotechnologies.org/vDISCO/.

vDISCO whole-mount immunolabeling of individual organs. vDISCO was performed on dissected organs as well: dissected brains were stained using the immunolabeling protocol for dissected organs. First, the post-fixed brains were pretreated, incubating them for 2 d at 37 °C with gentle shaking in 4.5 ml of same solution used at the permeabilization step (see above). Subsequently, the brains were incubated in 4.5 ml of this same permeabilization solution plus the nanobooster of interest with the concentration adjusted to expression of the target (for example, Atto647N-conjugated anti-GFP nanobooster dilution 1:600, which is ~5–8 µg of nanobooster in 4.5 ml (1.1–1.8 µg ml^{-1}; stock concentration, 0.5–1 mg ml^{-1}) for *Thy1*-GFP-M brains) for 12–14 d at 37 °C with gentle shaking, then brains were washed for 2 h 3 times and once overnight with the washing solution (1.5% goat serum, 0.5% Triton X-100, 0.05% of sodium azide in 0.1 M PBS) at room temperature and in the end washed for 2 h 4 times with 0.1 M PBS at room temperature. The immunostained brains were cleared with 3DISCO clearing: first they were put in the Eppendorf 5 ml tubes, and then they were incubated at room temperature with gentle shaking in 4.5 ml of the following gradient of THF in distilled water (2 h for each step): 50 vol% THF, 70 vol% THF, 80 vol% THF, 100 vol% THF and overnight ;vol% THF; after dehydration, the samples were incubated for 1 h in dichloromethane and finally in BABB until transparency. During all the clearing steps, the tubes were wrapped with aluminum foil to keep them in dark. See Supplementary Table 1.

For the comparison of deep-tissue staining efficiency in terms of penetration of the staining of nanobody versus conventional antibody (Supplementary Fig. 2), we followed the same protocol described above in this section for both nanobody and antibody experimental groups. The only exception was that for the antibody group, in the immunostaining step, we replaced the nanobooster with Alexa647-conjugated anti-GFP antibody (Invitrogen, A31852) with the same concentration (see above).

Pumping pressure measurement. A KKmoon Digital Manometer Pressure Gauge Manometer (HT-1891) was used to measure the pressure. To achieve one additional measuring channel to connect with the manometer, a two-head connector (B.Braun Discofix C Dreiwegehahn, 16494C) was inserted into the pumping channel, and the second head was further connected to the manometer with extended PVC tubing. The pumping channel was set in the standard way as described including a transcardiac perfusion needle. First, the switch on the two-head connector was set without connecting the measuring tubing, and pumping was started until all the air bubbles were excluded from the pumping channel. Subsequently, the switch was set to connect the measuring tubing while pumping was continued, and the pressure was measured when the manometer readouts stabilized. Three measurements were made at different time points including morning, afternoon and evening to exclude the variation of room temperature, and the data were quantified by averaging.

Comparison of high-pressure versus low-pressure perfusion with methylene blue. The diffusion of methylene blue (Sigma-Aldrich, M9140), perfused into the body of the animals, was used to compare the efficiency of high-pressure versus low-pressure perfusion (Supplementary Fig. 8). For this purpose, we used 3 BL6 animals (4 months old) per experimental group: post-fixed whole bodies were perfused for 15 min with 0.05% methylene blue in 0.1 M PBS, at either 50 r.p.m. (~180 mmHg) for the high-pressure group or 25 r.p.m. (~70 mmHg) for the low-pressure group. The same pump setting explained in the section 'vDISCO whole-body immunostaining, PI labeling and clearing' was used, including the usage of superglue to fix the needle in place inside the hole in the heart.

iDISCO+. *Antibody validation: methanol compatibility test.* Before performing the comparison of the efficiency between vDISCO nanobody staining and iDISCO+ antibody staining on whole brains, we verified the compatibility of the chosen antibody with the iDISCO+ protocol (Supplementary Fig. 3a–d). This was done performing the antibody validation step, which tested the compatibility of the antibody with the methanol pretreatment required by iDISCO+. To do so, we followed the original iDISCO+ publication[23] and the latest protocol updates from https://idisco.info. Briefly, post-fixed brains from *Thy1*-GFP-M and CX3CR1$^{GFP/+}$

mice (2–3 months old) were cut into 600 µm slices with a vibratome. First, the slices were incubated overnight in 100% methanol (Roth, 4627.6) at room temperature; then, after rehydrating and washing with 0.1 M PBS, the iDISCO+ immunostaining protocol was done as normally using 3 h as permeabilization time, 6 h as blocking time and overnight as immunolabeling time, adding 1:850 of Alexa647-conjugated anti-GFP antibody (already used in the previous section) in 500 µl of incubation solution. Non-methanol-treated slices were used as positive controls. In the end, the slices were imaged using the Zeiss AxioZoom stereomicroscope (see 'Fluorescence stereomicroscopy imaging' section below).

iDISCO+ on dissected brains. After having verified that the previously mentioned conventional anti-GFP antibody is compatible with iDISCO+, we performed comparison of staining efficiency between vDISCO with nanobody and iDISCO+ with conventional antibody (Supplementary Fig. 3e–i). For this purpose, 3 $CX3CR1^{GFP/+}$ post-fixed brains (6–7 months old) were used per experimental group. The brains allocated into the vDISCO group were processed following the vDISCO protocol for dissected brains (see 'vDISCO whole-mount immunolabeling of individual organs' section), while the brains allocated into the iDISCO+ group were processed using 1:730 of the above-mentioned Alexa647-conjugated anti-GFP antibody following the iDISCO+ protocol and its updates from https://idisco.info (ref. [23]).

Different whole-body labeling protocols comparison. To show that vDISCO with nanobody is the only method that can efficiently boost the GFP signal in mouse whole bodies, we performed the following comparison using 3 GFP-M animals (2–3 months old) per experimental group: (1) high-pressure active perfusion vDISCO with nanobody, (2) passive incubation vDISCO with nanobody, (3) high-pressure active perfusion vDISCO with conventional antibody, (4) high-pressure active perfusion iDISCO+ with conventional antibody, and (5) high-pressure active perfusion iDISCO+ with nanobody. Group 1 was processed using the above-described vDISCO whole-body immunostaining and clearing method; the group 2 was processed following all the steps of the vDISCO whole-body immunostaining and clearing protocol described above, but replacing all the original steps done in perfusion with passive incubation; group 3 was processed using the same vDISCO whole-body immunostaining and clearing protocol, but replacing the nanobooster with Alexa647-conjugated anti-GFP antibody at the same concentration as the nanobooster during the staining step; groups 4 and 5 were processed performing the iDISCO+ methanol pretreatment on the animals followed by sequential perfusion of all the iDISCO+ solutions[23] (except that the clearing was done with passive incubation): the timing of each iDISCO+ step was adjusted considering the size of a whole body compared with a dissected brain (for example, during the methanol dehydration, each step was increased to 5 h versus 1 h for dissected brains). The antibody used for group 4 is the Alexa647-conjugated anti-GFP antibody mentioned above.

Previously published whole-body clearing methods for comparison. For PARS clearing, 10% EDTA adopted from Bone-CLARITY[25] was transcardially perfused through the whole mouse bodies after PFA fixation for 5–7 d to decalcify the bones. Then, the standard PARS procedure was followed[53]. CUBIC[18], uDISCO[17] and PEGASOS[16] were conducted based on the original publications. It is worth noting that among all the clearing methods tested, PARS, PEGASOS and vDISCO were characterized by a decalcification step using EDTA solutions.

Light-sheet microscopy imaging. Single-plane illuminated (light-sheet) image stacks were acquired using an Ultramicroscope II (LaVision BioTec), featuring an axial resolution of 4 µm with the following filter sets: ex 470/40 nm, em 535/50 nm; ex 545/25 nm, em 605/70 nm; ex 560/30 nm, em 609/54 nm; ex 580/25 nm, em 625/30 nm; ex 640/40 nm, em 690/50 nm. For low-magnification whole-body imaging of the *Thy1*-GFP-M mouse, we used a ×1 Olympus air objective (Olympus MV PLAPO ×1/0.25 NA (WD = 65 mm)) coupled to an Olympus MVX10 zoom body, which provided zoom-out and zoom-in ranging from ×0.63 up to ×6.3. Using ×1 objective and ×0.63 of zoom, we imaged a field of view of 2 × 2.5 cm, covering the entire width of the mouse body. Tile scans with 60% overlap along the longitudinal *y* axis of the mouse body were obtained from ventral and dorsal surfaces up to 13 mm in depth, covering the entire volume of the body using a *z*-step of 8 µm. Exposure time was 120 ms, laser power was adjusted depending on the intensity of the fluorescent signal (in order to never reach the saturation) and the light-sheet width was kept at maximum. After tile imaging of the sample within the entire field of view, already scanned regions were cut using a thin motorized dental blade (0.2 mm; Dremel 8200) for further imaging. After low-magnification imaging of the whole body, a forelimb of the *Thy1*-GFP-M animal was imaged with a ×2 objective (Olympus MVPLAPO2XC/0.5 NA (WD = 6 mm)) coupled with the same Olympus MVX10 zoom body at zoom magnification ×1.6. Moreover, the same ×2 objective with different zooms was used to perform high-magnification imaging of specific body regions (for example, the back of the animal at the level of lumbar vertebra, the inguinal lymph node area or the head). Individual organs (including brain, lungs, intestine and thymus) were imaged individually using high-magnification objectives: ×2 objective (Olympus MVPLAPO2XC/0.5 NA (WD = 6 mm)) coupled with the same Olympus MVX10 zoom body, ×4 objective (Olympus XLFLUOR ×4 corrected/0.28 NA (WD = 10 mm)), ×25 objective (Olympus XLPLN ×25/0.95 NA (WD = 4 mm)) and ×20 objective (Zeiss ×20 Clr Plan-Neofluar/0.1 NA (WD 5.6 = mm)) coupled to an Olympus revolving zoom body unit (U-TVCAC) kept at ×1. High-magnification tile scans were acquired using 8–30% overlap, and the light-sheet width was reduced to obtain maximum illumination in the field. For the specific imaging settings used in each figure panel, see Supplementary Table 2.

Fluorescence stereomicroscopy imaging. For images in Supplementary Fig. 3, brain slices were kept immersed in PBS. For nanobody validation, cleared slices were put on a glass lid and kept immersed in BABB. The imaging was performed with Zeiss AxioZoom EMS3/SyCoP3 fluorescence stereomicroscope using Zen 2 software (v.2.0.0.0; Carl Zeiss AG) using a ×1 long-working-distance air objective lens (Plan Z ×1, 0.25 NA, WD = 56 mm; Supplementary Table 2). For the comparison of YFP-H mouse tissues after high-pressure pumping versus low-pressure pumping in Supplementary Fig. 9, the mouse brains were cut into 1 mm slices using a vibratome and imaged with magnification ×7 for overview and with magnification ×112 in GFP channel for their detailed cell structures. See Supplementary Table 2.

Laser-scanning confocal microscopy imaging. After imaging with light-sheet microscopy, areas of interest from the cleared specimens, such as whole heads and body parts, were imaged with an inverted laser-scanning confocal microscope (Zeiss, LSM 880) using Zen 2 software (v.10.0.4.910; Carl Zeiss AG). Before imaging, samples were mounted by placing them onto the glass surface of a 35 mm glass-bottom petri dishes (MatTek, P35G-0-14-C) and adding a few drops of BABB to make sure that the imaging region was immersed in BABB. Closing or sealing of the petri dish was not necessary because BABB has a high evaporation point and doesn't dry out for several days. The only precaution taken was to check the resistance of the dish against BABB, by testing that the glue sealing the glass to the dish and the plastic parts were not dissolved after several hours of exposure to BABB.

The imaging was done using a ×40 oil-immersion objective lens (Zeiss, ECPlan-NeoFluar ×40/1.30 oil DIC M27, 1.3 NA, WD = 0.21 mm) and a ×25 water-immersion long-working-distance objective lens (Leica, 0.95 NA, WD = 2.5 mm) mounted on a custom mounting thread. See Supplementary Table 2.

Reconstructions of whole-mouse body scans. We acquired light-sheet microscope stacks using ImSpector (v.5.295, LaVision BioTec) as 16-bit grayscale TIFF images for each channel separately. In each pair of neighboring stacks, alignment was done by manually selecting 3 to 4 anatomic landmarks from the overlapping regions, and then the stitching was done sequentially with the Scope Fusion module of the Vision4D (v.2.12.6 × 64, Arivis) software. Landmarks were mainly chosen from the skeletal bones or occasionally from the neuronal structures on the basis of visual inspection of the anatomical features. After completing the 3D reconstructions, the data visualization was done with Amira (v.6.3.0, FEI Visualization Sciences Group), Imaris (v.9.1, Bitplane) and Vision4D in both volumetric and maximum-intensity projection color mapping. Depth coding was done using the Temporal-Color Code plugin in Fiji (ImageJ2, v.1.51, https://fiji.sc/).

Image processing. Processing, data analysis, 3D rendering and video generation for the rest of the data were done on an HP workstation Z840, with 8 core Xeon processor, 196 GB RAM, and Nvidia Quadro k5000 graphics card and HP workstation Z840 dual Xeon 256 GB DDR4 RAM, nVidia Quadro M5000 8GB graphic card. We used Imaris, Amira and Fiji (ImageJ2) for 3D and 2D image visualization. Tile scans were stitched by Fiji's stitching plugin49. Stitched images were saved in TIFF format and optionally compressed in LZW format to enable fast processing. We removed tiles with acquisition errors using Fiji's TrakEM2 plugin and Imglib2library. In case of tiling errors in the *z* dimension, we used TeraStitcher (v.1.10; https://abria.github.io/TeraStitcher/) with its default settings to globally optimize the tiled volumes and reconstruct the entire dataset. To increase the quality of the images, we used the following functions in Fiji: to enhance the contrast of microglia cells (Fig. 1n and Supplementary Fig. 2a–f), we used 'Enhance Local Contrast (CLAHE)'; to equalize the images (Fig. 4a,b and Supplementary Fig. 2a–f), we used 'Pseudo Flat-Field Correction'; to enhance the contrast over the background of the axonal terminals in Fig. 4c,d, we used the custom-made macro for Fiji that we utilized to generate the pre-processed data for NeuroGPS-Tree (see the section 'Neuron tracing' below).

Neuron tracing. For automated neuron tracing in our light-sheet datasets obtained with Zeiss ×20 Clr Plan-Neofluar/0.1 NA (WD = 5.6 mm) objective, we used the NeuroGPS-Tree algorithm[22]. NeuroGPS-Tree was developed for tracing relatively small volumes of confocal microscopy data; therefore, we initially reduced the file size to under 1 GB (approximate maximum data size for NeuroGPS-Tree computation) by using the Fiji scale function. Due to high signal intensity discrepancy between soma and neurites, we next pre-processed the data with a custom-made macro in Fiji (available upon request), which consisted of background removal, pseudo-background correction, noise filtering

and sharpening. Next, the pre-processed data were loaded and analyzed first in NeuroGPS for soma detection and later in NeuroGPS-Tree for neurite detection (both steps are part of the same algorithm package). The best parameters for soma and neurite detection were chosen following the original publication. To quantify the features (such as the number of neurites per cell and the number of somas with at least one neurite) of these detected neuronal cells, we used Amira software: we chose the 10 neurons with the biggest file size per group and analyzed them using the Spatial Graph Statistics function of the software.

Quantifications. All the details of imaging settings used to acquire the data for the quantifications described in this section are available in Supplementary Table 2.

Analysis of fluorescence signal profiles from light-sheet images. The fluorescence signal profiles from each channel (excitation 470 nm, 560 nm and 647 nm) were plotted in the same *z*-stack and normalized as percentage over the maximum peak using Fiji (Supplementary Fig. 1).

To compare vDISCO boosted and unboosted protocols and consequently the reduction of the background and the improvement of the signal over background ratio in the far-red channel, we analyzed neurons and axonal bundles expressing GFP imaged with excitation at 470 nm, and neurons and axonal bundles labeled with anti-GFP nanobody conjugated with Atto647N imaged with excitation at 640 nm at the same anatomic region. First, the scans were taken with the light-sheet microscope using the ×4 objective (Olympus XLFLUOR ×4 corrected/0.28 NA (WD = 10 mm)). Then, the signal profiles were analyzed in Fiji and measured from a defined straight line covering the neuronal structure and surrounding tissue background, and the normalized plots of the signal profile (Fig. 1i) were calculated by normalizing the plots of neuronal structures obtained as described above over the average signal intensity of the respective surrounding background. Each experimental group consisted of 3 animals, and for each animal at the same anatomic region we plotted 3 profiles.

The same analysis of signal profile was used to compare the labeling efficiency of vDISCO with nanobody and iDISCO+ with antibody (Supplementary Fig. 3g–i): in this case the signal of interest was the one coming from microglia. Each experimental group consisted of 3 animals, and for each animal at the same anatomic region we plotted 3 profiles from 3 different microglia. The same analysis of signal profile was used to compare different clearing methods in Supplementary Fig. 12.

Fluorescence level. Fluorescence level quantification was expressed as a signal-to-background ratio and was calculated using Fiji[17] at the following time points: 0, 2, 3, 4.5, 5.5, 12 and 18 months after nanoboosting (Fig. 1n,o). Each ×4 light-sheet microscopy brain scan was taken with the same imaging parameters, and an image in TIFF format of the same anatomic region for all the samples was quantified. The mean value of the background for each image was obtained by averaging the background values of 12–40 regions from equally sized areas of the image in regions of the sample without signal. To calculate the mean value of the signal for each image, we used the threshold function of the software: the threshold was adjusted to consider the fluorescence signal visible in the image. After adjusting the threshold, only the sharp signal from specific cellular structures was analyzed per image. To this end, we used Fiji's 'analyze particles' function to measure the signal intensity only of particles sized between 5–10 and 100–150 pixels (visible fluorescent cells) and calculated the average value from all the particles. Next, this value was divided by the mean value of the background of the respective image, obtaining the fluorescence level over the background. The corresponding images, visually showing the preservation of signal over time in relation to the respective fluorescence levels, were processed using the Enhance Local Contrast (CLAHE) function in Fiji to increase the contrast of fluorescent cells in the tissue.

Quantification of deep-tissue staining efficiency of nanobody versus antibody. To quantify the depth of staining and therefore to compare whole-organ staining efficiency of nanobody versus antibody labeling (Supplementary Fig. 2), we used CX3CR1$^{GFP/+}$ animals (3–7 months old), 3 whole brains per experimental group. The tile scans of the brains were taken with light-sheet microscopy in axial view using the ×4 objective (Olympus XLFLUOR ×4 corrected/0.28 NA (WD = 10 mm)). After stitching we chose the *z*-plane showing the same anatomic structures from all brains for comparison. These axial-view 2D images of whole brains were analyzed in Fiji; the distance of staining depth was quantified using the 'line' function in the *z*-plane at the greatest width of the brain, measuring from the surface until the last visible boosted microglia. Then, for each image, this staining depth value was normalized over the total thickness of the brain at the considered *z*-level, measuring a line drawn from the same point of the surface until the axial middle line of the brains.

Quantification of whole-body labeling efficiency of different whole-body labeling protocols. To quantify the rate of staining of the different whole-body labeling protocols in Supplementary Fig. 11, the tile scans of 3 whole heads per method were taken with light-sheet microscopy in axial view using the ×2 objective described in the 'Light-sheet microscopy imaging' section above with a total magnification of ×1.26. For the analysis, we used Fiji to choose 3 regions in *z* in the 2D visualization, to have comparative data in 3 different depths (see Supplementary Fig. 2a,b). For each region, we chose the *z*-plane displaying the same anatomic structures in each sample. Next, the 2D images were opened in Fiji and, after adjusting the threshold to the fluorescence signal visible in the image, the stained area in the brain in each image was quantified using the 'freehand selections' function. Next, this stained area value was normalized over the total area of the brain visible in that 2D image. This total area was quantified using the same 'freehand selections' function in Fiji, following the brain outline. Statistical comparison was performed considering each set of corresponding regions from the different samples separately.

ClearMap. To quantify microglia distribution, we used ClearMap[23]. Since the script was originally developed for quantification of the cFos$^+$ cells, to comply with the offered method, we did the following pre-processing steps on our microglia data using Fiji before ClearMap:

- Background equalization to homogenize intensity distribution and appearance of the microglia cells over different regions of the brain, using pseudo-flat-field correction function from Bio-Voxxel toolbox.
- Convoluted background removal, to remove all particles bigger than relevant cells. This was done with the median option in the Bio-Voxxel toolbox.
- Two-dimensional median filter to remove remaining noise after background removal. The filter radius was chosen to ensure the removal of all particles smaller than microglia cells.
- Unshapen mask to amplify the high-frequency components of a signal and increase overall accuracy of the cell detection algorithm of ClearMap.

After pre-processing, ClearMap was applied by following the original publication and considering the threshold levels that we obtained from the pre-processing steps. As soon as the quantification was completed, the data was exported as an Excel file for further analysis. For example, the cellular density per brain region was obtained considering the absolute number of cells detected by ClearMap and the volume of that specific brain region, which was calculated using a custom script (available upon request) based on ClearMap (Elastix registration).

Quantification of peripheral neuronal degeneration in acute brain injury. Peripheral neuronal degeneration in TBI animals versus unlesioned control animals was done in the *Thy1*-GFP-M line and was assessed considering the complexity of axonal ramifications that projected from the left (left = contralateral side) cervical and thoracic vertebra to the left muscles of the back at the level of the torso of the mouse, including the left spinotrapezius and latissimus dorsi. The complexity was expressed as number of axonal endpoints (nerve terminals that appear as a button-like shape; see Fig. 4) over the total length of axonal ramifications that were protruding from a main branch. To calculate this index, first a 3 × 3 tile of *z*-stacks of this anatomic region was taken from the animals by light-sheet microscopy using the ×2 objective described in the 'Light-sheet microscopy imaging' section with a total magnification of ×5, to have enough resolution to manually trace the axonal ramifications and axonal end-feet. Then, the analysis was done over the maximum intensity projections of the tile scans with Fiji software. To measure the length of the ramifications, we used the 'free hand line' function and the 'ROI manager tool' of Fiji to record all the traced axonal ramifications of interest, which were coming from a main branch; later, we calculated the sum of the length of all of the recorded ramifications with the 'measure' function of Fiji. To count the nerve terminals, we used the 'point tool' function and the same 'ROI manager tool' to record all the visible axonal endpoints protruding from the traced ramifications. The analysis was performed over 2–4 branches from the same anatomic region for each animal, in 6 animals (3–6 months old) per experimental group. The same quantification procedure was followed to analyze the complexity at the equivalent ipsilateral (right side from dorsal view) side of the animals, in 6 and 5 animals for the TBI and unlesioned groups, respectively.

Quantification of CD68 GFP$^+$ cells with spinal cord injury. The spine areas of interest from *CD68*-EGFP line mice with spinal cord injury or sham surgery and from naïve animals were imaged with light-sheet microscopy using the ×2 objective described in the 'Light-sheet microscopy imaging' section with a total magnification of ×3.2 and with 2 × 3 tile *z*-stacks. After stitching, the entire *z*-stacks of scans were loaded in Fiji software with the 'use virtual stack' mode. To segment the spinal cord tissue from surrounding tissue, including bone and muscles, and count the cell numbers separately, the border of the spinal cord was marked by using the 'free hand line' function in Fiji as a manual selection. These manual selections were done in every 6–9 image slices and were recorded by the 'ROI manager tool' function. The complete selections for the entire *z*-stacks were then achieved by using the 'interpolate ROIs' function and were saved as .zip files. Then, the entire *z*-stacks of scans were loaded in Fiji software again, without selecting the 'use virtual stack' mode. By loading the complete selections generated from former steps respectively, each spinal cord was segmented by using a custom-made macro with the 'clear outside' function and saved as a new 'image sequence'. To maintain the integrity of the raw data, one should not save the changes when closing the window after running the macro. Then, the intact original *z*-stacks and complete selections were loaded again in the same way, and surrounding tissues including bone and muscles were segmented by using another custom-made macro with

the 'clear' function. All the custom-made macros are available upon request. Next, the segmented image stacks of spinal cord or surrounding tissue were loaded with Imaris respectively, and the 'surface' function was used to segment the CD68 GFP$^+$ cells. By generating the 'surface' selection, the 'statistic' function was available to count the number of cells in the region of interest.

Quantification of short SMCs with MCAO. The transparent skulls from *LysM*-EGFP line mice with MCAO or sham were imaged with intact heads from the sagittal view with light-sheet microscopy using the ×2 objective described in the 'Light-sheet microscopy imaging' section with a total magnification of ×3.2 and with 2×4 tile *z*-stacks. After stitching, the entire *z*-stacks of scans were loaded in Imaris, and the length, width and cell numbers in the SMCs were manually calculated by using the 'measure-line' function. Then, the length and width of the channels were corrected by a shrinkage rate of DISCO clearing[17].

Statistical analysis. Data collection and analysis were not performed blind to the conditions of the experiments. Data distribution was assumed to be normal, but this was not formally tested. Data are presented as mean ± s.d. except for in Fig.6 and Supplementary Fig. 22, where they are presented as mean ± s.e.m. Sample sizes are indicated in the figure legends. Statistical analysis was performed using Prism GraphPad software v.6 with 95% confidence interval. *P* values were calculated using two-tailed unpaired *t* test to compare data between two groups. *P* values were calculated using one-way ANOVA followed by Dunnett's *post hoc* test to compare data in Supplementary Figs. 4 and 11. For *CD68*-EGFP quantification in Supplementary Fig. 22, *P* values were calculated using one-way ANOVA followed by Tukey multiple comparison test to compare data between SCI (spinal cord injury), sham and naïve groups. A *P* value of <0.05 was considered statistically significant. In ANOVA analysis the reported *P* values are adjusted in GraphPad prism to account for multiple comparisons. The protocols described in this study were replicated successfully more than five times in independent experiments, and they were also reproduced at least by three different operators. See also the Life Sciences Reporting Summary.

Reporting Summary. Further information on research design is available in the Nature Research Reporting Summary linked to this article.

Code availability. The custom codes used to analyze the data in this study are available from the corresponding author upon request.

Data availability

The data that support the findings of this study are available from the corresponding author upon reasonable request.

References

51. Niess, J. H. et al. CX3CR1-mediated dendritic cell access to the intestinal lumen and bacterial clearance. *Science* **307**, 254–258 (2005).
52. Nikic, I. et al. A reversible form of axon damage in experimental autoimmune encephalomyelitis and multiple sclerosis. *Nat. Med.* **17**, 495–499 (2011).
53. Treweek, J. B. et al. Whole-body tissue stabilization and selective extractions via tissue-hydrogel hybrids for high-resolution intact circuit mapping and phenotyping. *Nat. Protoc.* **10**, 1860–1896 (2015).

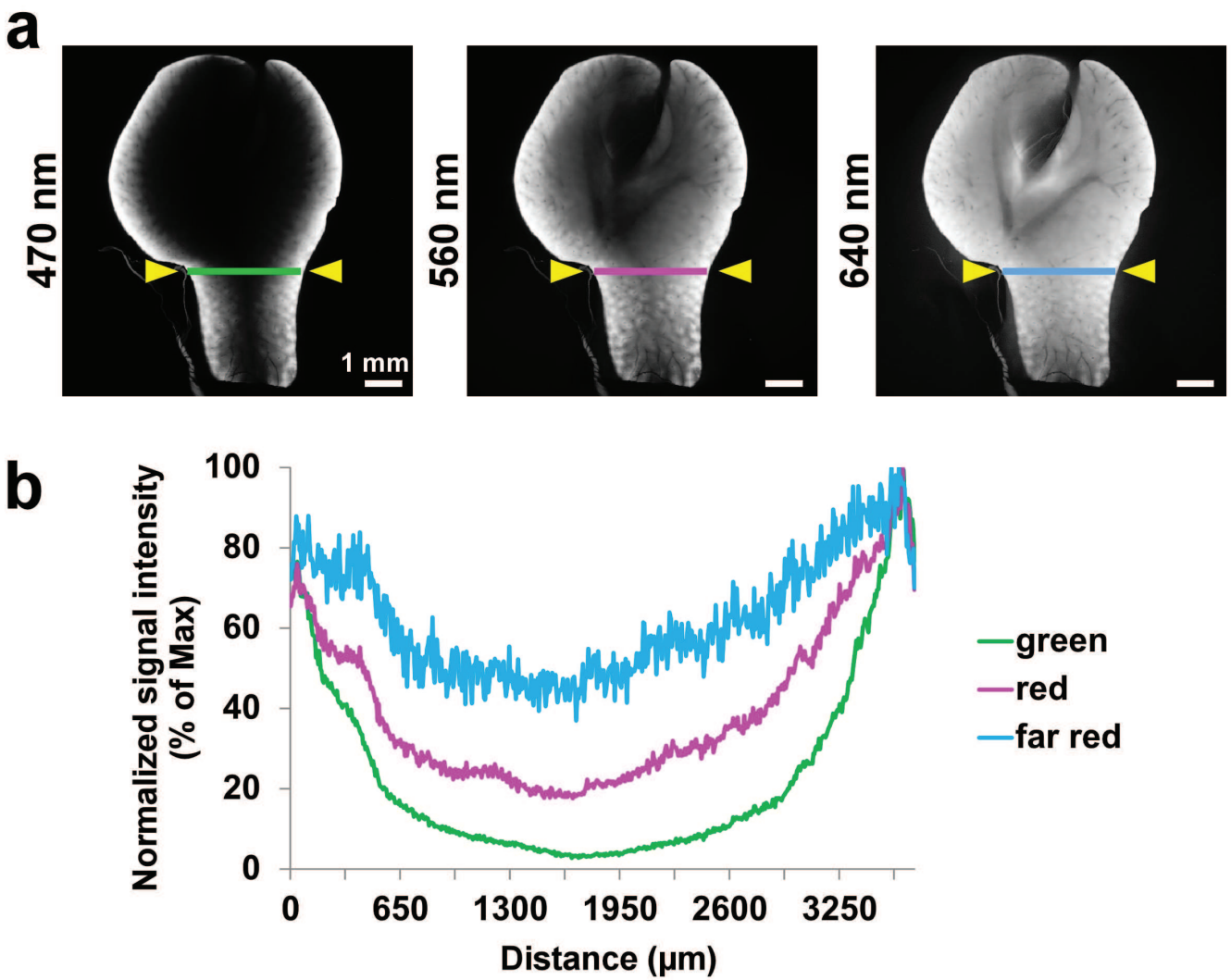

Supplementary Figure 1

Light penetration deep in tissue at different wavelengths

(**a**) Demonstration of tissue penetration of the light at different imaging wavelengths. The same liver region (without any labeling) of a cleared mouse imaged in green (ex: 470 nm) (left), red (ex: 560 nm) (middle) and far-red channels (ex: 640 nm) (right) using light-sheet microscopy. (**b**) Fluorescence signal intensity profiles normalized over the maximum intensity of the regions indicated by the lines in a. Complete illumination of cleared liver at 640 nm compared to other wavelengths is evident. Similar results were observed in 10 independent animals.

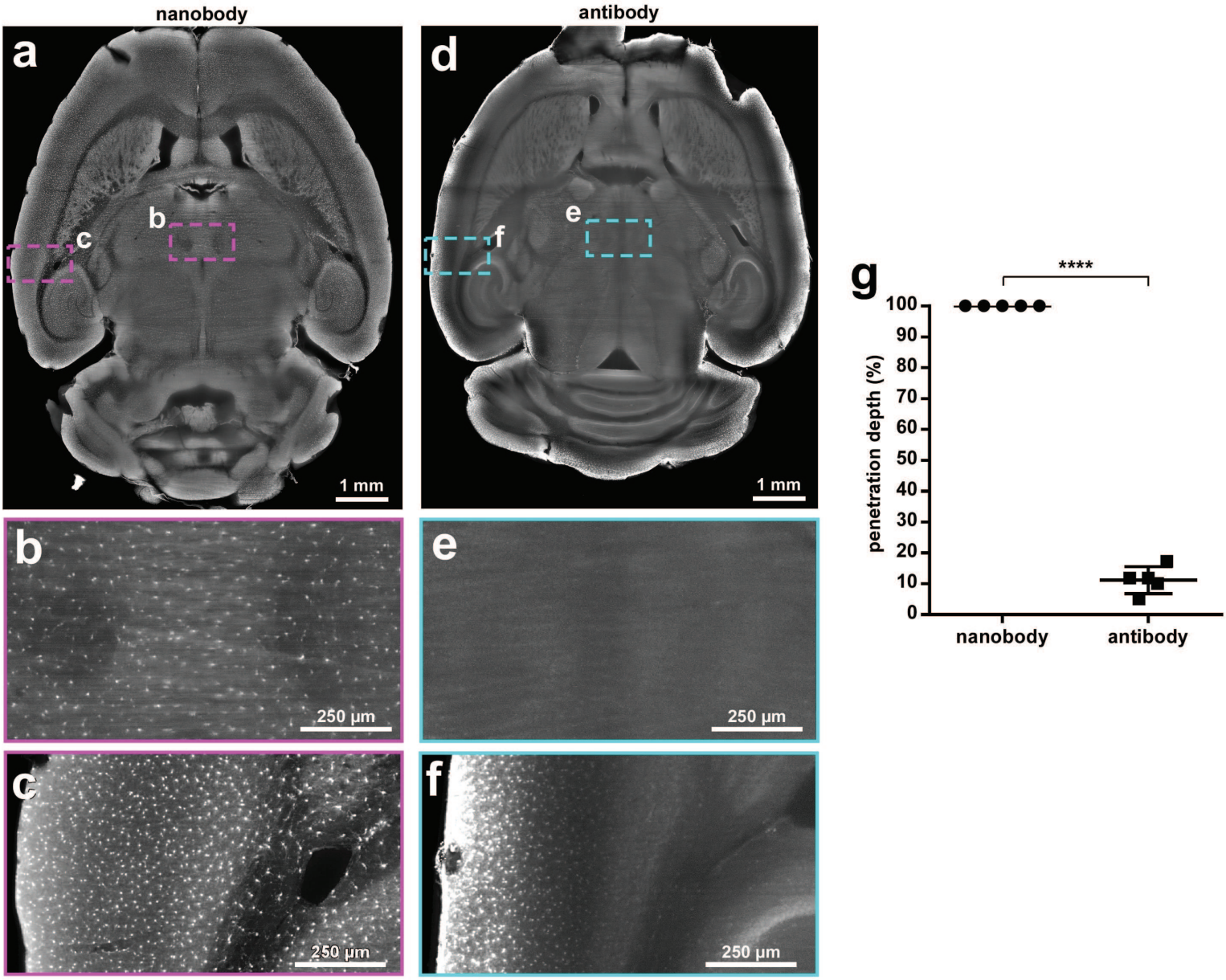

Supplementary Figure 2

Deep tissue staining efficiency of nanobody vs conventional antibody

Penetration depth comparison between anti-GFP nanobody (**a**-**c**) vs. conventional anti-GFP antibody (**d**-**f**) from brains coming from CX3CR1$^{GFP/+}$ mice. Representative images of 1 brain from each group consisting of 5 independent animals. (**g**) Penetration depth quantifications of anti-GFP nanobody vs. conventional anti-GFP antibody stained brains from 5-12 months old CX3CR1$^{GFP/+}$ mice (mean ± s.d.; n=5 mice per group; statistical significance (****$p < 0.0001$) was assessed by two tailed *t*-test)

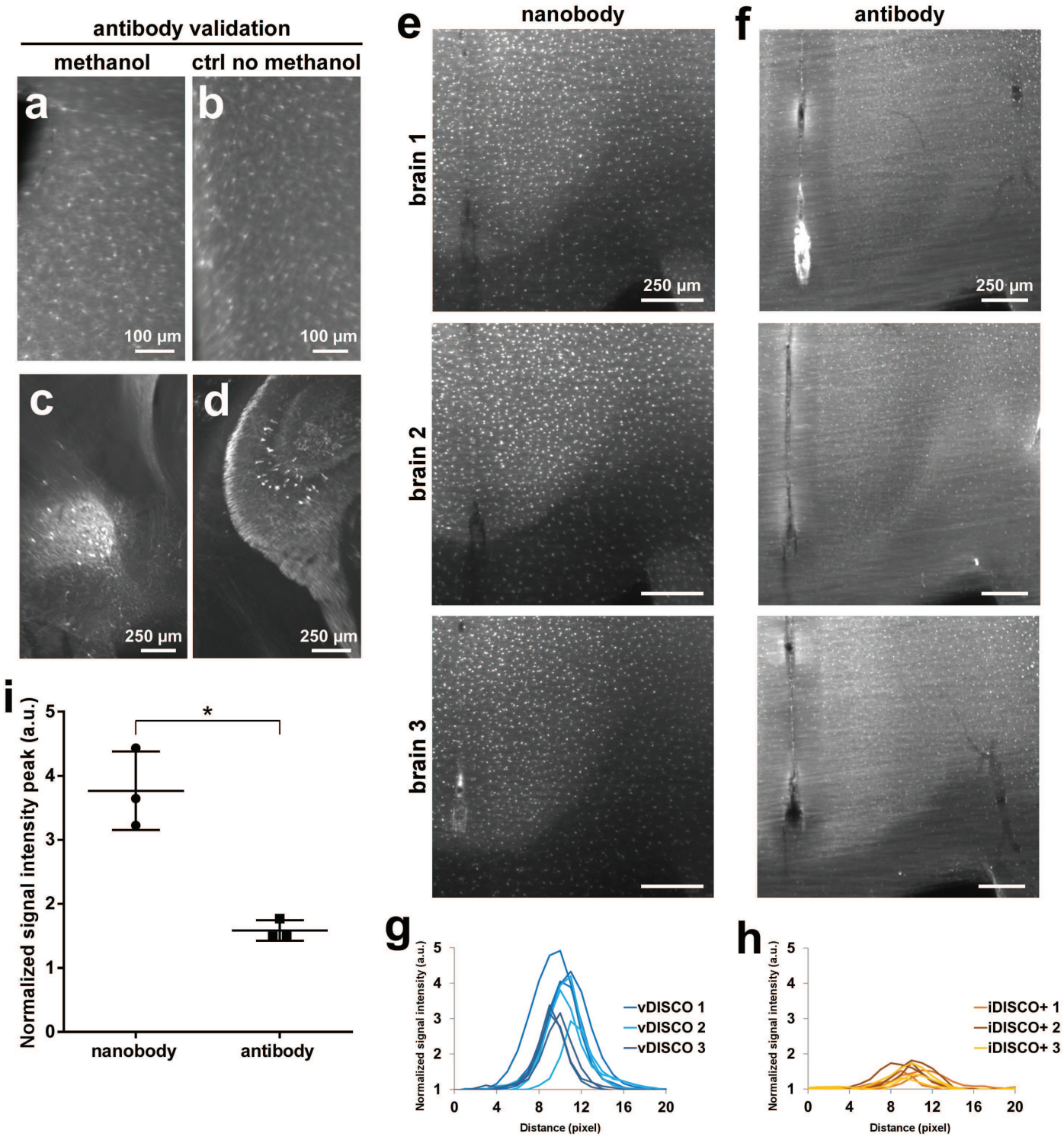

Supplementary Figure 3

Compatibility test of conventional anti-GFP antibody with iDISCO+ protocol and comparison between vDISCO passive boosting with anti-GFP nanobooster vs iDISCO+ passive labeling with conventional anti-GFP antibody on CX3CR1$^{GFP/+}$ brains

(**a**-**d**) Fluorescent stereomicroscope images of 600 µm brain slices from CX3CR1$^{GFP/+}$ animal (**a**,**b**), and GFPM animal (both 2-3 months old) (**c**,**d**) showing the compatibility of a conventional anti-GFP antibody with methanol pretreatment: (**a**) slice from CX3CR1$^{GFP/+}$ brain and (**c**) slice from GFPM brain both pretreated with methanol and labeled with the conventional anti-GFP antibody showing the persistence of fluorescence signal compared with: (**b**) slice from the same CX3CR1 brain and (**d**) slice from the same GFPM brain labeled with the conventional anti-GFP antibody without methanol pretreatment as positive control. Similar results were observed in 2 independent animals. (**e**-**i**) Comparison between passive vDISCO boosting with anti-GFP nanobooster (conjugated with Atto-647N) vs. passive iDISCO+ labeling with the tested conventional anti-GFP antibody (conjugated with Alexa-647) on CX3CR1$^{GFP/+}$ whole brains from 5-7 months old mice: (**e**,**f**) light-sheet images showing the difference in labeling after vDISCO (**e**) vs. iDISCO+ (**f**) at the level of the same anatomical region (cortex and corpus callosum) in 3 different independent brains per each group; (**g**,**h**) plots of signal intensity profiles from vDISCO boosted brains in e (**g**) and iDISCO+ labeled brains in f (**h**); (**i**) Comparison of the peaks of the signal intensity profiles in g vs. h (mean ± s.d., n=3 animals per group, statistical significance (*p = 0.02) was assessed by two tailed t-test).

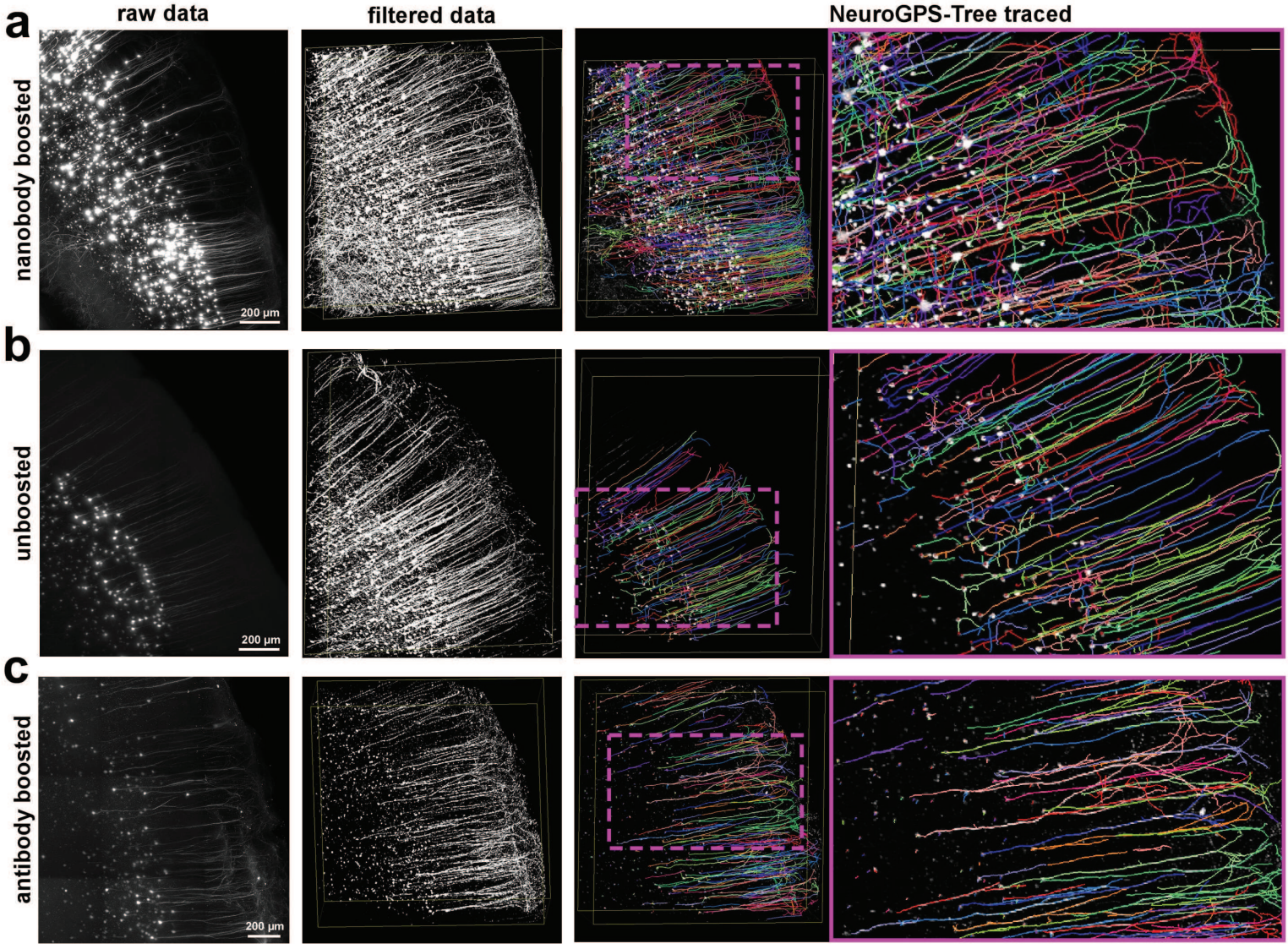

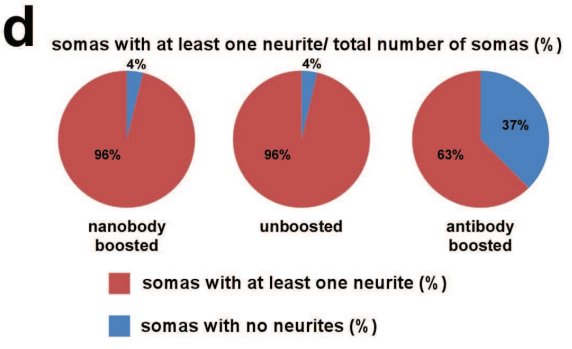

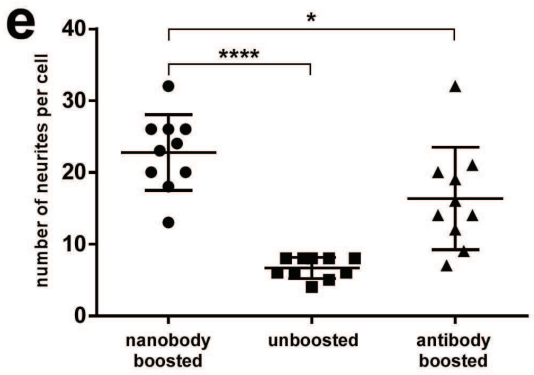

Supplementary Figure 4

Neuron tracing with NeuroGPS-Tree

(**a**-**c**) Tracing of neurons in vDISCO nanobody boosted (**a**), unboosted (**b**) and iDISCO+ conventional anti-GFP antibody boosted (**c**) brains from 6-13 weeks old *Thy1*-GFPM mice using NeuroGPS-Tree algorithms. The scans were obtained with a commercial light-sheet microscope (Ultramicroscope II, LaVision Biotec), optimized for large cleared tissue imaging, thereby with lower resolution compared to standard confocal microscopes. From left to right: raw image, equalized & filtered images, and NeuroGPS-Tree traced neuronal structures are shown: all the neurites belonging to a neuron are represented by the same color. Neuronal soma identified by NeuroGPS-Tree are represented by red dots. Single experiment per each method. (**d**) Quantification of number of detected neurons characterized by their soma with at least one detected neurite over the total number of detected somas in vDISCO boosted vs unboosted and conventional antibody boosted samples. While in vDISCO boosted and unboosted cases almost all the neurons were detected with at least one neurite per soma, in the antibody boosted case only 63% was detected with neurites (**e**) Quantification of number of detected neurites per neuron in vDISCO boosted vs. unboosted and conventional antibody boosted samples, showing that only vDISCO allows the tracing of more neurites per cell (mean ± s.d; n=10 neurons per group; statistical significance ($F_{2,27}$=24.30, ****p < 0.0001,*p = 0.02) was assessed by one-way ANOVA followed by Dunnett´s *post hoc* test).

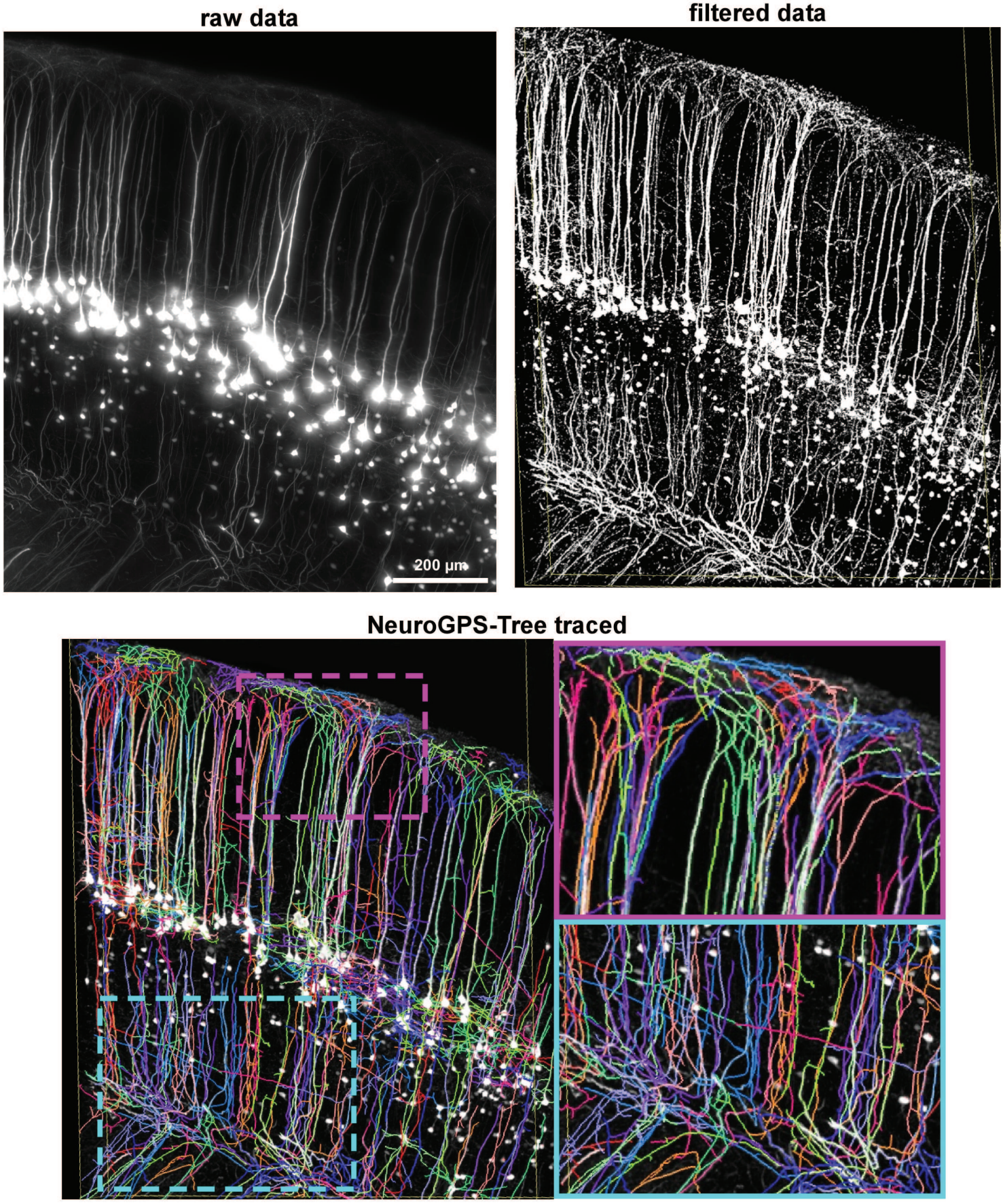

Supplementary Figure 5

Neuron tracing with NeuroGPS-Tree, secondary somatosensory cortex

Tracing of neurons in vDISCO boosted brain from a 6 weeks old *Thy1*-GFPM mouse using NeuroGPS-Tree algorithms. The displayed region is around the secondary somatosensory cortex (Region S2 of the Figure 152 of the Franklin & Paxinos atlas, Bregma -2.80, Interaural 3.00). The scans were obtained with a commercial light-sheet microscope (Ultramicroscope II, LaVision Biotec), optimized for large cleared tissue imaging, thereby with lower resolution compared to standard confocal microscopes. From left, right to down: raw image, equalized & filtered images, and NeuroGPS-Tree traced neuronal structures are shown: all the neurites belonging to a neuron are represented by the same color. Axons projecting out from the somas to the corpus callosum are visible and traced. Single experiment.

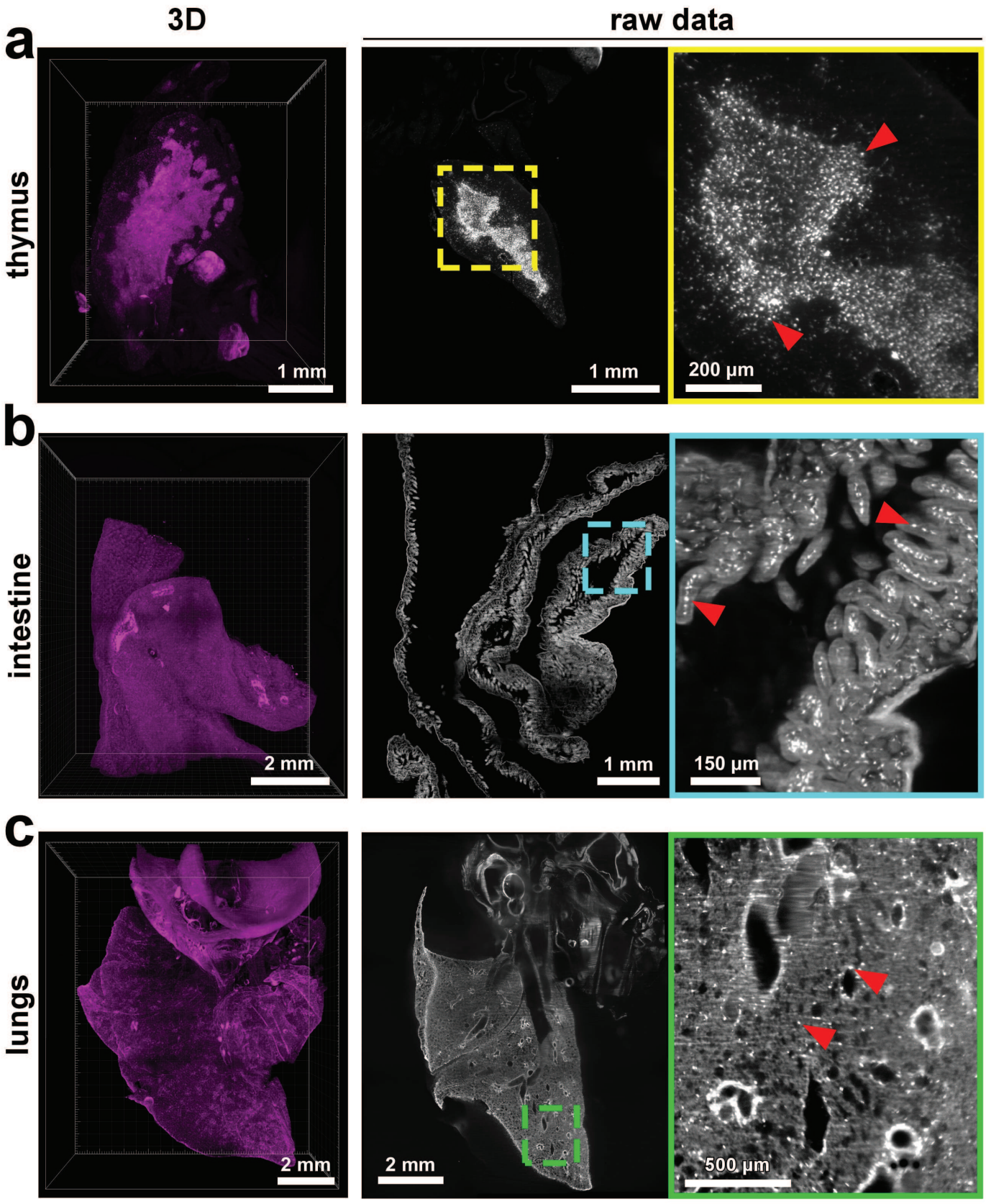

Supplementary Figure 6

Visualization of CX3CR1 GFP+ cells in individual organs

(**a**-**c**) 3D visualization (magenta) and raw data images (grey) of individual organs including thymus (**a**), intestine (**b**), and lungs (**c**) from a 6 months old CX3CR1$^{GFP/+}$ mouse imaged by light-sheet microscopy. Individual CX3CR1 GFP+ cells are indicated by red arrow-heads in the zoomed images from the boxed regions. Similar results were observed in 3 independent animals.

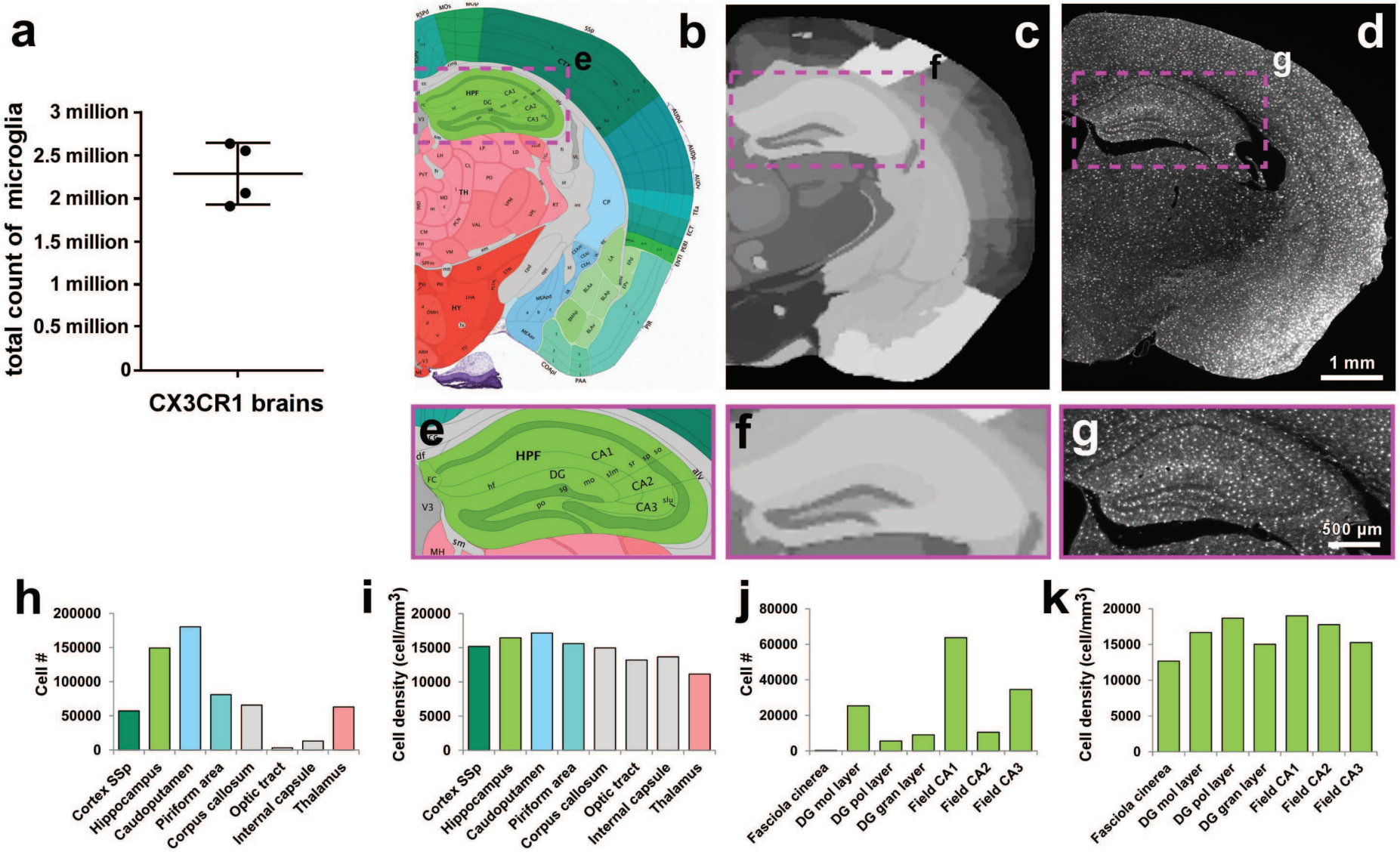

Supplementary Figure 7

Visualization and quantification of the signal from CX3CR1$^{GFP/+}$ mouse by vDISCO boosting

(**a**-**k**) Automated analysis of fluorescent cells quantification and distribution in CX3CR1$^{GFP/+}$ mouse brain after vDISCO boosting (mean ± s.d.; n = 4 2-5 months old mice: 2.647, 2.553, 1.909, 2.061 millions respectively (**a**)): (**b**) reference image from the Allen brain atlas, (**c**) registered reference annotation image, (**d**) the corresponding region in raw data in coronal view. (**e**-**g**) High magnification images of the region indicated in b-d containing the hippocampus. Automated quantification of absolute cell numbers (**h**) and cell densities (**i**) of the anatomical regions visible in b-d. Absolute cell numbers (**j**) and cell densities (**k**) of sub-regions of hippocampus shown in e-g. The quantifications include the cells in both brain hemispheres.

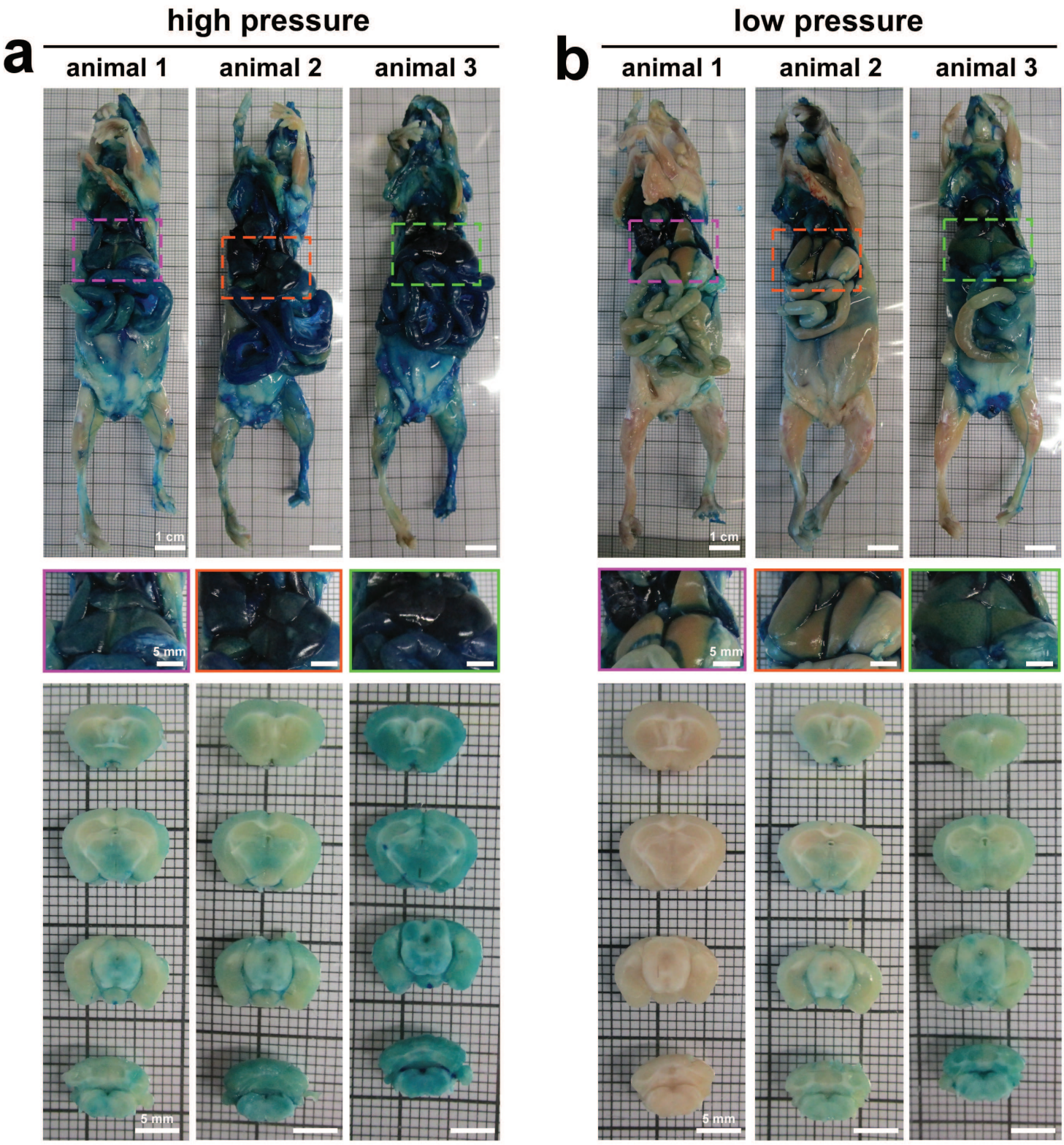

Supplementary Figure 8

Comparison between high vs low pressure transcardial perfusion
Diffusion of blue dye in the body (up) and brain (down) of 4 months old C57BL/6J animals trascardially perfused for 15 minutes with methylene blue with high pressure (approx. 180 mmHg) (**a**) vs low pressure (approx. 70 mmHg) (**b**). The colored rectangles (middle) show the high magnification images of the dashed regions at the level of the liver.

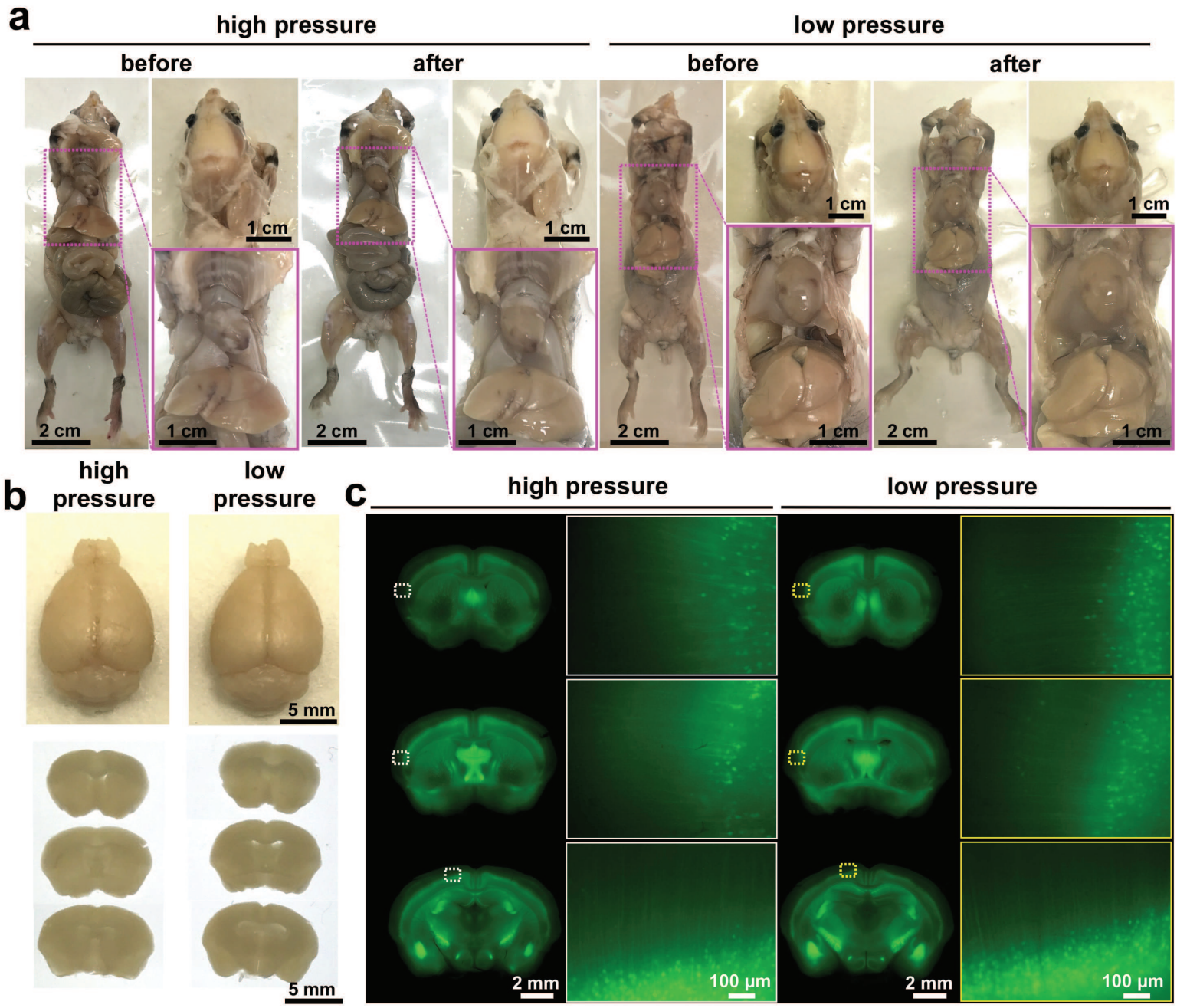

Supplementary Figure 9

Comparison between *Thy1*-YFPH line mice perfused with high (230 mmHg) or low pressure (110 mmHg)

(**a**) Images of 3 months old mice taken before and after high or low pressure perfusion for 3 days, showing no morphological organ changes due to high pressure perfusion. (**b**) Comparison of dissected brains and brain slices from mice after high or low pressure perfusion, showing that the brain was not deformed or disrupted by high pressure perfusion at the macroscopic scale (similar results were observed from 2 independent mice per group) (**c**) Using a stereo-fluorescent microscope, the cortical neurons were imaged at single cell resolution. No morphology changes in neuronal structures were detected at the microscopic scale indicating that the high (230 mmHg) pressure perfusion in the vDISCO protocol does not damage the tissue (single experiment).

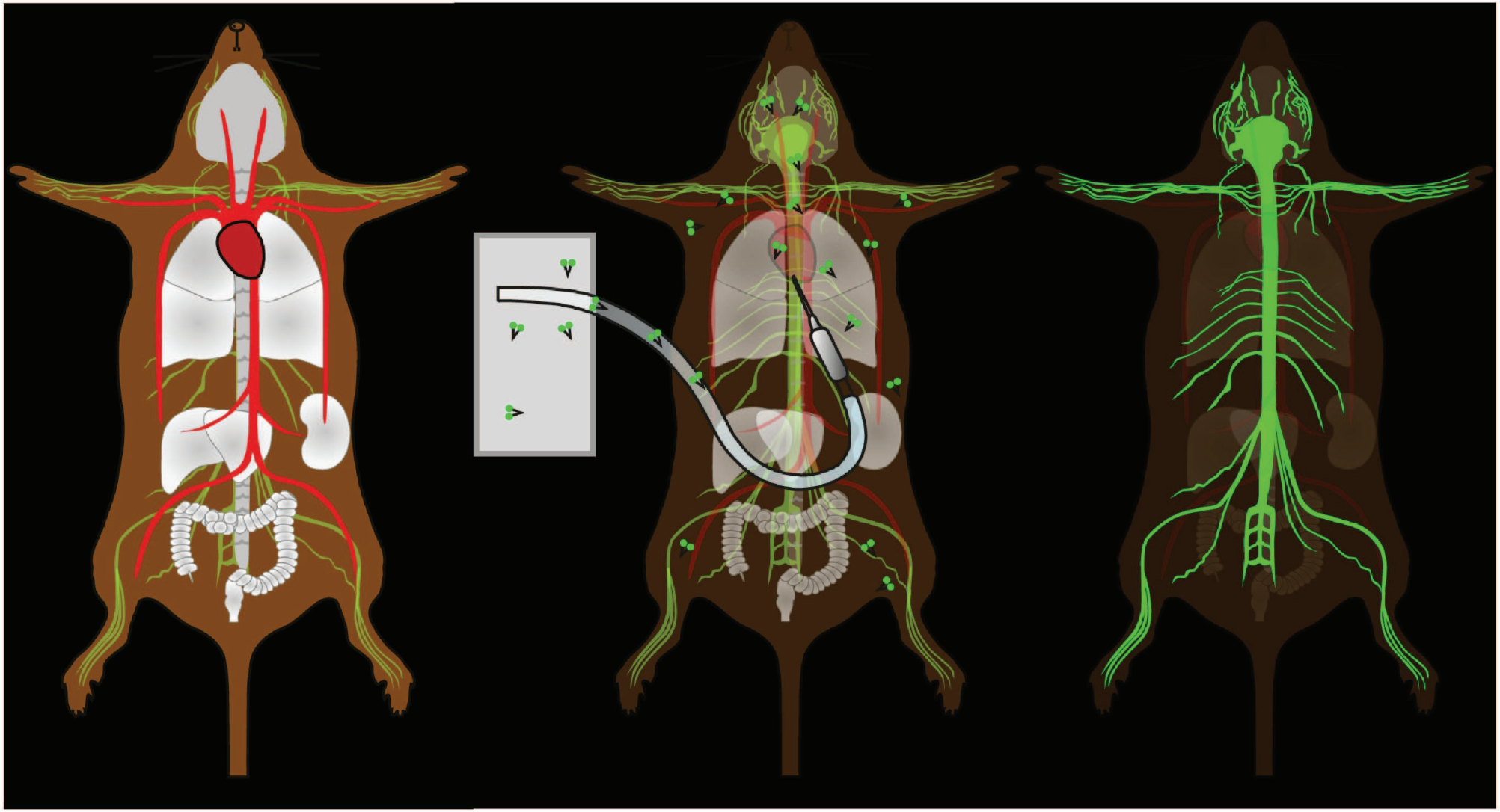

Supplementary Figure 10

Schematic illustration of whole-body vDISCO boosting method

The decolorization, decalcification, and nanoboosting steps are performed via transcardiac perfusion. After boosting, the boosted fluorescence signal becomes highly visible over the reduced background in the intact transparent animals.

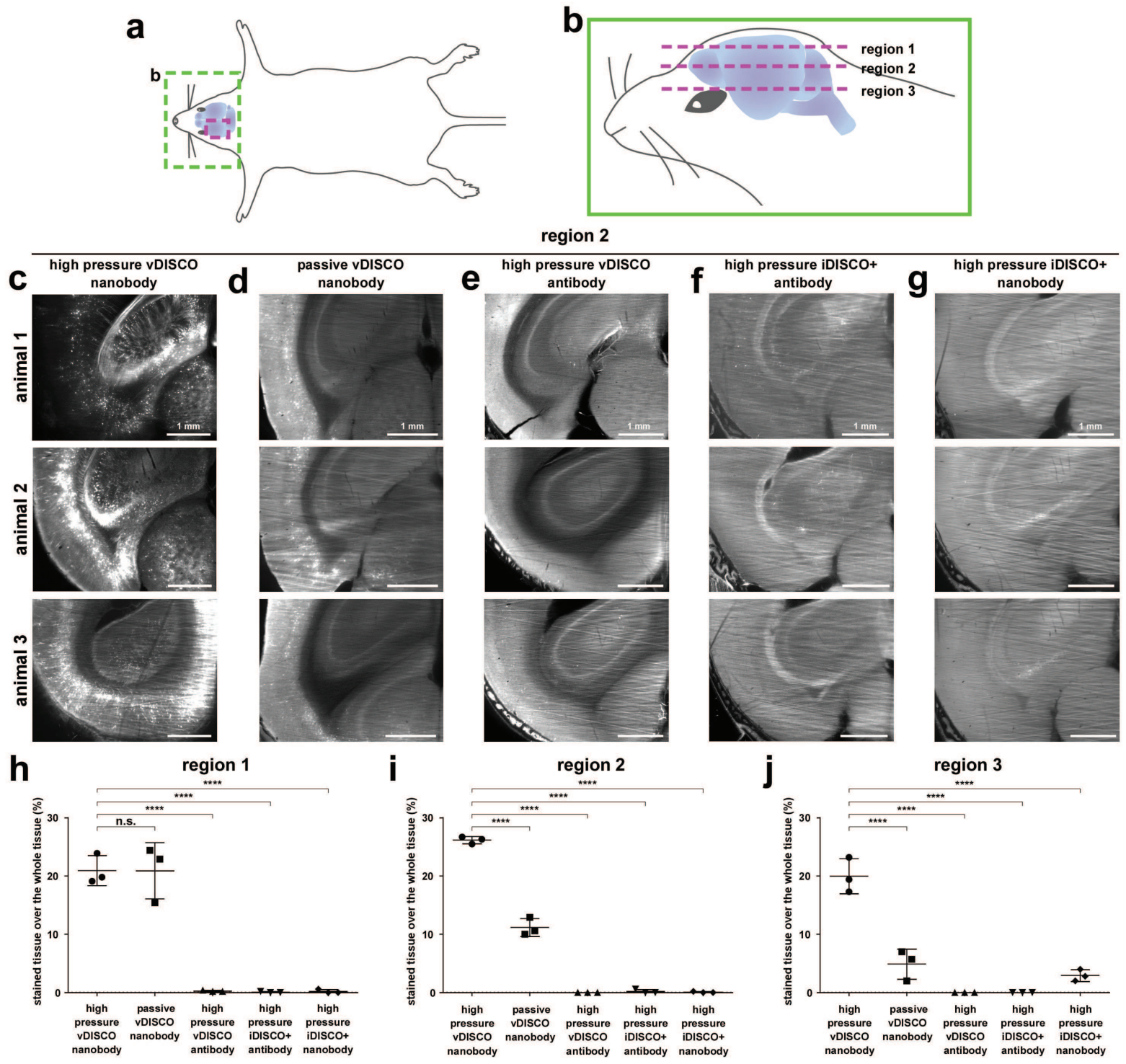

Supplementary Figure 11

Whole-body immunolabeling by vDISCO vs. other labeling methods

(**a**) Illustration showing the anatomic region (dashed magenta rectangle) of the cleared mice imaged for the comparative analysis. (**b**) Zoom-in illustration at the level of the head of the representative animal showing the 3 different z regions of interest considered for the comparative analysis. (**c**-**g**) Light-sheet images of 3 brains from 3 independent cleared animals per each group at the level of region 2 indicated in a and b showing the complete penetration of the nanobody in animals processed with vDISCO method using active high pressure perfusion (**c**) vs. the partial labeling of the surface of the brain in animals processed with vDISCO with passive incubation of the nanobody (**d**) and vs. the limited labeling of the brain in animals processed with vDISCO using active high pressure pumping of conventional anti-GFP antibody (**e**), in animals processed with iDISCO+ using active high pressure pumping of conventional anti-GFP antibody (**f**) and in animals processed with iDISCO+ using active high pressure pumping of nanobody (**g**). (**h**-**j**) Quantification of the % of stained tissue from the described protocols at the level of region 1 (**h**), region 2 (**i**) and region 3 (**j**). mean ± s.d.; n=3 2-3 months old animals per group; statistical significance (n.s.=no significant, ****$p < 0.0001$, in h: $F_{4\text{-}10}$=64.26, in i $F_{4\text{-}10}$=693.0, in j $F_{4\text{-}10}$=62.19) was assessed by one-way ANOVA followed by Dunnett´s *post hoc* test).

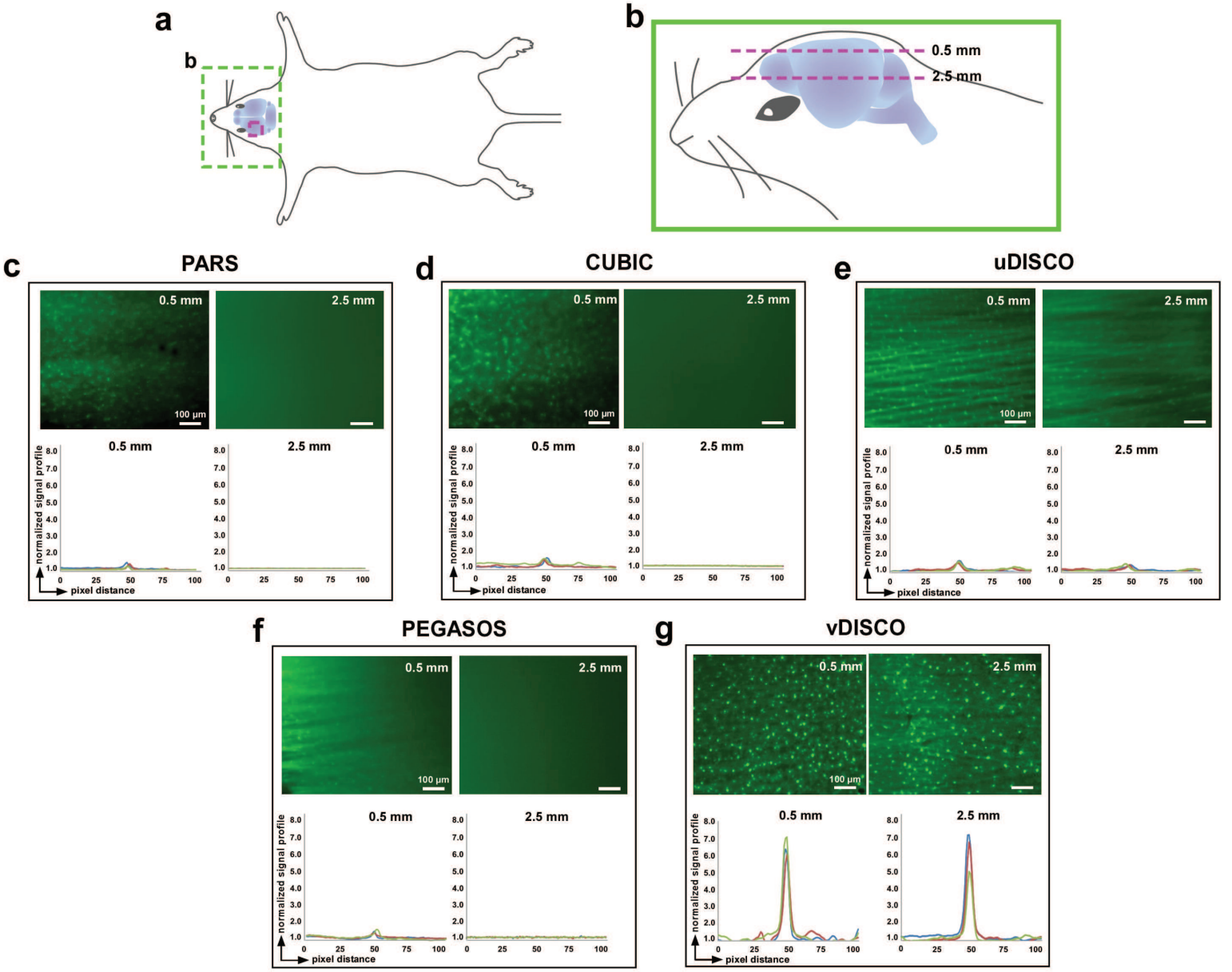

Supplementary Figure 12

Quality of imaging single cells deep in the brain through the skull by different whole-body clearing approaches
(**a**) Illustration showing the anatomic region (dashed magenta rectangle) of the cleared mice imaged for the comparative analysis. (**b**) Zoom-in illustration at the level of the head of the representative animal showing the 2 different z regions (0.5 mm and 2.5 mm deep from the dorsal brain surface) considered for the comparative analysis. (**c**-**g**) To compare different clearing methods, whole-bodies of 2 months old CX3CR1$^{GFP/+}$ mice were cleared by PARS (**c**), CUBIC-R (**d**), uDISCO (**e**), PEGASOS (**f**) and vDISCO (**g**). After clearing, the whole-heads of mice with intact skull were taken for light-sheet microscopy for signal comparison. Representative images and normalized signal profiles at 0.5 mm and 2.5 mm depth indicate that vDISCO is the only method providing reliable detection of microglia cells through the intact skull. Similar results were observed from 3 independent mice per group. Among all the clearing methods tested, PARS, PEGASOS and vDISCO were characterized by a decalcification step using EDTA solutions.

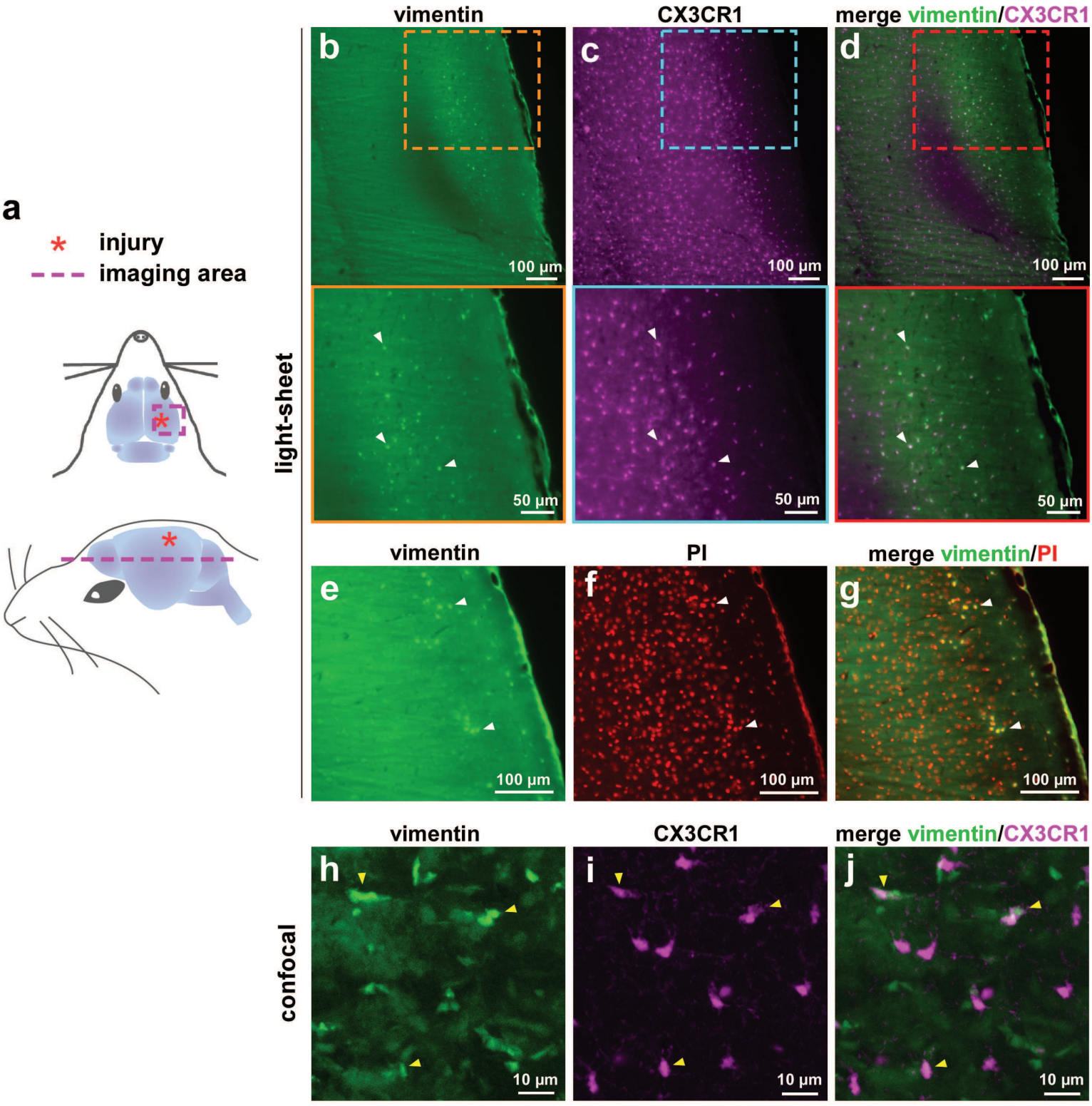

Supplementary Figure 13

vDISCO labeling of vimentin expressing cells using anti-vimentin nanobody

(**a**) Illustration showing the injury location of the brain trauma (red asterisk) and the imaging area (magenta dashed line). (**b-d**) Light-sheet imaging of a mouse brain from traumatic brain injured 4 months old CX3CR1$^{GFP/+}$ animal 1 month after the injury: vimentin was labeled using anti-vimentin 488-nanobooster (green), in which the autofluorescence of the tissue is much higher than in the far-red spectrum. (**b**) CX3CR1 GFP+ cells were boosted using anti-GFP 647-nanobooster (magenta) (**c**), the colocalization of CX3CR1 GFP+ immune cells expressing vimentin is visible in white in the merge panel (**d**). The colored rectangles show zoom-in images of the dashed regions in b-d. White arrow-heads indicate examples of colocalizing signal in cells. (**e-g**) Light-sheet imaging of the same brain from the TBI CX3CR1$^{GFP/+}$ animal in b-d: vimentin is shown in green (**e**), while all nuclei of the cells were labeled using propidium iodide (PI) (red) (**f**), the colocalization of the signal in cells expressing vimentin and stained with PI is visible in yellow in the merge panel (**g**). White arrow-heads indicate examples of colocalizing signal in cells. (**h-j**) Confocal imaging of the mouse brain in b-d showing vimentin (green) (**h**) and CX3CR1 GFP+ cells (magenta) (**i**), the colocalization of CX3CR1 GFP+ immune cells expressing vimentin is visible in white and indicated by yellow arrow-heads in the merge panel (**j**). Single experiment.

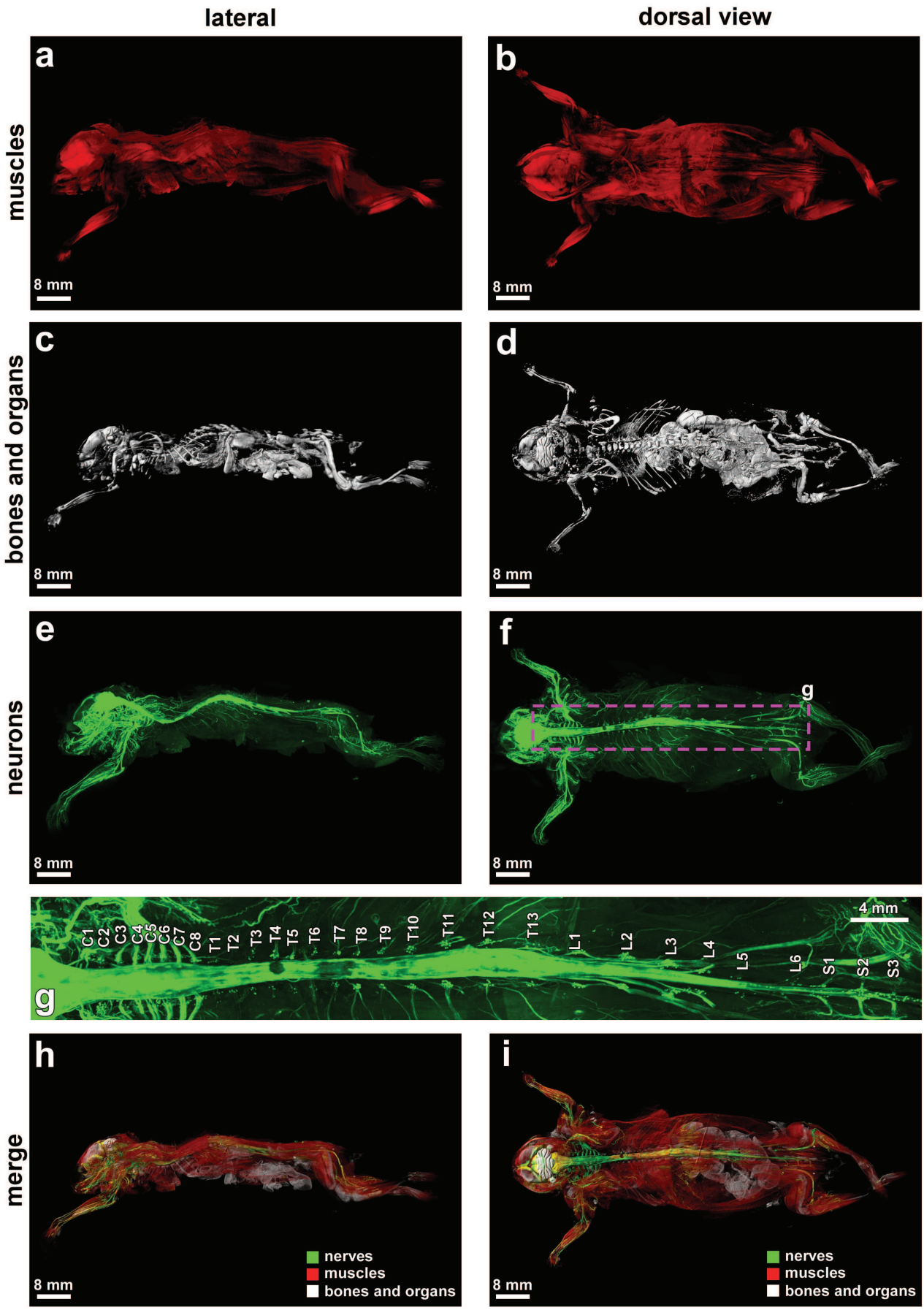

Supplementary Figure 14

Whole body neuronal projections of a *Thy1*-GFPM mouse by panoptic imaging
(**a-d**) The lateral and dorsal views of autofluorescence (muscles), and PI (bones and organs) channels. (**e**,**f**) Neuronal projections of the whole body in lateral and dorsal views. (**g**) High magnification view from the indicated region in **f** showing details of spinal cord segments. (**h**,**i**) The merge channels in lateral (**h**) and dorsal (**i**) views of neurons, bones and organs, and muscles are shown. Comparable labeling and imaging results were achieved in 5 independent animals, whole body reconstruction was done in one mouse.

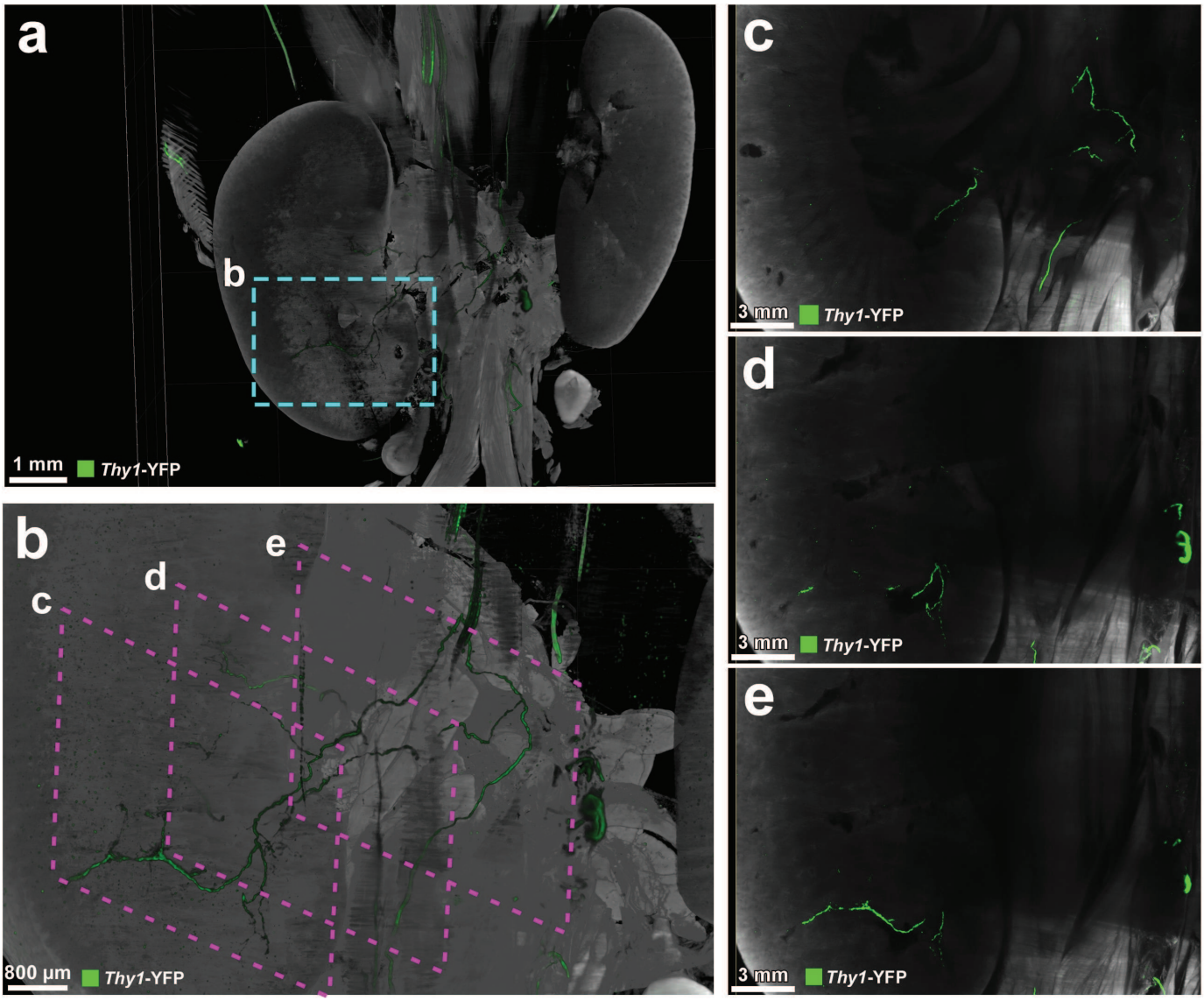

Supplementary Figure 15

Peripheral nerves innervating kidneys in *Thy1*-YFPH mouse

(**a**) 3D visualization of nerves innervating the kidneys of a 7 months old *Thy1*-YFPH animal. (**b**) Zoom image from the marked region in **a**. (**c**-**e**) 2D projection images of the kidney at the indicated depths in **b**. Single experiment.

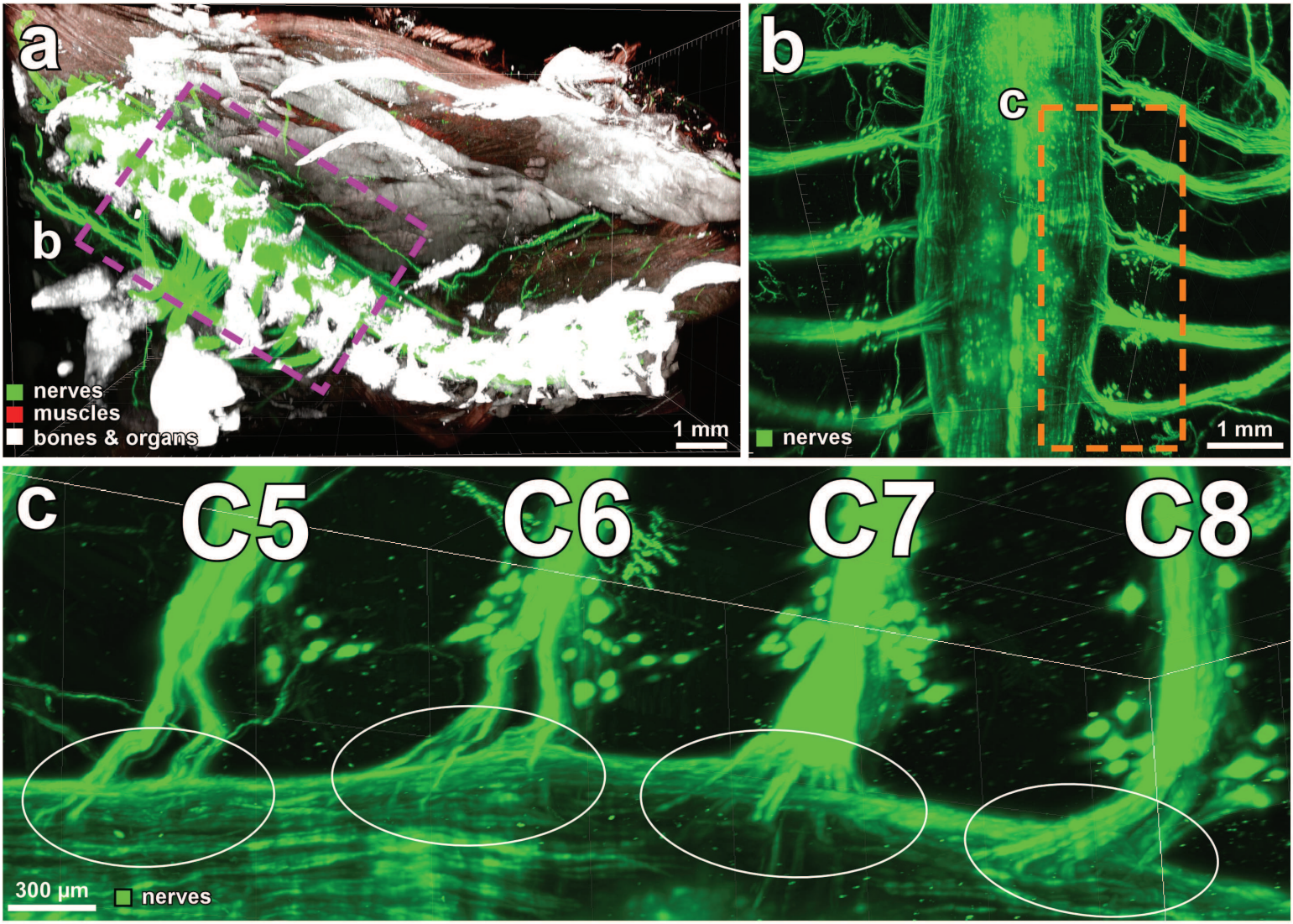

Supplementary Figure 16

Upper torso and individual spinal cord roots

(**a**) Panoptic imaging of the upper torso of the 6 weeks old transparent mouse showing individual spinal cord roots. The bones and organs are in white, mostly the muscles are visible in autofluorescence channel and displayed in red, and the nerves are in green. (**b**) High magnification view from the region indicated in **a** showing only nerve signal (ventral roots). (**c**) High magnification view from the region indicated in **b** demonstrating non-overlapping entry of axons in C5-C8 ventral spinal cord segments (white circles). Comparable labeling and imaging results were achieved in 5 independent animals.

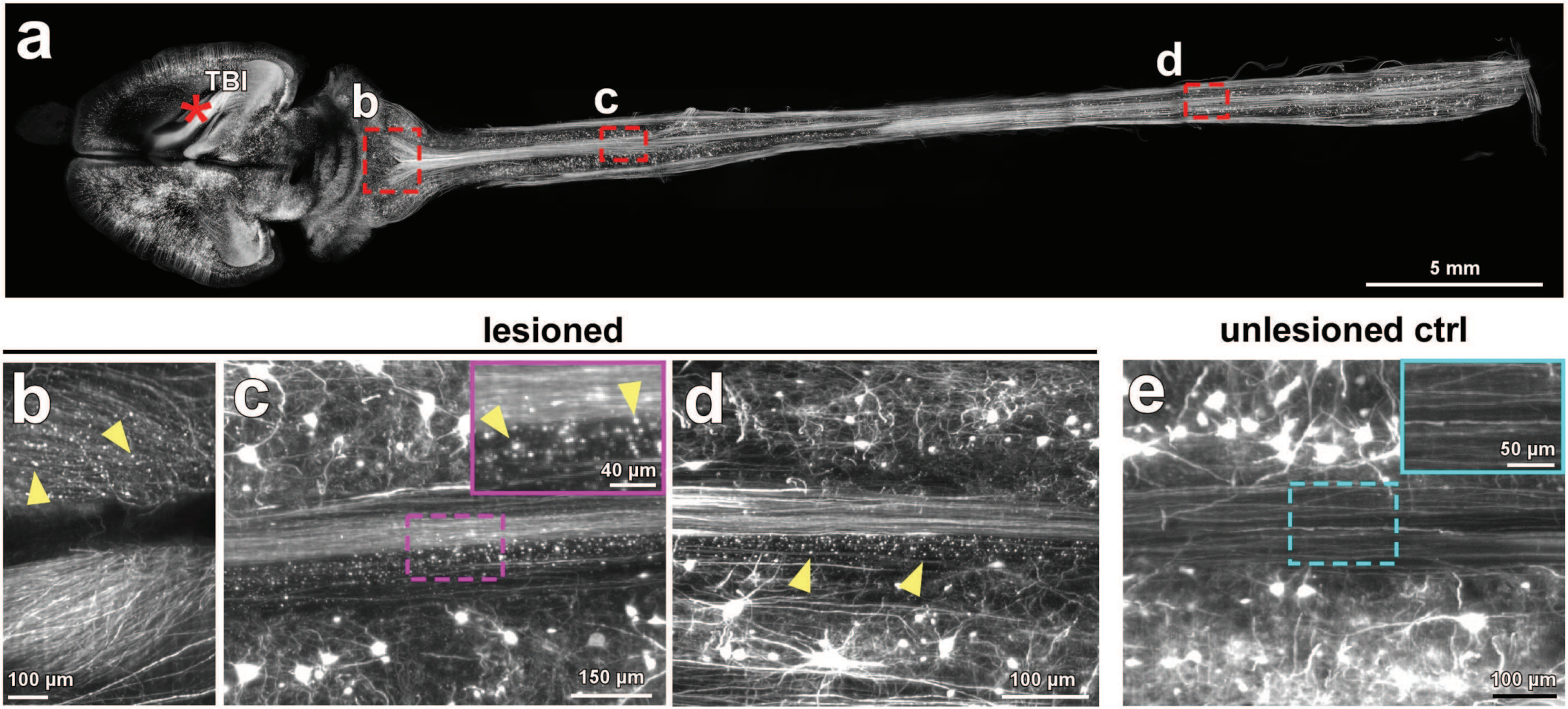

Supplementary Figure 17

TBI induces the degeneration of descending motor axons in the central nervous system

(**a**) To investigate a potential degeneration of the descending motor axons upon TBI, we applied vDISCO on the intact CNS (brain and spinal cord) from *Thy1*-GFPM mice already 1 week after TBI. (**b-d**) High magnification images coming from the indicated spinal cord regions marked in a. The fragmentation (yellow arrow-heads) of the descending motor axons ipsilaterally in the brainstem before the decussation (**b**), and contra-laterally after decussation is evident throughout the spinal cord (**c,d**). (**e**) An unlesioned spinal cord view at the same region shown in the lesioned animal in d. Similar results were observed from 2 independent animals.

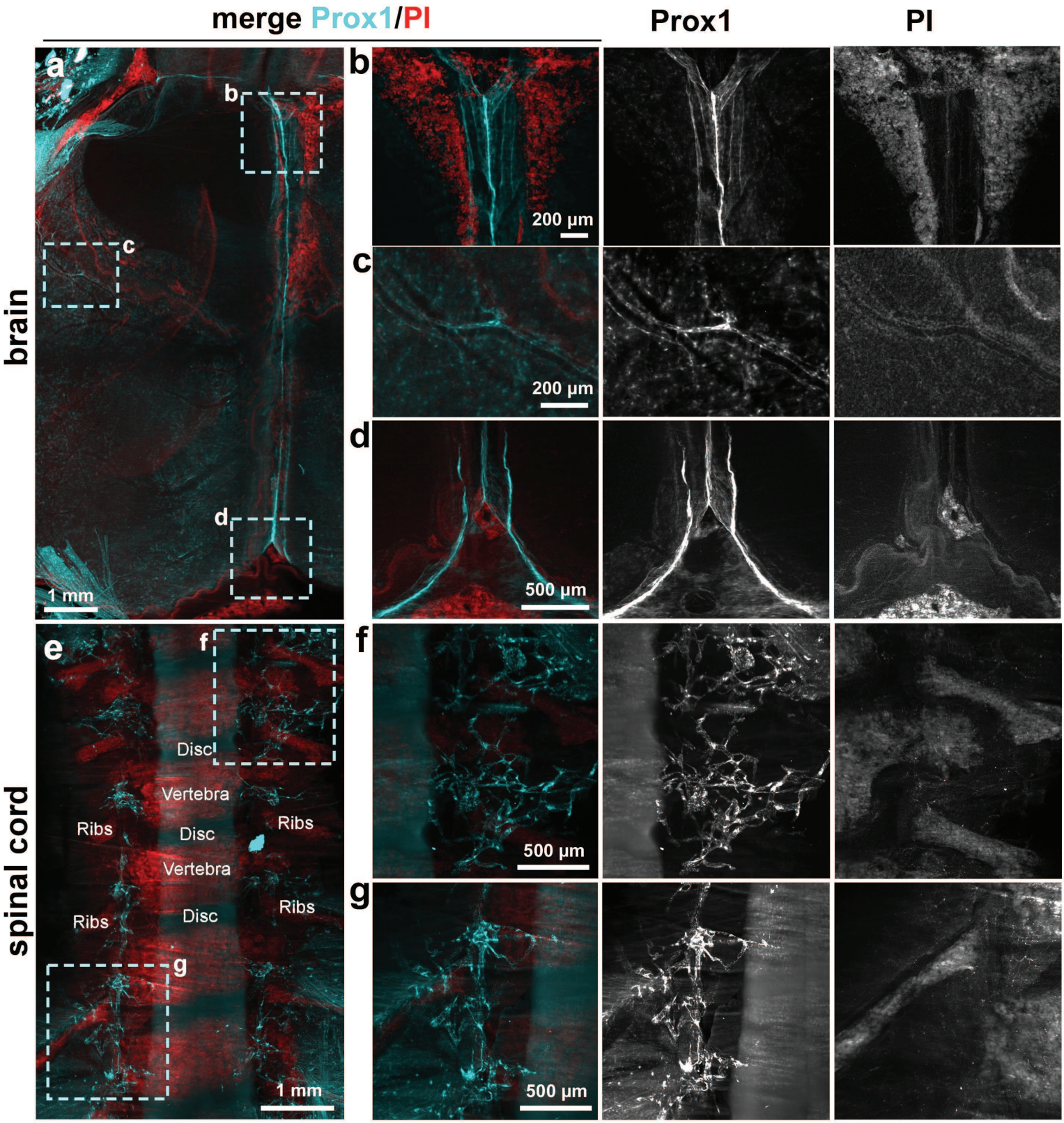

Supplementary Figure 18

Meningeal lymphatic vessels through transparent skull and vertebra by vDISCO

After applying vDISCO pipeline, the 4 weeks old *Prox1*-EGFP mouse was imaged with light-sheet microscopy. Prox1 and PI channels are shown in merge and separate views. (**a-d**) *Prox1*-EGFP mouse head showing the brain lymphatic vessels (cyan) along the sagittal sinus (**b**), pterygopalatine artery (**c**) and transverse sinus (**d**) (similar results were observe from 5 independent mice). (**e-g**) Images from the thoracic region of the spine show the lymphatic vessels (cyan) in the spine region (single experiment).

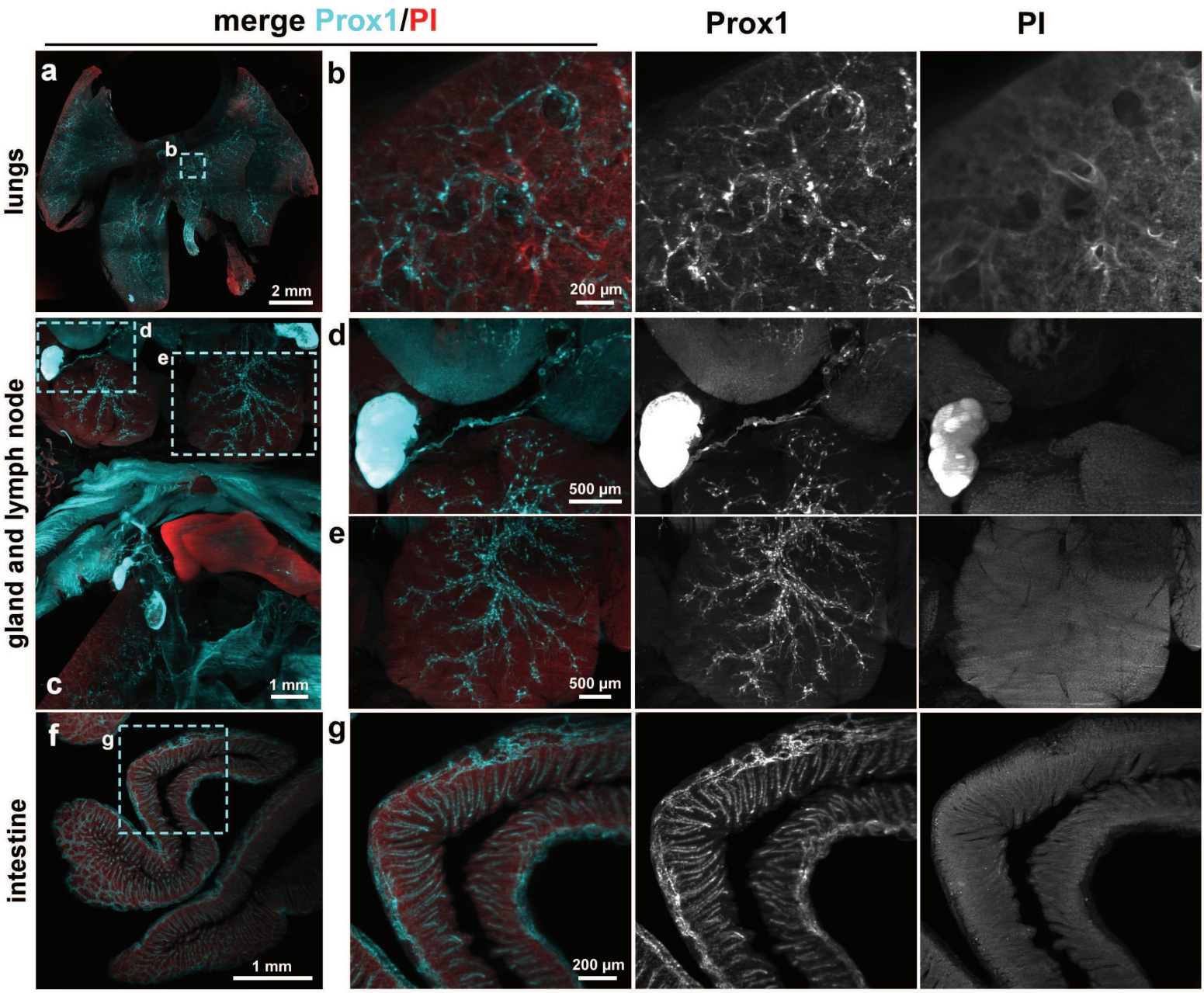

Supplementary Figure 19

Lymphatic vessels in internal organs by vDISCO

After applying vDISCO pipeline, the 4 weeks old *Prox1*-EGFP mouse was imaged with light-sheet microscope (single experiment). Prox1 and PI channels are shown in merge and separate views. The lymphatic vessels (cyan) in lungs (**a-b**), in cervical lymph node (**c**,**d**), in salivery gland (**c**,**e**) and in intestine (**f**,**g**) are evident. See also Supplementary Video 6.

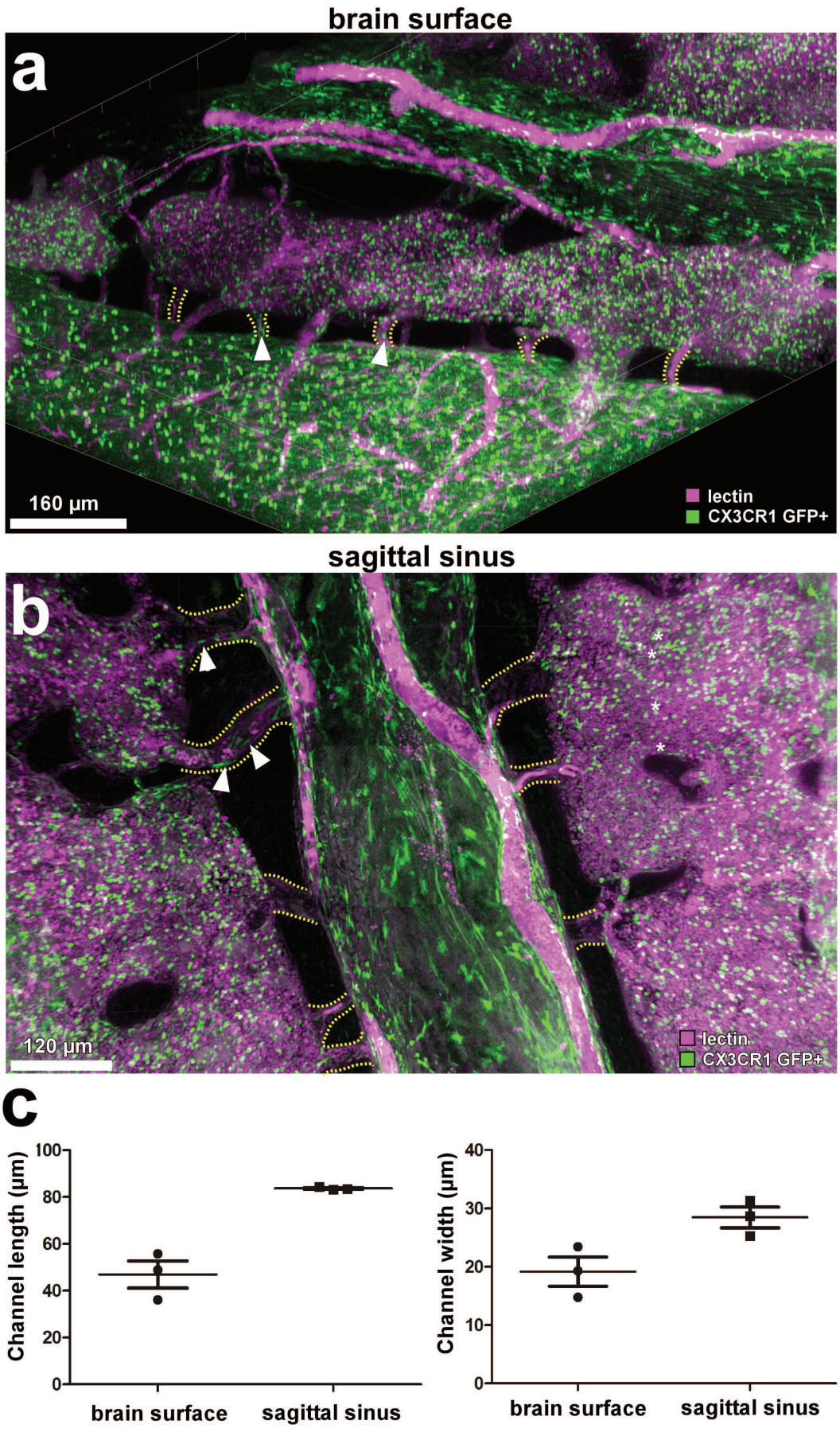

Supplementary Figure 20

Structural features of short skull-meninges connections (SMCs)

(**a**,**b**) 3D confocal images of brain-skull interface. A 4 months old CX3CR1$^{GFP/+}$ mouse (CX3CR1 GFP+ cells in green) was injected with lectin dye (magenta). Vascular connections between the skull marrow and meninges at the brain surface (**a**) and sagittal sinus (**b**) are visible, including the CX3CR1 GFP+ cells (white-arrow heads) in the connections (similar results were observed from 3 independent mice). See also Supplementary Video 9. (**c**) Quantifications of length and width of the SMCs at sagittal sinus and brain surface (mean ± SEM; n=3 animals per group).

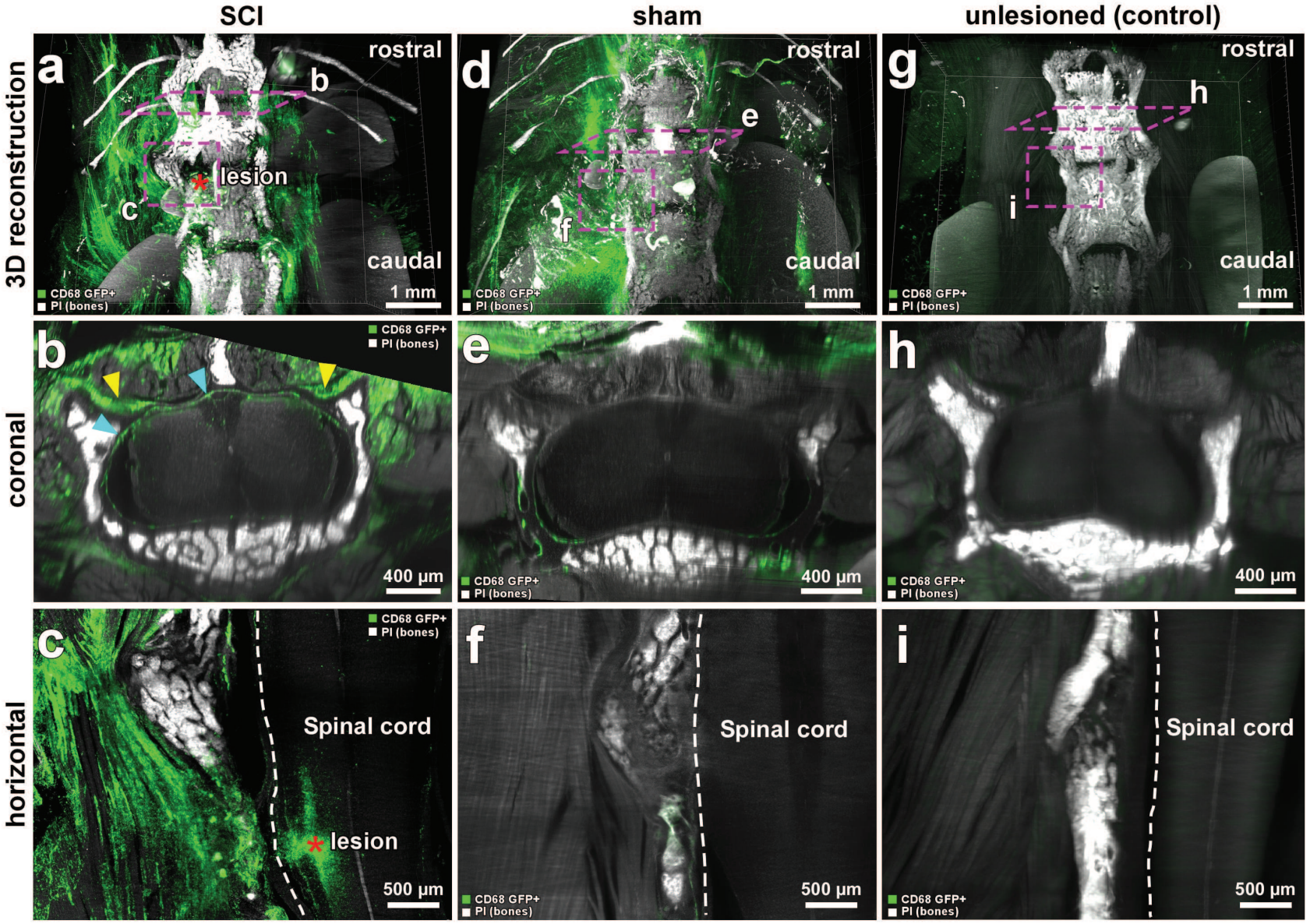

Supplementary Figure 21

Immune cell activation and invasion induced by spinal cord injury

3D visualization of spinal cord from 3 months old *CD68*-EGFP transgenic mice with spinal cord injury (**a**-**c**) compared to mice with sham surgery (**d**-**f**) and unlesioned controls (**g**-**i**). CD68 GFP+ cells are shown in green and PI labeled bones in white. Red asterisks indicate the lesion site. Increased CD68 GFP+ cells throughout the muscles, spinal cord roots (yellow arrow-heads) and meninges (cyan arrow-heads) are evident in the injured spinal cord (**a**-**c**) compared to the controls (**g**-**i**). In the group with sham surgery, the CD68 GFP+ cells increased in the muscles but not in the spinal cord (similar results were observed from 3 independent mice per group). See also Supplementary Video 11.

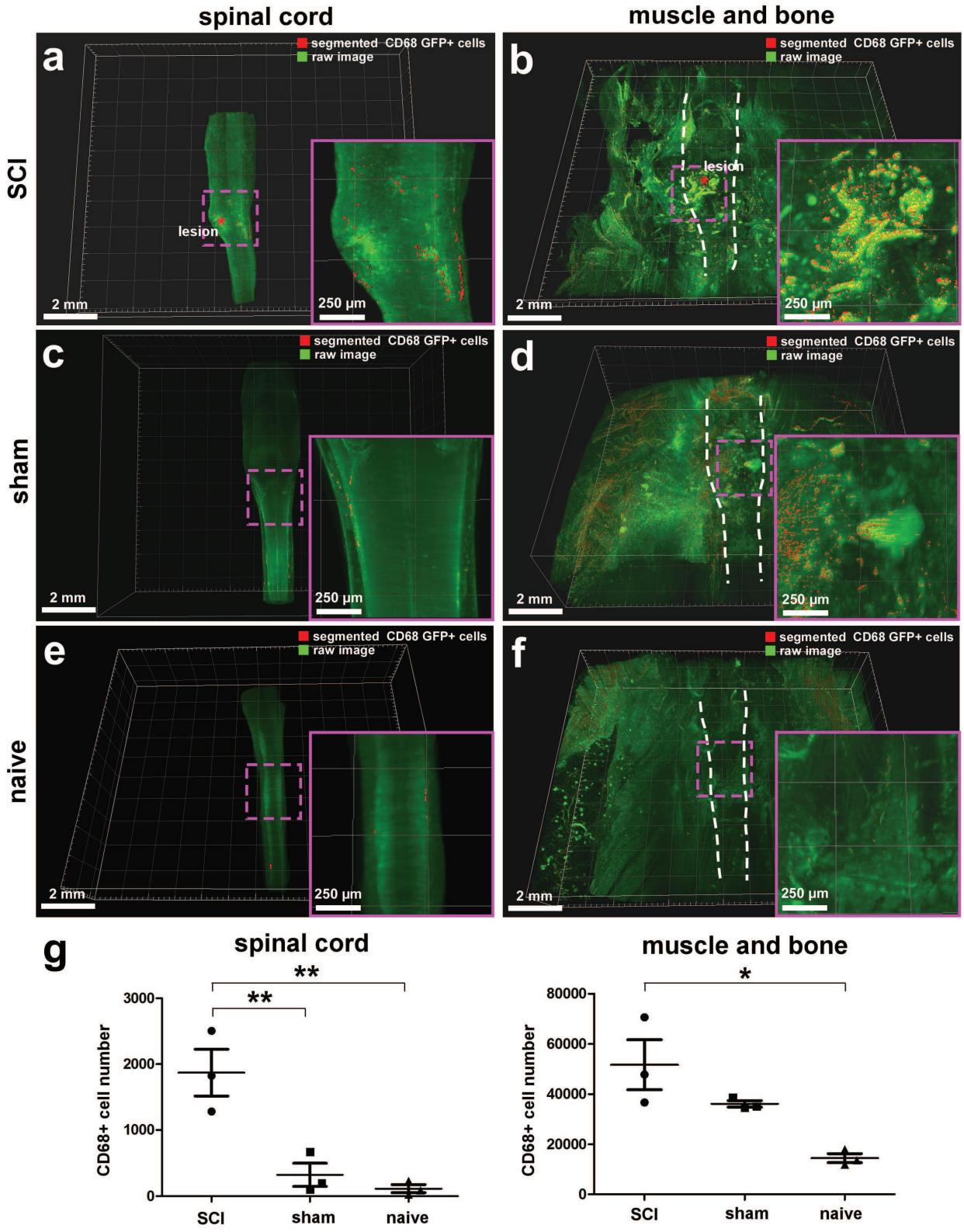

Supplementary Figure 22

CD68 GFP+ cell number increased significantly both in spinal cord and peripheral tissues after spinal cord injury (SCI)

(**a**-**f**) 3D visualization of the spine region from 3 months old *CD68*-EGFP mice with SCI (**a**,**b**) vs. mice with sham surgery (**c**,**d**) and naive mice (**e**,**f**) cleared by vDISCO and imaged by light-sheet microscope. To better visualize the region, spinal cords (**a**,**c** and **e**) were segmented out from their locations in the surrounding tissues (muscle and bone) (**b**,**d** and **f**) using Fiji and afterwards CD68 GFP+ cells were segmented (red) and quantified by IMARIS (similar results were observed from 3 independent mice per group). (**g**) Quantification of CD68 GFP+ cells in spinal cord showing significant cell number increase after SCI compared to sham and naive animals. While CD68 GFP+ cell number increased significantly in surrounding tissue (muscle and bone) in SCI group compared to naive animals (mean ± SEM; n=3 animals per group; statistical significance (for spinal cord, $F_{2,6}$=17.22, SCI vs. sham ***p*=0.0077, SCI vs. naive ***p*=0.0041 and sham vs. naive ns=0.8049. For muscle and bone, $F_{2,6}$=10.05, SCI vs. sham ns=0.2273, SCI vs. naive **p*=0.0101 and sham vs. naive ns=0.0905) was assessed by one-way ANOVA followed by Tukey multiple comparison Test).

DISSECTED ORGANS

steps

tissue type / passive incubation (with shaking)	whole organs such as brain, heart or spleen	soft and porous organs such as gut, lungs or thymus	small organs such as adrenal glands, lymphnodes, organoids or 1 mm slices
pretreatment with permeabilization solution at 37°C	1-2 days	overnight	6 hours
incubation with immunostaining solution at 37°C	10-14 days	4-5 days	3-4 days
washing with washing solution at room temperature	2 hours x 4 times (optionally last step overnight)	1.5 hours x 4 times	1 hour x 4 times
PBS washing at room temperature	2 hours x 4 times	1.5 hours x 4 times	1 hour x 4 times
DISCO clearing			
50% THF at room temperature	1-2 hours	1 hour	1 hour
70% THF at room temperature	1-2 hours	1 hour	1 hour
80% THF at room temperature	1-2 hours	1 hour	1 hour
100% THF at room temperature	1 hour and overnight	1 hour and overnight	1 hour and 5 hours
100% DCM at room temperature	1 hour	45 minutes	30 minutes
BABB at room temperature	overnight	> 6 hours	> 4 hours
cost per sample	~25-30 $	~15-20 $	~6-8 $
imaging time (light-sheet microscopy)	~1.5-3 hours	~3-6 hours	~0.5-1.5 hours

WHOLE BODY

steps

	modality	timing	temperature
PBS washing	active perfusion	overnight	at room temperature
decolorization with 25% CUBIC#1 in PBS	active perfusion	12 hours x 4 times	at room temperature
PBS washing	active perfusion	3 hours x 3 times	at room temperature
decalcification with 10% of EDTA in PBS pH8-9	active perfusion	2 days	at room temperature
PBS washing	active perfusion	3 hours x 3 times	at room temperature
pretreatment with permeabilization solution	active perfusion	12 hours	at room temperature
boosting with immunostaining solution	active perfusion	6 days	with infrared lamp (up to 30°C)
boosting with immunostaining solution	passive shaking	2 days	at 37°C
wash with washing solution	active perfusion	3 hours x 3 times	at room temperature
PBS washing	active perfusion	3 hours x 3 times	at room temperature
DISCO clearing			
50% THF in distilled water	passive shaking	12 hours	at room temperature
70% THF in distilled water	passive shaking	12 hours	at room temperature
80% THF in distilled water	passive shaking	12 hours	at room temperature
100% THF	passive shaking	12 hours x 2 times	at room temperature
100% DCM	passive shaking	3 hours	at room temperature
BABB	passive shaking	> 12 hours	at room temperature
cost per animal	~180-200 $		
imaging time (light-sheet microscopy)	~3-5 days		

permeabilization solution: 1.5% goat serum , 0.5% Triton X-100, 0.5 mM Methyl-beta-cyclodextrin, 0.2% trans-1-Acetyl-4-hydroxy-L-proline, 0.05% Sodium Azide in 0.1 M PBS

washing solution: 1.5% goat serum , 0.5% Triton X-100, 0.05% Sodium Azide in 0.1 M PBS

immunostaining solution: permeabilization solution + nanobooster

THF: tetrahydrofuran
DCM : dichloromethane
BABB: benzyl alcohol + benzyl benzoate (1:2) in volume
CUBIC#1: 25 wt% urea , 25 wt% N,N,N´,N´-tetrakis (2-hydroxypropyl)ethylenediamine, 15 wt% Triton X-100 in 0.1 M PBS

Supplementary Table 1

Notes for vDISCO protocol

The timing for each experimental step can be shortened or extended based on tissue size to improve nanobooster penetration or clearing performance. We found that active (perfusion mediated) whole-body boosting provides more homogeneous and even nanobooster staining compared to passive staining of dissected organs e.g. the brain, if the perfusion is done properly. The costs were estimated only based on the reagents and considering organs from transgenic mouse lines that highly express GFP, such as *Thy1*-GFPM. If other lines (which express less GFP) are used, the amount of nanobooster needed for the protocol can be reduced and the cost might reduce significantly as well. The imaging time has been estimated considering the imaging only with one channel using the Ultramicroscope II (LaVision BioTec) with a 4x objective and it can significantly vary based on many factors: z-step, magnification, different microscope version etc. More information available at www.discotechnologies.org/vDISCO.

FIGURES		SYSTEM	OBJECTIVE SPECIFICATIONS					ACQUISITION PARAMETERS			DATA SIZE
			Magnification	NA	RI	WD	Zoom	Image pixel size	z-step	type	
Figures											
1	a-f	UM II	4X corr.	0.28	1.56	10mm		1.625µmx1.625µm	4µm	single slice	(a)24.8GB, (e)34.7GB
	g,h	UM II	4X corr.	0.28	1.56	10mm		1.625µmx1.625µm	(i)8µm, (j)12µm	single slice	(i)29.5GB, (j)9.90GB
	i	UM II	4X corr.	0.28	1.56	10mm		1.625µmx1.625µm	4-12µm	quantification on single slice	67GB
	j,l,n	UM II	4X corr.	0.28	1.56	10mm		1.625µmx1.625µm	8-10 µm	single slice	(j,l)12.8GB, (n)6.94GB
	k,m	UM II	Oly. 25X	0.95	1.31-1.52	4mm		0.26µmx0.26µm	4µm	single slice	(m)1.37GB, (o)222MB
	o	UM II	4X corr.	0.28	1.56	10mm		1.625µmx1.625µm	8µm	single slice	456GB
2	b-d	UM II -MVX10	Oly. 1X	0.25	1.0	65mm	0.63x	10.32µmx10.32µm	8µm	3D reconstruction	3.27TB
	f-i	UM II -MVX10	Oly. 2X	0.5	1.33/1.56	6mm	1.6x	2.03µmx2.03µm	6µm	3D reconstruction	1.5TB
3	d	UM II	4X corr.	0.28	1.56	10mm		1.625µmx1.625µm	8µm	3D reconstruction	140GB
	e,g	LSM880	Leica 25x	0.95	1.33	2.5mm		0.67µmx0.67µm	4µm	(e) 3D reconstr., (g) single slice	3.89GB
	f,h	LSM880	Leica 25x	0.95	1.33	2.5mm		0.67µmx0.67µm	4µm	96µm thick projection	same data from Fig.6e,g
	j	UM II -MVX10	Oly. 2X	0.5	1.33/1.56	6mm	0.8x	4.06µmx4.06µm	8µm	1440µm thick projection	117GB
	k	LSM880	Leica 25x	0.95	1.33	2.5mm		0.4µmx0.4µm	2.50 µm	180µm thick projection	2.45GB
4	a-d	UM II -MVX10	Oly. 1X	0.25	1.0	65mm	(a,c)1.25x, (b,d)0.63x	(a,c)5.2µmx5.2µm, (b,d)10.32µmx10.32µm	8µm	entire scan projection	(a,c)52.2GB, (b,d)16.8GB
	c,d (yellow, green rectangles)	UM II	Zeiss 20x	1	1.45	5.6mm		0.325µmx0.325µm	2µm	(c)824µm, (d)430µm thick projections	(c)64.8GB, (d)62.7GB
	e	UM II -MVX10	Oly. 2X	0.5	1.33/1.56	6mm	2.5x	1.3µmx1.3µm	8µm	quantification entire scan projection	1TB
5	b	UM II -MVX10	Oly. 2X	0.5	1.33/1.56	6mm	1x	3.25µmx3.25µm	8µm	1.6mm thick projection	105GB
	c-e	UM II -MVX10	Oly. 2X	0.5	1.33/1.56	6mm	2x	1.625µmx1.625µm	10µm	(c)600µm, (d) 500µm, (e)400µm thick projections	(c,e) 42.5GB, (d) 28.4GB
	f	UM II -MVX10	Oly. 2X	0.5	1.33/1.56	6mm	2x	1.625µmx1.625µm	7µm	3D reconstruction	87GB
	g,h	UM II	Zeiss 20x	1	1.45	5.6mm		0.325µmx0.325µm	3µm	15µm thick projections	552GB
	i,j	UM II -MVX10	Oly. 2X	0.5	1.33/1.56	6mm	2x	1.625µmx1.625µm	10µm	single slices	(i)102GB, (j)86.5GB
6	a	UM II	4X corr.	0.28	1.56	10mm	2x	0.8µmx0.8µm	6µm	3D reconstruction	5.8GB
	b-d	UM II -MVX10	Oly. 1X	0.25	1.0	65mm	3.2x	2µmx2µm	8µm	80µm thick projections	5.5GB
	e,f	UM II -MVX10	Oly. 1X	0.25	1.0	65mm	0.63x	8µmx8µm	3µm	single slices	77.9GB
	g,h	UM II -MVX10	Oly. 2X	0.5	1.33/1.56	6mm	1.6x	2µmx2µm	8µm	40µm thick projections	(g)349GB, (h)550GB
	i	UM II -MVX10	Oly. 2X	0.5	1.33/1.56	6mm	1.6x	2µmx2µm	8µm	quantification 40µm projection	1.38 TB for 6 samples
Sup. Figures											
S1	a	UM II -MVX10	Oly. 1X	0.25	1.0	65mm	1x	6.5µmx6.5µm	10µm	single slice	9.37GB
S2	a-f	UM II	4X corr.	0.28	1.56	10mm		1.625µmx1.625µm	10-12 µm	40-48µm thick projection	(a,b,c)30.2GB, (d,e,f) 31.7 GB
	g	UM II	4X corr.	0.28	1.56	10mm		1.625µmx1.625µm	8-16 µm	quantification single slide	71.31GB
S3	a-d	AxioZoom	Zeiss 1X	0.25	1.0	56mm		(a,b)1.14µmx1.14µm, (c,d) 1.82µmx1.82µm	n.a.	single slice	5.46MB x 4= 21.84MB
	e,f	UM II	4X corr.	0.28	1.56	10mm		1.625µmx1.625µm	10µm	50µm thick projection	(e)43.01GB, (f)5.93GB
	g-i	UM II	4X corr.	0.28	1.56	10mm		1.625µmx1.625µm	10µm	quantification single slice	same data from Fig.S3e,f
S4	a-e	UM II	Zeiss 20x	1	1.45	5.6mm		0.325µmx0.325µm	2µm	800 µm thick projection, 3D reconstr.	193.1GB
S5		UM II	Zeiss 20x	1	1.45	5.6mm		0.325µmx0.325µm	2µm	800 µm thick projection, 3D reconstr.	same data as Fig.S4
S6	a-c	UM II	4X corr.	0.28	1.56	10mm		1.625µmx1.625µm	4µm	3D reconstr. 8µm, thick projection	2.1GB
S7	a,h-k	UM II	4X corr.	0.28	1.56	10mm		1.625µmx1.625µm	10µm		118.1 GB
	d,g	UM II	4X corr.	0.28	1.56	10mm		1.625µmx1.625µm	3µm	single slice	32 GB
S9	c	AxioZoom	Zeiss 1X	0.25	1.0	56mm		6.49µmx6.49µm, zoom in 0.405µmx0.405µm	n.a.	single slice	106MB
S11	c-j	UM II -MVX10	Oly. 2X	0.5	1.33/1.56	6mm	0.63x	5.16µmx5.16µm	8-20µm	quantification on single slice	117.1GB
S12	c-g	UM II	4X corr.	0.28	1.56	10mm		1.625µmx1.625µm	8µm	single slices	10-50GB for each sample
S13	b-g	UM II -MVX10	Oly. 2X	0.5	1.33/1.56	6mm	4x	0.81µmx0.81µm	6µm	single slice	10.6GB
	h-j	LSM880	Leica 25x	0.95	1.33	2.5mm		0.10µmx0.10µm	2.5µm	single slice	120MB
S14	a-i	UM II -MVX10	Oly. 1X	0.25	1	65mm	0.63x	10.32µmx10.32µm	8µm	3D reconstruction	same data from Fig. 2b-d
S15	a-e	UM II -MVX10	Oly. 1X	0.25	1	65mm	1x	6.5µmx6.5µm	10µm	3D reconstruction	24GB
S16	a-c	UM II -MVX10	Oly. 2X	0.5	1.33/1.56	6mm	1.25x	2.6µmx2.6µm	4µm	3D reconstruction	39GB
S17	a	UM II	4X corr.	0.28	1.56	10mm		1.625µmx1.625µm	8µm	entire scan projection	57.8GB
	b-d	UM II	4X corr.	0.28	1.56	10mm		1.625µmx1.625µm	8µm	80µm thick projection	same data from Fig S17a
	e	UM II	4X corr.	0.29	1.57	10mm		1.625µmx1.625µm	8µm	80µm thick projection	42.1 GB
S18	a	UM II -MVX10	Oly. 2X	0.5	1.33/1.56	6mm	1x	3.25µmx3.25µm	8µm	1.6mm thick projection	same data from Fig. 5b
	b-d	UM II -MVX10	Oly. 2X	0.5	1.33/1.56	6mm	2x	1.625µmx1.625µm	10µm	(b)600µm, (c) 500µm, (d)400µm thick projections	same data from Fig. 5c-e
	e-g	UM II -MVX10	Oly. 2X	0.5	1.33/1.56	6mm	2x	1.625µmx1.625µm	6µm	1.6mm thick projection	61GB
S19	a,b	UM II	4X corr.	0.29	1.57	10mm		1.625µmx1.625µm	8µm	(a) 1.92mm, (b)640µm thick projections	474GB
	c-e	UM II -MVX10	Oly. 1X	0.25	1	65mm	2x	3.25µmx3.25µm	10µm	800 µm thick projections	103GB
	f-g	UM II -MVX10	Oly. 1X	0.25	1	65mm	3.2x	2µmx2µm	8µm	240µm thick projections	18GB
S20	a,b	LSM880	Zeiss 40X	1.3	1.518	0.21mm	1x	0.21µmx0.21µm	4µm	3D reconstruction	13GB
S21	a,d,g	UM II -MVX10	Oly. 2X	0.5	1.33/1.56	6mm	1.6x	2µmx2µm	6µm	3D reconstructions	(a)232GB, (d)114GB, (g)199GB
	b,e,h	UM II -MVX10	Oly. 2X	0.5	1.33/1.56	6mm	1.6x	2µmx2µm	6µm	30µm thick projections	(b)232GB, (e)114GB, (h)199GB
	c,f,i	UM II -MVX10	Oly. 2X	0.5	1.33/1.56	6mm	1.6x	2µmx2µm	6µm	single slices	(c)232GB, (f)114GB, (i)199GB
S22	a,b	UM II -MVX10	Oly. 2X	0.5	1.33/1.56	6mm	1.6x	2µmx2µm	6µm	3D reconstructions	18GB
	c,d	UM II -MVX10	Oly. 2X	0.5	1.33/1.56	6mm	1.6x	2µmx2µm	6µm	3D reconstructions	62GB
	e,f	UM II -MVX10	Oly. 2X	0.5	1.33/1.56	6mm	1.6x	2µmx2µm	6µm	3D reconstructions	73GB
	g	UM II -MVX10	Oly. 2X	0.5	1.33/1.56	6mm	1.6x	2µmx2µm	6µm	quantification on 3d reconstructions	3.35TB for 9 samples

Legend of abbreviations

Imaging Systems

UM II	LaVision BioTec - UltraMicroscope II
UM II -MVX10	LaVision BioTec - UltramicroscopeM II -MVX10
LSM880	Zeiss confocal LSM880 with Airyscan
AxioZoom	Zeiss AxioZoom EMS3/SyCoP3

NA	Numerical aperture
RI	Refractive Index
WD	Working distance
n.a.	not applicable

Objectives

Oly. 1X	Olympus MV PLAPO 1x/0.25 NA
Oly. 2X	Olympus MVPLAPO2XC
4X corr.	Olympus XLFLUOR4x corrected
Oly. 25X	Olympus XLPLN25X
Zeiss 20X	Zeiss Clr Plan-Neofluar 20x
Zeiss 40X	Zeiss ECPlan-NeoFluar 40x/1.30 Oil DIC M27
Leica 25X	Leica HCX IRAPO L 25x

Supplementary Table 2

Imaging specifications

2.3 Research Article 3: Deep learning reveals cancer metastasis and therapeutic antibody targeting in whole body

9 out of 10 cancer patients die because of the global cancer metastasis but not the primary tumors suggests that understanding the metastasis mechanism is extremely critical for cancer therapy. Although tissue clearing has been widely used in biomedical research field, mapping the cancer metastasis and therapeutic drugs through the whole mouse body requires an advanced methodology for reliable detection and automated high-throughput quantification.

As a robust whole-body tissue clearing method which improves the imaging quality two orders of magnitude, vDISCO enables the unbiased detection of cancer metastasis with single cell level resolution. To improve the efficacy of signal identification and quantification, we developed a deep learning based algorithm, termed DeepMACT, to automatically quantify the breast cancer metastasis and therapeutic antibody distribution through the whole mouse bodies. Applying the DeepMACT pipeline, we found that the majority of metastasis were located in lungs, which is line with previous report that lungs are one of the most common metastasize target for breast cancer (Jin et al., 2018). Comparing with the performance of human operator, DeepMACT reached similar detection accuracy while 300 times faster in speed. Next, in order to study the bio-distribution and targeting efficacy of therapeutic antibody, we injected 6A10 antibody conjugated with Alexa dye and found that 77% of metastasis were targeted, specifically 85% in lungs and 66% in rest body tissue. Furthermore, we did not find the correlation between the size and targeting effect of metastasis but Intriguingly, we found that the targeted metastasis are clustered and close to each other. This indicates that microenvironment of the metastasis niches might play an important role in antibody targeting. Overall, DeepMACT achieved reliable detection and automated quantification of cancer metastasis throughout the whole mouse body and is a robust platform readily applicable to various types of cancer and therapeutic drug studies.

Author contribution: performed 2D epifluorescence microscopy of cleared whole-body samples; performed 3D high resolution light-sheet microscopy for individual organs; performed confocal microscopy and analysis for vessel quantification; wrote the manuscript with colleagues (please see section 7 for further details).

Deep learning reveals cancer metastasis and therapeutic antibody targeting in whole body

Authors

Chenchen Pan, Oliver Schoppe, Arnaldo Parra-Damas, Ruiyao Cai, Mihail Ivilinov Todorov, Gabor Gondi, Bettina von Neubeck, Alireza Ghasemi, Madita Alice Reimer, Javier Coronel, Boyan K. Garvalov, Bjoern Menze, Reinhard Zeidler and Ali Ertürk

Graphical Abstract

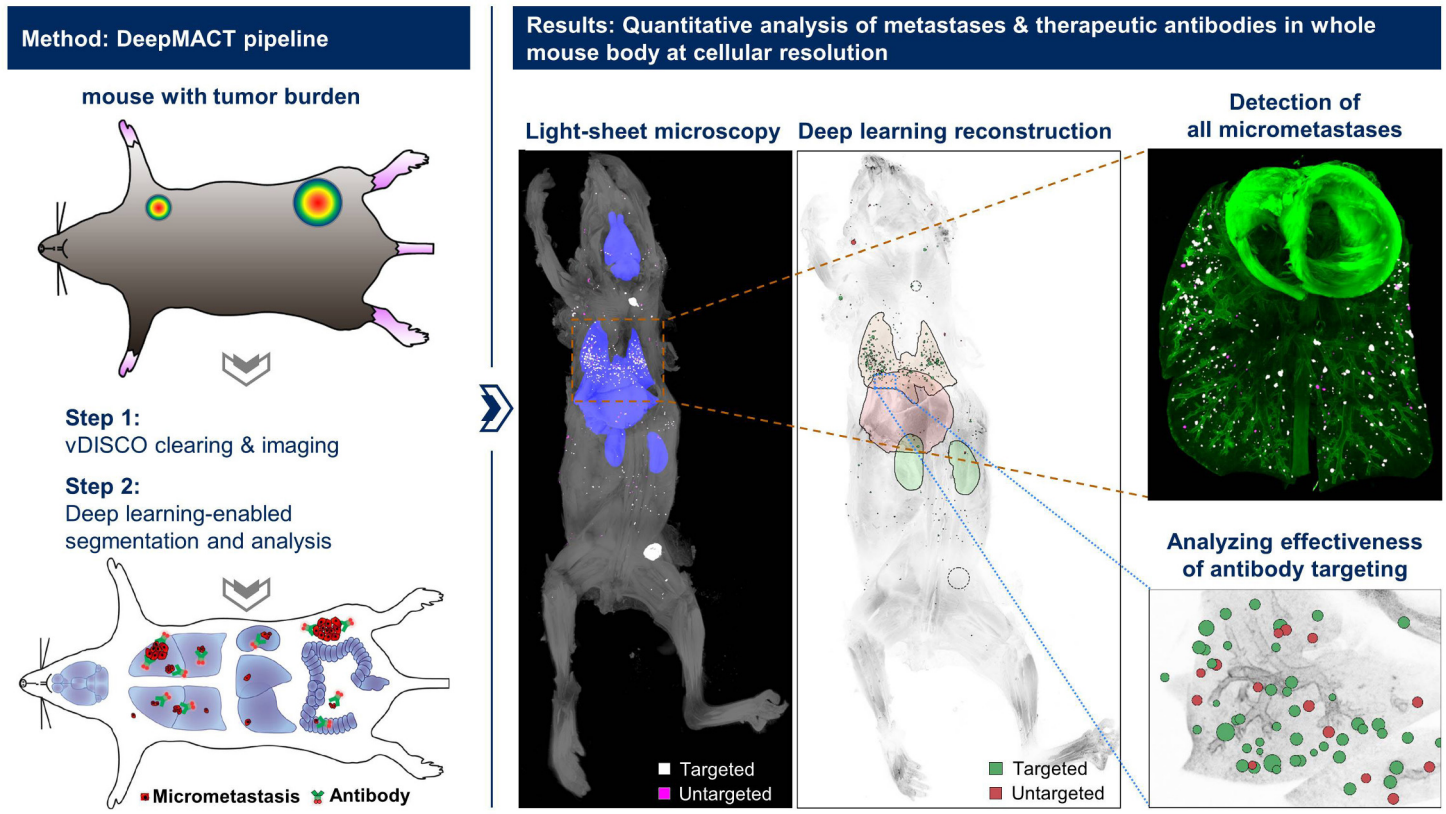

- DeepMACT showed that the majority of the micrometastases had size of 75µm or smaller, which could not be detected by other whole-body imaging methods
- DeepMACT reveled that antibody-based therapeutics can miss as many as 23% of the micrometastases
- We found that tumor microenvironment is critical for the efficacy of antibody drug targeting

Supplementary Movies and deep learning algorithms of DeepMACT are available at http://discotechnologies.org/DeepMACT/

Deep learning reveals cancer metastasis and therapeutic antibody targeting in whole body

Chenchen Pan[*1,3], Oliver Schoppe[*2], Arnaldo Parra-Damas[*1], Ruiyao Cai[1,3], Mihail Ivilinov Todorov[1], Gabor Gondi[4], Bettina von Neubeck[4], Alireza Ghasemi[1], Madita Alice Reimer[1], Javier Coronel[2], Boyan K. Garvalov[5], Bjoern Menze[2,8], Reinhard Zeidler[4,6] and Ali Ertürk[1,3,7]

1 Institute for Stroke and Dementia Research, Klinikum der Universität München, Ludwig Maximilian University of Munich (LMU), Munich, Germany
2 Center for Translational Cancer Research (TranslaTUM) & Department of Computer Science,
3 Graduate School of Neuroscience (GSN), Munich, Germany
4 Helmholtz Zentrum München, Research Unit Gene Vectors, Munich, Germany
5 Department of Microvascular Biology and Pathobiology, European Center for Angioscience (ECAS), Medical Faculty Mannheim, University of Heidelberg, Germany
6 Department for Otorhinolaryngology, Klinikum der Universität München, Munich, Germany
7 Munich Cluster for Systems Neurology (SyNergy), Munich, Germany
8 Munich School of Bioengineering, Technical University of Munich, Munich, Germany
* These authors contributed equally to this work
Correspondence: Ali.Ertuerk@med.uni-muenchen.de

February 2019

SUMMARY

Reliable detection of disseminated tumor cells and of the biodistribution of tumor-targeting therapeutic antibodies within the entire body has long been needed to better understand and treat cancer metastasis. Here, we developed an integrated pipeline for automated quantification of cancer metastases and therapeutic antibody targeting, named DeepMACT. First, we enhanced the fluorescent signal of tumor cells more than 100-fold by applying the vDISCO method to image single cancer cells in intact transparent mice. Second, we developed deep learning algorithms for automated quantification of metastases with an accuracy matching human expert manual annotation. Deep learning-based quantifications in a model of spontaneous metastasis using human breast cancer cells allowed us to systematically analyze clinically relevant features such as size, shape, spatial distribution, and the degree to which metastases are targeted by a therapeutic monoclonal antibody in whole mice. DeepMACT can thus considerably improve the discovery of effective therapeutic strategies for metastatic cancer.

INTRODUCTION

Metastasis is a complex process affecting diverse organs[1-3]. As most cancer patients die of metastases at distant sites developing from disseminated tumor cells with primary or acquired resistance to therapy, a comprehensive and unbiased detection of disseminated tumor cells and tumor targeting drugs within the entire body at the single cell level is crucial[4]. Such technology would help to explore mechanisms affecting tumor metastasis and drug targeting much more reliably, hence substantially contributing to the development of improved therapeutics. So far, such efforts have been hampered by the lack of 1) imaging technologies to reliably detect single cancer cells in intact mouse bodies, and 2) algorithms to quickly and accurately quantify large-scale imaging data. Here, we developed an analysis pipeline that allows us to efficiently solve these limitations.

First, we built upon recently developed whole mouse clearing methods[5-8] to address the imaging problem. Typically, fluorescent labeling of cancer cells *in vitro* or *in vivo* is achieved by endogenous expression of fluorescent proteins such as GFP, YFP, and mCherry, which emit light in the visible spectrum. However, many tissues in the body show high autofluorescence in this range[9,10], which hinders reliable detection of single cancer cells or small cell clusters in intact mouse bodies based on their endogenous fluorescent signal. To circumvent this problem, we chose to implement the vDISCO technology[8], which amplifies the signal of fluorescent proteins of cancer cells more than 100-fold, enabling reliable imaging not only of large metastases but also micrometastases down to single cells throughout the entire body.

Second, systematic analysis of metastasis in whole adult mouse bodies requires quantitative information such as location, size and shape of all individual metastases. Manual detection and segmentation of numerous metastases in highly resolved full body scans is an extremely laborious task that may take several months per mouse for an expert annotator. In addition, automation by filter-based 3D object detectors is not reliable as different body tissues have different levels of contrast[5], causing a high

rate of false positive and false negative cancer cell detection. Recent studies have started to show the high-efficacy of deep learning-based analysis of biomedical images, as well as pre-clinical studies, compared to filter-based or manual segmentation methods[11-17]. To enable automated, robust, and fast mapping of all tumor cells in transparent mice, we developed an efficient deep learning approach based on convolutional neural networks (CNNs) and optimized it for the vDISCO imaging data and tumor cell distribution patterns.

Together, resolving these two bottlenecks allowed us to build an integrated, highly automated pipeline for analysis of metastasis and tumor-targeting therapeutics, which we named DeepMACT (Deep learning-enabled Metastasis Analysis in Cleared Tissue). Using DeepMACT, we detected cancer metastasis and therapeutic antibody targeting at the single cell level in entire mouse bodies, including many metastases previously overlooked by human annotators. As a scalable, easily accessible, fast, and cost-efficient method, DeepMACT enables a wide range of studies on cancer metastasis and therapeutic strategies. To facilitate adoption, the protocols for clearing and imaging, as well as the deep learning algorithm, the training data, and the trained model are freely available online for adaptations to address diverse questions in pre-clinical and clinical research.

RESULTS

Focusing on a clinically relevant tumor model, we transplanted human MDA-MB-231 mammary carcinoma cells, expressing mCherry and firefly luciferase, into the mammary fat pad of NOD *scid* gamma (NSG) mice and allowed the tumors to grow and metastasize for 6-10 weeks (**Figure 1A**)[18-20]. Furthermore, we injected the fluorescently-tagged 6A10 therapeutic antibody that has been shown to reduce tumor burden in this model[19,20]. To investigate cancer metastasis and therapeutic antibody targeting in whole mouse bodies at the single cell level, we developed DeepMACT. In short, we transcardially perfused the animals using standard PFA fixation and applied the vDISCO method to boost the fluorescent signal of tumor cells in transparent mice. After light-sheet microscopy, the 3D image stacks of whole mouse bodies were analyzed using deep learning algorithms. The DeepMACT pipeline consists of 1) vDISCO panoptic imaging of transparent mice at the single cell level and 2) deep learning-based analysis of cancer metastasis and antibody drug targeting (**Figure 1B**).

DeepMACT step 1: vDISCO imaging of cancer metastases at cellular resolution in intact mice

We previously developed the vDISCO technology to image single cells in mouse bodies through intact bones and skin[8]. The vDISCO method utilizes bright fluorescent dyes tagged to nanobodies to boost the signal of fluorescent proteins expressed in the target cells. Here, we first applied vDISCO to increase the fluorescence signal of mCherry-expressing cancer cells. Boosting the tumor cell fluorescence with anti-mCherry nanobodies conjugated to Atto-594 or Atto-647N dyes, we found that nanoboosters can enhance the signal quality of cancer cells over 100 times compared to imaging the endogenous mCherry signal (**Figure S1**). Owing to this significant enhancement in signal contrast, we could readily detect single cancer cells buried in centimeters-thick mouse bodies, e.g., in deep brain regions through the intact skull (**Figure S1F**, yellow arrowhead). To confirm the specificity of vDISCO boosting of mCherry expressing cancer cells, we performed the following experiments: 1) we stained control mice without a tumor transplant, thereby lacking mCherry expression, and found no labeling in any of the analyzed organs; 2) we analyzed the primary tumors and lung metastases from the vDISCO-processed mouse bodies by staining them using a specific anti-luciferase antibody, which confirmed that endogenous mCherry fluorescence co-localized with both the nanobooster and the luciferase signals; and 3) we confirmed the colocalization of nanoboosters with mCherry expressing single tumor cells (**Figure S2**).

Since the detection of smaller-sized tumor cell clusters, which may represent dormant cancer cells or incipient metastatic nodules, is critical, we next tested if vDISCO allows imaging cancer metastases in whole-mouse bodies at the single cell level. In order to compare our approach to conventional methods, we also acquired bioluminescence images of mice before applying DeepMACT. In line with previous findings[18], we detected the earliest large metastasis of transplanted MDA-MB-231 cells at the axillary lymph node of mice by bioluminescence (**Figure 2A, Figure S3**). However, bioluminescence imaging did not reveal any detailed information such as size or shape and failed to show the presence of micrometastases.

After bioluminescence assessment, we applied vDISCO using anti-mCherry nanoboosters conjugated to Atto-647N and imaged the whole-mouse bodies first using epifluorescence in 2D (**Figure 2B-G**), then using light-sheet microscopy in 3D (**Figure 2H-O**). In epifluorescence, we could readily see both the primary tumor (**Figure 2F**) and the major metastases at the axillary lymph node (**Figure 2D**), which were also detected by bioluminescence imaging (**Figure 2A**), albeit as

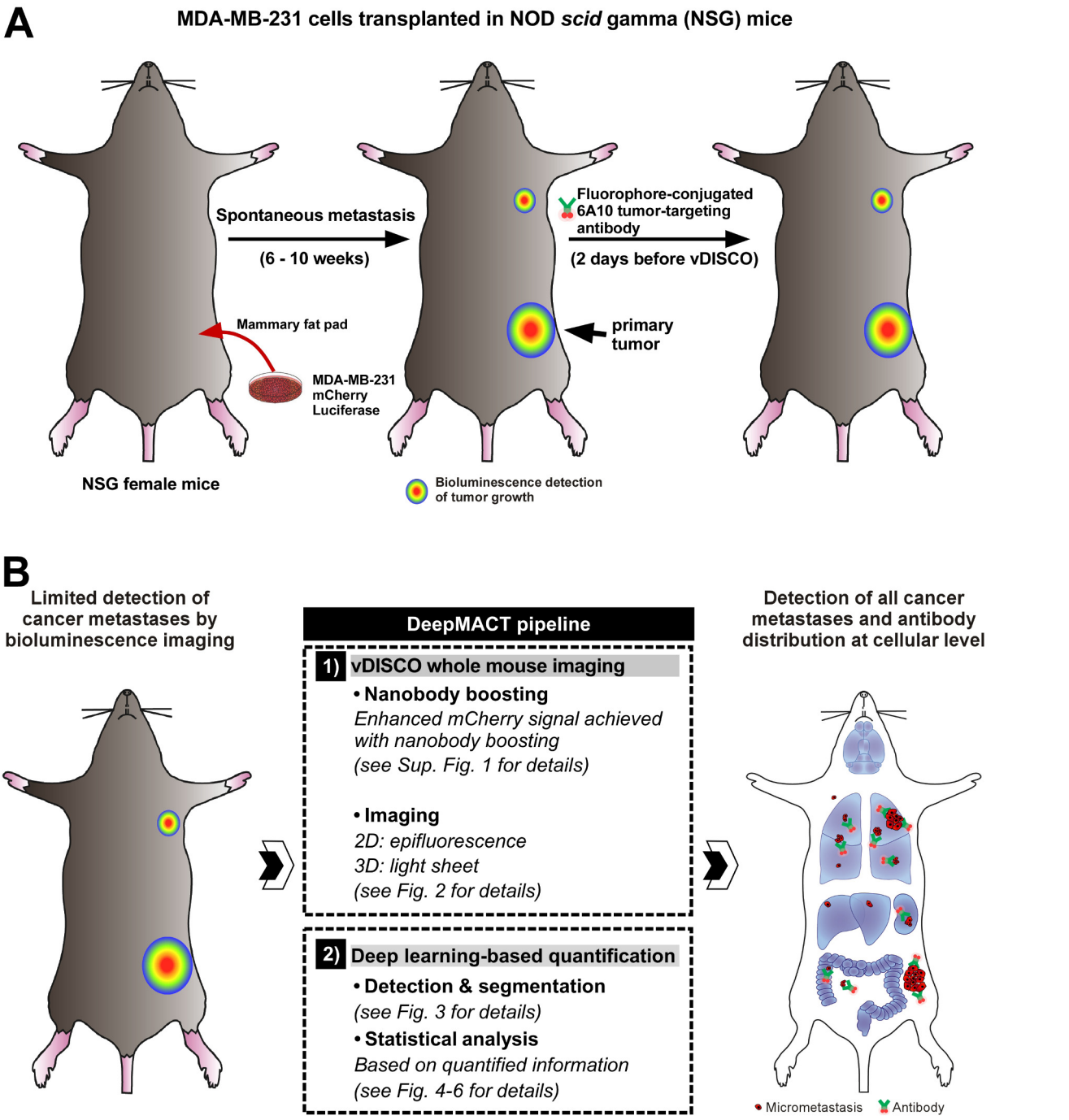

Figure 1

Experimental design and schematic of DeepMACT pipeline for analysis of cancer metastases and antibody drug targeting at single cell level

(**A**) Illustration of the experimental workflow for tumor transplantation and antibody application. (**B**) Steps of the DeepMACT pipeline on whole mouse bodies. First, the whole mice are fixed and processed with the vDISCO protocol to amplify the fluorescent signal of cancer cells. Whole transparent mice are subsequently imaged using light-sheet microscopy from head to toe at single cell resolution. Light-sheet images are assembled into a complete 3D image of the mouse. Next, convolutional neural networks are trained to identify and segment all micrometastases in the fluorescence signal. The trained algorithms are then applied to 3D images to detect cancer metastases and an antibody-based drug targeting in whole transparent mice at single cell level.

a bulk signal, lacking information on real size and shape. By contrast, our approach allowed the visualization of several micrometastases in the lungs with conventional epifluorescence imaging, which were not visible in bioluminescence (compare the magenta marked regions in **Figure 2A** with **Figure 2B,** and red arrowheads in **Figure 2E**; more examples shown in **Figure S3**). Thus, vDISCO followed by epifluorescence imaging, which can be completed within minutes, already provided greater details and sensitivity compared to bioluminescence imaging. Next, we imaged entire transparent mice using a light-sheet microscope[8] at cellular resolution in 3D to detect micrometastases throughout the

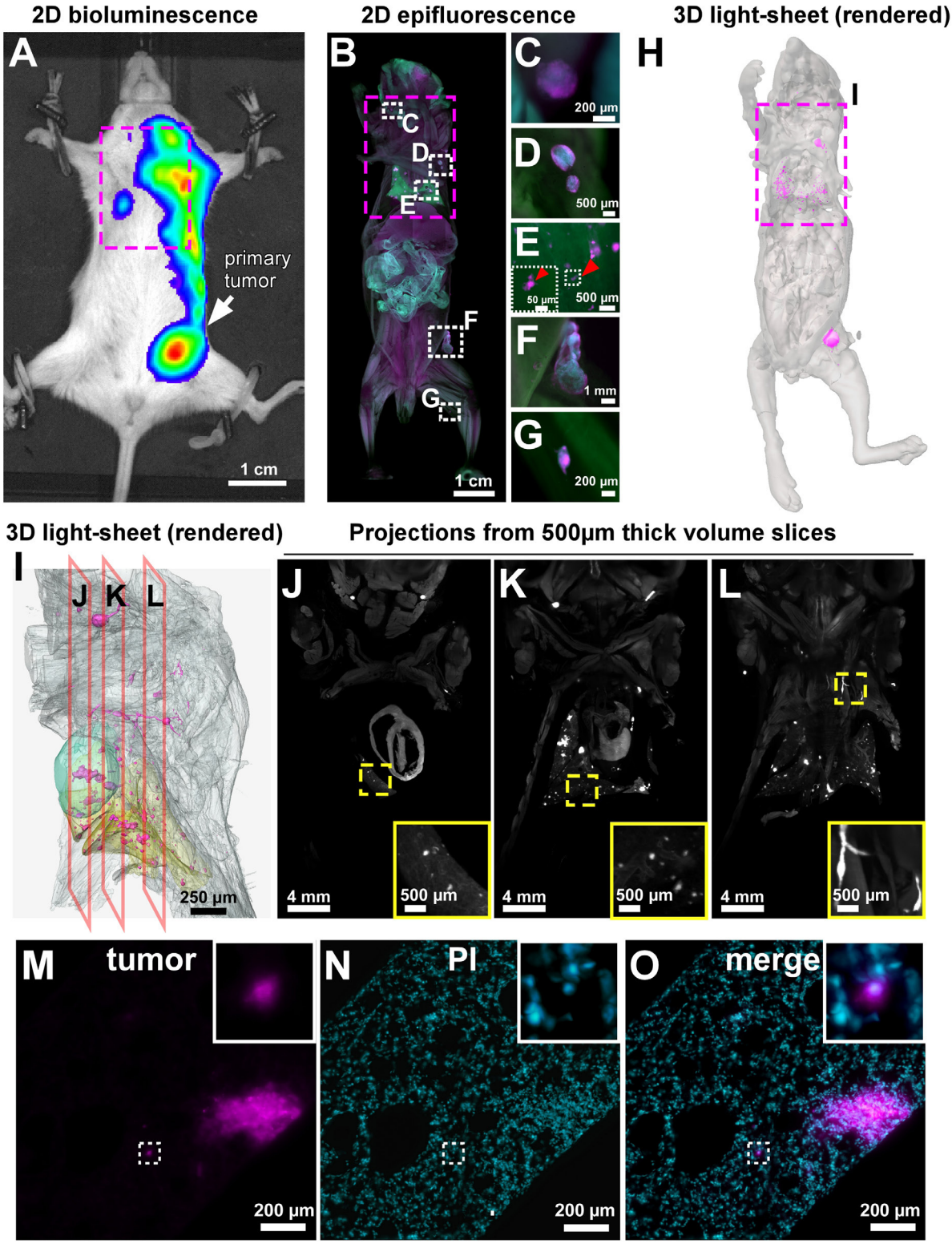

Figure 2

DeepMACT step 1: vDISCO visualization of metastases in an intact whole mouse body

(**A**) Bioluminescence image of a tumor-bearing mouse before vDISCO. (**B**-**G**) Epifluorescence images of the same mouse after vDISCO show metastases (magenta) in greater detail compared to bioluminescence, including small micrometastases that can be readily detected in the lungs (**E**, red arrowhead) and in the leg (**G**), in addition to the primary tumor (**F**) and major metastases (**C** and **D**) that are also visible in bioluminescence as bulk signal (A). (**H**) 3D visualization of the intact transparent body of the same mouse, imaged by light-sheet microscopy. (**I**) Lateral views of the 3D segmentation obtained from the light-sheet imaging data corresponding to the magenta-boxed region indicated in (A, B, and H). For simplicity, only a few organs are segmented: the heart (cyan) and the lungs (yellow); the mouse body is shown in transparent gray and the metastases are in magenta. (**J**-**L**) Original light-sheet microscopy data (500 µm projections) showing tumors from the sagittal planes indicated in (J). (**M**-**O**) High resolution light-sheet microscopy images (single planes) showing single tumor cells (magenta) and nuclei (labeled with propidium iodide, PI; cyan) revealed by vDISCO. See Figure S1-S4, Movie S1 and S2.

body (**Figure 2H**). In the chest area, we could see various metastases not only in the lungs (yellow segmented region in **Figure 2I**) and lymph nodes, but also at the base of the neck and surrounding tissues (**Figure 2J-L** and **Movie S1**). Importantly, light-sheet microscopy scanning allowed us to image micrometastases down to the single cell level in the intact mouse body. An example of a single-cell metastasis is shown in the dashed box in **Figure 2M** (also see **Movie S2**) as verified by nuclear staining with PI (**Figure 2N-O)**. Thus, our approach allows, for the first time, to image micrometastases in intact mice in 3D down to single cell resolution.

DeepMACT step 2: Deep learning for detection and quantification of metastases

We developed a novel deep learning-based approach to detect and segment all cancer cells in whole mouse bodies. This framework solves the 3D task of detecting and segmenting metastases in volumetric scans with CNNs that process 2D projections of small sub-volumes (**Figure 3A**). In brief, we first derived three 2D maximum intensity projections (aligned with the x-, y-, and z-axes) for each sub-volume in order to increase the signal-to-noise ratios (SNR). We fed the resulting projections to the CNN and obtained 2D probability maps, in which each pixel value represents the estimated probability that this pixel identifies a metastasis under the given projection. We then reconstructed a 3D segmentation from the three projections observing increased reliability in detecting true positive metastases while safely ignoring non-metastatic tissue that would be false positives in the individual projections. For example, in **Figure 3B**, the green arrows show successful detection of a real metastasis and the red arrows show successful ignoring of a structure that could be mistaken for a metastasis from a single 2D projection. This approach was highly effective in detecting and segmenting metastases in the imaging data, yielding a binary mask for all metastases in the body.

The core of the architecture makes use of CNNs (**Figure 3C**), structurally similar to the established U-net[21], which learn to distinguish metastases from the background signal. This is achieved by using a deep stack of encoding units, which detect characteristic cancer features, and a corresponding stack of decoding units, which segment each metastasis at pixel-level. Each encoding unit performs two convolutions, extracting information about the environment for each pixel and representing that information in a third dimension - the feature channels. Before being passed on to the next encoding unit, the image is spatially down-sampled. Together, this means that the neural network is steadily increasing the feature channels and steadily decreasing the spatial resolution, enforcing the network to learn even more abstract representations of the data (i.e., features) in the deeper layers, before mapping the information relevant to cancer cells back to the original resolution in the decoding upward path. This happens by up-sampling the abstract, low-resolution information from lower layers and concatenating it with the less abstract, but higher-resolution information from the encoding path via skip connections (some exemplary visualizations of the computational stages are presented in **Figure S4A-C**).

To assess the reliability of our automated deep learning architecture, we applied it to a fresh test set of a full-body scan, which was neither used for training the CNNs nor to optimize hyperparameters. The data sets were manually annotated by human experts and any disagreements between experts were jointly reviewed and discussed in order to derive a refined, commonly agreed reference annotation (see methods for details). We then systematically compared the performance of our deep learning approach to that of established detection methods as well as the performance of a single human annotator, calculating F1-score (also known as Dice score), a common performance measure based on both the metastasis detection rate (recall) and false positive rate (precision).

We found that DeepMACT reached an F1-score of 80%, outperforming existing filter-based detectors by a large margin and coming very close to the level of a single human annotator with an F1-score of 83% (**Figure 3D**). The slightly higher F1-score of a single human annotator is mainly driven by the high precision. However, the human annotator missed around 29% of all micrometastases (examples are shown in **Figure S4D-F**) and detecting those false negatives would require a repetitive and very laborious re-analysis of the whole animal scans – several months of human work time. On the other hand, the F1-score of DeepMACT is a result of a balance between precision and recall, which can be freely adjusted via the model's threshold. For DeepMACT, we can increase detection rate (recall) over 95%. While this also increases the false-positive rate, correcting the false positive data requires only a review of marked signals by a human annotator, which we completed within hours for the data of this study (an example is shown in **Figure S4G-I**). A more detailed analysis on the trade-off between precision and recall is shown in **Figure S4J**. Notably, DeepMACT could detect micrometastases about 30 times faster than filter-based detectors and over 300 times faster than a human annotator (**Figure 3E**) who was already supported by a dedicated and interactive software, custom-built for this task and these data; without annotation software, the human manual annotation

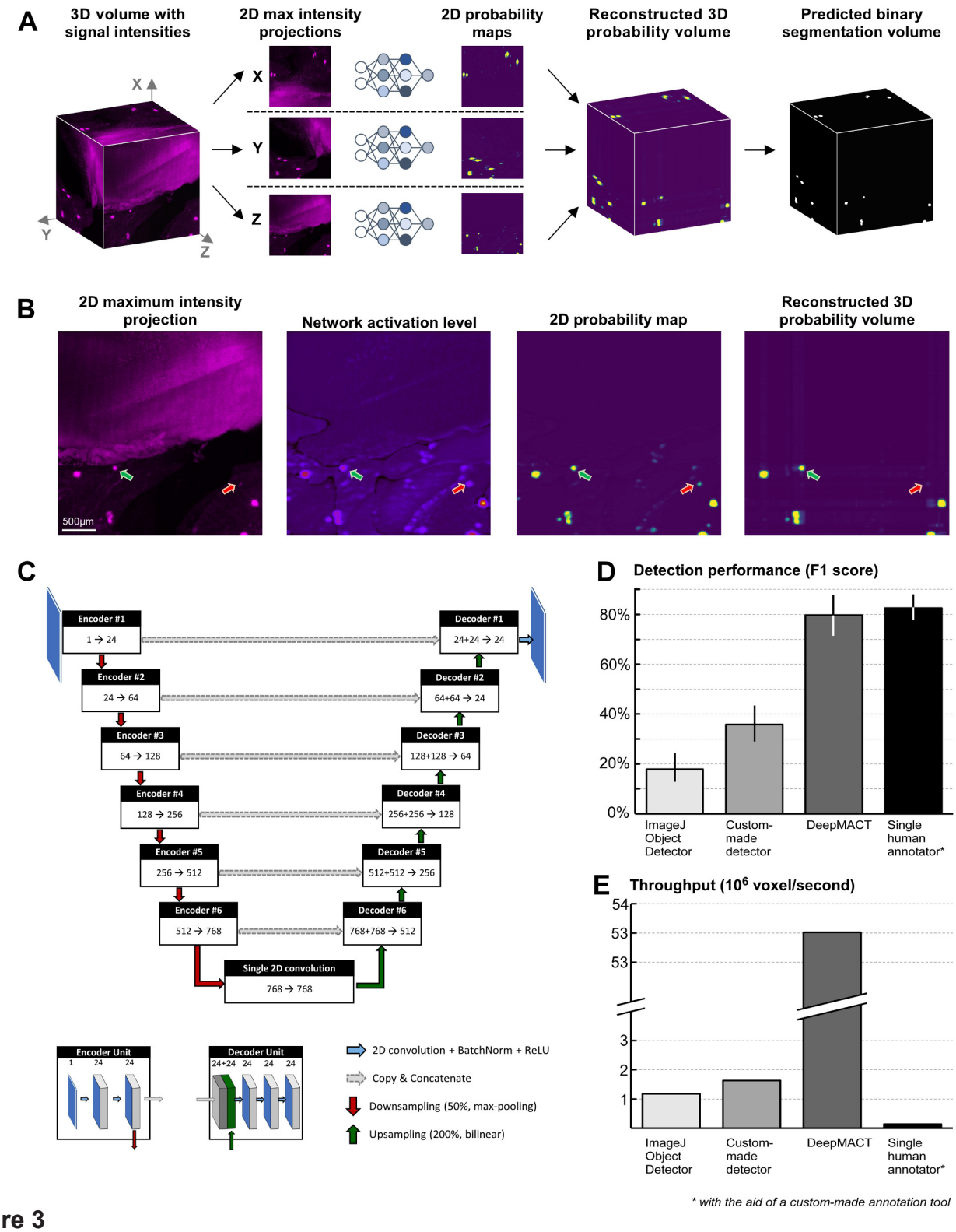

Figure 3

DeepMACT step 2: Architecture and performance of the deep learning algorithm

(**A**) Representation of the deep learning inference workflow to efficiently derive 3D detection and segmentation exploiting three 2D computational operations. (**B**) Visualization of the computational stages; the green arrow shows successful detection of a metastasis, the red arrow shows elimination of a potential false positive detection after 3D recombination. (**C**) High-level representation of the network architecture with an encoding and a decoding path. (**D**-**E**) Comparison of our deep learning pipeline to alternative automated methods and manual segmentation by a human expert in terms of performance (**D**) and speed (**E**).

would be estimated to take several months for a single mouse. Thus, DeepMACT can complete months to years of human labor in within hours without compromising on segmentation quality.

DeepMACT detects micrometastases at the cellular level

After establishing the DeepMACT pipeline, we used it to analyze whole mouse bodies. In addition to

the primary tumor and the macrometastasis in the axillary lymph node, we could detect hundreds of micrometastases of varying sizes throughout the body, especially in the lungs (**Figure 4A-B)**. Overall, DeepMACT identified 520 micrometastases throughout the entire body in this particular mouse, of which there were 306 in the lungs, 5 in the liver, 1 in the left kidney and 208 in the rest of the body (**Figure 4C**). We found that micrometastases are mostly located in the inner tissue layers (about 1 cm depth from the surface), as shown by color-coding in **Figure 4D,** making them extra difficult to detect by other methods. To analyze the spatial distribution with regard to the lung anatomy, we registered all 306 lung micrometastases to the mouse lung lobes. We found that micrometastases were evenly distributed in all lobes (**Figure 4E,F**). Interestingly, the micrometastases were randomly distributed throughout the lungs regardless of their size, suggesting independent colonization at multiple sites. Furthermore, we quantified the size and relative location of all micrometastases in the entire body (**Figure 4G-L**). While 79% of micrometastases were within 1 mm to the nearest neighboring micrometastasis, we also found highly isolated micrometastases as distant as 9.3 mm apart from their nearest neighbor (**Figure 4G**). Importantly, we found a large number of micrometastases with only a few hundred cells (**Figure 4H**) and diameters less than 50-100 µm (**Figure 4I**), which would be very difficult to detect in intact mice by other methods. Comparing the micrometastases in the lungs with the torso, we found that the tumor burden in the lungs was more than a hundred times higher (**Figure 4J**). Also, micrometastases in the lungs were, on average, 30% larger in diameter (**Figure 4K**) containing more than twice as many cells per metastasis as micrometastases in the rest of the torso (**Figure 4L**). In sum, our pipeline is the first to enable quantitative analyses of whole-body scans at cellular resolution, yielding important insights into understanding the metastatic process.

DeepMACT reveals therapeutic antibody targeting at the cellular level

A number of tumor-targeting monoclonal antibodies have become part of the standard treatment for various solid and hematological malignancies and many more are in early or late stages of clinical development[22,23]. However, so far there has been no methodology to determine the distribution of therapeutic antibodies in the entire body at cellular resolution. Here, we used DeepMACT to assess biodistribution of the therapeutic monoclonal antibody 6A10 directed against human carbonic anhydrase XII (CA12)[19,20,24]. CA12 is overexpressed in various types of cancers and blocking its activity with the antibody 6A10 reduces tumor growth[19] and increases the sensitivity of tumor to chemotherapy[20]. We intravenously injected 20 µg of 6A10 conjugated to Alexa-568 (with tumor signal boosted with Atto-647N) nine weeks after transplantation of MDA-MB-231 cells and perfused the mice two days after the antibody injection for whole-body analysis. Because Alexa-568 excitation/emission spectra overlap with the endogenous mCherry signal of the transplanted cancer cells, we confirmed that the vDISCO pipeline eliminates all the signal from endogenously expressed mCherry[8] (**Figure S5**).

We first acquired 2D images with epifluorescence microscopy and observed an accumulation of the 6A10 antibody at the primary tumor (**Figure 5A,E**; tumor shown in magenta, therapeutic antibody in cyan) and the metastases at the axillary lymph node (**Figure 5A,B**). Focusing on the lungs, we detected micrometastases that were targeted by the 6A10 antibody (**Figure 5C**, white arrow) and others that were not (**Figure 5D**, yellow arrow). Acquiring 3D scans with light-sheet microscopy, we assessed the complete biodistribution of the therapeutic antibody and micrometastases in the whole body at cellular resolution (**Figure 5F-H, Movie S3)**. The axillary lymph node metastases and the micrometastases in the lungs are shown in **Figure 5F**. Analyzing the signal of individual micrometastases and the 6A10 antibody by light-sheet microscopy in 3D, we could evaluate the efficiency of antibody drug targeting for even the smallest micrometastases (**Figure 5G**, white arrowhead). We also verified the targeting of micrometastases by the 6A10 antibody in various organs such as lungs and kidney, using confocal microscopy (**Figure S6**).

Next, we used DeepMACT to systematically assess and quantify the effectiveness of antibody drug targeting in whole animals at the cellular level (**Figure 5I**). While overall 77% of all metastases were targeted by the antibody, we found that significantly more micrometastases ($p < 0.001$, two-sided *t*-test) were targeted in the lungs (85%) as compared to the rest of the body (66%) (**Figure 5J, Movies S3 and S4**). To further assess the efficacy of drug targeting for micrometastases in the lung versus the rest of the body, we assessed the antibody concentration by quantifying the antibody signal contrast (relative signal strength versus local surrounding; see methods for details) (**Figure 5K**). Metastases in the lungs generally tend to have a higher antibody signal ratio. This is in line with the higher share of targeted metastases. Also, the antibody signal ratio is much more narrowly distributed compared with micrometastases outside the lungs. The lower average and wider distribution

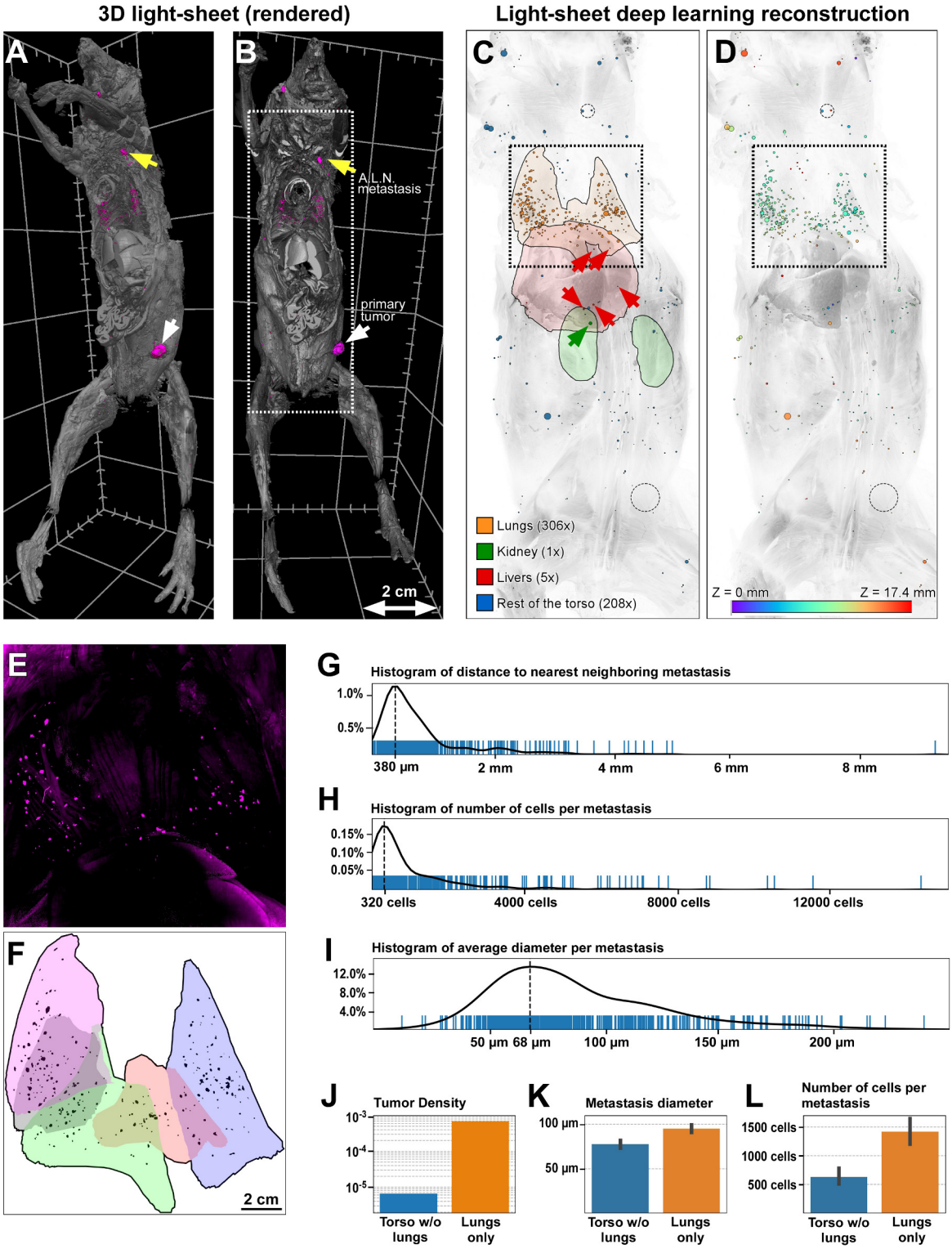

Figure 4

Deep learning-based detection and segmentation enables quantitative analysis at the level of individual metastases

(**A**,**B**) 3D rendering of the entire mouse after light-sheet microscopy imaging in ventral and lateral views, respectively. Metastases in the mouse body are shown in magenta. The white arrow indicates the primary tumor and the yellow arrow indicates metastases in the axillary lymph node (A.L.N.). (**C**,**D**) Deep learning reconstructions of all detected metastases (A.L.N. and primary tumor indicated with dashed circles) color-coded by organ (**C**) and depth along z-axis (**D**), cropped to white box of (A) to show higher level of detail. (**E**,**F**) Detailed view of metastases in the lung region (corresponding to the black box in C) in a maximum intensity projection of a 3D light-sheet scan (**E**) and projection of 3D deep learning-based detection, with metastases registered to individual lung lobes (shown in different colors) (**F**). (**G**-**L**) Deep learning-based distributions; blue bars show individual metastases, the black line shows the Gaussian kernel density estimation. (**G**) 3D distance to nearest neighboring metastasis. (**H**) Cell count estimation per metastasis. (**I**) Metastasis diameter averaged in 3D space. (**J**-**L**) Quantitative comparison between metastases in the lungs and the rest of the torso; bars indicate 95%-confidence intervals. (**J**) Tumor density as share of metastatic tissue of the entire volume. (**K**) Metastasis diameter averaged in 3D space. (**L**) Cell count estimation per metastasis.

of antibody signal ratio in the micrometastases in the rest of the body indicates that there is a substantially higher variance in the antibody targeting to the cells of those micrometastases. While some are very strongly targeted, many others are not targeted at all. Also, the largest quartile of micrometastases was significantly more likely ($p < 0.001$, two-sided *t*-test) targeted (88%) than the smallest quartile (67%) (**Figure 5L**). We also identified various off-target binding sites throughout the body, i.e. binding of the therapeutic antibody to mouse tissues, which is presumably due to unspecific binding since

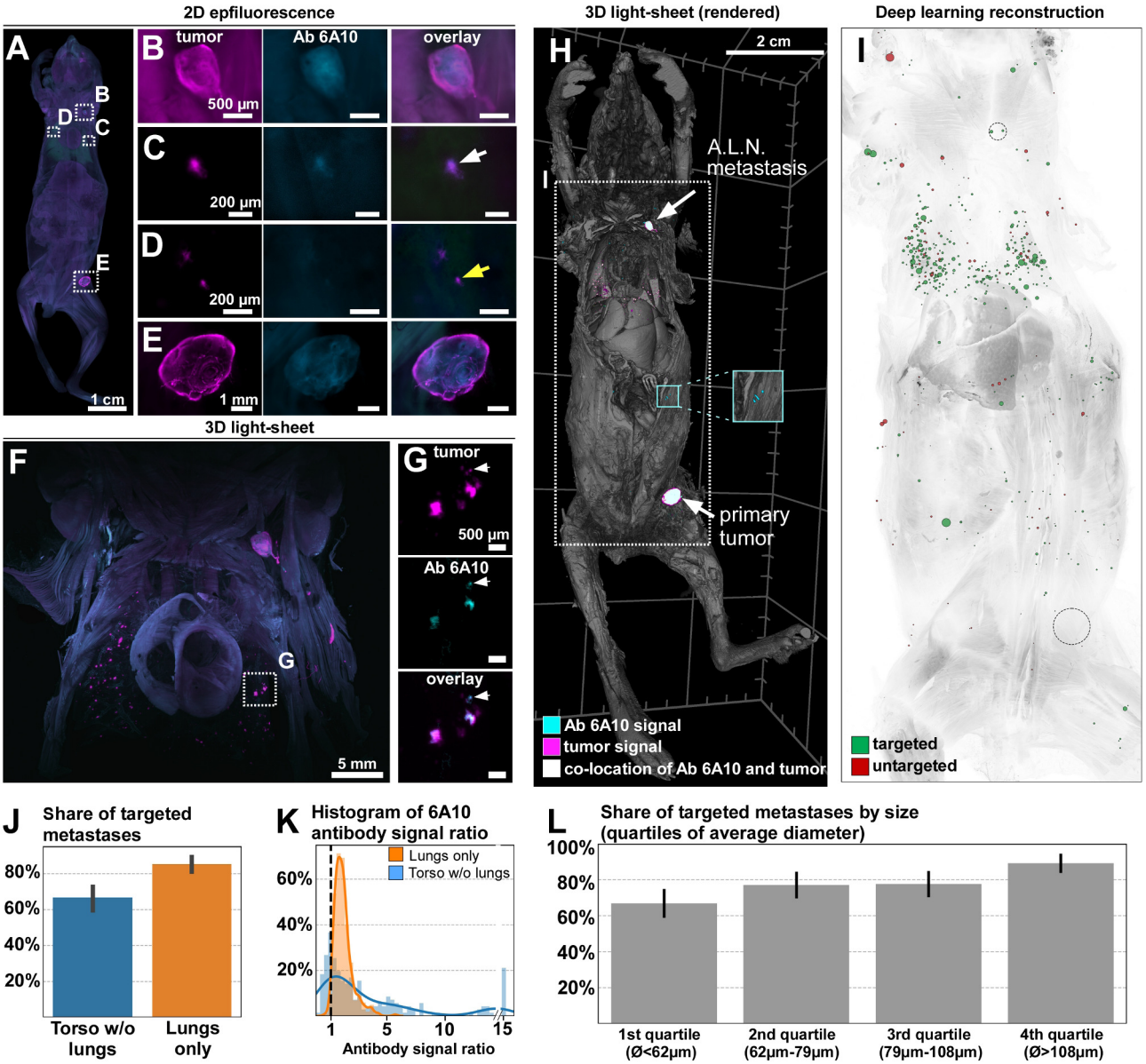

Figure 5

The DeepMACT pipeline enables quantitative analysis of drug delivery effectiveness at the level of single metastases

(**A**) Epifluorescence images of a processed mouse show details (**B**-**E**) of both tumor metastases (boosted with Alexa647 nanobody, shown in magenta) and 6A10 antibody (conjugated with Alexa568, shown in cyan) distributions and their overlay. While most of the micrometastases are targeted by the antibody (**C**, white arrow), there are some that are not (**D**, yellow arrow). (**F**) Full body 3D light-sheet scan, cropped to the chest region, shows the distributions of metastases (magenta) and antibody (cyan). (**G**) Detailed view of the boxed region in (F) showing very small micrometastases targeted by the therapeutic antibody (white arrows). (**H**) 3D rendering of a whole mouse body light-sheet scan showing the tumor signal in magenta, the 6A10 antibody signal in cyan (co-localization of the signals is shown in white). The cyan inlet shows an example of off-target accumulation of the 6A10 antibody. (**I**) Deep learning-based reconstruction of the animal in (H) showing targeted metastases in green and untargeted metasases in red; the dashed circles represent the primary tumor A.L.N metastases. (**J**) Comparison of the share of targeted metastases in the lungs versus the rest of torso. (**K**) Comparison of the distributions of 6A10 antibody signal ratio (signal strength in metastasis versus local surrounding; see the methods for further details) per metastasis in the lungs versus the rest of torso. (**L**) Share of targeted metastases as a function of their size (split into quartiles of average metastasis diameter).

6A10 does not bind to murine CA12 (cyan inlet in **Figure 5H**). Overall, these data demonstrate that DeepMACT provides a powerful platform to track the biodistribution of therapeutic antibodies along with micrometastases in intact mouse bodies. Thus, it represents the first methodology that allows quantitative analysis of the efficacy of antibody-based drug targeting in the whole body at cellular resolution.

Exploring potential mechanisms of antibody drug targeting

The above results demonstrated that antibody-based drugs, which are the basis of many targeted/personalized treatments, may miss as many as 23% of the micrometastases. Next, we aimed to explore potential mechanisms that might explain this failure. We first hypothesized that the efficacy of targeting of micrometastases might depend on the presence of nearby blood supply transporting the therapeutic antibody. To explore if the vascularization of defined tissue regions can have an effect on antibody drug targeting, we performed lectin labeling of vessels in the lungs, where most of the micrometastases are located. Analyzing diverse micrometastases of different sizes, we found that each of them had blood vessels as close as 1-6 µm (**Figure 6A,B**). This distance is smaller than even a single cell diameter (˜10 µm) suggesting that the proximity of blood vessels could not be the major reason for the lack of antibody drug targeting[25].

Next, we hypothesized that the tumor micro-environment at the sites of metastases could be related to the efficiency of targeting. If so, we would expect a non-random spatial distribution of targeted and untargeted metastasis on a local scale. To address this, we turned to DeepMACT and assessed

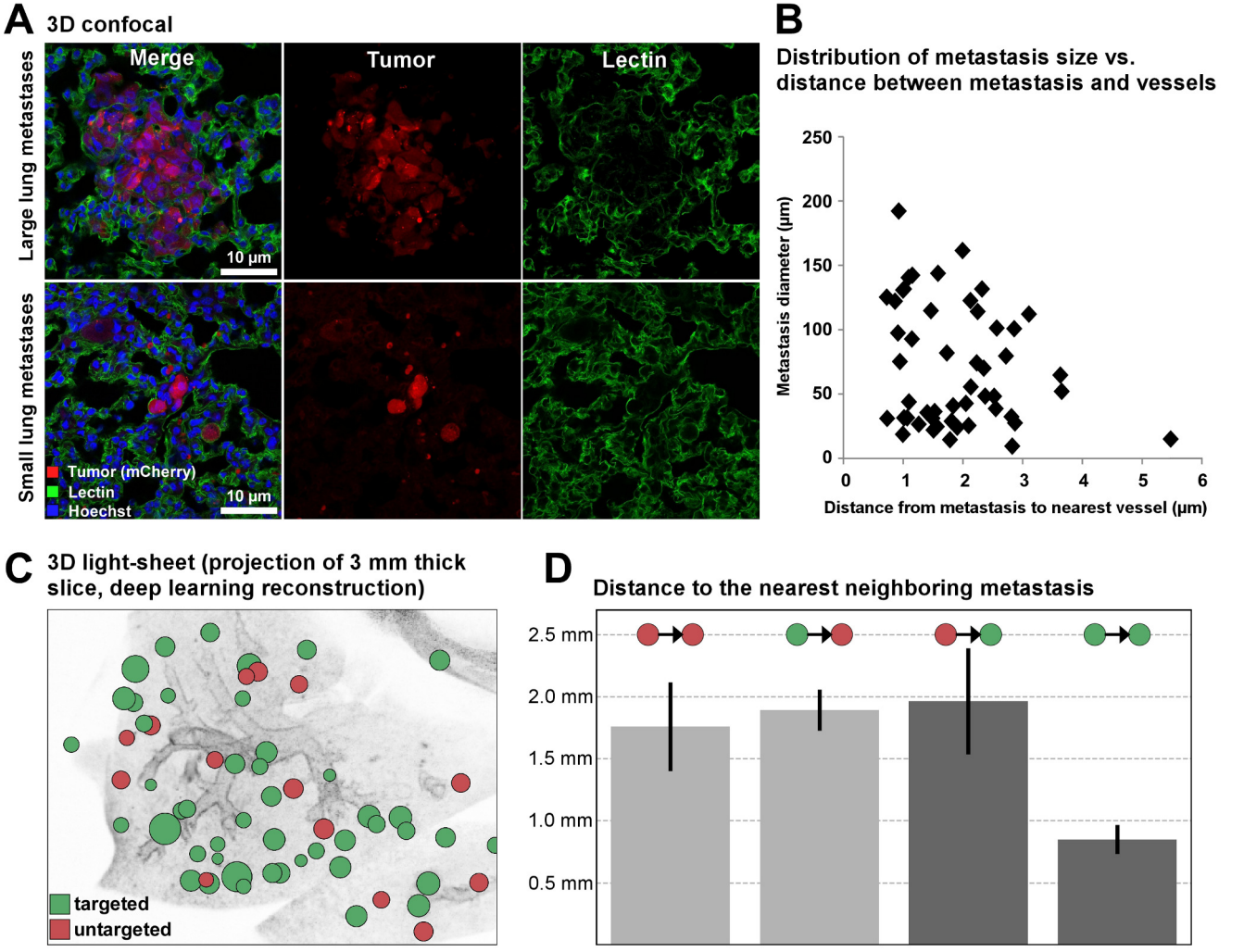

Figure 6

Potential mechanisms of tumor targeting by therapeutic antibody

(**A**) Confocal images of a large and a small metastasis (less than 5 cancer cells) in lungs labeled with Lectin (green) and Hoechst (blue). (**B**) Distribution of metastasis size and distance to the nearest vessel, showing that most of the metastases are close to vessels (distance less than 6 µm) (n=50). (**C**) Deep learning-based reconstruction of lung metastases with and without 6A10 antibody targeting. (**D**) Deep learning-based quantification of distance between metastases and their nearest neighbor, showing local clustering of targeted and untargeted metastases (see the Methods for further details)

local clustering of micrometastases targeted by the antibody. We quantified the distances between micrometastases and their nearest neighbor for all micrometastases in the entire body, differentiating between targeted and untargeted nearest neighbors. The distance between two neighboring metastases is significantly smaller for two targeted metastases (about 0.8 mm) than for two untargeted or a mixed pair of an untargeted and a targeted metastasis (consistently at about 1.7-2.0 mm) (**Figure 6C,D**). Importantly, the average distance from an untargeted to the nearest targeted metastasis is significantly larger than from a targeted one. This would not be expected in a random distribution and indicates a clustering on a local scale. Thus, these analyses suggest the existence of factors in tumor microenvironments on a millimeter scale influencing the efficacy of antibody drug targeting.

DISCUSSION

Unbiased detection of cancer metastasis and the biodistribution of tumor-targeting therapeutics at the single cell level would substantially accelerate pre-clinical cancer research. Towards this goal, we capitalized on a powerful whole-body clearing and imaging method combined with deep learning-based analysis, enabling us to visualize and analyze cancer metastasis in intact transparent mouse bodies. The resulting DeepMACT workflow is a straightforward methodology for systemic analysis of micrometastases and therapeutic antibody drug distribution in whole mouse bodies at cellular resolution within days, a task that would otherwise take several months to years of human labor. Notably, DeepMACT can readily be applied in diverse labs without the need for highly specialized equipment as we provide detailed instructions on VDISCO whole body clearing and imaging, and make the algorithms, the training data, and the trained model publicly available (see methods). Thus, DeepMACT-based evaluation of whole mouse bodies instead of selected tissues/organs at the single cell level can foster the translation of new therapies into the clinic much more efficiently than traditional methods.

DeepMACT technology

Here we set out make use of recent technologies that are providing scalable and unbiased histological assessment of entire biological specimens. Most whole-body clearing and imaging studies have so far relied on visualization of endogenous fluorescent signal, which did not allow imaging and quantification in intact transparent mice[5,26]. To overcome this, here we adopted the vDISCO whole mouse transparency technology, as it amplifies the signal of cancer cells more than 100 times, ensuring reliable detection of single cells through intact bones and skin[8]. Because vDISCO employs nanobody enhancement of the endogenous fluorescent signal, currently up to 21 types of fluorescent proteins can be boosted with available nanobodies. In addition, conjugation of existing nanobodies with fluorescent dyes at diverse spectra, including those in the near infrared range would help to generate more options for multiplex experiments including imaging of more than one type of fluorescently labeled cell along with conjugated therapeutic antibodies.

Secondly, we developed a highly efficient deep learning architecture based on U-net like CNNs exploiting 2D maximum-intensity projections with high SNR to reliably detect metastases in 3D. Deep learning-based detection not only serves the purpose of automation, but is also provides a very effective tool in finding metastases that would be easily overlooked by humans. In our data, a single human annotator missed around 29% of all metastases. This is in line with previous studies where human experts missed 1 in 4 breast cancer metastases in histopathology[27], an issue that even increases substantially if humans work under time pressure[28]. Motivated by this, deep learning based approaches for cancer and metastasis detection recently gained substantial momentum for various imaging modalities, also beyond microscopy[29-32].

Here we used an MDA-MB-231 cancer cell-based tumor model to train the algorithms. While training deep networks in general may require large training datasets to diversify their applications, the Unet-like architecture in the core of DeepMACT can be easily adopted to other cancer models[33-36]. In other words, DeepMACT learned to detect the characteristic shape and appearance of micrometastases against the background signal, and thus, is independent of the cancer cell model used. Therefore, it would require little effort to apply our algorithms to different types of tumor models. Also, adapting the algorithm to applications in which, for instance, shape and size differ substantially from MDA-MB-231 metastases, would not require training from scratch. Adjusting design parameters such as the size of subvolumes (see methods for details) allows the straightforward adaptation of the algorithm to new data with different SNR, metastasis sizes, or spatial resolution of the scan. Furthermore, building upon our pre-trained algorithms, which are freely available online, allows retraining the algorithm with substantially less training data.

To ensure high computational efficiency, our approach solves the three-dimensional task of detecting and segmenting the metastases by

exploiting two-dimensional representations of the data. This is important because 2D max-intensity-projections increase SNR when there is little background noise owing to the high specificity of the labels in vDISCO clearing. 3D convolutions are exponentially more expensive in computing time than 2D convolutions, thus requiring more powerful computing resources and more data annotated in 3D to train the algorithm. Importantly, annotating projections in 2D is substantially easier and faster than slice-by-slice 3D annotations. In addition, the exponentially more efficient nature of our approach allows training the entire algorithm on a standard workstation with an ordinary GPU within a few hours; applying the trained algorithm to a new dataset takes in the order of 15 minutes, highlighting the scalability and cost-efficiency of our pipeline. Thus, this architecture is designed to enable widespread adaptation of our approach by minimizing data annotation and computing requirements while allowing for easy adaptation for other experimental setups (such as different imaging modalities or tumor models).

DeepMACT detection of micrometastases and tumor-targeting drugs

Methods such as magnetic resonance imaging (MRI), computed tomography (CT), and bioluminescence imaging have been widely used to visualize cancer growth at the primary site and distal body regions[37-42]. While these methods provide crucial longitudinal information on the size of the primary tumor and large metastases, they typically can only resolve structures larger than 75 µm, hence they do not have the resolution to detect smaller micrometastases consisting of fewer cells.

Unbiased high-throughput mapping of tumor micrometastases at cellular resolution in entire rodent bodies can be a valuable tool to uncover the biology behind the dissemination of tumor cells. We show here that DeepMACT is an ideal tool for detecting and mapping cancer metastases in whole mouse bodies at the cellular level, allowing identification of the precise locations of single disseminated cancer cells. Complex analysis, e.g., of the size, location and density of micrometastases could be performed in a short time throughout the body, without dissecting any pre-defined region. In addition to detecting the micrometastases in the predicted organs such as the lungs and liver, we also identified numerous micrometastases throughout the torso. These may include cells that have metastasized to other organs, e.g. bones, peritoneum, bladder, intestines, as well as circulating tumor cells (or cells clusters) in the vasculature.

While precise assessment of antibody drug biodistribution is critical for evaluating its specificity and utility for tumor treatment, there have been no methods so far that can provide such information at the cellular level in the whole organism. Here, we applied DeepMACT to study not only the distribution of single tumor cells, but also of a therapeutic monoclonal antibody. We demonstrated that the “on” and “off” targeting of antibody drugs throughout the body can readily be assessed by DeepMACT. For example, we observed that not all micrometastases in the lungs were targeted by the anti-CA12 therapeutic antibody 6A10. Understanding why antibody-based therapeutics do not target all tumor cells would be important for developing more effective treatments. Towards this goal, we studied the potential mechanisms that could contribute to the lack of targeting. Vascular staining demonstrated that blood vessels were present in the immediate vicinity of all examined metastases in the lung, suggesting that insufficient vascularization is unlikely to be a common cause for the failure of antibody drug targeting. Interestingly, DeepMACT analysis found that micrometastases located in close proximity are more likely to be targeted. This suggests that the local microenvironment within metastatic niches plays an important role in determining the efficiency of antibody targeting, e.g. by altering antibody penetration, binding affinity and clearance. Furthermore, heterogeneity of antigen expression on the surface of tumor cells and internalization and degradation of antigen/antibody complexes might also affect therapeutic antibody targeting efficacy.

In conclusion, DeepMACT is a powerful technology combining unbiased whole mouse body imaging with automated analysis. It enables visualization, quantification, and analysis of tumor micrometastases and antibody-based therapies at single cell resolution in intact mice, with an accuracy equivalent to that of human experts, but speeding up the workflow by orders of magnitude compared to traditional methods. Because this technology is time- and cost-efficient, scalable, and easily adoptable, it can be used to study metastasis and optimize antibody-based drug targeting in diverse tumor models.

ACKNOWLEDGMENTS:

This work was supported by the Vascular Dementia Research Foundation, Synergy Excellence Cluster Munich (SyNergy), ERA-Net Neuron (01EW1501A to A.E.), the Helmholtz-Center for Environment Health (grants to R.Z.), and the German Federal Ministry of Education and Research via the Software Campus initiative (O.S.). Furthermore, NVIDIA supported this work with a Titan XP via the

GPU Grant Program. We thank I. Jeremia for the luciferase/mCherry construct and the Monoclonal Antibody Core Facility at the Helmholtz Center Munich for providing the 6A10 antibody. We thank Dr. W. Ouyang for constructive comments on the manuscript. C.P. and R.C. are members of Graduate School of Systemic Neurosciences (GSN), Ludwig Maximilian University of Munich.

AUTHOR CONTRIBUTIONS:
C.P., A.P.D. and R.C. performed the tissue processing, clearing and imaging experiments. R.C. and C.P. developed the whole-body nanobody labeling protocol. M.T. stitched and assembled the whole mouse body scans. O.S. and J.D.B developed the deep learning architecture and performed the quantitative analyses. A.G. performed the image rendering and parts of the data analysis. O.S. developed annotation tools and the custom-made object detector, M.A.R. annotated the data. G.G.,B.N. and R.Z., performed tumor transplantation experiments and bioluminescence imaging. B.K.G. helped with data interpretation. B.M. provided guidance in developing the deep learning architecture and helped with data interpretation. A.E., C.P. and O.S. wrote the manuscript. All the authors edited the manuscript. A.E. initiated and led all aspects of the project.

COMPETING FINANCIAL INTERESTS
A.E. has filed a patent related to some the technologies presented in this work.

METHODS

Spontaneous metastasis model and injection of therapeutic antibody

Female NSG (NOD/SCID/IL2 receptor *gamma* chain knockout) mice were obtained from Jackson Laboratory and housed at the animal facility of the Helmholtz Center Munich. All animal experiments were conducted according to institutional guidelines of the Ludwig Maximilian University of Munich and Helmholtz Center Munich after approval of the Ethical Review Board of the Government of Upper Bavaria (Regierung von Oberbayern, Munich, Germany). MDA-MB-231 breast cancer cells transduced with a lentivirus expressing mCherry and enhanced Firefly luciferase[43] were counted, filtered through a 100 µm filter and resuspended in RPMI 1640 medium. $2x10^6$ cells per mouse were injected transdermally in a volume of 50 µl into the 4th left mammary fat pad. Tumor growth was monitored by bioluminescence measurement (photons/second) of the whole body using an IVIS Lumina II Imaging System (Caliper Life Sciences) as described[19]. Briefly, mice were anesthetized with isoflurane, fixed in the imaging chamber and imaged 15 minutes after Luciferin injection (150 mg/kg; i.p.). Bioluminescence signal was quantified using the Living Image software 4.2 (Caliper). 9 weeks after tumor cell injections, mice were randomly assigned to different experimental procedures including injection of a human carbonic anhydrase (CA) XII-specific antibody (6A10)[24], boosting of endogenous mCherry fluorescence, immunolabeling and clearing, as described below. 48 hours before perfusion mice were injected into the tail vein with 20 µg of 6A10 antibody conjugated with Alexa-568.

Perfusion and tissue processing

Mice were deeply anesthetized using a combination of midazolam, medetomidine and fentanyl (MMF) (1ml/100g of body mass for mice; i.p.) before intracardial perfusion with heparinized 0.01 M PBS (10 U/ml of Heparin, Ratiopharm; 100-125 mmHg pressure using a Leica Perfusion One system) for 5-10 minutes at room temperature until the blood was washed out, followed by 4% paraformaldehyde (PFA) in 0.01 M PBS (pH 7.4) (Morphisto, 11762.01000) for 10-20 minutes. The skin was carefully removed and the bodies were postfixed in 4% PFA for 1 day at 4 °C and transferred to 0.01 M PBS. The vDISCO pipeline was started immediately or whole mouse bodies were stored in PBS at 4 °C for up to 4 weeks or in PBS containing 0.05% sodium azide (Sigma, 71290) for up to 6 months.

uDISCO whole-body clearing

The uDISCO protocol to clear whole body of mice was already described in details in ref (Pan et al., 2016). In brief, a transcardial-circulatory system was established involving a peristaltic pump (ISMATEC, REGLO Digital MS-4/8 ISM 834; reference tubing, SC0266). Two channels from the pump were set for the circulation through the heart into the vasculature: the first channel pumped the clearing solution into the mouse body and the second channel collected the solution exiting the mouse body and recirculated the solution back to the original bottle. For the outflow tubing of the first channel, which injected the solution into the heart, the tip of a syringe (cut from a 1 ml syringe-Braun, 9166017V) was used to connect the perfusion needle (Leica, 39471024) to the tubing. Meanwhile, the inflow tubing of the second channel, which recirculated the clearing solutions, was fixed to the glass chamber containing the mouse body. The amount of solutions for circulation depended on the capacity of the clearing glass chamber. For example, if the maximum volume of glass chamber is 400 ml, 300 ml of volume of solution was used for circulation.

All clearing steps were performed in a fume hood. Firstly, the mouse body was put in a glass chamber and the perfusion needle was inserted into the heart through the same hole that was used for

PFA perfusion. Then, after covering the chamber with aluminum foil the transcardial circulation was started with a pressure of 230 mmHg (60 rpm on the ISMATEC pump). The mouse bodies were perfused for 6 hours with the following gradient of *tert*-butanol: 30 Vol%, 50 Vol%, 70 Vol%, 90 Vol% (in distilled water),100 Vol% twice, and finally with the refractive index matching solution BABB-D4 containing 4 parts BABB (benzyl alcohol + benzyl benzoate 1:2, Sigma, 24122 and W213802), 1 part diphenyl ether (DPE) (Alfa Aesar, A15791) and 0.4% Vol vitamin E (DL-alpha-tocopherol, Alfa Aesar, A17039), for at least 6 hours until achieving transparency of the bodies. As the melting point of *tert*-butanol is between 23 to 26 °C, a heating mat set at 35-40 °C was used for the two rounds of 100% *tert*-butanol circulation to prevent the solution from solidifying.

vDISCO whole-body immunostaining and clearing

The detailed protocol of vDISCO is described in ref (Cai et al, 2018). The following nanobodies and dyes were used for whole body immunostaining: Atto647N conjugated anti-RFP/mCherry nanobooster (Chromotek, rba647n-100), Atto594 conjugated anti-RFP/mCherry nanobooster (Chromotek, rba594-100), Hoechst 33342 (Thermo Fisher Scientific, 21492H), Propidium iodide (PI, Sigma, P4864).

After PBS perfusion and PFA fixation, the animals were placed into a 300-ml glass chamber and the same transcardial-circulatory system with a peristaltic pump was established to perfuse the mice during decolorization and immunostaining steps. The animals were firstly perfused with decolorization solution for 2 days at room temperature to remove remaining heme and blood before immunostaining. The decolorization solution which is a 1:3 dilution of CUBIC reagent 1 (Susaki et al., 2014) in 0.01 M PBS was refreshed every 12 hours. CUBIC reagent 1 was prepared as a mixture of 25 wt% N,N,N,N'-tetrakis (2-hydroxypropyl) ethylenediamine (Sigma-Aldrich, 122262), 25 wt% urea (Carl Roth, 3941.3) and15 wt% Triton X-100 in 0.1 M PBS, as described in the original publication. Before the immunostaining step, additional 0,22 µm syringe filters (Sartorius 16532) were attached to the tubing to prevent the potential accumulation of nanobody aggregates and ~230 mmHg high pressure pumping was maintained through the entire labeling process. Subsequently the animals were perfused for 5-6 days at room temperature with 300 ml of immunostaining solution containing 0.5% Triton X-100, 1.5% goat serum (Gibco, 16210072), 0.5 mM of Methyl-beta-cyclodextrin (Sigma, 332615), 0.2% trans-1-Acetyl-4-hydroxy-L-proline (Sigma, 441562), 0.05% sodium azide (Sigma, 71290), 25 µL of nano-booster (stock concentration 0.5 – 1 mg/ml), 10 µg/ml Hoechst and/or 350 µL of propidium iodide (stock concentration 1mg/ml) in 0.01 M PBS. Then the mice were perfused with washing solution (1.5% goat serum, 0.5% Triton X-100, 0.05% of sodium azide in 0.01 M PBS) for 12 hours twice at room temperature and at the end with 0.01 M PBS for 12 hours twice at room temperature.

After the whole body immunolabeling, the whole mouse bodies were passively cleared using 3DISCO. In short, mice were cleared at room temperature inside a glass chamber with gentle shaking under a fume hood. For dehydration, mice bodies were incubated in 250 ml of the gradient tetrahydrofuran THF (Sigma, 186562) in distilled water (6-12 hours for each step): 50 Vol% THF, 70 Vol% THF, 80 Vol% THF, 100 Vol% THF and again 100 Vol% THF; then mice were incubated for 1 hour in dichloromethane (Sigma, 270997), and finally in BABB. During all clearing steps, the glass chamber was sealed with parafilm and covered by aluminum foil. Further details on the vDISCO protocols are available at http://discotechnologies.org/vDISCO/.

Lectin vasculature labeling in lungs tissue sections

The whole bodies of mice were perfused and collected as described above. After checking with epifluorescence stereomicroscopy (Zeiss AxioZoom EMS3/SyCoP3), the lung lobes with multiple metastases were dissected and sliced into 20 µm thick tissue sections by using a cryostat (Leica, CM3050S). The lung sections were washes 2 times with 0.01 M PBS and then incubated in Alexa 488 conjugated Lectin (4 µg/ml, invitrogen, W11261) at 4 °C overnight. The sections were then stained with Hoechst 33342 (10 µg/ml, Thermo Fisher Scientific, 21492H) for 5 minutes at room temperature to visualize the nucleus. After washing 2 times with PBS, the slides were mounted with fluorescent mounting medium (Dako, 10097416) and were ready for confocal microscopy.

mCherry nanoboosting in lung tissue sections

20 µm thick lung tissue sections were washed with 0.01 M PBS 2 times before starting the boosting process. One hour incubation in blocking solution containing 1% Bovine Serum Albumin (Sigma, A7906), 2% goat serum (Gibco, 16210-072), 0.1% Triton X-100 and 0.05% Tween 20 (Bio-Rad, 161-0781) in PBS, was performed at room temperature. Then the staining solution was prepared in 1% Bovine Serum Albumin and 0.5% Triton X-100 in PBS. Atto647N conjugated anti-RFP/mCherry nanobooster was diluted 1:500 in the staining solution and the lungs sections were incubated overnight at 4°C. After the nanoboosting, the lungs

sections were washed 3 times with PBS for 5 minutes with gentle shaking. After nuclear staining by Hoechst 33342 (10 µg/ml) and post wash with PBS as described before, the slides were mounted with fluorescence mounting medium and were ready for confocal microscopy.

Epifluorescence stereomicroscopy imaging
Cleared whole mouse bodies were fixed in the original clearing chamber and were imaged with Zeiss AxioZoom EMS3/SyCoP3 fluorescence stereomicroscope using a 1x long working distance air objective lens (Plan Z 1x, 0.25 NA, Working distance (WD) = 56 mm). The magnification was set as 7x and imaging areas were selected manually to cover the entire mouse bodies. The images were taken with GFP, RFP and Cy5 filters and files were exported as RGB images.

Light-sheet microscopy imaging
Single plane illumination (light-sheet) image stacks were acquired using an Ultramicroscope II (LaVision BioTec), allowing an axial resolution of 4 µm. For low magnification whole-body screening of tumor and antibody signals we used a 1x Olympus air objective (Olympus MV PLAPO 1x/0.25 NA [WD = 65mm]) coupled to an Olympus MVX10 zoom body, which provides zoom-out and -in ranging from 0.63x up to 6.3x. Using 1x objective, we imaged a field of view of 2 x 2.5 cm, covering the entire width of the mouse body. Tile scans with 60% overlap along the longitudinal y-axis of the mouse body were obtained from ventral and dorsal surfaces up to 13 mm in depth, covering the entire volume of the body using a z-step of 10 µm. Exposure time was 150 ms, laser power was 3 to 4 mW (70% to 95% of the power level) and the light-sheet width was kept at maximum. After low magnification imaging of the whole body, individual organs (including lungs, liver, kidneys, brain, spleen, intestines and bones) were dissected and imaged individually using high magnification objectives (Olympus XLFLUOR 4x corrected/0.28 NA [WD = 10 mm] and Zeiss 20x Clr Plan-Neofluar/0.1 NA [WD 4 = mm]) coupled to an Olympus revolving zoom body unit (U-TVCAC) kept at 1x. High magnification tile scans were acquired using 20% overlap and the light-sheet width was reduced to obtain maximum illumination in the field of view keeping the same NA. For the data used for the comparison of signal profile plots of lung metastases taken in red and far-red channels and for the analysis of endogenous fluorescence signal depletion after the uDISCO protocol, we used the same MVX10 zoom body, coupled this time with a 2x objective (Olympus MVPLAPO2XC/0.5 NA [WD = 6mm]) at zoom body magnification 6.3x and 2.5x respectively.

Confocal microscopy imaging
For imaging the thick cleared specimens such as dissected tissues, pieces of organs or whole organs were placed on 35 mm glass bottom petri dishes (MatTek, P35G-0-14-C), then the samples were covered with one or two drops of the refractive index matching solution such as BABB or BABB-D4. Sealing of this mounting chamber was not necessary. The samples were imaged with an inverted laser-scanning confocal microscopy system (Zeiss, LSM 880) using a 40x oil immersion lens (Zeiss, EC Plan-Neofluar 40x/1.30 Oil DIC M27) and a 25x water immersion long-working distance objective lens (Leica, NA 0.95, WD = 2.5mm), the latter one was mounted on a custom mounting thread. The z-step size was 1-2.50 µm. For imaging the lung tissue sections with lectin staining and with nanoboosters, the slides were imaged with the same inverted laser-scanning confocal microscopy system (Zeiss, LSM 880) using a 40x oil immersion lens (Zeiss, EC Plan-Neofluar 40x/1.30 Oil DIC M27). The z-step size was 2 µm.

Reconstructions of whole-mouse body scans
Epifluorescence (2D montage of whole mouse):
The collected epifluorescence images were stitched semi-automatically using Adobe Photoshop photomerge function (File\automate\photomerge). The different channels were stitched separately and merged in Adobe Photoshop to generate the composite images.

Light-sheet microscopy (3D montage of whole mouse):
We acquired light-sheet microscope stacks using ImSpector (LaVision BioTec GmbH) as 16-bit grayscale TIFF images for each channel separately. The stacks were first aligned and fused together with Vision4D (Arivis AG). Further image processing was done mostly in Fiji (ImageJ2): first, the autofluorescence channel (imaged in 488 excitation) was equalized for a general outline of the mouse body. The organs were segmented manually by defining the regions of interests (ROIs). Data visualization was done with Amira (FEI Visualization Sciences Group), Imaris (Bitplane AG), Vision4D in both volumetric and maximum intensity projection color mapping.

General data processing
All data processing after image volume reconstruction was performed in Python using custom scripts based on publicly available standard packages comprising SciPy[44], Seaborn[45], and Pandas[46]. Deep Learning models were build using the PyTorch framework[47]. Since a single whole body scan is in the order of several terabytes due to its high resolution (the data used for training had a voxel size of $(10\mu m)^3$), the volume was divided into 1176 subvolumes of $(350px)^3$ (or $(3.5mm)^3$) to enable efficient processing. Subvolumes were overlapping by 50px to ensure any given metastasis is fully captured by at least one subvolume to avoid artefacts of divided metastases at subvolume interfaces. Please note

that the size and overlap of subvolumes are design choices that allow easy adaptation to different data sets, e.g. with different SNR, metastasis sizes, or spatial resolution of the scan. Final analyses were conducted on the re-assembled full volume whereby reconcatenation ruled out any double-counting at previously overlapping subvolumes.

Data annotation by human experts

To provide ground truth in the form of a commonly agreed upon reference annotation for training, as well as for evaluation of the algorithms developed, full body scans of two mice were manually annotated by a group of human experts. This manual process was augmented with a set of tools to reduce the total workload from an estimated total duration of several months down to 150 person-hours net annotation time.

Automatic pre-annotation with custom-made filter-based detector

To avoid starting from scratch to annotate two volumes of several thousand z-slices, an automatic detection and segmentation method was applied to provide a basis for manual correction. Due to the insufficient performance of established methods (in this case: the 3D Object Detector for ImageJ[48], we developed a custom-made filter based detector tailored to the specifics of this dataset. In brief, we handcrafted a spatial filter kernel optimized to detect the most common metastases and applied it with 3D convolutions to the dataset; subsequent binarization and connected-component analysis yielded *seed points* collocated with metastases. This allowed for further analyses of the immediate local neighborhood of these candidate regions; a local 3D segmentation was derived by selective region growing around these seed points based on the local signal intensity distribution up to a mean *foreground signal* limited to 4 standard deviations above the mean signal in the local surrounding. Finally, obvious false positives were filtered out. Together, this approach generated a first proposal for the data annotation that at least captured the most obvious metastases while producing an acceptable rate of false positives. As shown in the results section, the quality of this proposal was about twice as good as compared to the 3D Object Detector in ImageJ (35% instead of 18% in F1-score). Importantly, further fine-tuning of filters and parameters and any additional automated pre- or post-processing did not improve the results, indicating that a F1-score of 35% may be close to the performance limit of such approaches with fixed filter kernels and fixed decision rules for such kind of data.

Manual annotation correction by human experts

This first proposal served as a basis for human annotation. In general, three kinds of manual correction were needed to derive a good annotation: removal of false positives, addition of false negatives (previously missed metastases) and adjustment of the 3D segmentation of each metastasis. To avoid the need to perform this task individually for each of the 350 layers of a $(350px)^3$ data subvolume, a custom tool with an interactive graphical user interface was developed. Based on maximum intensity projections along each dimension, the tool allowed to review, adjust, add, and remove each potential metastasis in the subvolume with a few mouse clicks, drastically speeding up the annotation process from hours to minutes per subvolume. Different perspectives (X, Y, Z) and viewing modes (e.g., projections, orthogonal slices, adjusted contrasts, 3D renderings) for each individual metastasis allowed the annotator to take maximally informed decisions even in less obvious cases.

Refinement of annotation to commonly agreed upon ground truth

A small fraction (3%) of the entire data set was labeled several times by the annotators without their awareness to assess human labeling consistency. Since the difference in annotation for a given subvolume between two trials of a single annotator was about as big as between two independent annotators and quite substantial (the agreement between two trials of the same annotator or between annotators only reached an F1-score of 80-85%) we decided to invest additional time to refine the entire data set. First, all experts (3 graduate students with extensive experience in the field of imaging and tumor biology) jointly discussed examples of annotation differences to build a common understanding. Annotations of subvolumes with the biggest discrepancies were again reviewed and refined. Furthermore, this analysis revealed that the most prevalent source of annotation error was overlooked metastases (false negatives). Here, around 29% of metastases were missed in the human annotation, in line with previous studies[27,28]. To effectively identify all missed metastases in the entire data set, our deep learning algorithm (see next section) was trained on the status quo of the annotations and applied to the data set with high sensitivity. This yielded a long list of potential candidates. With the help of another custom-built, interactive graphical user interface, all potential candidates were manually reviewed by the annotators and either discarded or manually adjusted and added to the segmentation. A small set of potential metastases, for which human annotators could not take a conclusive decision even after

joint discussion, was recorded separately, but not added to the segmentation. These laborious steps ensured the generation of a high-quality *ground truth* for training the algorithm and, importantly, for evaluating its performance in comparison to a single human annotator. Here, this selectively iterative approach of refining annotations based on the input of several human experts was chosen due to the substantial amount of manual work involved with reviewing our high-resolution scans. Since a full review of one person takes about a month of full-time work, repeating this process several times would be desirable but too costly. In applications where several, independent full annotations are available, advanced mathematical frameworks for refining decisions from different experts to a single decision can be applied in order to avoid a bias towards individual decisions[49,50].

Deep learning algorithm for metastasis detection and segmentation

Implementation details of the model architecture

Inspired by the established U-net architecture[21], we designed a deep learning approach that is depicted in **Figures 3A** and briefly described in the results section. The architecture of the CNN at its core (**Figure 3C**) is characterized by an encoding downward path and a decoding upward path comprising a total of 7 levels, in which each level also has a lateral skip-connection that bypasses the deeper levels and feeds the output of the encoding unit directly to the corresponding decoding unit. Each encoding unit increases the number of feature channels per pixel with the help of two kernel-based convolutions (kernel size: 3; padding: 1; dilation: 1; stride: 1) followed by batch normalization and a rectifying linear unit (ReLU). While the first convolutional step increases the number of feature channels, this number stays constant for the second convolutional step. Before being passed on to the next encoding stage, the spatial resolution is halved using max-pooling (kernel size: 2, stride: 2). Decoding units take two inputs: the output from the previous layer is spatially upsampled by a factor of two (bilinearly) and concatenated along the feature dimension with the output of the corresponding encoding unit, bypassing the deeper levels. A first convolutional step (same parameters as before) decreases the number of feature channels, which is again kept constant in the two subsequent convolutions. The 24-feature channel output of the last decoder is mapped to logits in the 2D space with a convolutional step without padding, batch normalization, or a rectifying linear unit.

Training, validation and test sets

Following established standards, model training and evaluation was based on k-fold cross-validation (k=5). Thus, the data set was split into mutually exclusive sets for training and validation (80%) and for testing (20%). This process was repeated k times, yielding a total of 5 mutually exclusive test sets that are collectively exhaustive. The network weights and all design choices and hyperparameters (such as batch size, learning rate, etc) were optimized solely with the training and validation set to avoid overfitting on the specifics of the test set. The data set was confined to subvolumes within the torso of the mouse body as subvolumes containing near-zero values outside the body contain no useful information to train or test on. In contrast to all metastases in the entire body, the tumor tissues of the primary tumor and the auxiliary lymph node are several orders of magnitude larger (i.e., they follow very different statistics than all micrometastases) and were thus excluded. The signal from one subvolume was corrupted by a dirt particle and thus also excluded. In total, these exclusions made up less than 1% of the total scan volume. The split between the three subsets (training, validation, testing) of the data was done on a subvolume level (from which the three projections are created afterwards) to avoid information leak between different projections from the same subvolume.

Training and validation procedure

The model training was conducted in two steps. First, a large number of models spanning a broad set of different hyperparameters were trained for 10 epochs using another (nested) k-fold cross-validation (k=5) within the training and validation set. Second, the model with the best-performing set of hyperparameters (presented here) was trained for the remaining epochs. Thus, any hyperparameter choice was made without looking at the performance on the test set. The model was trained for 40 epochs of the entire training data set, using random vertical and horizontal flips of the data to augment its variance (further training epochs did not improve the predictive power). We used a batch size B of 4 but found that other batch sizes work similarly well. Each input was normalized by its local subvolume peak value, which was found to work better than normalization to the global volume peak value or non-linear normalizations. To calculate the gradients for network weight optimization (i.e., to train the model), we used weighted binary cross entropy as a loss function for a given prediction $\hat{Y}$ compared to the ground truth Y, giving more weight w for foreground (FG) pixels p versus background pixels (BG) to account for the *class imbalance* (i.e.,

that metastases are very sparsely distributed in space):

$$wBCE_{\hat{Y},Y} = (-1)\sum_{b}^{B}\sum_{p}^{P}\left(w_{FG}\, y_{b,p}\log(y_{b,p}+\varepsilon) + w_{BG}\,(1-y_{b,p})\log(1-y_{b,p}+\varepsilon)\right)$$

A small numerical offset $\varepsilon = 10^{-4}$ was applied for numerical stability. We found equal weights or a slightly stronger bias to foreground to work almost equally well (here, we used $w_{FG}=2$ and $w_{BG}=0.5$), larger biases had negative effects. Additionally, we allowed the network to optimize the share of training data that contains at least some foreground by ignoring parts of training data in which no foreground is present. A share of 90% training data with at least some foreground optimized the performance on the validation set and was thus chosen. The network was trained using the Adam optimizer[51]; the initial learning rate was set to 10^{-4} and was gradually decreased by a factor of 10 to a minimum of 10^{-7} every time the loss function reached a plateau for more than 2 epochs. A single training run over 40 epochs takes only around 20-30 minutes on a normal workstation equipped with a NVIDIA Titan Xp GPU.

Testing and inference mode

As mentioned before, we applied k-fold cross-validation. Thus, in each of the $k=5$ folds the model was tested on data that was not seen by the model during training and validation. Together, all 5 test sets span the entire data set. As depicted in **Figure 3A**, the trained algorithm was used to generate probability masks for each of the three projection perspectives (P_{XY}, P_{YZ}, P_{ZX}), in which the pixel value indicates the network's confidence that this pixel is part of a metastasis in the given sub-volume s. Building the outer product of the three probability masks allows to recombine the three somewhat independent judgements of the network in 3D space:

$$P_{V,s} \in [0,1]^3 = \left(P_{XY,s} \in [0,1]^2 \otimes P_{YZ,s} \in [0,1]^2 \otimes P_{ZX,s} \in [0,1]^2\right)^{1/3}$$

This 3D recombination P_V of the 2D probability maps yields a final predicted segmentation mask after binarization. By default, the confidence threshold was set to 50%; however, changing this parameter allows to manually adjust the trade-off between sensitivity and specificity, if desired (also see **Figure S4**). Please note that the F1-score for evaluation is not affected by this trade-off (i.e., a better detection rate at the cost of a higher false positive rate would not artificially increase the F1-score and vice versa). Subsequent connected-component analysis converts the output to an explicit list and segmentation of predicted metastases in 3D space.

Performance evaluation

The same performance evaluation procedure was used for the comparison shown in **Figure 3D**, including the performance of a single human annotator. A standard test for detection tasks, the F1 score quantifies the accuracy of a model by combining precision (share of true positives among all positive predictions, including false positives) and recall (share of predicted positives among the sum of the true positive and false negative predictions). It is mathematically equivalent to the Sørensen–Dice coefficient ("Dice score"), which is the commonly used name for pixel-wise image segmentation problems. The F1 score is given as:

$$F1 = 2 \cdot \frac{precision \cdot recall}{precision + recall}$$

For all comparisons of detection and segmentation performance, the ground truth (refined by several human experts as described above) is used as a reference. We quantified the performance of the proposed deep learning algorithm based on its prediction of the test set. For a comparison, the segmentations as provided by established tools like the 3D Object Detector in ImageJ, our custom-made detector as described above, as well as the annotation as provided by a single human annotator (before joint refinement) were quantified in the same manner. Overlapping segmentations for metastases were counted as true positive predictions, non-overlapping predictions as false positives and metastases not detected by the prediction as false negatives. Predictions corresponding to the small set of cases unclear to the group of human experts (see above) were neither counted as true positive predictions nor as false negatives, i.e. they neither increased nor decreased the performance evaluation. All performance evaluations were conducted on the entirety of the test set as a whole. To quantify the inherent variance, the distribution of performance results was estimated with n=1000 resampled test sets (of same size) using the bootstrapping approach.

The DeepMACT algorithms can be downloaded at: http://discotechnologies.org/DeepMACT.

Quantifications and statistical analysis

Organ registration

For the full body light-sheet scans (e.g., **Figure 4C,F**) the outlines of selected organs of interest (all lung lobes, both kidneys, liver) were manually segmented as multi-point polygons in a stack of slices in 3D using Fiji. For each metastasis detected by our deep learning architecture we assessed whether its center of mass falls into the 3D segmentation of one of those organs using a custom Python script. Any

metastasis not registered to one of these organs is referred to as located in “the rest of the torso” in this manuscript. The 3D segmentation of the lungs was also used to compute the overall lung volume to assess the tumor density in **Figure 4J**, which we quantified as the share of the sum of the volume of all metastases registered to an organ of the entire organ volume.

Metastasis characterization

The output of our deep learning architecture is a binary segmentation volume for all metastases. We developed a custom-made, highly efficient implementation of a connected component analysis (available online) to derive an explicit list of metastases fully characterized in 3D. Based on each metastasis 3D shape and voxel-based volume V, we computed its average diameter as

$$d_{avg} = 2\sqrt[3]{\frac{3V}{4\pi}}$$

To quantify the number of cells in each metastasis, we measured the size of several isolated single cells (~1700 µm^3) and estimated the total numbers in metastases based on volumetric interpolation. We confirmed the accuracy of the estimations by the number of nuclei (PI or Hoechst labeled) in selected micrometastases. The distance of each metastasis i to its nearest neighboring metastasis was measured in 3D space as the Euclidian distance between their center of masses *CoM*:

$$distNN_i = \min_j \sqrt{(CoM_{i,x} - CoM_{j,x})^2 + (CoM_{i,y} - CoM_{j,y})^2 + (CoM_{i,z} - CoM_{j,z})^2}$$

Drug targeting analysis

We assessed the 6A10 antibody targeting of a given metastasis by analyzing the distribution of the fluorescent signal strength within the 3D segmentation of each metastasis (ξ_m) versus the distribution in its local surrounding (250 µm around the metastasis) ξ_s. For each signal distribution, the number of voxels within the metastasis segmentation n_m or in its local surrounding n_s can be seen as the number of observations of the underlying true (but unknown) distributions. The degree of targeting was estimated by quantifying the ratio of mean signal strength within the segmentation to the mean signal strength in its surrounding (e.g., in **Figure 5K**). We refer to this as antibody signal ratio. A ratio larger than 1 means that the antibody signal strength within then 3D segmentation of the metastasis is higher than around it (see dashed line in **Figure 5K**). Whether or not a metastasis was deemed “targeted” was assessed with a version of the *t*-test to determine whether mean of the observed signal distribution in the metastasis ξ_m was significantly at least Δ*=50% (ratio of 1.5)* above the mean of the observed signal distribution in the local surrounding ξ_s. Importantly, a *t*-test is valid for the signals despite their highly non-normal underlying distribution as the number of observations far exceeds the requirements of the central limit theorem (i.e., while the signals are not normally distributed, the estimation of their means is normally distributed due the high number of observations). This was verified manually. However, due to a typically much larger number of observations in the local surrounding ξ_s than for the metastasis itself ξ_m, the statistical test was not performed with a *Student’s t-test* but with the *Welch’s t-test* that corrects the *degrees of freedom* for an unequal number of observations for both distributions:

$$t = \frac{mean(\xi_m) - (1+\Delta)mean(\xi_s)}{\sqrt{\frac{std(\xi_m)^2}{n_m} + \frac{std(\xi_s)^2}{n_s}}}$$

$$DF_{adjusted} = \left(\frac{std(\xi_m)^2}{n_m} + \frac{std(\xi_s)^2}{n_s}\right)^2 \Big/ \frac{\left(\frac{std(\xi_m)^2}{n_m}\right)^2}{n_m - 1} + \frac{\left(\frac{std(\xi_s)^2}{n_s}\right)^2}{n_s - 1}$$

Analysis of fluorescence signal profiles from light-sheet images:

We considered the fluorescence signal profiles from each channel: excitation 470 nm, 561 nm and 647 nm. These profiles were plotted in the same z-stack and normalized as percentage over the maximum peak. To compare the reduction of the background and the improvement of the signal over background ratio (SBR) in far-red and near far-red channels, we analyzed lung metastases expressing mCherry imaged with excitation 545/561 nm, lung metastases labeled with anti-mCherry nanobody conjugated with Atto594 imaged with excitation 590 nm, and lung metastases labeled with anti-mCherry nanobody conjugated with Atto647N imaged with excitation 640 nm (n=9 tumors per each experimental group which consisted of 3 animals per each imaging modality). The signal profile was measured from a defined straight line covering the tumors and surrounding tissue background and all the values of the plot from a representative animal per each experimental group were shown in a representative line chart (**Figure S1D**). Finally, the normalized plots represented in **Figure S1E** were calculated by normalizing the plots of lung metastases obtained as described above over the average signal intensity of the respective surrounding background.

Quantification of metastasis diameter and distance between metastases and vessels

Metastasis diameters were verified manually. For quantifying the distance between metastases and vessels, ten points on the border of each metastasis were randomly selected and the shortest distance from these points to the closest vessel wall were measured. The presented distance between each metastasis and nearest vessels was quantified by averaging these ten measurements. In Figure 6B,

50 metastases were quantified to generate the distribution map and each bullet point represent one single metastasis.

References

1 Lambert, A. W., Pattabiraman, D. R. & Weinberg, R. A. Emerging Biological Principles of Metastasis. *Cell* **168**, 670-691, doi:10.1016/j.cell.2016.11.037 (2017).

2 Massague, J. & Obenauf, A. C. Metastatic colonization by circulating tumour cells. *Nature* **529**, 298-306, doi:10.1038/nature17038 (2016).

3 Hanahan, D. & Weinberg, R. A. Hallmarks of cancer: the next generation. *Cell* **144**, 646-674, doi:10.1016/j.cell.2011.02.013 (2011).

4 de Jong, M., Essers, J. & van Weerden, W. M. Imaging preclinical tumour models: improving translational power. *Nat Rev Cancer* **14**, 481-493, doi:10.1038/nrc3751 (2014).

5 Pan, C. *et al.* Shrinkage-mediated imaging of entire organs and organisms using uDISCO. *Nat Methods*, doi:10.1038/nmeth.3964 (2016).

6 Tainaka, K. *et al.* Whole-body imaging with single-cell resolution by tissue decolorization. *Cell* **159**, 911-924, doi:10.1016/j.cell.2014.10.034 (2014).

7 Yang, B. *et al.* Single-cell phenotyping within transparent intact tissue through whole-body clearing. *Cell* **158**, 945-958, doi:10.1016/j.cell.2014.07.017 (2014).

8 Cai, R. *et al.* Panoptic imaging of transparent mice reveals whole-body neuronal projections and skull-meninges connections. *Nat Neurosci*, doi:10.1038/s41593-018-0301-3 (2018).

9 Zipfel, W. R. *et al.* Live tissue intrinsic emission microscopy using multiphoton-excited native fluorescence and second harmonic generation. *Proc Natl Acad Sci U S A* **100**, 7075-7080, doi:10.1073/pnas.0832308100 (2003).

10 Tuchin, V. V. Editor's Introduction: Optical Methods for Biomedical Diagnosis. (2016).

11 Topol, E. J. High-performance medicine: the convergence of human and artificial intelligence. *Nat Med* **25**, 44-56, doi:10.1038/s41591-018-0300-7 (2019).

12 Kermany, D. S. *et al.* Identifying Medical Diagnoses and Treatable Diseases by Image-Based Deep Learning. *Cell* **172**, 1122-1131 e1129, doi:10.1016/j.cell.2018.02.010 (2018).

13 Christiansen, E. M. *et al.* In Silico Labeling: Predicting Fluorescent Labels in Unlabeled Images. *Cell* **173**, 792-803 e719, doi:10.1016/j.cell.2018.03.040 (2018).

14 Sullivan, D. P. *et al.* Deep learning is combined with massive-scale citizen science to improve large-scale image classification. *Nat Biotechnol* **36**, 820-828, doi:10.1038/nbt.4225 (2018).

15 Camacho, D. M., Collins, K. M., Powers, R. K., Costello, J. C. & Collins, J. J. Next-Generation Machine Learning for Biological Networks. *Cell* **173**, 1581-1592, doi:10.1016/j.cell.2018.05.015 (2018).

16 Esteva, A. *et al.* Dermatologist-level classification of skin cancer with deep neural networks. *Nature* **542**, 115-118, doi:10.1038/nature21056 (2017).

17 Wang, H. *et al.* Deep learning enables cross-modality super-resolution in fluorescence microscopy. *Nat Methods* **16**, 103-110, doi:10.1038/s41592-018-0239-0 (2019).

18 Iorns, E. *et al.* A new mouse model for the study of human breast cancer metastasis. *PloS one* **7**, e47995, doi:10.1371/journal.pone.0047995 (2012).

19 Gondi, G. *et al.* Antitumor efficacy of a monoclonal antibody that inhibits the activity of cancer-associated carbonic anhydrase XII. *Cancer Res* **73**, 6494-6503, doi:10.1158/0008-5472.CAN-13-1110 (2013).

20 von Neubeck, B. *et al.* An inhibitory antibody targeting carbonic anhydrase XII abrogates chemoresistance and significantly reduces lung metastases in an orthotopic breast cancer model in vivo. *Int J Cancer* **143**, 2065-2075, doi:10.1002/ijc.31607 (2018).

21 Ronneberger, O., Fischer, P. & Brox, T. 234-241 (Springer International Publishing).

22 Pandey, M. & Mahadevan, D. Monoclonal antibodies as therapeutics in human malignancies. *Future Oncol* **10**, 609-636, doi:10.2217/fon.13.197 (2014).

23 Barker, N. & Clevers, H. Mining the Wnt pathway for cancer therapeutics. *Nat Rev Drug Discov* **5**, 997-1014, doi:10.1038/nrd2154 (2006).

24 Battke, C. *et al.* Generation and characterization of the first inhibitory antibody targeting tumour-associated carbonic anhydrase XII. *Cancer Immunol Immunother* **60**, 649-658, doi:10.1007/s00262-011-0980-z (2011).

25 Tabrizi, M., Bornstein, G. G. & Suria, H. Biodistribution mechanisms of therapeutic monoclonal antibodies in health and disease. *AAPS J* **12**, 33-43, doi:10.1208/s12248-009-9157-5 (2010).

26 Kubota, S. I. *et al.* Whole-Body Profiling of Cancer Metastasis with Single-Cell Resolution. *Cell Rep* **20**, 236-250, doi:10.1016/j.celrep.2017.06.010 (2017).

27 Vestjens, J. H. *et al.* Relevant impact of central pathology review on nodal classification in individual breast cancer patients. *Ann Oncol* **23**, 2561-2566, doi:10.1093/annonc/mds072 (2012).

28 Ehteshami Bejnordi, B. *et al.* Diagnostic Assessment of Deep Learning Algorithms for Detection of Lymph Node Metastases in Women With Breast Cancer. *JAMA* **318**, 2199-2210, doi:10.1001/jama.2017.14585 (2017).

29 Litjens, G. *et al.* Deep learning as a tool for increased accuracy and efficiency of histopathological diagnosis. *Sci Rep* **6**, 26286, doi:10.1038/srep26286 (2016).

30 Liu, Y. *et al.* Artificial Intelligence-Based Breast Cancer Nodal Metastasis Detection. *Arch Pathol Lab Med*, doi:10.5858/arpa.2018-0147-OA (2018).

31 Steiner, D. F. *et al.* Impact of Deep Learning Assistance on the Histopathologic Review of Lymph Nodes for Metastatic Breast Cancer. *Am J Surg Pathol* **42**, 1636-1646, doi:10.1097/PAS.0000000000001151 (2018).

32 Wang, J. *et al.* A multi-resolution approach for spinal metastasis detection using deep Siamese neural networks. *Comput Biol Med* **84**, 137-146, doi:10.1016/j.compbiomed.2017.03.024 (2017).

33 Falk, T. *et al.* U-Net: deep learning for cell counting, detection, and morphometry. *Nat Methods* **16**, 67-70, doi:10.1038/s41592-018-0261-2 (2019).

34 Bhatia S., S. Y., Goel L. . Lung Cancer Detection: A Deep Learning Approach. *Advances in Intelligent Systems and Computing* **817**.

35 Wang N., C. B., Yi Wang, Min Xu, Chenchen Qin, Xin Yang, Tianfu Wang, Anhua Li, Dinggang Shen, Dong Ni.

Densely Deep Supervised Networks with Threshold Loss for Cancer Detection in Automated Breast Ultrasound. *Medical Image Computing and Computer Assisted Intervention – MICCAI 2018 - 21st International Conference, 2018, Proceedings*, 641-648 (2018).
36 NM, R. S. C. L. E. D. P. S. K. M. R. Mimo-net: A multi-input multi-output convolutional neural network for cell segmentation in fluorescence microscopy images. *Biomedical Imaging (ISBI 2017), 2017 IEEE 14th International Symposium*, 337-340 (2017).
37 Massoud, T. F. & Gambhir, S. S. Molecular imaging in living subjects: seeing fundamental biological processes in a new light. *Genes Dev* **17**, 545-580, doi:10.1101/gad.1047403 (2003).
38 Timpson, P., McGhee, E. J. & Anderson, K. I. Imaging molecular dynamics in vivo--from cell biology to animal models. *J Cell Sci* **124**, 2877-2890, doi:10.1242/jcs.085191 (2011).
39 Ntziachristos, V. Going deeper than microscopy: the optical imaging frontier in biology. *Nat Methods* **7**, 603-614, doi:10.1038/nmeth.1483 (2010).
40 Massoud, T. F. & Gambhir, S. S. Integrating noninvasive molecular imaging into molecular medicine: an evolving paradigm. *Trends Mol Med* **13**, 183-191, doi:10.1016/j.molmed.2007.03.003 (2007).
41 Pichler, B. J., Wehrl, H. F. & Judenhofer, M. S. Latest advances in molecular imaging instrumentation. *J Nucl Med* **49 Suppl 2**, 5S-23S, doi:10.2967/jnumed.108.045880 (2008).
42 Condeelis, J. & Weissleder, R. In vivo imaging in cancer. *Cold Spring Harb Perspect Biol* **2**, a003848, doi:10.1101/cshperspect.a003848 (2010).
43 Vick, B. *et al.* An advanced preclinical mouse model for acute myeloid leukemia using patients' cells of various genetic subgroups and in vivo bioluminescence imaging. *PloS one* **10**, e0120925, doi:10.1371/journal.pone.0120925 (2015).
44 Jones, E., Oliphant, T. & Peterson, P. SciPy: Open Source Scientific Tools for Python. **URL http://www.scipy.org/** (2001).
45 Waskom, M. seaborn: statistical data visualization. **URL https://seaborn.pydata.org/** (2012).
46 McKinney, W. Pandas. **URL https://pandas.pydata.org/** (2008).
47 Paszke, A. PyTorch. **URL https://pytorch.org/** (2016).
48 Bolte, S. & Cordelieres, F. A guided tour into subcellular colocalization analysis in light microscopy. *Journal of Microscopy* **224**, 213-232, doi:doi:10.1111/j.1365-2818.2006.01706.x (2006).
49 Mavandadi, S. *et al.* A mathematical framework for combining decisions of multiple experts toward accurate and remote diagnosis of malaria using tele-microscopy. *PloS one* **7**, e46192, doi:10.1371/journal.pone.0046192 (2012).
50 Mavandadi, S. *et al.* Distributed medical image analysis and diagnosis through crowd-sourced games: a malaria case study. *PloS one* **7**, e37245, doi:10.1371/journal.pone.0037245 (2012).
51 Kingma, D. P. & Ba, J. Adam: A Method for Stochastic Optimization. *arXiv e-prints* (2014). <https://ui.adsabs.harvard.edu/\#abs/2014arXiv1412.6980K>.

MOVIE LEGENDS

Movie S1
3D reconstruction of an intact mouse torso scanned by light-sheet microscopy. The left side shows the segmented view, in which the torso is represented in gray, the lungs in yellow and the heart in green. The right side shows the original 2D data from the light-sheet microscopy. Various macro- and micro-metastases (magenta) are visualized in high contrast over the background.

Movie S2
3D visualization of some micrometastases in the lungs showing the single cell resolution obtained by light-sheet microscopy. The tumors are shown in magenta and PI nuclear labeling in green.

Movie S3
3D animation of whole mouse body scanned by light-sheet microscopy at the cellular level. The outline of the mouse (scan of the unlabeled autofluorescence channel at 488 nm excitation) shown in gray, some segmented organs (lungs, kidney, liver and brain) in blue, the tumors in magenta, and the tumor & therapeutic antibody 6A10 co-localization in white. The first part of the animation shows tumor macro- and micrometastasis throughout the body, and the second part shows the biodistribution of the therapeutic antibody 6A10 along with tumor macro- and micrometastases.

Movie S4
3D animation of the lungs demonstrating the details of the therapeutic antibody binding. Micrometastases are shown in magenta and the co-localization of micrometastases and therapeutic antibody in white. While most of the micrometastases are targeted by the therapeutic antibody (white), a fraction was not (the ones remaining magenta throughout the movie).

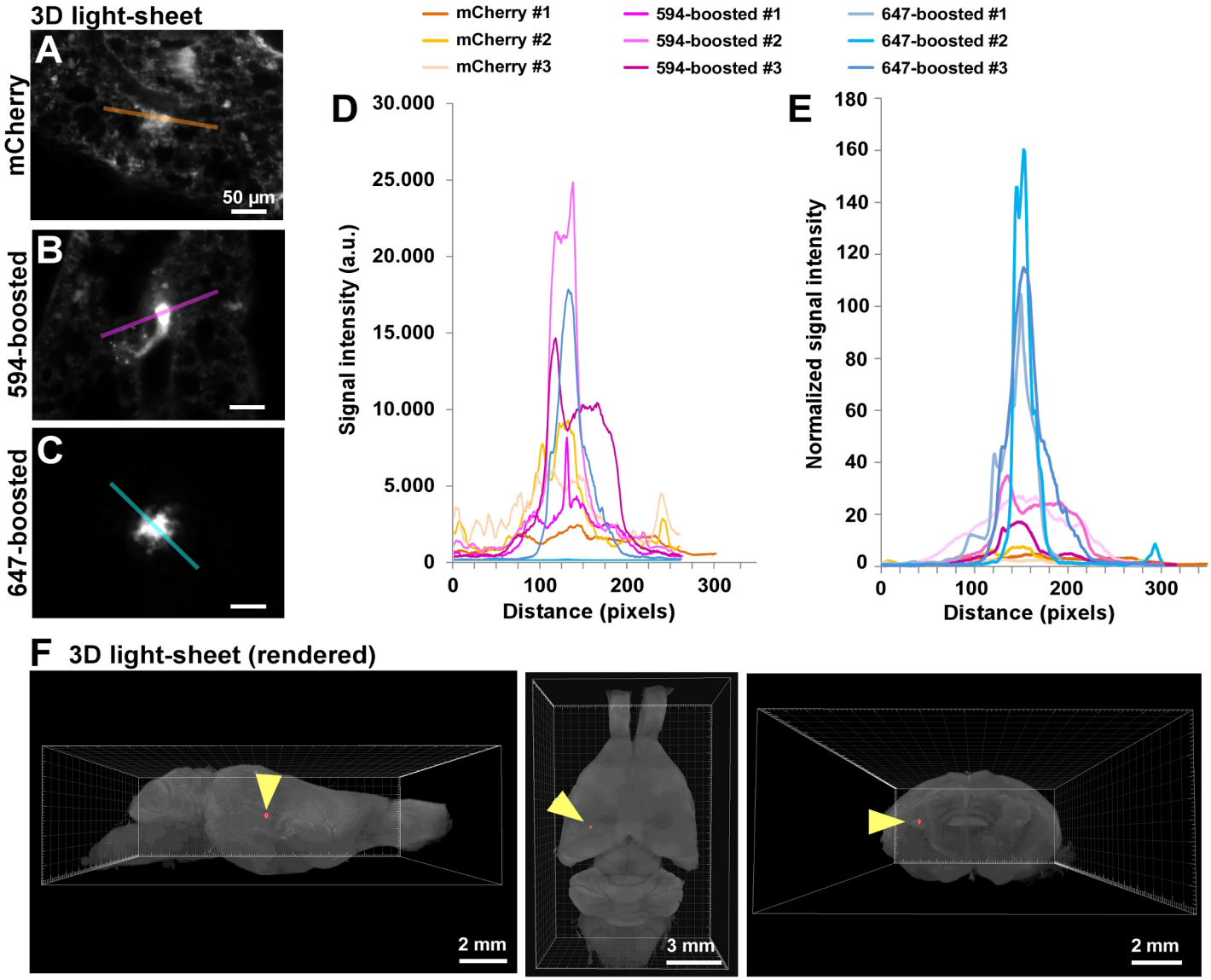

Figure S1; related to Figure 2

vDISCO nanoboosting of the fluorescent signal of cancer cells

(**A-C**) Representative light-sheet images of mCherry expressing tumor metastases in the lungs of cleared mice that were not nanobody-boosted (**A**), metastases boosted with an anti-mCherry nanobody conjugated to Atto594 (**B**) or an anti-mCherry nanobody conjugated to Atto647N (**C**). (**D**) Plots of signal intensity profiles along the yellow lines in panels A-C: non-boosted mCherry (orange), mCherry boosted with Atto594 (magenta) or mCherry boosted with Atto647N (cyan) (n=3 representative metastases). (**E**) Intensity profiles of the fluorescence signal in (D) normalized over the background. (**F**) Example of deep-tissue imaging of Atto647N-boosted tumor metastases in the brain in the far-red spectrum of transparent mice after vDISCO. A tumor micrometastasis, which is located several millimeters deep in the brain tissue, can be readily detected (yellow arrowhead).

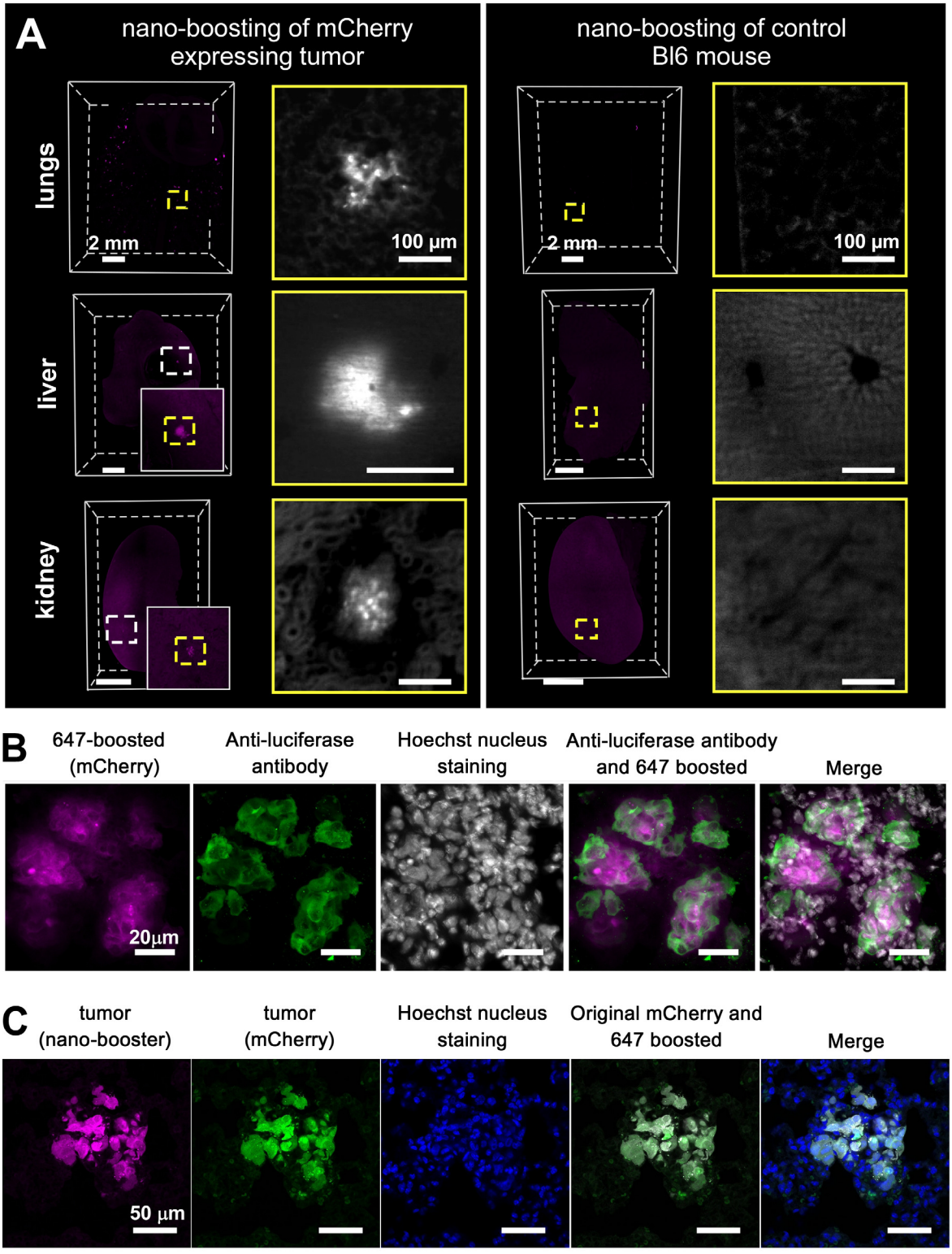

Figure S2; related to Figure 2

Confirmation of specificity of nano-booster staining in mice bearing mCherry-expressing tumors

(**A**) Comparison between an animal bearing an mCherry expressing tumor and a C57BL/6N control animal, which were both boosted with an anti-mCherry nanobody conjugated to Atto647N (magenta) and imaged by light-sheet microscopy. No signal is detected in organs from the C57BL/6N control. Note that the background is enhanced to demonstrate the absence of signal in the high-magnification images. (**B**) Confocal images of metastatic lung tissue immunolabeled with an anti-firefly luciferase antibody (green) after rehydration of the cleared tissue; Atto647N-boosted cancer cells and cell nuclei are shown in magenta and grey, respectively. (**C**) Confocal images of a metastasis in the lung of an animal labeled with an anti-mCherry nano-booster conjugated to Atto647N. The nano-booster is shown in magenta, mCherry is shown in green and cell nuclei are shown in blue indicating that nano-boosting specifically detects mCherry.

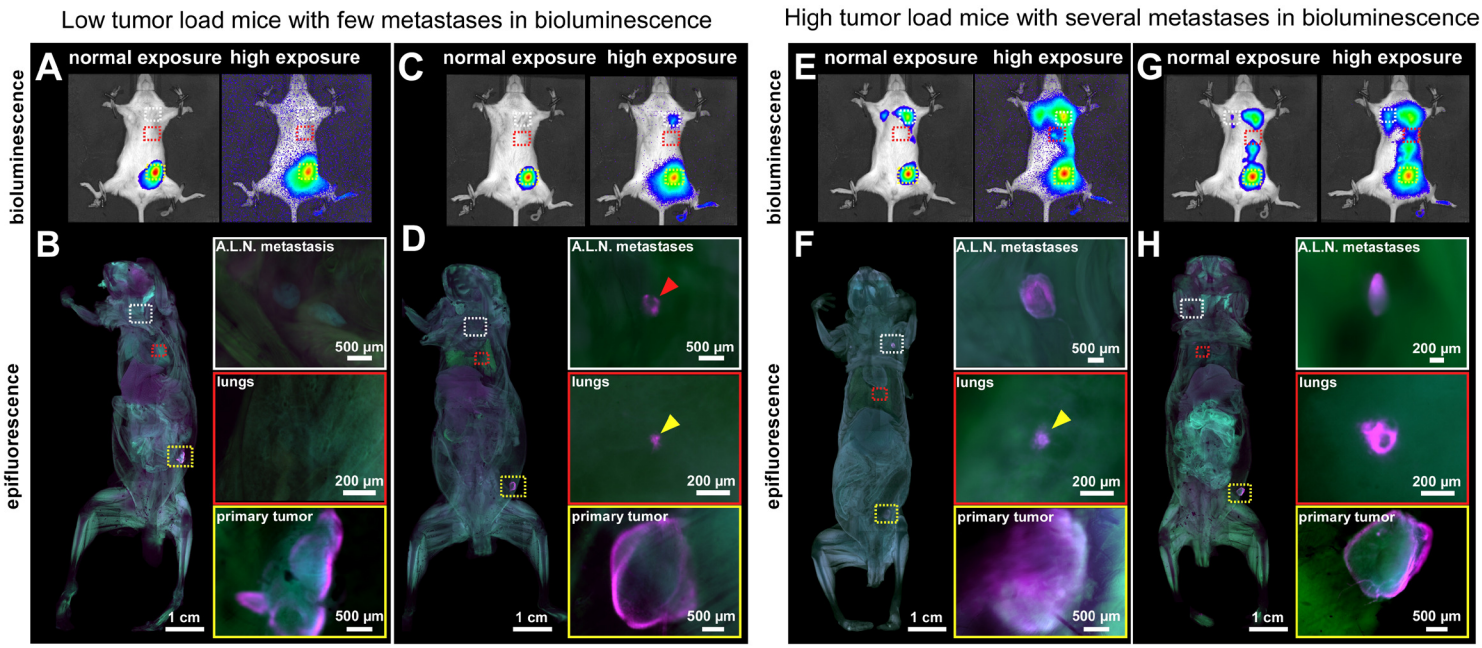

Figure S3; related to Figure 2

Examples of tumor metastasis detection in mice using bioluminescence imaging versus vDISCO and epifluorescence microscopy

(**A**-**D**) We found that bioluminescence imaging with normal exposure is not sufficiently sensitive to detect all the metastases in low tumor load mice. For example, the mice in (**A**,**B**) and (**C**,**D**) had very similar bioluminescence images with normal exposure. Applying vDISCO to these mice, we found no tumor metastases in one case (**A**,**B**) and a large metastasis (red arrowhead) in axillary lymph nodes (A.L.N. metastasis) (**C**,**D**) using a fluorescence stereo microscope. Although the signal from the primary tumor is strong in both normal and high exposure bioluminescence images (**A**,**C**, yellow box), metastases in lungs (**A**,**C**, red boxes) are not visible, but are detected by epifluorescence imaging (D, yellow arrowhead). In epifluorescence images, the tumors (A647 labeled) are shown in magenta and the background, scanned in 488 nm, is shown in green. (**E**-**H**) In mice with high tumor load, a bulk heat map of metastatic distribution can be obtained by in the bioluminescence imaging, without detailed shape and size information. In contrast, vDISCO resolved single micrometastases in whole mouse bodies even with a fluorescence stereo microscope. Especially in the lungs, even micrometastases with a diameter smaller than 100 µm could be resolved in intact mice (**F**, yellow arrowhead).

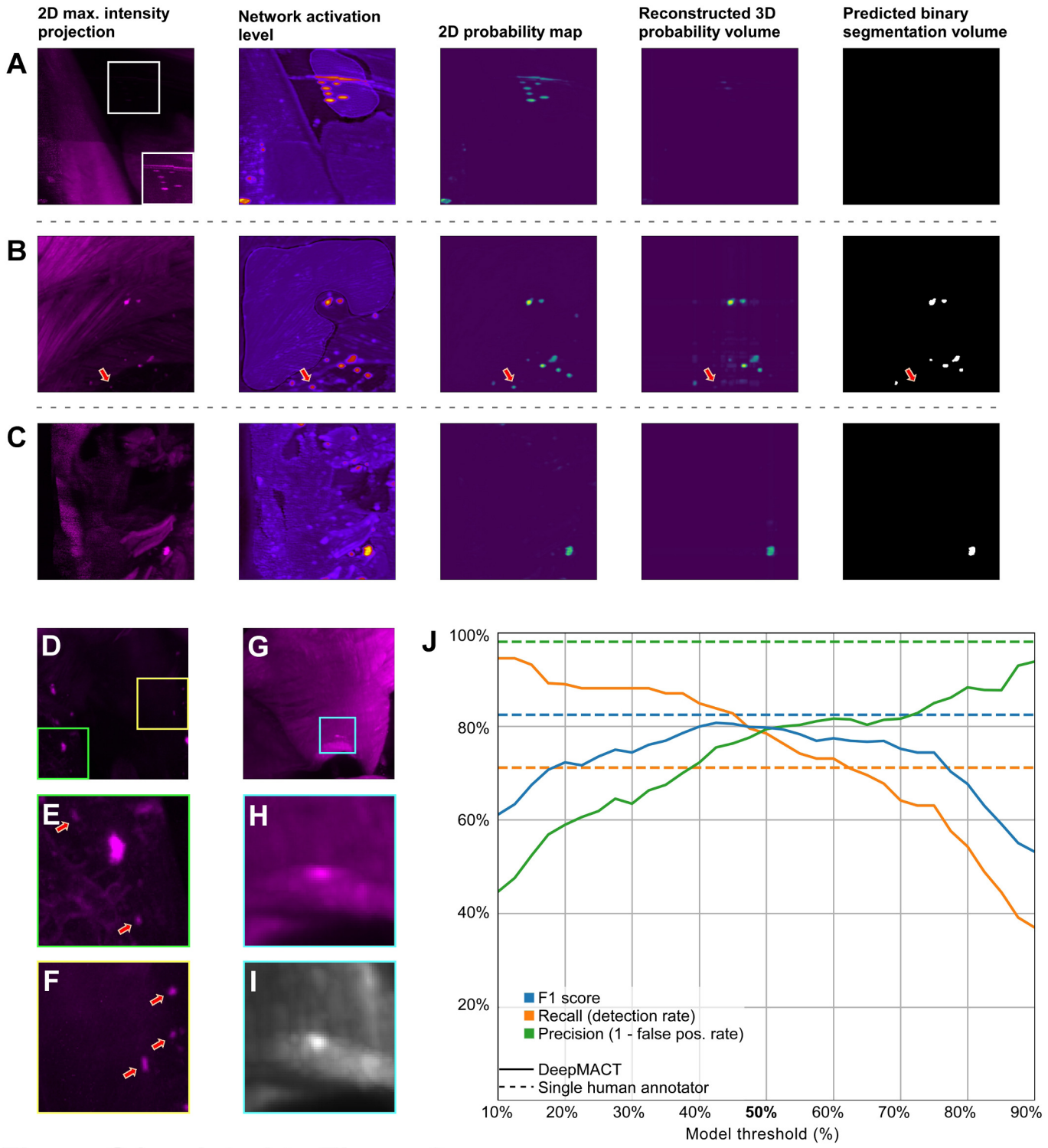

Figure S4; related to Figure 3

Performance of DeepMACT

(**A**-**C**) Visualization of the computational stages of DeepMACT for three different regions. (**A**) DeepMACT is capable of identifying very low signal peaks but correctly disregards them at the 3D reconstruction stage; the white inlet shows 10-fold increased brightness. (**B**) While most metastases are correctly identified, few small and dim metastases may be obscured by background structures from some perspectives and consequently be removed at the 3D reconstruction stage (red arrow) (**C**) In many cases, even a single 2D probability map may already be sufficient for a correct prediction. (**D-F**) Example of metastases that were missed by humans but found by DeepMACT (red arrows); brightness of (**G**) and (**F**) increased by 200% compared to (D). (**G**,**H**) Example of false positive prediction by DeepMACT. The image in (**I**) shows the same region as in (H) but in the autofluorescence channel (excitation: 488 nm) to confirm that the signal peak in (H) is not caused by metastatic tissue. (**J**) DeepMACT performance as a function of model confidence threshold (default: 50%) compared to a single human annotator. While the DeepMACT F1 score peaks around 40-50%, the threshold can be adjusted to increase recall or precision.

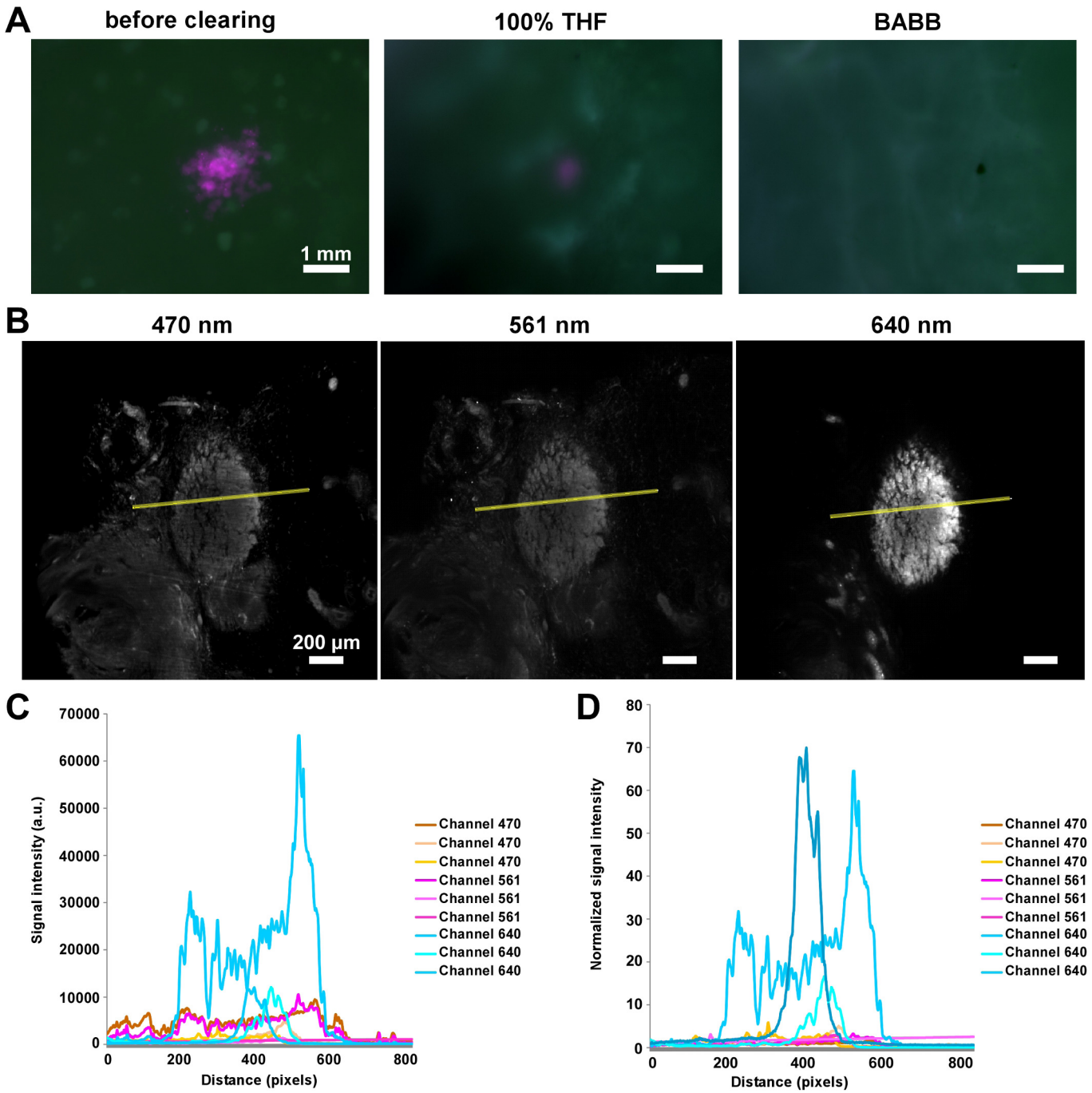

Figure S5; related to Figure 5

Elimination of endogenously expressed mCherry signal from tumors after vDISCO

(**A**) Tumor metastases in lungs were imaged with a fluorescence stereomicroscope before and after vDISCO clearing, showing that the endogenously expressed mCherry signal was eliminated after THF and BABB incubation steps. (**B**) Light-sheet microscopy images of primary tumor with background imaged in green (ex: 470 nm, left), with mCherry signal in the red (ex: 561 nm, middle) channel, and the boosted signal (Atto647N) in the far-red channel (ex: 640, right). (**C**) Signal intensity profiles along the yellow lines in panel B were plotted: Channel 470 (orange), Channel 561 (magenta) and Channel 640 (cyan) (n=3 mice). (**D**) Normalized fluorescence signal profiles of the data in (**C**), showing that after vDISCO clearing the endogenous mCherry signal was depleted to background levels.

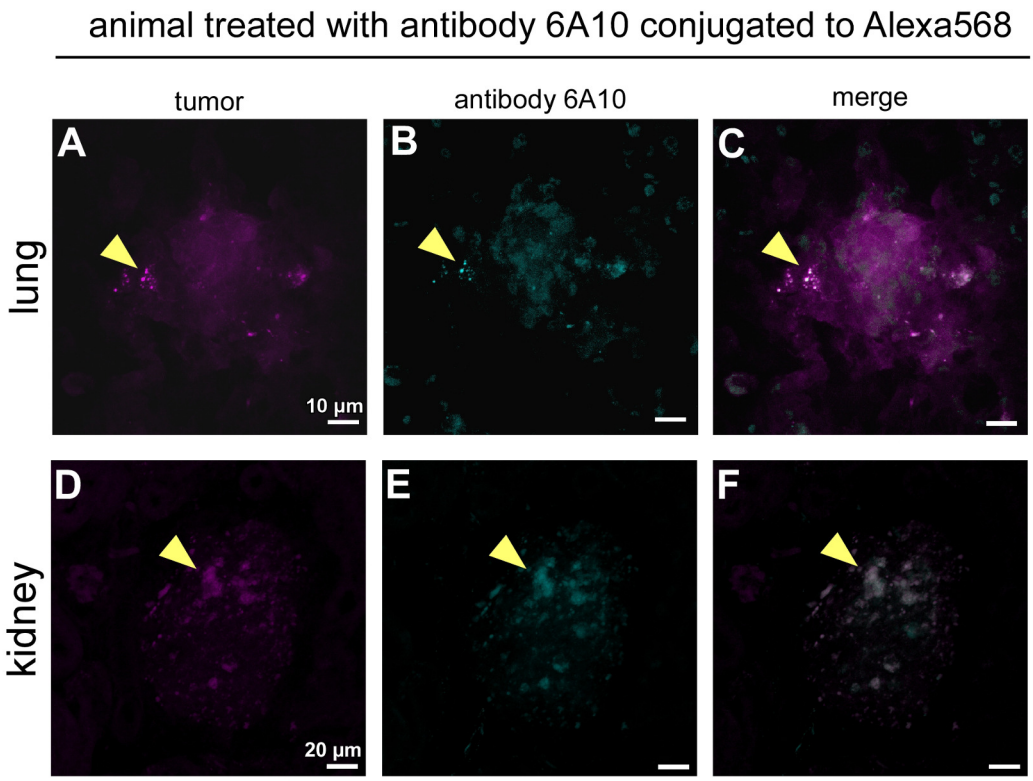

Figure S6; related to Figure 5

Verification of antibody targeting in different organs by confocal microscopy
(**A**-**F**) Confocal images of metastases in the lung (**A**-**C**) and kidney (**D**-**F**) of an animal labeled with an anti-mCherry nanobody conjugated to Atto647 (magenta) and treated with therapeutic antibody 6A10 conjugated to Alexa568 (cyan). The colocalization of the metastases with the 6A10 antibody is indicated with yellow arrowheads (**C** and **F**).

3. Discussion

Aiming to provide practical tools for systems biology studies, we developed u/vDISCO whole-body tissue clearing methods which achieved complete light-sheet fluorescent scanning of intact rodent bodies for the first time. Novel findings of anatomic structures and global distribution map of disease related pathologies revealed by u/vDISCO indicate the importance of unbiased whole-body screening without sectioning. Comparing with other whole-body clearing methods, uDISCO and vDISCO provided a time and labor efficient solution for studying the structure or cell subtypes labeled by endogenously expressed fluorescent proteins with cellular level light-sheet microscopy and systemic analysis through entire organisms.

3.1 Combining transcardial circulation and organic solvents achieved robust whole-body tissue clearing

In terms of the experimental setting, uDISCO creatively established a constant transcardial circulation system which improved the clearing efficiency and thereby helped to preserve the fluorescent signal. In addition, the continuous transcardial perfusion was utilized to build a high pressure driven nanobody delivery system and led to the complete deep tissue immunolabeling in vDISCO. In fact, most whole-body tissue clearing methods appeared after uDISCO utilized the transcardial perfusion system. For instance, by using a mixture of tert-butonal and PEG400 as clearing solutions and by combing with decalcification and decolorization, PEGASOS achieved 2-photon imaging of tdTomato labeled neurons through transparent spinal cord by circulating the clearing solutions at 37 °C (Jing et al., 2018).

On the other hand, another key step of uDISCO was screening fluorescent protein compatible organic solvents which could provide better preservation of fluorescent signal. In this study, we utilized tert-butonal as dehydration solution instead of THF used in 3DISCO and added DPE which has high RI while less prone to oxidation for RI matching. However, more attempts of screening new candidates which could provide even better signal preservation are still on the way. And it is worth noting that some promising approaches have already been achieved. For example, Inspired by the fact that maintaining the pH in alkaline range helps to stabilize the fluorescent proteins (Schwarz et al., 2015), Zhu et al. utilized a mixture a tert-butonal and Quadrol to achieve better signal preservation (Li et al., 2018). Applying the same

concept to THF, the FDISCO overcomes the fast fluorescence quenching and preserves the fluorescent signal of GFP and tdTomato even better than uDISCO (Qi et al., 2019). Park et al. recently developed a protein preservation strategy by generating the intramolecular epoxide linkages which maintains the protein fluorescence and tissue architecture from harsh chemical treatment (Park et al., 2018). All these existing and upcoming approaches could be utilized as good candidates to improve whole-body tissue clearing.

3.2 Applying far red dye conjugated nanobodies for deep tissue immunolabeling

GFP has been widely used to label cell populations or biological structures in multiple transgenic animal lines. However, the excitation and emission wavelengths of GFP is in the blue/green spectrum which generate severe light scattering and autofluorescence (Piatkevich et al., 2017). As a result, core of the heme rich tissue such as liver could hardly be imaged with blue wavelengths even after tissue clearing (Cai et al., 2019). In fact, engineered fluorescent proteins which can be excited by light with far red or infrared wavelength have been used for non-invasive deep-tissue imaging in mammals (Chu et al., 2014; Hong et al., 2017). This indicates that these far red or infrared fluorescent proteins should be considered for generating transgenic mouse lines and imaging in far red spectrum helps to achieve better laser penetration and imaging quality.

On the other hand, whole mount antibody immunolabeling has been used to study neuronal projections and to map the brain activities (Belle et al., 2017; Renier et al., 2016). However, the antibody labeling efficiency varies not only between different antibodies or suppliers but also between different batches even from the same producer. This makes the variation of suitable antibodies time and labor consuming. Attempts have been made to increase the penetration of conventional antibodies for whole mount immunostaining. For instance, SWITCH achieved homogenous immunolabeling by blocking the initial binding between antibody and antigen, thereby improved the deep tissue staining quality (Ku et al., 2016). We reasoned that nanobody, which is the variable domain of heavy chain antibodies (V_HH), has unique advantage for deep-tissue labeling because of their small size (12–15 kDa) comparing to conventional antibodies (~150 kDa). Indeed, vDISCO utilized far red

dye conjugated nanobodies to enhance the fluorescent signal intensity while shifting the imaging laser wavelength to far red spectrum which significantly minimized the tissue autofluorescence and improved the imaging quality through intact transparent bone and skin.

Last but not least, tissue shrinkage mediated by organic solvent clearing is particularly suitable for imaging cleared samples originally with large scale. One major hurdle for large sample imaging is the limitation of microscopy system, especially the working distance of objectives. In general, the working distance of high NA (Numerical Aperture) long working distance objectives is around 10 mm, which is far from overcoming the thickness of an adult mouse (2-3 cm). By reducing the size of biological samples up to 30% from each dimension, an entire body of adult mouse can be fit into the commercially available LSFM system and imaged with its entirety from one side firstly and then the other side. In contrast, although the subcellular level or even molecular level resolution imaging achieved by expansion microscopy should be highly appreciated (Chen et al., 2016; Gao et al., 2019), the size of biological samples could be imaged by expansion microscopy limits its application in large scale tracing and quantifications. Taken together, enhanced fluorescent imaging quality complemented with shrinkage light-sheet microscopy makes uDISCO and vDISCO a practical and powerful platform for whole-body mapping at cellular level.

3.3 Evaluating risks for BMSCs transplantation

Although BMSCs transplantation has been widely used as an effective therapeutic approach, the potential risks need be considered. Firstly, pulmonary complications were reported after hematopoietic stem cell transplantation including pulmonary veno-occlusive disease and cytolytic thrombi (Diab et al., 2016). In fact, in **Research Article 1**, we detected the clusters of BMSCs in the vasculature in lungs (data not shown). Although whether these stem cell clusters will form thrombosis in lungs needs to be further evaluated, strategy of systemic administrations of BMSCs should be improved. Indeed, Kelkela et al. compared intravenous vs. intra-arterial administration of BMSCs and found the intra-arterial transplantation significantly reduced the accumulation of BMSCs in lungs (Kerkela et al., 2013), therefore could potentially decrease the risk to form pulmonary veno-occlusion.. As a practical

cellular mapping methodology, uDISCO and vDISCO whole-body clearing could be readily used to clarify the distribution of intra-arterial injected BMSCs as well as the fate and clearance pathways of transplanted BMSCs which still remains elusive (Leibacher and Henschler, 2016).

3.4 Systemic inflammatory response triggered by tissue damage

Whether inflammation is beneficial or harmful for CNS regeneration is still controversial (Gadani et al., 2015). Negative effect of inflammation upon proliferation of neural stem/progenitor cells has been observed which results in reduced numbers of newborn neurons and ineffective repair of the damaged circuitry (Ekdahl et al., 2003; Monje et al., 2003). Other studies showed that peripheral leukocytes which infiltrated into the lesion site enhanced the proliferation of progenitor cells and thereby lead to higher neuronal survival rates (Ziv et al., 2006). The protective or detrimental effects of inflammation is highly dependent on different cell types (e.g. neutrophils vs. leukocytes). To manipulate inflammation as a potential therapeutic approach for CNS injuries requires comprehensive understanding of disease-specific immune cell populations and the dynamic changes of their functions at different stages of the injury. Apart from the whole-body mapping tools we developed, high-through-put transcriptome and proteomics analysis will also play important roles from this perspective (Jordao et al., 2019).

On the other hand, discovering novel infiltration routes of peripheral immune cells and clarifying their roles in CNS disease will provide potential therapeutic target to block the invasion of harmful cell types. Here, we identified vascular connections between skull bone marrow and brain meninges which were filled with trafficking neutrophils after stroke as an additional immune cell infiltration route. Considering that skull bone marrow is close to brain in distance, it could be considered as administration targets or source of beneficial immune cells for brain diseases therapy. However, better understanding of the cellular content of skull bone marrow and molecular signaling pathways involving immune cells recruitment from these connections is needed. It is also worth noting that trans-cortical vessels (TCVs) in the long bones were recently discovered by using simpleCLEAR tissue clearing method (Grüneboom et al., 2019). Taking together with the skull-meningeal vascular connections revealed by vDISCO, this further suggests that tissue clearing has

unique advantage to study the fragile anatomic structures which may largely be destroyed or distorted during dissection.

In addition, in **Research Article 2**, we evaluated the immune response after spinal cord injury (SCI). It is not surprising that CD68 positive immune cells increased significantly at the lesion core (Wang et al., 2015). However, since CD68 expressed both in activated microglia and macrophages (Chiu et al., 2009), we could not distinguish the invasion peripheral immune cells from the local microglia. A potential strategy to overcome this hurdle could be using double transgenic mouse lines such as CCR2 line crossed with Tmem119 line. Since Tmem119 is a microglia marker more specific than widely used CX3CR1 transgenic line (Bennett et al., 2016), it would help to study the interaction or communication between local microglia and peripheral immune cells. Interestingly, comparing with naïve mice without any injury, we detected CD68 positive immune cells accumulated in the spinal meninges in the mice with sham surgery which only hurts the muscle tissue but not the vertebra. This finding indicates that injury in periphery might in turn affect the CNS. Therefore, systemic analysis through the entire organism is needed for investigating diseases with global impact.

3.5 Deep learning based methodology facilitates cancer related studies

Although progress has been made in cancer therapy and 5-year relative survival rate of patients has been significantly improved (Howlader N, 2017), cancer is still the biggest killer in 12 major European countries (SanjayTanday, 2016). Searching potential molecular targets as well as evaluating therapeutic efficacy of tumor-specific drugs requires novel technology with improved detection and quantification of pathologies in cancer animal models and in human biopsies. As a practical methodology improvement, tissue clearing has been used in cancer studies to achieve the intact volumetric information of the tumors (Tanaka et al., 2017; Zhao et al., 2017). Furthermore, as briefly mentioned above, Kubota et al. apply CUBIC whole-body clearing to the cancer mouse model and quantified the metastasis in lungs using a threshold-based algorithm (Kubota et al., 2017). However, it is challenging to apply threshold-based algorithm to quantify the whole-body because the background signal varies from different tissue. For instance, lung tissue usually has low level background while muscle tissue creates high level background.

Applying the universal filter normally results in either low detection rate of metastasis or high false positive signal (see **Research Article 3**, Figure 3 D).

In fact, the emerging robust artificial intelligence based tools have shown great values in clinical diagnose of various diseases and automated experiments in biomedical research (Yu et al., 2018). In cancer study, deep learning has been used to improve the accuracy of histopathological diagnosis (Litjens et al., 2016) and to detect the breast cancer metastases in the lymph nodes (Ehteshami Bejnordi et al., 2017). Here, we developed a deep learning based algorithm which achieved the automated detection and quantification of cancer metastasis through the whole mouse bodies with cellular resolution. The result DeepMACT pipeline reaches the similar detection accuracy with human operator while outperformed threshold-based algorithm. After training, DeepMACT is able to quantify a whole-body data set over 300 times faster than a human annotator. Overall, DeepMACT provides a time efficient and high-through put methodology for cancer metastasis studies.

3.6 Potential mechanisms of therapeutic antibody targeting

Systemic evaluation of bio-distribution as well as better understanding of the mechanisms related to targeting efficacy of therapeutic antibodies is important for cancer immunotherapy development. It is known that a variety of factors could affect the molecule movement from blood to organ parenchyma such as antibody size, concentration, polarity and membrane permeability (Tabrizi et al., 2010). In tumors, the abnormal endothelial cells of tumor vessels lead to disrupted vasculature and unstable blood supply (Carmeliet and Jain, 2000; McDonald and Baluk, 2002). This would further hinder the delivery of therapeutic antibody (Jain, 2012). However, in this study, we found that all the metastasis in lungs were next to blood vessels suggesting that the insufficient blood supply might not be the major reason of antibody off-targeting. One possibility is that the metastasis in lungs are relatively small comparing with the primary tumors (~100 μm vs. 5 mm) and antibody can already reach the target cancer cells by passive diffusion. In fact, we barely found vessel structure in the center of lung metastasis indicating that the size of these metastasis did not reach the threshold to angiogenesis (Hillen and Griffioen, 2007).

On the other hand, the expression level of antigen, which is CAXII, might directly influence the binding of 6A10 antibody. We evaluated the presence of CAXII mRNA by using fluorescence in situ hybridization (FISH) and found the heterogeneity of CAXII expression even within the same metastasis (data not shown). However, better membrane staining to distinguish each tumor cells as well as CAXII immunostaining is needed to study the co-localization of CAXII and 6A10 antibody. Last but not least, we found that the metastasis targeted by 6A10 antibody in lungs seems to be clustered, suggesting the microenvironment of the metastatic niches might play an important role of antibody targeting. Considering the recent work from Lee et al. that the hepatocytes may change the microenvironment of liver and make it the primary metastatic organ for various types of cancer (Lee et al., 2019), whether specific cells subtypes or cellular factors involves in the therapeutic antibody targeting remains unknown and requires further investigation.

3.7 Limitations of current whole-body tissue clearing

Although u/vDISCO whole-body tissue clearing are robust techniques for life science studies at systems level, they are developed for endpoint experiments of fixed rodent samples and not applicable for longitudinal analysis. To achieve large scale longitudinal analysis, natural transparency of the organism is quite important for *in vivo* deep tissue imaging. For instance, multiple model organisms such as Caenorhabditis elegans (Venkatachalam et al., 2016) and zebrafish (Barbosa et al., 2016) are widely used for *in vivo* neuronal structure and activity investigations because their larva are naturally transparent. Furthermore, genetic modifications had been approached to knockout the skin pigmentation and to make the adult transgenic zebrafish transparent (Antinucci and Hindges, 2016). Although we are still far from generating a living transparent mouse line, understanding the genetic and physical basis of biological transparency will contribute to this perspective in the future (Johnsen, 2001).

On the other hand, approaches involving bio-compatible reagents or solutions had also been applied to reach *in vivo* tissue transparency. For instance, by using a solution composed with fructose, polyethylene glycol-400 and thiazone, Shi et al. achieved a switchable skin window to study the blood flow distribution in the footpad of a living mouse (Shi et al., 2017). Zhao et al. utilized another reagent containing

collagenase, EDTA disodium and glycerol to image the mouse cortex through transparent skull *in vivo* (Zhao et al., 2018). Although these technical approaches are not sufficient to render an entire living mouse optically transparent, they already helped to achieve non-invasive *in vivo* deep tissue imaging for specific studies. Taken together, combining genetic, physical and chemical approaches will provide the possibility to achieve biocompatible whole-body tissue clearing for longitudinal studies.

In conclusion, as presented above, we developed uDISCO and vDISCO whole-body tissue clearing methods which brings the systems biology studies to the next level. Applying these techniques, we identified novel anatomic structures between skull bone marrow and brain meninges and analyzed the bio-distribution of stem cells, cancer metastasis and therapeutic antibody through the entire mouse bodies. As practical and time efficient methodologies, uDISCO and vDISCO will facilitate studies in various biological and biomedical research fields. Technical revolutions from other fields including the development of large scale high resolution light-sheet microscope, solutions for large data storage and computer cluster operation, as well as AI or deep learning based automated algorithm will further boost the applications of u/vDISCO whole-body tissue clearing in the future.

4. References

Alvarez, R.H. (2010). Present and future evolution of advanced breast cancer therapy. Breast cancer research : BCR *12 Suppl 2*, S1.

Amulic, B., Cazalet, C., Hayes, G.L., Metzler, K.D., and Zychlinsky, A. (2012). Neutrophil function: from mechanisms to disease. Annual review of immunology *30*, 459-489.

Antinucci, P., and Hindges, R. (2016). A crystal-clear zebrafish for in vivo imaging. Scientific reports *6*, 29490.

Barbash, I.M., Chouraqui, P., Baron, J., Feinberg, M.S., Etzion, S., Tessone, A., Miller, L., Guetta, E., Zipori, D., Kedes, L.H*., et al.* (2003). Systemic delivery of bone marrow-derived mesenchymal stem cells to the infarcted myocardium: feasibility, cell migration, and body distribution. Circulation *108*, 863-868.

Barbosa, J.S., Di Giaimo, R., Gotz, M., and Ninkovic, J. (2016). Single-cell in vivo imaging of adult neural stem cells in the zebrafish telencephalon. Nature protocols *11*, 1360-1370.

Baselga, J., Norton, L., Albanell, J., Kim, Y.M., and Mendelsohn, J. (1998). Recombinant humanized anti-HER2 antibody (Herceptin) enhances the antitumor activity of paclitaxel and doxorubicin against HER2/neu overexpressing human breast cancer xenografts. Cancer research *58*, 2825-2831.

Becker, K., Jahrling, N., Saghafi, S., Weiler, R., and Dodt, H.U. (2012). Chemical clearing and dehydration of GFP expressing mouse brains. PloS one *7*, e33916.

Belle, M., Godefroy, D., Couly, G., Malone, S.A., Collier, F., Giacobini, P., and Chedotal, A. (2017). Tridimensional Visualization and Analysis of Early Human Development. Cell *169*, 161-173 e112.

Benakis, C., Llovera, G., and Liesz, A. (2018). The meningeal and choroidal infiltration routes for leukocytes in stroke. Therapeutic advances in neurological disorders *11*, 1756286418783708.

Bennett, M.L., Bennett, F.C., Liddelow, S.A., Ajami, B., Zamanian, J.L., Fernhoff, N.B., Mulinyawe, S.B., Bohlen, C.J., Adil, A., Tucker, A*., et al.* (2016). New tools for studying microglia in the mouse and human CNS. Proceedings of the National Academy of Sciences of the United States of America *113*, E1738-1746.

Brancato, S.K., and Albina, J.E. (2011). Wound macrophages as key regulators of repair: origin, phenotype, and function. The American journal of pathology *178*, 19-25.

Bray, F., Ferlay, J., Soerjomataram, I., Siegel, R.L., Torre, L.A., and Jemal, A. (2018). Global cancer statistics 2018: GLOBOCAN estimates of incidence and mortality worldwide for 36 cancers in 185 countries. CA: a cancer journal for clinicians *68*, 394-424.

Cai, R., Pan, C., Ghasemigharagoz, A., Todorov, M.I., Forstera, B., Zhao, S., Bhatia, H.S., Parra-Damas, A., Mrowka, L., Theodorou, D*., et al.* (2019). Panoptic imaging of transparent mice reveals whole-body neuronal projections and skull-meninges connections. Nature neuroscience *22*, 317-327.

Carmeliet, P., and Jain, R.K. (2000). Angiogenesis in cancer and other diseases. Nature *407*, 249-257.

Chen, F., Wassie, A.T., Cote, A.J., Sinha, A., Alon, S., Asano, S., Daugharthy, E.R., Chang, J.B., Marblestone, A., Church, G.M*., et al.* (2016). Nanoscale imaging of RNA with expansion microscopy. Nature methods *13*, 679-684.

Chiu, I.M., Phatnani, H., Kuligowski, M., Tapia, J.C., Carrasco, M.A., Zhang, M., Maniatis, T., and Carroll, M.C. (2009). Activation of innate and humoral immunity in the peripheral nervous system of ALS transgenic mice. Proceedings of the National Academy of Sciences of the United States of America *106*, 20960-20965.

Chu, J., Haynes, R.D., Corbel, S.Y., Li, P., Gonzalez-Gonzalez, E., Burg, J.S., Ataie, N.J., Lam, A.J., Cranfill, P.J., Baird, M.A*., et al.* (2014). Non-invasive intravital imaging of cellular differentiation with a bright red-excitable fluorescent protein. Nature methods *11*, 572-578.

Chung, K., and Deisseroth, K. (2013). CLARITY for mapping the nervous system. Nature methods *10*, 508-513.

Chung, K., Wallace, J., Kim, S.Y., Kalyanasundaram, S., Andalman, A.S., Davidson, T.J., Mirzabekov, J.J., Zalocusky, K.A., Mattis, J., Denisin, A.K*., et al.* (2013). Structural and molecular interrogation of intact biological systems. Nature *497*, 332-337.

Clendenon, S.G., Young, P.A., Ferkowicz, M., Phillips, C., and Dunn, K.W. (2011). Deep tissue fluorescent imaging in scattering specimens using confocal microscopy. Microscopy and microanalysis : the official journal of Microscopy Society of America, Microbeam Analysis Society, Microscopical Society of Canada *17*, 614-617.
Cooper, B. (2001). Nature, nurture and mental disorder: old concepts in the new millennium. British Journal of Psychiatry *178*, s91-s101.
D'Souza, N., Rossignoli, F., Golinelli, G., Grisendi, G., Spano, C., Candini, O., Osturu, S., Catani, F., Paolucci, P., Horwitz, E.M.*, et al.* (2015). Mesenchymal stem/stromal cells as a delivery platform in cell and gene therapies. BMC medicine *13*, 186.
Da Mesquita, S., Louveau, A., Vaccari, A., Smirnov, I., Cornelison, R.C., Kingsmore, K.M., Contarino, C., Onengut-Gumuscu, S., Farber, E., Raper, D.*, et al.* (2018). Functional aspects of meningeal lymphatics in ageing and Alzheimer's disease. Nature *560*, 185-191.
Dall'Ara, E., Boudiffa, M., Taylor, C., Schug, D., Fiegle, E., Kennerley, A.J., Damianou, C., Tozer, G.M., Kiessling, F., and Muller, R. (2016). Longitudinal imaging of the ageing mouse. Mechanisms of ageing and development *160*, 93-116.
Derecki, N.C., Cardani, A.N., Yang, C.H., Quinnies, K.M., Crihfield, A., Lynch, K.R., and Kipnis, J. (2010). Regulation of learning and memory by meningeal immunity: a key role for IL-4. The Journal of experimental medicine *207*, 1067-1080.
Deverman, B.E., Pravdo, P.L., Simpson, B.P., Kumar, S.R., Chan, K.Y., Banerjee, A., Wu, W.L., Yang, B., Huber, N., Pasca, S.P.*, et al.* (2016). Cre-dependent selection yields AAV variants for widespread gene transfer to the adult brain. Nature biotechnology *34*, 204-209.
Diab, M., ZazaDitYafawi, J., and Soubani, A.O. (2016). Major Pulmonary Complications After Hematopoietic Stem Cell Transplant. Experimental and clinical transplantation : official journal of the Middle East Society for Organ Transplantation *14*, 259-270.
Dodt, H.U., Leischner, U., Schierloh, A., Jahrling, N., Mauch, C.P., Deininger, K., Deussing, J.M., Eder, M., Zieglgansberger, W., and Becker, K. (2007). Ultramicroscopy: three-dimensional visualization of neuronal networks in the whole mouse brain. Nature methods *4*, 331-336.
Ehteshami Bejnordi, B., Veta, M., Johannes van Diest, P., van Ginneken, B., Karssemeijer, N., Litjens, G., van der Laak, J.A.W.M., and Consortium, a.t.C. (2017). Diagnostic Assessment of Deep Learning Algorithms for Detection of Lymph Node Metastases in Women With Breast CancerMachine Learning Detection of Breast Cancer Lymph Node MetastasesMachine Learning Detection of Breast Cancer Lymph Node Metastases. JAMA *318*, 2199-2210.
Ekdahl, C.T., Claasen, J.H., Bonde, S., Kokaia, Z., and Lindvall, O. (2003). Inflammation is detrimental for neurogenesis in adult brain. Proceedings of the National Academy of Sciences of the United States of America *100*, 13632-13637.
Erturk, A., Becker, K., Jahrling, N., Mauch, C.P., Hojer, C.D., Egen, J.G., Hellal, F., Bradke, F., Sheng, M., and Dodt, H.U. (2012). Three-dimensional imaging of solvent-cleared organs using 3DISCO. Nature protocols *7*, 1983-1995.
Erturk, A., and Bradke, F. (2013). High-resolution imaging of entire organs by 3-dimensional imaging of solvent cleared organs (3DISCO). Experimental neurology *242*, 57-64.
Erturk, A., Mauch, C.P., Hellal, F., Forstner, F., Keck, T., Becker, K., Jahrling, N., Steffens, H., Richter, M., Hubener, M.*, et al.* (2011). Three-dimensional imaging of the unsectioned adult spinal cord to assess axon regeneration and glial responses after injury. Nature medicine *18*, 166-171.
Finsen, B., and Owens, T. (2011). Innate immune responses in central nervous system inflammation. FEBS letters *585*, 3806-3812.
Gadani, S.P., Walsh, J.T., Lukens, J.R., and Kipnis, J. (2015). Dealing with Danger in the CNS: The Response of the Immune System to Injury. Neuron *87*, 47-62.
Gao, R., Asano, S.M., Upadhyayula, S., Pisarev, I., Milkie, D.E., Liu, T.L., Singh, V., Graves, A., Huynh, G.H., Zhao, Y.*, et al.* (2019). Cortical column and whole-brain imaging with molecular contrast and nanoscale resolution. Science *363*.

Gondi, G., Mysliwietz, J., Hulikova, A., Jen, J.P., Swietach, P., Kremmer, E., and Zeidler, R. (2013). Antitumor efficacy of a monoclonal antibody that inhibits the activity of cancer-associated carbonic anhydrase XII. Cancer research *73*, 6494-6503.
Gorio, A., Madaschi, L., Zadra, G., Marfia, G., Cavalieri, B., Bertini, R., and Di Giulio, A.M. (2007). Reparixin, an inhibitor of CXCR2 function, attenuates inflammatory responses and promotes recovery of function after traumatic lesion to the spinal cord. The Journal of pharmacology and experimental therapeutics *322*, 973-981.
Greenbaum, A., Chan, K.Y., Dobreva, T., Brown, D., Balani, D.H., Boyce, R., Kronenberg, H.M., McBride, H.J., and Gradinaru, V. (2017). Bone CLARITY: Clearing, imaging, and computational analysis of osteoprogenitors within intact bone marrow. Science translational medicine *9*.
Grüneboom, A., Hawwari, I., Weidner, D., Culemann, S., Müller, S., Henneberg, S., Brenzel, A., Merz, S., Bornemann, L., Zec, K.*, et al.* (2019). A network of trans-cortical capillaries as mainstay for blood circulation in long bones. Nature Metabolism *1*, 236-250.
Gu, W., Zhang, F., Xue, Q., Ma, Z., Lu, P., and Yu, B. (2010). Transplantation of bone marrow mesenchymal stem cells reduces lesion volume and induces axonal regrowth of injured spinal cord. Neuropathology : official journal of the Japanese Society of Neuropathology *30*, 205-217.
Habgood, M.D., Bye, N., Dziegielewska, K.M., Ek, C.J., Lane, M.A., Potter, A., Morganti-Kossmann, C., and Saunders, N.R. (2007). Changes in blood-brain barrier permeability to large and small molecules following traumatic brain injury in mice. The European journal of neuroscience *25*, 231-238.
Hama, H., Hioki, H., Namiki, K., Hoshida, T., Kurokawa, H., Ishidate, F., Kaneko, T., Akagi, T., Saito, T., Saido, T.*, et al.* (2015). ScaleS: an optical clearing palette for biological imaging. Nature neuroscience *18*, 1518-1529.
Hama, H., Kurokawa, H., Kawano, H., Ando, R., Shimogori, T., Noda, H., Fukami, K., Sakaue-Sawano, A., and Miyawaki, A. (2011). Scale: a chemical approach for fluorescence imaging and reconstruction of transparent mouse brain. Nature neuroscience *14*, 1481-1488.
Herisson, F., Frodermann, V., Courties, G., Rohde, D., Sun, Y., Vandoorne, K., Wojtkiewicz, G.R., Masson, G.S., Vinegoni, C., Kim, J.*, et al.* (2018). Direct vascular channels connect skull bone marrow and the brain surface enabling myeloid cell migration. Nature neuroscience *21*, 1209-1217.
Hillen, F., and Griffioen, A.W. (2007). Tumour vascularization: sprouting angiogenesis and beyond. Cancer metastasis reviews *26*, 489-502.
Hong, G., Antaris, A.L., and Dai, H. (2017). Near-infrared fluorophores for biomedical imaging. Nature Biomedical Engineering *1*, 0010.
Hou, B., Zhang, D., Zhao, S., Wei, M., Yang, Z., Wang, S., Wang, J., Zhang, X., Liu, B., Fan, L.*, et al.* (2015). Scalable and DiI-compatible optical clearance of the mammalian brain. Frontiers in neuroanatomy *9*, 19.
Howlader N, N.A., Krapcho M, Miller D, Bishop K, Kosary CL, Yu M, Ruhl J, Tatalovich Z, Mariotto A, Lewis DR, Chen HS, Feuer EJ, Cronin KA (eds) (2017). SEER Cancer Statistics Review, 1975-2014. https://seercancergov/csr/1975_2014/ *based on November 2016 SEER data submission, posted to the SEER web site, April 2017.*
Hunter, K.W., Crawford, N.P., and Alsarraj, J. (2008). Mechanisms of metastasis. Breast cancer research : BCR *10 Suppl 1*, S2.
Jain, R.K. (2012). Delivery of molecular and cellular medicine to solid tumors. Advanced drug delivery reviews *64*, 353-365.
Jin, L., Han, B., Siegel, E., Cui, Y., Giuliano, A., and Cui, X. (2018). Breast cancer lung metastasis: Molecular biology and therapeutic implications. Cancer biology & therapy *19*, 858-868.
Jing, D., Zhang, S., Luo, W., Gao, X., Men, Y., Ma, C., Liu, X., Yi, Y., Bugde, A., Zhou, B.O.*, et al.* (2018). Tissue clearing of both hard and soft tissue organs with the PEGASOS method. Cell research *28*, 803-818.
Johnsen, S. (2001). Hidden in plain sight: the ecology and physiology of organismal transparency. The Biological bulletin *201*, 301-318.

Jordao, M.J.C., Sankowski, R., Brendecke, S.M., Sagar, Locatelli, G., Tai, Y.H., Tay, T.L., Schramm, E., Armbruster, S., Hagemeyer, N.*, et al.* (2019). Single-cell profiling identifies myeloid cell subsets with distinct fates during neuroinflammation. Science *363*.
Kawada, H., Fujita, J., Kinjo, K., Matsuzaki, Y., Tsuma, M., Miyatake, H., Muguruma, Y., Tsuboi, K., Itabashi, Y., Ikeda, Y.*, et al.* (2004). Nonhematopoietic mesenchymal stem cells can be mobilized and differentiate into cardiomyocytes after myocardial infarction. Blood *104*, 3581-3587.
Ke, M.T., Fujimoto, S., and Imai, T. (2013). SeeDB: a simple and morphology-preserving optical clearing agent for neuronal circuit reconstruction. Nature neuroscience *16*, 1154-1161.
Kerkela, E., Hakkarainen, T., Makela, T., Raki, M., Kambur, O., Kilpinen, L., Nikkila, J., Lehtonen, S., Ritamo, I., Pernu, R.*, et al.* (2013). Transient proteolytic modification of mesenchymal stromal cells increases lung clearance rate and targeting to injured tissue. Stem cells translational medicine *2*, 510-520.
Kitano, H. (2002). Systems biology: a brief overview. Science *295*, 1662-1664.
Koc, O.N., Gerson, S.L., Cooper, B.W., Dyhouse, S.M., Haynesworth, S.E., Caplan, A.I., and Lazarus, H.M. (2000). Rapid hematopoietic recovery after coinfusion of autologous-blood stem cells and culture-expanded marrow mesenchymal stem cells in advanced breast cancer patients receiving high-dose chemotherapy. Journal of clinical oncology : official journal of the American Society of Clinical Oncology *18*, 307-316.
Koh, T.J., and DiPietro, L.A. (2011). Inflammation and wound healing: the role of the macrophage. Expert reviews in molecular medicine *13*, e23.
Ku, T., Swaney, J., Park, J.Y., Albanese, A., Murray, E., Cho, J.H., Park, Y.G., Mangena, V., Chen, J., and Chung, K. (2016). Multiplexed and scalable super-resolution imaging of three-dimensional protein localization in size-adjustable tissues. Nature biotechnology *34*, 973-981.
Kubota, S.I., Takahashi, K., Nishida, J., Morishita, Y., Ehata, S., Tainaka, K., Miyazono, K., and Ueda, H.R. (2017). Whole-Body Profiling of Cancer Metastasis with Single-Cell Resolution. Cell reports *20*, 236-250.
Kyritsis, N., Kizil, C., and Brand, M. (2014). Neuroinflammation and central nervous system regeneration in vertebrates. Trends in cell biology *24*, 128-135.
Lambert, A.W., Pattabiraman, D.R., and Weinberg, R.A. (2017). Emerging Biological Principles of Metastasis. Cell *168*, 670-691.
Langlois, J.A., Rutland-Brown, W., and Wald, M.M. (2006). The epidemiology and impact of traumatic brain injury: a brief overview. The Journal of head trauma rehabilitation *21*, 375-378.
Lee, E., Choi, J., Jo, Y., Kim, J.Y., Jang, Y.J., Lee, H.M., Kim, S.Y., Lee, H.J., Cho, K., Jung, N.*, et al.* (2016). ACT-PRESTO: Rapid and consistent tissue clearing and labeling method for 3-dimensional (3D) imaging. Scientific reports *6*, 18631.
Lee, J.W., Stone, M.L., Porrett, P.M., Thomas, S.K., Komar, C.A., Li, J.H., Delman, D., Graham, K., Gladney, W.L., Hua, X.*, et al.* (2019). Hepatocytes direct the formation of a pro-metastatic niche in the liver. Nature.
Leibacher, J., and Henschler, R. (2016). Biodistribution, migration and homing of systemically applied mesenchymal stem/stromal cells. Stem cell research & therapy *7*, 7.
Li, Y., Xu, J., Wan, P., Yu, T., and Zhu, D. (2018). Optimization of GFP Fluorescence Preservation by a Modified uDISCO Clearing Protocol. Frontiers in neuroanatomy *12*, 67.
Liebmann, T., Renier, N., Bettayeb, K., Greengard, P., Tessier-Lavigne, M., and Flajolet, M. (2016). Three-Dimensional Study of Alzheimer's Disease Hallmarks Using the iDISCO Clearing Method. Cell reports *16*, 1138-1152.
Lin, Y.T., Chern, Y., Shen, C.K., Wen, H.L., Chang, Y.C., Li, H., Cheng, T.H., and Hsieh-Li, H.M. (2011). Human mesenchymal stem cells prolong survival and ameliorate motor deficit through trophic support in Huntington's disease mouse models. PloS one *6*, e22924.
Litjens, G., Sanchez, C.I., Timofeeva, N., Hermsen, M., Nagtegaal, I., Kovacs, I., Hulsbergen-van de Kaa, C., Bult, P., van Ginneken, B., and van der Laak, J. (2016). Deep learning as a tool for increased accuracy and efficiency of histopathological diagnosis. Scientific reports *6*, 26286.

Llovera, G., Benakis, C., Enzmann, G., Cai, R., Arzberger, T., Ghasemigharagoz, A., Mao, X., Malik, R., Lazarevic, I., Liebscher, S.*, et al.* (2017). The choroid plexus is a key cerebral invasion route for T cells after stroke. Acta neuropathologica *134*, 851-868.
Louveau, A., Herz, J., Alme, M.N., Salvador, A.F., Dong, M.Q., Viar, K.E., Herod, S.G., Knopp, J., Setliff, J.C., Lupi, A.L.*, et al.* (2018). CNS lymphatic drainage and neuroinflammation are regulated by meningeal lymphatic vasculature. Nature neuroscience *21*, 1380-1391.
Louveau, A., Smirnov, I., Keyes, T.J., Eccles, J.D., Rouhani, S.J., Peske, J.D., Derecki, N.C., Castle, D., Mandell, J.W., Lee, K.S.*, et al.* (2015). Structural and functional features of central nervous system lymphatic vessels. Nature *523*, 337-341.
McCoy, M.K., Martinez, T.N., Ruhn, K.A., Wrage, P.C., Keefer, E.W., Botterman, B.R., Tansey, K.E., and Tansey, M.G. (2008). Autologous transplants of Adipose-Derived Adult Stromal (ADAS) cells afford dopaminergic neuroprotection in a model of Parkinson's disease. Experimental neurology *210*, 14-29.
McDonald, D.M., and Baluk, P. (2002). Significance of blood vessel leakiness in cancer. Cancer research *62*, 5381-5385.
Mendis, S. (2013). Stroke disability and rehabilitation of stroke: World Health Organization perspective. International journal of stroke : official journal of the International Stroke Society *8*, 3-4.
Monje, M.L., Toda, H., and Palmer, T.D. (2003). Inflammatory blockade restores adult hippocampal neurogenesis. Science *302*, 1760-1765.
Muldoon, L.L., Alvarez, J.I., Begley, D.J., Boado, R.J., Del Zoppo, G.J., Doolittle, N.D., Engelhardt, B., Hallenbeck, J.M., Lonser, R.R., Ohlfest, J.R.*, et al.* (2013). Immunologic privilege in the central nervous system and the blood-brain barrier. Journal of cerebral blood flow and metabolism : official journal of the International Society of Cerebral Blood Flow and Metabolism *33*, 13-21.
Muyldermans, S. (2013). Nanobodies: natural single-domain antibodies. Annual review of biochemistry *82*, 775-797.
Nathan, M.R., and Schmid, P. (2018). The emerging world of breast cancer immunotherapy. Breast *37*, 200-206.
Nicolini, A., Giardino, R., Carpi, A., Ferrari, P., Anselmi, L., Colosimo, S., Conte, M., Fini, M., Giavaresi, G., Berti, P.*, et al.* (2006). Metastatic breast cancer: an updating. Biomedicine & pharmacotherapy = Biomedecine & pharmacotherapie *60*, 548-556.
Odoardi, F., Sie, C., Streyl, K., Ulaganathan, V.K., Schlager, C., Lodygin, D., Heckelsmiller, K., Nietfeld, W., Ellwart, J., Klinkert, W.E.*, et al.* (2012). T cells become licensed in the lung to enter the central nervous system. Nature *488*, 675-679.
Pan, C., Cai, R., Quacquarelli, F.P., Ghasemigharagoz, A., Lourbopoulos, A., Matryba, P., Plesnila, N., Dichgans, M., Hellal, F., and Erturk, A. (2016). Shrinkage-mediated imaging of entire organs and organisms using uDISCO. Nature methods *13*, 859-867.
Pan, C., Schoppe, O., Parra-Damas, A., Cai, R., Todorov, M.I., Gondi, G., von Neubeck, B., Ghasemi, A., Reimer, M.A., Coronel, J.*, et al.* (2019). Deep learning reveals cancer metastasis and therapeutic antibody targeting in whole body. bioRxiv, 541862.
Parekkadan, B., and Milwid, J.M. (2010). Mesenchymal stem cells as therapeutics. Annual review of biomedical engineering *12*, 87-117.
Park, Y.G., Sohn, C.H., Chen, R., McCue, M., Yun, D.H., Drummond, G.T., Ku, T., Evans, N.B., Oak, H.C., Trieu, W.*, et al.* (2018). Protection of tissue physicochemical properties using polyfunctional crosslinkers. Nature biotechnology.
Perbal, L. (2015). The case of the gene: Postgenomics between modernity and postmodernity. EMBO reports *16*, 777-781.
Piatkevich, K.D., Suk, H.J., Kodandaramaiah, S.B., Yoshida, F., DeGennaro, E.M., Drobizhev, M., Hughes, T.E., Desimone, R., Boyden, E.S., and Verkhusha, V.V. (2017). Near-Infrared Fluorescent Proteins Engineered from Bacterial Phytochromes in Neuroimaging. Biophysical journal *113*, 2299-2309.
Poliakov, E., Cooper, D.N., Stepchenkova, E.I., and Rogozin, I.B. (2015). Genetics in genomic era. Genetics research international *2015*, 364960.

Qi, Y., Yu, T., Xu, J., Wan, P., Ma, Y., Zhu, J., Li, Y., Gong, H., Luo, Q., and Zhu, D. (2019). FDISCO: Advanced solvent-based clearing method for imaging whole organs. Science advances *5*, eaau8355.
Redig, A.J., and McAllister, S.S. (2013). Breast cancer as a systemic disease: a view of metastasis. Journal of internal medicine *274*, 113-126.
Reinhardt, R.L., Khoruts, A., Merica, R., Zell, T., and Jenkins, M.K. (2001). Visualizing the generation of memory CD4 T cells in the whole body. Nature *410*, 101-105.
Renier, N., Adams, E.L., Kirst, C., Wu, Z., Azevedo, R., Kohl, J., Autry, A.E., Kadiri, L., Umadevi Venkataraju, K., Zhou, Y.*, et al.* (2016). Mapping of Brain Activity by Automated Volume Analysis of Immediate Early Genes. Cell *165*, 1789-1802.
Renier, N., Wu, Z., Simon, D.J., Yang, J., Ariel, P., and Tessier-Lavigne, M. (2014). iDISCO: a simple, rapid method to immunolabel large tissue samples for volume imaging. Cell *159*, 896-910.
Richardson, D.S., and Lichtman, J.W. (2015). Clarifying Tissue Clearing. Cell *162*, 246-257.
Russo, M.V., and McGavern, D.B. (2015). Immune Surveillance of the CNS following Infection and Injury. Trends in immunology *36*, 637-650.
SanjayTanday (2016). Cancer overtakes heart disease as biggest killer in 12 countries. Lancet Oncology *17*, e382.
Schoder, H., and Gonen, M. (2007). Screening for cancer with PET and PET/CT: potential and limitations. Journal of nuclear medicine : official publication, Society of Nuclear Medicine *48 Suppl 1*, 4S-18S.
Schwarz, M.K., Scherbarth, A., Sprengel, R., Engelhardt, J., Theer, P., and Giese, G. (2015). Fluorescent-protein stabilization and high-resolution imaging of cleared, intact mouse brains. PloS one *10*, e0124650.
Scully, O.J., Bay, B.H., Yip, G., and Yu, Y. (2012). Breast cancer metastasis. Cancer genomics & proteomics *9*, 311-320.
Semple, B.D., Bye, N., Ziebell, J.M., and Morganti-Kossmann, M.C. (2010). Deficiency of the chemokine receptor CXCR2 attenuates neutrophil infiltration and cortical damage following closed head injury. Neurobiology of disease *40*, 394-403.
Shi, R., Feng, W., Zhang, C., Zhang, Z., and Zhu, D. (2017). FSOCA-induced switchable footpad skin optical clearing window for blood flow and cell imaging in vivo. Journal of biophotonics *10*, 1647-1656.
Susaki, E.A., Tainaka, K., Perrin, D., Kishino, F., Tawara, T., Watanabe, T.M., Yokoyama, C., Onoe, H., Eguchi, M., Yamaguchi, S.*, et al.* (2014). Whole-brain imaging with single-cell resolution using chemical cocktails and computational analysis. Cell *157*, 726-739.
Susaki, E.A., and Ueda, H.R. (2016). Whole-body and Whole-Organ Clearing and Imaging Techniques with Single-Cell Resolution: Toward Organism-Level Systems Biology in Mammals. Cell chemical biology *23*, 137-157.
Tabrizi, M., Bornstein, G.G., and Suria, H. (2010). Biodistribution mechanisms of therapeutic monoclonal antibodies in health and disease. The AAPS journal *12*, 33-43.
Tainaka, K., Kubota, S.I., Suyama, T.Q., Susaki, E.A., Perrin, D., Ukai-Tadenuma, M., Ukai, H., and Ueda, H.R. (2014). Whole-body imaging with single-cell resolution by tissue decolorization. Cell *159*, 911-924.
Tainaka, K., Kuno, A., Kubota, S.I., Murakami, T., and Ueda, H.R. (2016). Chemical Principles in Tissue Clearing and Staining Protocols for Whole-Body Cell Profiling. Annual review of cell and developmental biology *32*, 713-741.
Tanaka, N., Kanatani, S., Tomer, R., Sahlgren, C., Kronqvist, P., Kaczynska, D., Louhivuori, L., Kis, L., Lindh, C., Mitura, P.*, et al.* (2017). Whole-tissue biopsy phenotyping of three-dimensional tumours reveals patterns of cancer heterogeneity. Nature Biomedical Engineering *1*, 796-806.
Theer, P., and Denk, W. (2006). On the fundamental imaging-depth limit in two-photon microscopy. Journal of the Optical Society of America A, Optics, image science, and vision *23*, 3139-3149.
Tomer, R., Ye, L., Hsueh, B., and Deisseroth, K. (2014). Advanced CLARITY for rapid and high-resolution imaging of intact tissues. Nature protocols *9*, 1682-1697.

Treweek, J.B., Chan, K.Y., Flytzanis, N.C., Yang, B., Deverman, B.E., Greenbaum, A., Lignell, A., Xiao, C., Cai, L., Ladinsky, M.S*., et al.* (2015). Whole-body tissue stabilization and selective extractions via tissue-hydrogel hybrids for high-resolution intact circuit mapping and phenotyping. Nature protocols *10*, 1860-1896.
Trivedi, A., Olivas, A.D., and Noble-Haeusslein, L.J. (2006). Inflammation and Spinal Cord Injury: Infiltrating Leukocytes as Determinants of Injury and Repair Processes. Clinical neuroscience research *6*, 283-292.
Tuchin, V.V. (2015). Tissue Optics and Photonics: Light-Tissue Interaction. 2015 *1*, 37.
van de Stolpe, A., Pantel, K., Sleijfer, S., Terstappen, L.W., and den Toonder, J.M. (2011). Circulating tumor cell isolation and diagnostics: toward routine clinical use. Cancer research *71*, 5955-5960.
Venkatachalam, V., Ji, N., Wang, X., Clark, C., Mitchell, J.K., Klein, M., Tabone, C.J., Florman, J., Ji, H., Greenwood, J*., et al.* (2016). Pan-neuronal imaging in roaming Caenorhabditis elegans. Proceedings of the National Academy of Sciences of the United States of America *113*, E1082-1088.
Vercelli, A., Mereuta, O.M., Garbossa, D., Muraca, G., Mareschi, K., Rustichelli, D., Ferrero, I., Mazzini, L., Madon, E., and Fagioli, F. (2008). Human mesenchymal stem cell transplantation extends survival, improves motor performance and decreases neuroinflammation in mouse model of amyotrophic lateral sclerosis. Neurobiology of disease *31*, 395-405.
Vick, B., Rothenberg, M., Sandhofer, N., Carlet, M., Finkenzeller, C., Krupka, C., Grunert, M., Trumpp, A., Corbacioglu, S., Ebinger, M*., et al.* (2015). An advanced preclinical mouse model for acute myeloid leukemia using patients' cells of various genetic subgroups and in vivo bioluminescence imaging. PloS one *10*, e0120925.
von Neubeck, B., Gondi, G., Riganti, C., Pan, C., Parra Damas, A., Scherb, H., Erturk, A., and Zeidler, R. (2018). An inhibitory antibody targeting Carbonic Anhydrase XII abrogates chemoresistance and significantly reduces lung metastases in an orthotopic breast cancer model in vivo. International journal of cancer.
Wan, P., Zhu, J., Xu, J., Li, Y., Yu, T., and Zhu, D. (2018). Evaluation of seven optical clearing methods in mouse brain. Neurophotonics *5*, 035007.
Wang, X., Cao, K., Sun, X., Chen, Y., Duan, Z., Sun, L., Guo, L., Bai, P., Sun, D., Fan, J*., et al.* (2015). Macrophages in spinal cord injury: phenotypic and functional change from exposure to myelin debris. Glia *63*, 635-651.
Wu, Y., Sarkissyan, M., and Vadgama, J.V. (2016). Epithelial-Mesenchymal Transition and Breast Cancer. Journal of clinical medicine *5*.
Yang, B., Treweek, J.B., Kulkarni, R.P., Deverman, B.E., Chen, C.K., Lubeck, E., Shah, S., Cai, L., and Gradinaru, V. (2014). Single-cell phenotyping within transparent intact tissue through whole-body clearing. Cell *158*, 945-958.
Yang, C.C., Shih, Y.H., Ko, M.H., Hsu, S.Y., Cheng, H., and Fu, Y.S. (2008). Transplantation of human umbilical mesenchymal stem cells from Wharton's jelly after complete transection of the rat spinal cord. PloS one *3*, e3336.
Yu, K.-H., Beam, A.L., and Kohane, I.S. (2018). Artificial intelligence in healthcare. Nature Biomedical Engineering *2*, 719-731.
Zhang, Z.G., and Chopp, M. (2009). Neurorestorative therapies for stroke: underlying mechanisms and translation to the clinic. The Lancet Neurology *8*, 491-500.
Zhao, Y., Bucur, O., Irshad, H., Chen, F., Weins, A., Stancu, A.L., Oh, E.Y., DiStasio, M., Torous, V., Glass, B*., et al.* (2017). Nanoscale imaging of clinical specimens using pathology-optimized expansion microscopy. Nature biotechnology *35*, 757-764.
Zhao, Y.J., Yu, T.T., Zhang, C., Li, Z., Luo, Q.M., Xu, T.H., and Zhu, D. (2018). Skull optical clearing window for in vivo imaging of the mouse cortex at synaptic resolution. Light, science & applications *7*, 17153.
Zhu, D., Larin, K.V., Luo, Q., and Tuchin, V.V. (2013). Recent progress in tissue optical clearing. Laser & photonics reviews *7*, 732-757.

Ziv, Y., Ron, N., Butovsky, O., Landa, G., Sudai, E., Greenberg, N., Cohen, H., Kipnis, J., and Schwartz, M. (2006). Immune cells contribute to the maintenance of neurogenesis and spatial learning abilities in adulthood. Nature neuroscience *9*, 268-275.

5. Acknowledgements

To be honest, I am super happy that I just covered a long journey and coming to the end of my PhD study. Writing this last section of my thesis reminds me tons of beautiful memories. However, this would not happen if Dr. Ali Ertürk did not offer me an opportunity to work in his lab. As my supervisor, Ali guided me into the tissue clearing world and opened the gate of my scientific career. He not only shared with me his brilliant insights of biological studies but also supported me a lot of opportunities to learn and to cooperate with leading edge scientists throughout the whole world. With this thesis, I would like to bring my sincere thanks to Ali.

I am now sitting in my lovely apartment with warm coffee but I will never forget the first winter in Munich when Ruiyao (Marika) Cai walked with me in snow carrying the perfused mouse samples. We started our lab from there and we published two papers as shared co-first authors after four years of hard work. She is not only an intelligent colleague but also a nice friend. My sincere thanks to Marika. I would also like to thank current and previous lab members, Shan Zhao, Mihail Todorov, Francesca Paola Quacquarelli, Arnaldo Parra Damas, Oliver Schoppe, Benjamin Förstera, Harsharan S. Bhatia, Madita Reimer, Marin Bralo, Chongyue Zhao, Ana Toman, Muege Molbay, Ilgin Kolabas, Doris Kaltenecker, Zhouyi Rong, Hongcheng Mai, Alireza Ghasemi, Lamiaa Bahnassawy, Susanne Mentz, Lina Paulenz and Jasmin Sirin Gezgin for their constant help and support.

I am very thankful to my thesis advisory committee members, Prof. Dr. Martin Kerschensteiner, Dr. Alessio Attardo and Dr. Farida Hellal. They are not only supervisors giving me advices about my experiments and career, but also the contributing collaborators deeply involved in the projects. I really appreciate the fruitful discussion and critical comments during the TAC meetings.

I would further thank our cooperation partners, Prof. Dr. Martin Dichgans, Prof. Dr. Reinhard Zeidler, Prof. Dr. Bjoern Menze, Prof. Dr. Maiken Nedergaard, Prof. Dr. Nikolaus Plesnila, Dr. Benedikt Wefers, Dr. Arthur Liesz, Dr. Boyan K. Garvalov, Gabor Gondi, Bettina von Neubeck, Athanasios Lourbopoulos, Corinne Benakis, Anna L. R. Xavier and Delphine Theodorou for their solid input and technical support.

I thank my parents. We talk on phone every weekend and they walk me through the period with frustration or happiness, with achievements or failure…. They are, and will always be, my backbone.

Last but not least, thanks to Graduate School of Systemic Neurosciences for providing a creative community for students. Special thanks to Julia Brenndörfer, Stefanie Bosse, Maj-Catherine Botheroyd-Hobohm, Birgit Reinbold, Nadine Hamze and Lena Bittl for both academic and financial support.

Finally, many thanks to you all that I experienced a wonderful and precious time during my PhD study!

6. List of publications

2016

Pan, C.*, Cai, R.*, Quacquarelli, F.P.*, Ghasemigharagoz, A., Lourbopoulos, A., Matryba, P., Plesnila, N., Dichgans, M., Hellal, F., and Erturk, A. (2016). Shrinkage-mediated imaging of entire organs and organisms using uDISCO. Nature methods 13, 859-867. * These authors contributed equally. (*IF 2016: 25.062*)

2018

von Neubeck, B., Gondi, G., Riganti, C., **Pan, C.**, Parra Damas, A., Scherb, H., Erturk, A., and Zeidler, R. (2018). An inhibitory antibody targeting Carbonic Anhydrase XII abrogates chemoresistance and significantly reduces lung metastases in an orthotopic breast cancer model in vivo. International journal of cancer. (*IF 2018: 7.360*)

2019

Cai, R.*, **Pan, C.***, Ghasemigharagoz, A., Todorov, M.I., Forstera, B., Zhao, S., Bhatia, H.S., Parra-Damas, A., Mrowka, L., Theodorou, D., et al. (2019). Panoptic imaging of transparent mice reveals whole-body neuronal projections and skull-meninges connections. Nature neuroscience 22, 317-327. * These authors contributed equally. (*IF 2018: 19.912*)

2019

Pan, C.*, Schoppe, O.*, Parra-Damas, A.*, Cai, R., Todorov, M.I., Gondi, G., von Neubeck, B., Ghasemi, A., Reimer, M.A., Coronel, J., et al. (2019). Deep learning reveals cancer metastasis and therapeutic antibody targeting in whole body. bioRxiv, 541862. * These authors contributed equally.

7. Declaration of Author contributions

Research Article 1:
Pan, C.*, Cai, R.*, Quacquarelli, F.P.*, Ghasemigharagoz, A., Lourbopoulos, A., Matryba, P., Plesnila, N., Dichgans, M., Hellal, F., and Erturk, A. **Shrinkage-mediated imaging of entire organs and organisms using uDISCO**. A.E. designed and led all aspects of the project. **C.P.**, R.C., and F.P.Q. performed most of the experiments. A.G. performed the image rendering and developed algorithms for data analysis. **C.P.**, R.C., F.P.Q., and A.G. analyzed the data. A.L. interpreted data and performed the BMSC cultures, characterization, and transplantations; F.H. performed virus tracing; P.M. assisted first-clearing experiments; N.P. and M.D. supervised A.L. and F.H., respectively. A.E., **C.P.**, R.C., F.P.Q., and A.G. wrote the paper. All authors edited the paper.

Research Article 2:
Cai, R.*, **Pan, C.***, Ghasemigharagoz, A., Todorov, M.I., Forstera, B., Zhao, S., Bhatia, H.S., Parra-Damas, A., Mrowka, L., Theodorou, D., et al. **Panoptic imaging of transparent mice reveals whole-body neuronal projections and skull-meninges connections**. A.E. initiated and led all aspects of the project. R.C. and **C.P.** developed the method and conducted most of the experiments. R.C. A.G., **C.P.**, H.S.B., M.R., and B.M. analyzed data. M.I.T. stitched and analyzed the whole mouse body scans. A.P.D., B.F., S.Z. and L.M. helped to optimize the protocols. I.B., H.S.B., and S.L. helped to investigate skull–meninges connections. D.T. and M.K. contributed spinal cord injury experiments; C.B. and A.L., MCAO experiments; and A.X., B.K. and M.N., cisterna magna injection experiments. A.E., R.C. and **C.P.** wrote the paper. All the authors edited the manuscript.

Research Article 3:
Pan, C.*, Schoppe, O.*, Parra-Damas, A.*, Cai, R., Todorov, M.I., Gondi, G., von Neubeck, B., Ghasemi, A., Reimer, M.A., Coronel, J., et al. **Deep learning reveals cancer metastasis and therapeutic antibody targeting in whole body**. A.E. initiated and led all aspects of the project. **C.P.**, A.P.D. and R.C. performed the tissue processing, clearing and imaging experiments. R.C. and **C.P.** developed the whole-body nanobody labeling protocol. M.T. stitched and assembled the whole mouse body scans. O.S. and J.D.B developed the deep learning architecture and performed the quantitative analyses. A.G. performed the image rendering and parts of the data analysis. O.S. developed annotation tools and the custom-made object detector, M.A.R. annotated the data. G.G.,B.N. and R.Z., performed tumor transplantation experiments and bioluminescence imaging. B.K.G. helped with data interpretation. B.M. provided guidance in developing the deep learning architecture and helped with data interpretation. A.E., **C.P.** and O.S. wrote the manuscript. All the authors edited the manuscript.

Herewith, I confirm the contributions to the manuscripts.

Munich, 03.2019

PAN Chenchen	Dr. Ali Ertürk (supervisor)	Ruiyao Cai (Shared co-first author)
Dr. Francesca Paola Quacquarelli (Shared co-first author)	Dr. Arnaldo Parra-Damas (Shared co-first author)	Oliver Schoppe (Shared co-first author)